

การศึกษาโครงสร้างและสมบัติของวัสดุนาโนคอมพอสิตและผสม
ที่มีไคโตซานเป็นหลัก เพื่อประยุกต์เป็นวัสดุควบคุมการปล่อยยา
และพอลิเมอร์อิเล็กทรอนิกส์ชนิดแข็ง

นางสาวณัฐธิดา รักกะเปา

วิทยานิพนธ์นี้เป็นส่วนหนึ่งของการศึกษาตามหลักสูตรปริญญาวิทยาศาสตรดุษฎีบัณฑิต
สาขาวิชาเคมี
มหาวิทยาลัยเทคโนโลยีสุรนารี
ปีการศึกษา 2553

**STRUCTURE AND PROPERTIES OF CHITOSAN-
BASED NANOCOMPOSITE AND BLEND: FOR DRUG
CONTROLLED RELEASE AND SOLID POLYMER
ELECTROLYTE APPLICATIONS**

Natthida Rakkapao

**A Thesis Submitted in Partial Fulfillment of the Requirements for the
Degree of Doctor of Philosophy in Chemistry
Suranaree University of Technology
Academic Year 2010**

**STRUCTURE AND PROPERTIES OF CHITOSAN-BASED
NANOCOMPOSITE AND BLEND: FOR DRUG CONTROLLED
RELEASE AND SOLID POLYMER ELECTROLYTE
APPLICATIONS**

Suranaree University of Technology has approved this thesis submitted in partial fulfillment of the requirements for the Degree of Doctor of Philosophy.

Thesis Examining Committee


(Asst. Prof. Dr. Kunwadee Rangriwatananon)

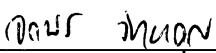
Chairperson


(Asst. Prof. Dr. Visit Vao-Soongnern)

Member (Thesis Advisor)


(Prof. Dr. Hiroshi Watanabe)

Member


(Assoc. Prof. Dr. Jatuporn Wittayakun)

Member


(Asst. Prof. Dr. Sanchai Prayoonpokarach)

Member


(Dr. Wut Dankittikul)

Acting Vice Rector for Academic Affairs


(Assoc. Prof. Dr. Prapun Manyum)

Dean of Institute of Science

ณัฐริดา รักกะเปา : การศึกษาโครงสร้างและสมบัติของวัสดุนาโนคอมพอสิตและผสมที่มีไคโตซานเป็นหลัก เพื่อประยุกต์เป็นวัสดุควบคุมการปล่อยยาและพอลิเมอร์อิเล็กโทรไลต์ชนิดแข็ง (STRUCTURE AND PROPERTIES OF CHITOSAN-BASED NANOCOMPOSITE AND BLEND: FOR DRUG CONTROLLED RELEASE AND SOLID POLYMER ELECTROLYTE APPLICATIONS) อาจารย์ที่ปรึกษา : ผู้ช่วยศาสตราจารย์ ดร.วิสิทธิ์ แวสูงเนิน, 234 หน้า.

“ไคโตซาน” จัดเป็นพอลิเมอร์จากธรรมชาติชนิดหนึ่ง ซึ่งมีการนำมาประยุกต์ใช้งานอย่างกว้างขวางและหลากหลาย หากแต่การประยุกต์ใช้วัสดุที่มีไคโตซานเป็นองค์ประกอบเพียงอย่างเดียวในงานบางชนิดยังด้อยประสิทธิภาพ อีกทั้งยังมีข้อจำกัดในสมบัติเชิงกายภาพและเชิงกล ส่งผลให้คุณสมบัติของพอลิเมอร์ชนิดนี้ยังไม่ดีพอที่จะตอบสนองในทุกๆ การใช้งาน ด้วยเหตุนี้เองงานวิจัยนี้จึงเกิดขึ้นเพื่อเอาชนะข้อจำกัดดังกล่าว โดยวัตถุประสงค์หลักของงานวิจัยนี้มุ่งเน้นในการเตรียมและพัฒนาวัสดุไคโตซานผสมชนิดใหม่ ซึ่งมีคุณสมบัติเหมาะสมสำหรับการประยุกต์ใช้งานที่เฉพาะเจาะจงตามต้องการ ซึ่งการพัฒนาดังกล่าวดำเนินไปด้วยวิธีที่ง่ายและไม่ซับซ้อน โดยการเติมอนุภาคดินเหนียวหรือพอลิเมอร์ชนิดอื่นลงไปผสม เพื่อปรับปรุงสมบัติต่างๆ ของไคโตซานให้มีความเหมาะสมและสอดคล้องกับการนำไปประยุกต์ใช้งานที่แตกต่างกัน โดยการพัฒนา ดังกล่าวดำเนินไปในสองแนวทางคือ (1) การพัฒนาวัสดุพอลิเมอร์นาโนคอมพอสิตของ ไคโตซาน/อนุภาคดินเหนียว (CS/MMT) เพื่อประยุกต์เป็นวัสดุควบคุมการปล่อยยา และ (2) การพัฒนาวัสดุพอลิเมอร์ผสมของ ไคโตซาน/พอลิเอทิลีนออกไซด์ (CS/PEO) เพื่อประยุกต์เป็นพอลิเมอร์อิเล็กโทรไลต์ชนิดแข็ง นอกจากนี้ยังศึกษาโครงสร้าง รวมถึงสมบัติต่างๆ ทั้งเชิงสัณฐานวิทยาและเชิงความร้อนของวัสดุไคโตซานผสมทั้งสองชนิดที่พัฒนาขึ้น รวมทั้งวิเคราะห์ความสัมพันธ์ระหว่างโครงสร้างและสมบัติต่างๆ ที่มีผลต่อประสิทธิภาพการควบคุมการปลดปล่อยยาของวัสดุนาโนคอมพอสิต CS/MMT และผลต่อประสิทธิภาพในการนำไฟฟ้าของวัสดุพอลิเมอร์ผสม CS/PEO ดังกล่าว เพื่อให้ได้วัสดุไคโตซานผสมที่มีประสิทธิภาพสูงสุดและมีความเหมาะสมกับงานที่ต้องการนำไปประยุกต์ใช้

ด้วยข้อจำกัดต่างๆ ในด้านการทดลอง งานวิจัยนี้จึงนำเทคนิคการจำลองแบบโมเลกุลด้วยคอมพิวเตอร์มาใช้ควบคู่ไปด้วย เพื่อช่วยอธิบายผลที่ได้จากการทดลองให้ชัดเจนยิ่งขึ้น นอกจากนี้ยังเพิ่มความเข้าใจและช่วยอธิบายปรากฏการณ์ต่างๆ ที่เกิดขึ้นในระดับอะตอมของวัสดุไคโตซานผสมทั้งสองชนิดข้างต้น อีกทั้งเทคนิคนี้ยังสามารถศึกษาพลวัตของโมเลกุลภายในวัสดุนาโน

คอมพอสิต CS/MMT และสามารถศึกษาพลวัตของไอออนในวัสดุพอลิเมอร์ผสม CS/PEO ดังกล่าวได้ ซึ่งข้อมูลดังกล่าวมานั้นยังไม่สามารถอธิบายได้อย่างชัดเจน โดยผลจากการทดลองเพียงอย่างเดียว

จากผลการทดลองพบว่าวัสดุนาโนคอมพอสิต CS/MMT ที่เตรียมได้ สามารถเพิ่มประสิทธิภาพการควบคุมการปลดปล่อยยา เมื่อเทียบกับการใช้วัสดุโคลโตซานเพียงอย่างเดียว และวัสดุนาโนคอมพอสิตซึ่งมีปริมาณ NH_3^+ ของโคลโตซาน เกินกว่าค่า Cationic Exchange Capacity (CEC) ของ MMT ซึ่งมักพบใน โครงสร้างการแทรกตัวของโคลโตซานใน MMT แบบสองชั้น นั้นมีความเหมาะสมในการนำไปประยุกต์เป็นวัสดุควบคุมการปลดปล่อยยา กลุ่มกรดได้ดีที่สุด แต่พบว่าไม่สามารถใช้วัสดุดังกล่าว ในการควบคุมการปลดปล่อยยา กลุ่มเบส เพราะอันตรกิริยาซึ่งเกิดขึ้นระหว่างกันนั้นค่อนข้างอ่อน

สำหรับวัสดุพอลิเมอร์ผสม CS/PEO ที่เตรียมขึ้น พบว่าสามารถเพิ่มประสิทธิภาพการนำไฟฟ้าได้ เมื่อเทียบกับการใช้พอลิเมอร์บริสุทธิ์ทั้งสองชนิดเป็นอิเล็กโทรไลต์เพียงอย่างเดียว โดยวัสดุพอลิเมอร์ผสมดังกล่าวให้ค่าการนำไฟฟ้าสูงสุดที่อัตราส่วน โดยโมลของ CS และ PEO เท่ากัน นอกจากนี้ยังพบว่าไอออนที่มีประจุ +1 มีความเหมาะสมในการใช้เป็น Doping Ion มากกว่า ไอออนที่มีประจุ +2 อันเนื่องมาจากอันตรกิริยา ระหว่าง ไอออน⁺¹/พอลิเมอร์ ที่อ่อนกว่าทำให้สามารถเคลื่อนที่ในพอลิเมอร์ผสมดังกล่าวได้อย่างอิสระ จึงให้ค่าการนำไฟฟ้าที่สูงกว่า

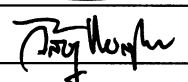
สาขาวิชาเคมี

ปีการศึกษา 2553

ลายมือชื่อนักศึกษา



ลายมือชื่ออาจารย์ที่ปรึกษา



NATTHIDA RAKKAPAO : STRUCTURE AND PROPERTIES OF
CHITOSAN-BASED NANOCOMPOSITE AND BLEND: FOR DRUG
CONTROLLED RELEASE AND SOLID POLYMER ELECTROLYTE
APPLICATIONS. THESIS ADVISOR : ASST. PROF. VISIT
VAO-SOONGNERN, Ph.D. 234 PP.

CHITOSAN/MONTMORILLONITE/NANOCOMPOSITE/POLY(ETHYLENE
OXIDE)/BLEND/DRUG/ION/SIMULATION

According to the disadvantage properties of pristine chitosan (CS), therefore frequently not good enough to fulfill all applications and limited its uses. To overcome this trouble, the main objective of this work focuses on the convenient and effective method to develop CS by adding of a second component (*i.e.* MMT clay and PEO), to create the novel CS-based materials with the target properties requirement. Accordingly, the Chitosan/Montmorillonite (CS/MMT) nanocomposite, suitable for drug controlled release application, and Chitosan/Poly(ethylene oxide) (CS/PEO) blend, suitable for solid polymer electrolyte application, were initiated and developed in this work. The structure, morphology, thermal property of these CS-based materials along with drug controlled release efficiency of CS/MMT nanocomposites and ionic conductive efficiency of CS/PEO blends were studied. The theoretical modeling and molecular simulation were also employed to fulfill the experimental findings and gain an inclusive understanding in atomistic level of these materials. Overall of this research can be summarized and established below.

CS/MMT nanocomposite exhibits the improvement in drug controlled release property of pristine CS. Accordingly, the bilayer CS/MMT nanocomposite with amount of NH_3^+ exceed the Cationic Exchange Capacity (CEC) of clay is most suitable for used as an acidic drug controlled release material. Although this material cannot be used for basic drug due to the rather weaker interaction between drug/CS/MMT.

CS/PEO blend also exhibits the improvement in ionic conductive efficiency of the pure polymers and the optimum blend composition such provides the highest ionic conductivity is the stoichiometric ratio of CS and PEO. Accordingly, the alkali metal ion is more suitable for used as a doping ion than the alkali earth metal ion associated to the weaker ion/polymers interaction to provide the freely moving of ions in the blends matrix.

School of Chemistry

Academic Year 2010

Student's Signature *Natthida Rakkaporn*

Advisor's Signature *Abhisit Vao*

ACKNOWLEDGEMENTS

I am grateful to my thesis advisor, Asst. Prof. Dr. Visit Vao-Soongnern, for his valuable advices, comments and suggestions for my thesis. I am also very thankful for thesis examining committee members for their efforts throughout the entire process. I really thank all professors at School of Chemistry, Suranaree University of Technology (SUT) for their kind attitude and providing me valuable knowledge. I would like to pay special thanks to Prof. Dr. Hiroshi Watanabe and Assoc. Prof. Dr. Yuichi Masubuchi as well as all members and staffs at Laboratory of Molecular Rheology, Institute for Chemical Research, Kyoto University, Japan for giving me the valuable advices, kind suggestions and providing me a good hospitality to join and work in their group. The gratitude is for all lecturers at Department of Chemistry, Maejo University who gave me valuable advices and knowledge when I did bachelor's degree. I am thankful to all members in Laboratory of Computational and Applied Polymer Science (LCAPS), and all graduate students and staffs at School of Chemistry, SUT for their support, encouragement and made this a fun time. I would like to thank the Office of the Higher Education Commission, Thailand for supporting by grant fund under the program Strategic Scholarships for Frontier Research Network for the Joint Ph.D. Program Thai Doctoral degree for this research. I would like to thank the National Nanotechnology Center (NANOTEC), National Science and Technology Development Agency (NSTDA), Thailand for the permission to use molecular simulation software through National Nanoscience Consortium (CNC) and

thank the NANOTEC for the financial support for the chitosan/clay nanocomposite project (Grant No. NN-B-22-m1-20-47-06). Last, but certainly not least, it is my pleasure to thank my beloved family for their support, believe, and encouragement.

Natthida Rakkapao

CONTENTS

	Page
ABSTRACT IN THAI.....	I
ABSTRACT IN ENGLISH.....	III
ACKNOWLEDGEMENTS.....	V
CONTENTS.....	VII
LIST OF TABLES.....	XIV
LIST OF FIGURES.....	XVI
LIST OF ABBREVIATIONS.....	XXVI
CHAPTER	
I INTRODUCTION.....	1
1.1 Research Objectives.....	7
1.2 Scope and Limitation of the Study.....	7
1.2.1 Chitosan/Montmorillonite (CS/MMT) Nanocomposite; for Drug Controlled Release Application.....	7
1.2.2 Chitosan/Poly(ethylene oxide) (CS/PEO) Blend; for Solid Polymer Electrolyte Application.....	9
II LITERATURE REVIEW.....	12
2.1 Chitosan.....	12
2.1.1 Availability of Chitosan.....	12
2.1.2 Structure, Properties and Characteristics of Chitosan.....	14

CONTENTS (Continued)

	Page
2.1.3 Applications of Chitosan.....	15
2.1.4 Modification of Chitosan.....	17
2.2 Chitosan/Montmorillonite (CS/MMT) Nanocomposite; for Drug Controlled Release Application.....	18
2.2.1 Controlled Release Drug Delivery.....	18
2.2.2 Potential and Limitation of Chitosan for Drug Controlled Release Application.....	20
2.2.3 Polymer/Layered Silicate Nanocomposite.....	22
2.2.4 Chitosan/Montmorillonite (CS/MMT) Nanocomposite.....	26
2.2.5 Potential of CS/MMT Nanocomposite for Drug Controlled Release Application.....	34
2.3 Chitosan/Poly(ethylene oxide) (CS/PEO) Blend; for Solid Polymer Electrolyte Application.....	37
2.3.1 Solid Polymer Electrolytes.....	37
2.3.2 Potential and Limitation of Chitosan for Solid Polymer Electrolyte Application.....	39
2.3.3 Poly(ethylene oxide).....	40
2.3.4 Potential and Limitation of Poly(ethylene oxide) for Solid Polymer Electrolyte Application.....	41
2.3.5 Chitosan/Poly(ethylene oxide) (CS/PEO) Blend.....	44

CONTENTS (Continued)

	Page
2.3.6 Potential of Chitosan/Poly(ethylene oxide) Blend for Solid Polymer Electrolyte Application.....	46
III COMPUTATIONAL MOLECULAR MODELING.....	49
3.1 Computational Chemistry.....	49
3.2 Molecular Dynamics (MD) Simulation.....	50
3.2.1 Theory in MD Simulations.....	50
3.2.2 Forcefields for MD Simulations.....	53
3.2.3 Periodic Boundary Conditions and Other Requirements.....	55
3.2.4 Structure and Dynamics from MD Simulation.....	58
3.2.4.1 Radial Distribution Function.....	58
3.2.4.2 Density Profile.....	59
3.2.4.3 Mean Square Displacement and Diffusion Coefficient.....	59
3.2.5 MD vs. Experiment.....	60
3.3 Mesoscopic Dynamic (MesoDyn) Simulation.....	61
3.3.1 Theory in MesoDyn Simulation.....	62
3.3.2 Dynamics of MesoDyn Simulation.....	63
3.3.3 Thermodynamics of MesoDyn Simulation.....	65
3.3.4 Parameterization: Mapping of Atomistic Level to Mesoscale Molecular Architecture.....	67

CONTENTS (Continued)

	Page
3.3.5 Numerics of MesoDyn Simulation.....	68
IV STRUCTURE, PROPERTIES AND DRUG CONTROLLED	
RELEASE EFFICIENCY OF CS/MMT NANOCOMPOSITE.....	69
4.1 Introduction.....	69
4.2 Research Methodology.....	71
4.2.1 Experimental Section.....	71
4.2.1.1 Materials and Apparatus.....	71
4.2.1.2 Sample Preparation.....	72
4.2.1.3 Characterization.....	73
4.2.2 Computational Section.....	75
4.2.2.1 Molecular Dynamics Simulation of Bulk Amorphous Chitosan and Salicylic Acid/Theophylline in Chitosan Matrix.....	75
4.2.2.2 Molecular Dynamics Simulation of SA/CS/MMT Nanocomposite.....	77
4.3 Results and Discussion.....	81
4.3.1 Experimental Section.....	81
4.3.1.1 Solubility of Acidic and Basic Drug in Chitosan Matrix.....	81

CONTENTS (Continued)

	Page
4.3.1.2 Sorption of Acidic and Basic Drug by Na ⁺ - Montmorillonite.....	87
4.3.1.3 Structure, Morphology and Thermal Stability of SA/CS/MMT Nanocomposites.....	89
4.3.1.4 <i>In vitro</i> Drugs-Released Study of SA/CS/MMT Nanocomposites.....	93
4.3.1.5 Structure, Morphology and <i>In vitro</i> Drugs-Released Study of Theophylline/Chitosan/Montmorillonite Materials.....	96
4.3.2 Computational Section.....	98
4.3.2.1 Molecular Dynamics Simulation of Bulk Amorphous Chitosan and Salicylic Acid/Theophylline in Chitosan Matrix.....	98
4.3.2.2 Molecular Dynamics Simulation of SA/CS/MMT Nanocomposites: Intercalation Structure.....	111
4.4 Concluding Remark.....	117
V STRUCTURE AND DYNAMICS OF ALKALI AND ALKALI EARTH METAL IONS DOPED CHITOSAN/POLY(ETHYLENE OXIDE) BLENDS.....	121
5.1 Introduction.....	121

CONTENTS (Continued)

	Page
5.2 Research Methodology.....	124
5.2.1 Experimental Section.....	124
5.2.1.1 Materials and Apparatus.....	124
5.2.1.2 Sample Preparation.....	124
5.2.1.3 Characterization.....	125
5.2.2 Computational Section.....	128
5.2.2.1 Molecular Dynamics Simulation of CS/PEO Blends	128
5.2.2.2 Mesoscopic Dynamics Simulation of CS/PEO Blends.....	130
5.2.2.3 Molecular Dynamics Simulation of Ions Incorporated CS/PEO Blend.....	132
5.3 Results and Discussion.....	134
5.3.1 Experimental Section.....	134
5.3.1.1 Thermodynamics of Polymer Blend.....	134
5.3.1.2 Miscibility of CS/PEO Blends Containing no Salt...	135
5.3.1.3 CS and PEO Doped with Metal Ions.....	143
5.3.1.4 CS/PEO Blends Doped with Metal Ions.....	144
5.3.1.5 Mobility of Ions in CS/PEO Blends.....	148
5.3.2 Computational Section.....	161
5.3.2.1 Molecular Dynamic Simulation of CS/PEO Blends.	162

CONTENTS (Continued)

	Page
5.3.2.2 Mesoscopic Dynamics Simulation of CS/PEO Blends.....	170
5.3.2.3 Molecular Dynamics Simulation of Ion Doped CS/PEO Blend.....	172
5.4 Concluding Remark.....	177
VI SUMMARY	180
REFERENCES	184
APPENDICES	207
APPENDIX A CALCULATION OF MOLAR VOLUME OF CHITOSAN AND POLY(ETHYLENE OXIDE) REPEATING UNIT...	208
APPENDIX B PAPER PUBLICATION.....	210
CURRICULUM VITAE	234

LIST OF TABLES

Table	Page
2.1 Chemical and biological properties of chitosan (Patel, 2006).....	15
2.2 Change in d_{001} spacing of CS nanocomposite depending on the ratio of CS to MMT (Darder <i>et al.</i> , 2003).....	28
2.3 Mechanical property of CS/Nanoclay composites (Xu <i>et al.</i> , 2006).....	29
2.4 Amounts of polymer, salt and its conductivity at room temperature (Mohamad <i>et al.</i> , 2007).....	48
4.1 Solubility parameters of CS, CS/SA and CS/THP	100
5.1 Atomistic simulation details of CS/PEO blends.....	129
5.2 Input parameters of CS/PEO blends for MesoDyn calculations.....	132
5.3 Equilibrium melting temperatures (T_m^e), degree of crystallinity (X_c^m) and stability parameters (ϕ) of PEO crystal for pure PEO and CS/PEO blends.....	138
5.4 Content of acetic acid remaining in 0.6 g of CS/PEO blends at $w_{PEO} =$ 0.2 with/without doped metal ions.....	149
5.5 Activation energy (kJ/mol) evaluated from Arrhenius plots for CS/PEO blend ($w_{PEO} = 0.2$) with/without doped K^+ and Ca^{2+}	160
5.6 Atomistic simulation details and results of CS/PEO blends.....	162
5.7 Energy components for CS/PEO Blends.....	166

LIST OF TABLES (Continued)

Table		Page
5.8	Correlation between FTIR data and the radial distance (r) from radial distribution functions (RDFs) analysis of CS/PEO blends.....	169
5.9	Coordination number (CN) and radial distance (r) of CS and PEO functional groups in the first coordination shell of K^+ and Ca^{2+}	175

LIST OF FIGURES

Figure		Page
2.1	Chitosan production flow diagrams.....	13
2.2	Structural units of chitin and chitosan. Chitin consists mostly of <i>N</i> -acetyl- <i>D</i> -glucosamine (GlcNAc) units. During the preparation of chitosan most units are deacetylated to <i>D</i> -glucosamine (GlcN) units (Mao <i>et al.</i> , 2004).....	15
2.3	Correlation of appropriate drug concentration and time with therapeutic range (Alvarez-Lorenzo <i>et al.</i> , 2004).....	19
2.4	Dissolution profiles of salicylic acid from 10% drug-loaded CS films prepared from CS of different grades in distilled water, (■) VL-82%DD, (▲) VL-100%DD, (■) H-80-85%DD, and (△) H-100%DD (VL and H referred to very low and high molecular weight CS, respectively) (Puttipipatkachorn <i>et al.</i> , 2001).....	21
2.5	Different types of composite arising from the interaction of layered silicates and polymers: (a) phase separated microcomposite; (b) intercalated nanocomposite and (c) exfoliated nanocomposite (Alexandre <i>et al.</i> , 2000).....	23
2.6	WAXD patterns and TEM images of three different types of nanocomposites (Sinha Ray <i>et al.</i> , 2003).....	24
2.7	Structure of 2:1 phyllosilicates (Sinha Ray <i>et al.</i> , 2003).....	25

LIST OF FIGURES (Continued)

Figure		Page
2.8	XRD patterns of (a) Na ⁺ -MMT, (b) CS film, and nanocomposites prepared from CS:MMT ratios of (c) 0.25:1, (d) 0.5:1, (e) 1:1, (f) 2:1, (g) 5:1, and (h) 10:1. The Scheme shows the intercalation of CS into Na ⁺ -MMT (Darder <i>et al.</i> , 2003).....	27
2.9	Basal spacings and Carbon content of CS-MMT of different loadings (0-1000% of the CEC applied) (An <i>et al.</i> , 2007).....	28
2.10	Formation of hydrogen bonds between CS and MMT (Wang <i>et al.</i> , 2005).....	30
2.11	TEM micrographs of nanocomposites with CS/Clay ratios of 12:1 (X. Wang <i>et al.</i> , 2006).....	31
2.12	Standard release rates of drug from pure CS and CS-MMT under cyclic on-off switching of electrostimulation (Liu <i>et al.</i> , 2008).....	35
2.13	Drug release profiles from the composite and interaction products in HCl 0.1 M (mean values \pm s.d.; n = 3 and VHS is referred to the pharmaceutical grade MMT) (Aguzzi <i>et al.</i> , 2010).....	36
2.14	Schematic illustrations of interactions between CS, OFL and MMT (Hua <i>et al.</i> , 2010).....	36
2.15	Schematic of polymer-based batteries. The thin-film composites are very flexible and can be folded or rolled into various geometries (Mendoliaa <i>et al.</i> , 1995).....	38

LIST OF FIGURES (Continued)

Figure	Page
2.16 Solvation of a salt by a PEO chain. The primary interaction is between the ether oxygens and the cation (Vincent, 1995).....	41
2.17 Typical polarized micrographs of spherulites of PEO (Huang <i>et al.</i> , 2001).....	42
2.18 Polarized micrographs of CS/PEO blend films with difference %w/w of PEO in blends; 100 × magnification and scale bar of 200 μm (Zivanovic <i>et al.</i> , 2007).....	45
2.19 (a) The relative elongation-at-break; ε and (b) the tensile strength; σ of CS/PEO blends films depending on the PEO content (M_v of PEO is 600,000 g/mol) (Alexeev <i>et al.</i> , 2000).....	45
2.20 Variation of the conductivity and activation energy as a function of salt content (Idris <i>et al.</i> , 2005).....	46
3.1 Periodic boundary conditions in Molecular Dynamics (CCL.NET, 1996).....	57
4.1 Chemical structures of (a) salicylic acid, (b) salicylate anion and (c) theophylline.....	70
4.2 (a) XRD patterns and (b) scanning electron photomicrographs of CS films with different %w/w of salicylic acid loading.....	82
4.3 FTIR spectra of (a) salicylic acid powder, (b) 70 %w/w salicylic acid loaded chitosan film, and (c) pristine chitosan flake.....	83

LIST OF FIGURES (Continued)

Figure		Page
4.4	Correlation of the protonation degree (<i>P</i>) of chitosan and pH of the solution versus the chitosonium salicylate concentration.....	85
4.5	(a) XRD patterns and (b) scanning electron micrographs of CS films with different % w/w of theophylline loading.....	86
4.6	XRD patterns of pristine Na ⁺ -MMT and Na ⁺ -MMT with different %w/v of salicylic acid loading.....	87
4.7	XRD patterns of pristine Na ⁺ -MMT and Na ⁺ -MMT with different %w/v of theophylline loading.....	88
4.8	XRD patterns of pristine MMT and SA/CS/MMT nanocomposites with different initial CS:MMT molar ratios.....	89
4.9	(a) Intercalation of CS into the interlayer of Na ⁺ -MMT through the cationic exchange process and (b) schematic representation of CS intercalated into the interlayer of Na ⁺ -MMT as a bilayer.....	90
4.10	TEM images of (a) pristine MMT and (b) SA/CS/MMT nanocomposites with initial CS:MMT molar ratio of 2:1.....	91
4.11	TGA curves in the temperature range of 30-900°C (under an nitrogen atmosphere) of (a) pure Na ⁺ -MMT and SA/CS/MMT nanocomposites with different initial CS:MMT molar ratios of (b) 0.5:1, (c) 1:1, and (d) 2:1. The DTA curve corresponding to the CS:MMT of 2:1 (e).....	92

LIST OF FIGURES (Continued)

Figure		Page
4.12	Dissolution profiles of salicylic acid from bulk chitosonium salicylate film and SA/CS/MMT nanocomposites with different initial CS:MMT molecular ratios of 0.5:1, 1:1, and 2:1.....	94
4.13	Comparison of XRD patterns before and after dissolution of SA/CS/MMT nanocomposites with different initial CS:MMT molar ratios; (a) 0.5:1, (b) 1:1, and (c) 2:1.....	95
4.14	XRD patterns bulk 30 %w/w THP/CS and THP/CS/MMT materials with different %w/w of MMT/CS (A: Anhydrous THP, M: Monohydrate THP).....	97
4.15	Dissolution profiles of theophylline from bulk THP/CS film and THP/CS/MMT materials with different amount of MMT.....	98
4.16	The atomistic models of (a) chitosan/salicylic acid and (b) chitosan/theophylline complexes.....	99
4.17	X-Ray scattering function of chitosan.....	101
4.18	X-Ray diffraction pattern of chitosan.....	101
4.19	Radial distribution function of chitosan.....	102
4.20	Radial distribution functions of intermolecular interaction between active functional groups of chitosan; representing the hydrogen atom of NH ₂ , C3-OH and C6-OH relative to the distance of nitrogen atom of NH ₂ and oxygen atom of C3-OH and C6-OH.....	103

LIST OF FIGURES (Continued)

Figure		Page
4.21	Potential and nonbonded energy vs simulation time of the CS/SA system.....	104
4.22	Mean-square displacements of salicylic acid and theophylline in chitosan matrix.....	105
4.23	Chemical structures of (a) chitosan and (b) salicylic acid.....	107
4.24	Radial distribution functions for CS/SA complex when considered CS as a H-donor; representing the hydrogen atom of NH ₂ , C3-OH and C6-OH of CS relative to the distance of oxygen atom of C=O, C1-OH and C3-OH of SA.....	107
4.25	Radial distribution functions for CS/SA complex when considered SA as a H-donor; representing the hydrogen atom of COOH and C3-OH of SA relative to the distance of nitrogen atom of NH ₂ along with oxygen atom of C3-OH and C6-OH of CS.....	109
4.26	Intermolecular hydrogen bonding between active functional groups of salicylic acid and chitosan proposed from RDFs analysis. The numbers adjacent to the bonds respect to the priority of H-bond formation.....	110

LIST OF FIGURES (Continued)

Figure		Page
4.27	Representative MD snapshots (pictures not scale) of Salicylate anion/Chitosonium/Montmorillonite, viewed along the y direction (a) SA ₀ /CS ₁₆ /MMT (b) SA ₄ /CS ₂₀ /MMT (c) SA ₈ /CS ₂₄ /MMT (d) SA ₁₂ /CS ₂₈ /MMT.....	112
4.28	The electrostatic hydrogen bonding between R-NH ₃ ⁺ head groups of chitosan and oxygen of the MMT surface proposed from MD simulation.....	113
4.29	Density profile of the SA ₀ /CS ₁₆ /MMT system at 298 K (only nitrogen and aluminium atoms); the interlayer spacing is 16.24 Å.....	114
4.30	Density profiles of different SA/CS/MMT systems at 298 K.....	115
4.31	Density profiles of the SA/CS/MMT systems at 298 K (only SA and CS).....	115
4.32	The schematic representation of SA/CS/MMT system.....	118
4.33	The schematic representation of THP/CS/MMT system.....	119
5.1	Solution blending of chitosan and poly(ethylene oxide).....	122
5.2	WAXD patterns for CS/PEO blends. The numbers adjacent indicate the CS content, w_{CS} (in %w/w).....	136
5.3	Hoffman-Weeks plots of the melting temperature (T_m) and crystallisation temperature (T_c), for CS/PEO blends with different w_{CS}	138

LIST OF FIGURES (Continued)

Figure		Page
5.4	Melting point depression analysis for CS/PEO blends. The interaction energy density $B = -1.06 \text{ cal/cm}^3$, obtained from the slope of the plot.....	140
5.5	FTIR spectra of CS, PEO and CS/PEO blends.....	142
5.6	Depression of the melting temperature of fully equilibrated PEO crystalline (T_m^c) in undoped and ion-doped CS/PEO blends.....	145
5.7	Degree of crystallinity (X_c^m) of PEO in undoped and ion-doped blends.....	145
5.8	Degradation temperature of CS in undoped and ion-doped CS/PEO blends.....	146
5.9	FTIR spectra of K^+ doped into CS, PEO and CS/PEO blends.....	147
5.10	FTIR spectra of Ca^{2+} doped into CS, PEO, and CS/PEO blends.....	147
5.11	Frequency (f) dependence of dynamic dielectric constant (ϵ') and dielectric loss (ϵ'') of CS/PEO blend ($w_{PEO} = 0.2$) with/without doped metals. The ϵ' and ϵ'' data at various temperatures are double-logarithmically plotted against f	150
5.12	The Cole-Cole plots of CS/PEO blends ($w_{PEO} = 0.8$), with/without doped K^+ and Ca^{2+} (at 318 K).....	153

LIST OF FIGURES (Continued)

Figure		Page
5.13	The normalized conductivity (at 318 K) for a series of CS/PEO blends with different weight fraction of PEO (w_{PEO}), with/without doped K^+ and Ca^{2+}	154
5.14	Variation of the real part of conductivity (σ') as a function of frequency at indicated temperatures for CS/PEO blend ($w_{\text{PEO}} = 0.2$) with/without doped K^+ and Ca^{2+}	156
5.15	Real (σ') and imaginary (σ'') parts of complex conductivity for neat CS/PEO blend ($w_{\text{PEO}} = 0.2$) with/without doped K^+ and Ca^{2+} at indicated temperatures. The solid lines are fits of Eqs. (5.12) and (5.13) to the data.....	158
5.16	Ac conductivity master plots at different temperatures for CS/PEO blend ($w_{\text{PEO}} = 0.2$) with/without doped K^+ and Ca^{2+}	159
5.17	BNN plots: $\log \sigma_0$ vs. $\log (1/\tau_e)$ for CS/PEO blend ($w_{\text{PEO}} = 0.2$) with/without doped K^+ and Ca^{2+}	159
5.18	Arrhenius plots for CS/PEO blend ($w_{\text{PEO}} = 0.2$) with/without doped K^+ and Ca^{2+} ; ω_c evaluated from the maximum in $\partial^2 \sigma' / \partial \omega^2$, while σ_0 and τ_e obtained from the fitting with Eqs. (5.12) and (5.13).....	160
5.19	Flory-Huggins interaction parameters (χ) as a function of the PEO weight fraction (w_{PEO}) in CS/PEO blends.....	164

LIST OF FIGURES (Continued)

Figure		Page
5.20	Change in the enthalpy of mixing (ΔH_m) as a function of PEO weight fraction (w_{PEO}) in CS/PEO blends.....	165
5.21	Radial distribution functions (RDFs) of the CS/PEO blends with different PEO weight fraction (w_{PEO}).....	168
5.22	Iso-density profiles for CS/PEO blends with different PEO weight fractions (w_{PEO}). Green (light) and red (dark) color represent CS and PEO component, respectively.....	170
5.23	Mesophase order parameters (P_i) of both CS and PEO portion as a function of the PEO weight fractions (w_{PEO}) in the CS/PEO blends....	172
5.24	Radial distribution functions (RDFs) for the system of K^+ - and Ca^{2+} -doped CS/PEO blends with $w_{\text{PEO}} = 0.2$. RDF represents the relative distances between metal ions (K^+ and Ca^{2+}) and N atom in amino (NH_2) group, O atom in hydroxyl (C3-OH) and hydroxymethyl (C6-OH) groups of CS as well as PEO ether oxygen atom.....	173
5.25	Radial distribution functions (RDFs) for undoped CS/PEO blends at $w_{\text{PEO}} = 0.2$ and for CS/ K^+ /PEO and CS/ Ca^{2+} /PEO blends.....	176

LIST OF ABBREVIATIONS

$\langle A \rangle$	averaged property
Abs	Absorbance
A_i	cross-sectional area of the box
Å	Angstrom
Å ³	cubic Angstrom
Å ⁻¹	per Angstrom
<i>ca.</i>	circa (approximately)
cf.	compare
cm ⁻¹	per centimeter, wave number
cm ² /s	square centimeter per second
C	concentration
C_∞	characteristic ratio
C_n	characteristic ratio ($n \rightarrow \infty$)
C ^α	alpha carbon
C3-OH	hydroxyl group connected to C3 of chitosan
C6-OH	hydroxymethyl group connected to C6 of chitosan
Ca ²⁺	Calcium cation
CEC	cation exchange capacity
CED	cohesive energy density
CN	coordination number

LIST OF ABBREVIATIONS (Continued)

COMPASS	condensed-phase optimized molecular potentials for atomistic simulation studies
CS	chitosan
d	wall-to-wall distance or interlayer spacing
D	diffusion coefficient
DFT	density functional theory
DP	degree of polymerization
DSC	differential scanning calorimeter
<i>e.g.</i>	exempli gratia (for example)
<i>et al.</i>	et alia (and other)
eV	electron Volt
E	identity matrix
E	potential energy
E_{coh}	cohesive energy
f_w	weight fraction
fs	femtosecond
F	force
FTIR	Fourier Transform Infrared Spectroscopy
$g(g^+, g^-)$	<i>gauche</i> (<i>gauche</i> plus, <i>gauche</i> minus)
g/cm^3	gram per cubic centimeter
g/mol	gram per mole
$g(r)$	atomic pair distribution function

LIST OF ABBREVIATIONS (Continued)

G	super generator matrice
h	Planck constant
\hbar	reduced Planck constant or Dirac constant ($= h/2\pi$)
h_i	interlayer height
<i>i.e.</i>	id est (that is)
J	Joule
k	wave-vector
k_B, k	Boltzmann constant ($\sim 1.38 \times 10^{-23} \text{ J K}^{-1}$)
kcal/mol	kilocalorie per mole
kcal/mol/Å	kilocalorie per mole per Angstrom
kJ/mol	kiloJoule per mole
kV	kiloVolt
K	Kelvin
K^+	potassium cation
l	bond length
m	atomic mass
mA	milliAmpere
mbar	millibar
meq	milliequivalent
min	minute
mJ/m^2	milliJoule per square meter
ml/min	milliliter per minute

LIST OF ABBREVIATIONS (Continued)

M , mol/dm ³	mole per cubic decimeter or Molar
M_m	monomer molecular weight
M_p	polymer molecular weight
M_w	weight average molecular weight
M_v	viscosity average molecular weight
MC	Monte Carlo
MD	Molecular Dynamics
MesoDyn	Mesosopic Dynamics
MHz	megahertz
MM	Molecular Mechanics
MMT	Montmorillonite
MO	Molecular Orbital
MSD	mean square displacement
n	the number of repeating unit of polymer
nm	nanometer
ns	nanosecond
N_{meso}	MesoDyn chain length
NMR	nuclear magnetic resonance
NPT	isothermal-isobaric ensemble
NVE	microcanonical ensemble
NVT	canonical ensemble
pm	picometer

LIST OF ABBREVIATIONS (Continued)

ps	picoseconds
P	degree of protonation
P_i	order parameters
PCFF	polymer consistent force field
PEO	poly(ethylene oxide)
q	charge
Q	X-Ray structure factor
QM	quantum mechanics
QM/MM	quantum mechanics/molecular mechanics
QSPR	quantitative structure property relationship
r	radial distance
rpm	round per minute
R	gas constant ($\sim 8.314 \text{ J mol}^{-1} \text{ K}^{-1}$)
R_g	radius of gyration
RDF	radial distribution function
RIS	rotational isomeric state
RPA	random phase approximation
s	second
S/cm	Siemen per centimeter
SA	Salicylic acid
SEM	Scanning Electron Microscope
t	(1) time, (2) <i>trans</i> conformation

LIST OF ABBREVIATIONS (Continued)

T	absolute temperature (K)
T_c	crystallization temperatures
T_d	degradation temperature
T_g	glass transition temperature
T_m	melting temperature
T_m^0	melting temperature of pure polymer
T_m^e	melting temperature of fully equilibrated/developed crystalline
$T_m^{0,e}$	melting temperature of fully equilibrated/developed crystalline of pure polymer
TEM	Transmission Electron Microscopy
TGA	Thermogravimetric Analysis
THP	Theophilline
u	statistical weight
U	statistical weight matrix
USP	United States Pharmacopeia
UV/VIS	ultraviolet/visible
v	velocity
V	volume
V_i	interlayer volume
V_{mol}	molar volume
V_{Au}, V_{Bu}	molar volume of the repeating unit of polymer A and B

LIST OF ABBREVIATIONS (Continued)

w_{CS}	weight fraction of chitosan in blend
w_{PEO}	weight fraction of poly(ethylene oxide) in blend
W/m^2	Watt per square meter
WAXD	wide-angle X-ray diffraction
X_c^m	crystallinity
XRD	X-ray diffraction
z	coordination number
Z	partition function
%DA	degree of acetylation
%DD	degree of deacetylation
% v/v	percent volume/volume
% w/v	percent weight/volume
% w/w	percent weight/weight
°C	degree Celcius
°C/min	degree Celcius per minute
ΔE_{mix}	energy of mixing
ΔG	Gibbs free energy change
ΔH	enthalpy change
ΔH_{Bu}	molar enthalpy of fusion
ΔH_m	enthalpy of fusion
ΔH_m	Enthalpy of mixing
ΔH_m^0	enthalpy of fusion for the perfect crystalline

LIST OF ABBREVIATIONS (Continued)

ΔS	entropy change
Δt	time step
θ	(1) bond angle, (2) angle between chords
Φ	torsion angle
δ	Hildebrand's solubility parameter
ε	depth of Lennard-Jones potential
ε_0	permittivity of free space
ϕ	(1) crystalline stability, (2) torsion angle
γ	surface energy
σ	zero point of Lennard-Jones potential
σ, ω	the first-, second order interaction parameters
π	pi ($\pi = 3.14159265$)
ρ	density
μs	micro second
ν	volume fraction
$\nu^{-1} \epsilon_{ij}$	interacting energies between pair of interacting bead types
χ	Flory-Huggins interaction parameter
$\chi_{critical}$	critical value of Flory-Huggins interaction parameter
ψ	torsion angle
$\ F_i\ $	block diagonal matrices

CHAPTER I

INTRODUCTION

Polymer offers a wide variety of properties that make it ideal material for broad range of applications. However the choice of an ideal polymeric material for a new application in the real world is complex. The new applications usually come with a range of specific property. Unfortunately, it is often difficult to find out a polymer with the entire properties requirement. Chitosan is one of several polymers facing to this trouble.

Chitosan (CS) is a natural cationic biopolymer produced commercially by deacetylation of chitin, the second most abundant polymer in nature after cellulose (Ahmad *et al.*, 2004; Wu *et al.*, 2010). One perceptible improvement of this substance is that it can be obtained from ecologically natural sources, namely crab and shrimp shell wastes. CS has widely received considerable attention according to its remarkable fascinating properties. It has a wide array of pharmaceutical applications due to its low production costs, biocompatibility, biodegradability, low toxicity, high charge density, and mucoadhesion properties (Dodane *et al.*, 1998). Moreover, the monomer of CS consists of amino and hydroxyl functional groups with lone pair electrons. The existence of lone pair electrons enables the chelation of a proton donor, thus CS satisfies one of the criteria to act as a polymer host for solid polymer electrolytes (Morni *et al.*, 1999). Due to the reactive amino/hydroxyl groups, this polycation can interact with some other polyanions to form gels (Hamman, 2010),

moreover, they are amiable to chemical modification and form chelation complexes with metal ions (Krajewska, 2001; Ogawa *et al.*, 1993). Hence, CS is suitable for diverse applications from industrial manufacturing to medicine, *e.g.* absorbant for heavy metal removal, waste water purification, cosmetic and shampoo additive, ion exchange media, films controlling drug release (Ravi Kumar, 2000; Rinaudo, 2006) along with solid polymer electrolyte in the fabrication of proton batteries (Kadir *et al.*, 2009; 2010). However, there are some disadvantages of CS, such as, poor thermal stability, poor physical, mechanical, and gas barrier properties, low ionic conductivity, along with its limited solubility in water (Wu *et al.*, 2010). Those are frequently not good enough for pristine CS to meet the wide ranges of applications.

There is growing interest in modification of CS by several physical and chemical processes. A convenient and effective method to modify CS is addition of a second component into CS host polymer to create a new CS-based material with the target properties appropriated for specific applications (Wu *et al.*, 2010). In this work, the preparations of new CS-based materials with the target properties requirement were initiated and performed base on two approaches, (I) Nanocomposite by adding of clay particles and (II) Blend by adding of a flexible polymer, poly(ethylene oxide). This can enlarge the applications and increase the valuable of CS.

There are several recent literatures reporting about the enhancement of CS properties by using polymer layered silicate nanocomposites technology (Han *et al.*, 2010; Katti *et al.*, 2008; Wang *et al.*, 2005; 2008; Wu *et al.*, 2010). This technology has been proved to be an effective way to improve the mechanical, electrical and thermal properties of polymer (Wu *et al.*, 2010). Montmorillonite (MMT) is one of a number of layered silicate (*i.e.* clay) minerals within the smectite group widely

observed in various parts of the world. It is biocompatible and has been acceptable to use in medicine and pharmacology purposes (Ducrotte *et al.*, 2005; Lin *et al.*, 2002; 2006; Wai *et al.*, 1966). MMT is the most extensively used silicate in polymer nanocomposites. It is constructed with repeating triple-layer sheets composed of two tetrahedral silica sheets fused to an edge-shared octahedral sheet of alumina with a thickness of ~1 nm and a length of approximately 100 nanometers (Usuki *et al.*, 2001). Stacking of the layers creates a gap between the layers called the interlayer or gallery. Isomeric substitution within the layers generates negative charges that are counterbalanced by some cations, such as Na⁺ in the gallery (Ray *et al.*, 2003). Because of the weak interactions between the stacking layers, the cations inside the gallery can be easily exchanged by other cations.

In this work, the nanocomposites of Chitosan/Montmorillonite (CS/MMT) were prepared by direct mixing method of clay particles into CS acidic solution. The cationic biopolymer, CS, has been reported to directly intercalate into the MMT interlayer through the cationic exchange and hydrogen bonding processes (Darder *et al.*, 2003; 2005; Tan *et al.*, 2008) to initiate the novel bionanocomposite material with fascinating properties. CS/MMT nanocomposites have attracted considerable interest since they combine the structural, physical and chemical properties of both inorganic and organic materials. These nanocomposites are expected to have novel properties because the nanometric scale on which the nanoclay particles, with their plate-like shape, would alter physical and chemical properties, enhance mechanical and barrier properties, and improve thermal stability of this polymeric material (Darder *et al.*, 2003; 2005; Tan *et al.*, 2008).

The science of drug delivery is always affected by the choice of materials which act as carriers and one of the best choices is a natural biopolymer, *i.e.* CS. Several drug controlled release materials are based on pure CS (Dodane *et al.*, 1998; Ravi Kumar, 2000; Rinaudo, 2006), but the physical and mechanical properties along with drug controlled release efficiency is still required to improve. Therefore, the CS/MMT nanocomposite is a promising material to overcome this trouble, along with it is biocompatible, biodegradable and low cost. One effort of this work is to develop the CS/MMT nanocomposite with designed drug controlled release property. Accordingly, the MMT particles may act as barrier as well as implantable drug reservoir to provide on-demand release of drug molecules thus may improve the drug efficiency and reduce its side effect. To design the CS/MMT nanocomposite for drug controlled release application, a clue for choosing the proper drug to provide the highest controlled release efficiency is very important. Accordingly, two types of drug, acidic and basic drug, were investigated in this work; hence, salicylic acid and theophylline were considered as the representative models of acidic and basic drug, respectively. Technologically, this work has been driven by an interest in understanding of the correlation between the structure of CS/MMT nanocomposites and the drug diffusion-controlled phenomena. The main key issue is the development of this nanocomposite material appropriate for controlled release drug delivery application.

Blending is another approach that has been promisingly promoted in this work to improve physical, mechanical and conductivity properties of CS. Generally, CS has been blended with other polymers (Castro *et al.*, 2011; Khoo *et al.*, 2003; Thanpitcha *et al.*, 2006; Yin *et al.*, 2006). It has been shown that the blended CS-based materials

exhibited combinations of properties that could not be obtained by individual polymers and the mechanical and biological properties will be varied in the blended materials and compositions. Since molecular chains of CS are too rigid ($T_g \sim 203^\circ\text{C}$) (Sakurai *et al.*, 2000), one approach to improve the physical and mechanical properties of CS is the blending with another flexible polymer, poly(ethylene oxide) (PEO; $T_g \sim -59^\circ\text{C}$) (Rakkapao *et al.*, 2011), this may improve its rigidity. Besides, due to the existence of the ether oxygen in PEO structure, this polymer can interact with others including CS, giving rise to a homogeneous polymeric blend (Donoso *et al.*, 2007; Li *et al.*, 2010; 2011; Neto *et al.*, 2005; Zivanovic *et al.*, 2007). CS/PEO blend films provide additional functionality compared to the pure polymer films. PEO may contribute to the formation of colorless and more flexible film, while CS may improve mechanical property, reduce crystallinity and water solubility of PEO (Zivanovic *et al.*, 2007).

PEO, a synthetic polyether, is one of the most widely studied host polymer matrix for potential use as an electrolyte in high energy-density batteries (Cheung *et al.*, 2003; Reddy *et al.*, 2006; Kang *et al.*, 2001; Sukeshini *et al.*, 1998). However, the disadvantage of PEO as a salt host is due to a large degree of its crystallinity at room temperature. This becomes a major barrier for ions transport and the polymer electrolytes always end up with an undesirably low ionic conductivity (Gadjourova *et al.*, 2001; Matoba *et al.*, 2004). Moreover, the crystallinity also enhances the rigidity of the polymer and reduces the transparency of the materials (Fuentes *et al.*, 2007). Therefore, much research effort has been invested in modifying PEO to prevent it from crystallization (Reddy *et al.*, 2006; Park *et al.*, 2006; Pitawala *et al.*, 2007; Singh *et al.*, 2008). Accordingly, blending with amorphous CS may facilitate

the decrease of PEO crystallinity, giving an ideal material appropriate for solid polymer electrolyte application (Donoso *et al.*, 2007; Idris *et al.*, 2005; 2007). CS/PEO blends exhibit good electrical conductivity as well as the mechanical and chemical stability those are the most important properties of materials to be used as solid polymer electrolytes. Thus, the flexibility needed for getting films useful in microdevices or the transparenence in a given light frequency range required for electroptical applications may be also important in the development of new ion-conducting materials.

To design the CS/PEO blend for solid polymer electrolyte application, a clue for choosing the proper ions for doping into CS/PEO blend, to provide the highest ionic conductivity, is very important. Accordingly, two types of doping ions, alkali and alkali earth were investigated. The miscibility of CS/PEO blends and the effects of doping the alkali and alkali earth metal ions on the structure/property of the blends were studied to discuss a role of the ion valency in the interaction between the metal ions and each polymer component. In this respect, K^+ and Ca^{2+} were selected as the doping ions due to their similarity in both size and mass ($Z_K = 19$, $M_K = 39$ g/mol; $Z_{Ca} = 20$, $M_{Ca} = 40$ g/mol). Additionally, the compositional effect of the CS:PEO ratio on the ionic conductivity of the blends films was also discussed. Overall of this work provide us with a clue for developing of a novel CS/PEO blend film suitable for solid polymer electrolyte applications.

In addition to the experimental techniques, the computational molecular simulations were also employed in this work to provide deeper understanding at the microscopic level which cannot be achieved with the experimental techniques. Molecular simulations could improve our ability to describe the interaction and

diffusion phenomena of small penetrants (*i.e.* drugs and ions) as well as the change in segmental motion of polymers backbone in the CS-based mixtures in several ways. Molecular simulations provide an excellent opportunity to directly study the influence of dynamic heterogeneity of both CS/MMT nanocomposite and CS/PEO blend respectively on drugs and ions diffusion behavior. In this respect, the computational molecular modeling, including Molecular Dynamics (MD) and Mesoscopic Dynamics (MesoDyn) simulations, was employed in this study.

1.1 Research Objectives

1. To study the effects of drug-CS/drug-MMT interactions along with structural properties of CS/MMT nanocomposites on its controlled release efficiency.
2. To study the effects of ion-polymer interactions along with miscibility of CS/PEO blends on the ionic conductive efficiency.
3. To apply computational molecular modeling techniques to gain more understanding at the atomistic and mesoscopic level of CS/MMT nanocomposite and CS/PEO blend as well as study the diffusion behavior of small penetrants (*i.e.* drugs and ions) within these CS-based mixtures.

1.2 Scope and Limitation of the Study

1.2.1 Chitosan/Montmorillonite (CS/MMT) Nanocomposite; for Drug Controlled Release Application

Experimental Section

CS/MMT nanocomposite was prepared using solution casting method. The controlled release processes of Salicylic acid (SA) and Theophylline (THP) from the

nanocomposite matrix were considered as the representative models of acidic and basic drug molecules, respectively. The drug-polymer and drug-filler (*i.e.* clay particle) interactions along with the correlation between the structure of CS/MMT nanocomposites and the drug diffusion-controlled phenomena were studied. The overall results attempt to provide a clue for developing a novel CS/MMT nanocomposite suitable for drug controlled release application.

Characterization

- **Fourier Transform Infrared Spectroscopy (FTIR):** was employed to elucidate the interaction between CS-SA, CS-THP as well as CS-MMT.
- **Powder X-ray Diffraction (XRD):** was employed to verify the intercalation structure of CS chains inside MMT interlayer achieved in CS/MMT nanocomposites and also to study the crystallization of drugs in CS matrix.
- **Scanning Electron Microscope (SEM):** was employed to determine the crystallinity of SA and THP in bulk CS thereby specifying the dissolution limit of drugs in CS matrix.
- **Transmission Electron Microscopy (TEM):** was employed to verify the intercalation structure of CS chains inside MMT interlayer.
- **Thermogravimetric Analysis (TGA):** was employed to study thermal stability of CS/MMT nanocomposites.
- **Dissolution Apparatus:** was employed to study the controlled release efficiency of SA and THP from bulk CS and CS/MMT nanocomposite.

Computational Section

The computational atomistic simulations were performed in this work.

- **Molecular Dynamics (MD) Simulation:** MD simulation was employed to study the structure, interaction and diffusion of drug molecule in bulk CS matrix. MD simulation was performed at atomistic level of CS and its complex with SA and THP, *i.e.* a model of drug controlled release system. The results provided a detailed description of a disordered state of CS chains as well as an interaction with the model drugs. Moreover, MD simulation was also employed to study the intercalation structure of SA/CS/MMT nanocomposite. MD simulation was also used to investigate the basal spacing and to probe the layering behavior and interlayer structure of the SA/CS/MMT nanocomposite.

1.2.2 Chitosan/Poly(ethylene oxide) (CS/PEO) Blend; for Solid Polymer Electrolyte Application

Experimental Section

CS/PEO blends with several compositions were prepared with solution casting by using aqueous acetic acid as solvent. The miscibility of CS/PEO blends and the effects of doping the alkali and alkali earth metal ions into CS/PEO blend on the structure/property of the blend were studied. In this respect, K^+ and Ca^{2+} were considered as the model alkali and alkali earth ions due to their similarity in both size and mass. Accordingly, a role of the ion valency in the interaction between the metal ions and each polymer component can be discussed. Moreover, the effect of CS:PEO composition on the ionic conductivity was also investigated. The overall of this work

attempts to provide a clue for developing of a novel CS/PEO blend film suitable for solid polymer electrolyte application.

Characterization

- **Differential Scanning Calorimetry (DSC):** was employed to study the miscibility and thermal property of CS/PEO blends with/without doped metal ions.
- **Wide-Angle X-ray Diffraction (WAXD):** was employed to verify the decrease of PEO crystallinity by blending with CS and also employed to study the crystallinity of ionic salts doped in CS/PEO blends matrix.
- **Fourier Transform Infrared (FTIR) Spectroscopy:** was employed to elucidate the interaction between CS-PEO, CS-Ions, PEO-Ions as well as CS-PEO-Ions.
- **Nuclear Magnetic Resonance (NMR) Spectroscopy:** was employed to investigate the remaining amount of acetic acid (casting solvent) in the samples.
- **Dielectric/Conductive Measurement:** was employed to study the dielectric property and ionic conductivity correlated with the diffusion behavior of ions within the CS/PEO blend matrix.

Computational Section

The simulation techniques employed in this study consist of two parts: (1) the calculation via Molecular Dynamic (MD), (2) Mesoscopic Dynamic (MesoDyn) simulations. Materials Studio 4.2 simulations (Accelrys, 2007) package provided by National Nanotechnology Center of Thailand is the software used for MD and MesoDyn simulations.

- **Atomistic Simulation:** MD simulation was conducted for a series of CS/PEO blends with/without doped K^+ and Ca^{2+} , intending to study the miscibility of CS/PEO blends as well as the diffusion behavior and/or complex formation of ions within the blend matrix. Since the MD simulation is not possible to cover the length scale of phase separation in blends, it is necessary to combine MD technique with the mesoscopic simulation technique to study the phase morphology of this CS/PEO blend.
- **Mesoscale Simulation:** MesoDyn simulation was employed to simulate the phase separation dynamics of the CS/PEO blends. This approach is based on the dynamic variant of mean-field density functional theory.

CHAPTER II

LITERATURE REVIEW

2.1 Chitosan

Chitosan (CS) is a natural cationic biopolymer consequent commencing the hydrolysis of chitin, the second most abundant polymer in nature after cellulose (Ahmad *et al.*, 2004; Wu *et al.*, 2010). One perceptible improvement of this substance is that it can be obtained from ecologically sound natural sources, namely crab and shrimp shell wastes. Chitin accounts for approximately 70% of the organic components in such shells (Satpathy, 2008). In the world, several million tons of chitin is harvested annually. CS is prepared from chitin to obtain a more reactive polymer. The term CS is used when chitin could be dissolved in weak acid (Satpathy, 2008).

2.1.1 Availability of Chitosan

Chitin is isolated from shells of crustacean (for example: shrimp, crab and lobster) by treating the shells with 2.5 N NaOH at 75°C and with 1.7 N HCl at room temperature for 6 hours. CS is prepared by deacetylation of chitin. Deacetylation can be done by alkaline treatment or by enzymatic reaction. The alkaline deacetylation is carried out by treating chitin with NaOH at high temperature. The degree of deacetylation increases with increasing temperature or NaOH concentration.

Chang *et al.* showed that the optimum deacetylation can be done by mixing 23 ml of 60% NaOH per gram of chitin at 170°C (Chang *et al.*, 1997). Chitin deacetylation by enzymatic reaction was examined by Martinou *et al.* They demonstrated that chitin deacetylase isolated from *Mucor rouxii* has been used successfully to deacetylate chitin almost completely (98%) (Martinou *et al.*, 1995).

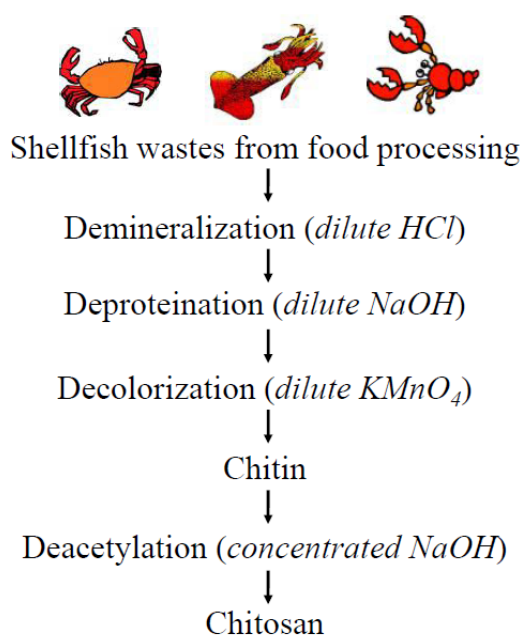


Figure 2.1 Chitosan production flow diagrams.

The CS polymer differs from chitin in that a majority of the *N*-acetyl groups in CS is hydrolyzed. The degree of hydrolysis has a significant effect on the solubility and rheological properties of the polymer. The amino group on the polymer has a pKa of 6.3 (Wang *et al.*, 2006a). At low pH, the polymer is soluble, with the sol-gel transition occurring at approximate pH 7. The pH sensitivity coupled with the reactivity of the primary amino groups makes CS a unique polymer for drug delivery applications (Patel *et al.*, 1996). CS is now available commercially in various

molecular weights (50-2,000 kDa) and different degree of deacetylation (40%-90%) (Varma, 2010). Changing the reaction conditions during the manufacture of CS from chitin can alter the degree of deacetylation (%DD) and molecular weight (MW) of CS.

2.1.2 Structure, Properties and Characteristics of Chitosan

Chitosan (poly [β -(1,4)-2-amino-2-deoxy-D-glucopyranose]) can be prepared by partial *N*-deacetylation of chitin with alkaline. The molecular formula is $C_6H_{11}O_4N$ and its structure is shown in Figure 2.2. The polymer is composed of *D*-glucosamine (GlcN) and *N*-acetyl-*D*-glucosamine (GlcNAc) units (Sato *et al.*, 1998). Chitin and CS have similar but not the same chemical structure. Chitin is made up of a linear chain of acetylglucosamine groups while CS is obtained by removing enough acetyl groups (CH_3-CO) for the molecule to be soluble in most diluted acids. This process is called deacetylation. The actual difference between chitin and CS is the acetyl content of the polymer. CS has one primary amino and two free hydroxyl groups for each C6 building unit to form extensive intra and inter-molecular hydrogen bonding (Aranaz *et al.*, 2010). Due to the easy availability of free amino groups in CS, it carries a positive charge and thus in turn reacts with many negatively charged surfaces/polymers (Sahoo *et al.*, 2010).

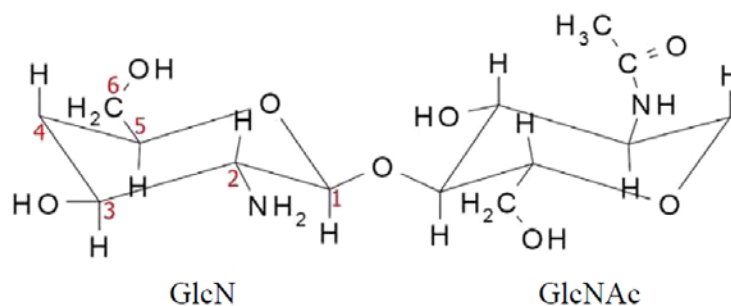


Figure 2.2 Structural units of chitin and chitosan. Chitin consists mostly of *N*-acetyl-*D*-glucosamine (GlcNAc) units. During the preparation of chitosan most units are deacetylated to *D*-glucosamine (GlcN) units (Mao *et al.*, 2004).

Table 2.1 Chemical and biological properties of chitosan (Patel, 2006).

Chemical properties of Chitosan	Biological properties of Chitosan
Cationic polyamine	Biocompatibility
High charge density at pH < 6.5	Natural polymer
Adheres to negatively charged surfaces	Safe and non-toxic
Forms gels with polyanions	Haemostatic
High MW linear polyelectrolyte	Biodegradable to body constituents
Viscosity, high to low	Bacteriostatic/Fungistatic
Chelates certain transitional metals	Spermicidal
Amiable to chemical modification	Anticancerogen
Reactive amino/hydroxyl groups	Anticholestermic

2.1.3 Applications of Chitosan

The intriguing properties of CS have been known for many years and this polycationic polymer has been used in the fields of agriculture, industry and medicine. Some of the industrial uses of CS are enlisted as follow (Bhupendra, 2009; Peniston *et al.*, 1970).

- Waste water purification
- Stabilizing oil spills
- Stabilizing fats in food preparation
- Antibacterial protection for deeds
- Flavor stabilizer
- Stabilizes perishable fruits/vegetables
- Ion exchange media
- Bacterial immobilizer
- Cosmetic and shampoo additive
- Tableting excipient
- Absorbant for heavy metal removal

Due to its good biocompatibility and low toxicity, CS has received considerable attention as a possible pharmaceutical excipient in recent decades for both conventional excipient applications as well as in novel application. CS has been extensively examined in the pharmaceutical industry for its potential in the development of drug delivery systems. It is presently considered as novel drug carrier material, as noted from the large number of studies published over the last few years.

Some of the general applications of CS in pharmaceutical fields are (Mia, 2003):

- Diluents in direct compression of tablets
- Binder in wet granulation
- Slow-release of drugs from tablets and granules
- Drug carrier in microparticle systems
- Films controlling drug release
- Preparation of hydrogels, agent for increasing viscosity in solutions

- Wetting agent, and improvement of dissolution of poorly soluble drug substances
- Disintegrant
- Bioadhesive polymer
- Site-specific drug delivery (*e.g.* to the stomach or colon)
- Absorption enhancer (*e.g.* for nasal or oral drug delivery)
- Biodegradable polymer (implants, microparticles)
- Carrier in relation to vaccine delivery or gene therapy

2.1.4 Modification of Chitosan

Although CS has been widely used for several applications, there are some disadvantages, such as poor mechanical properties, low thermal stability and poor water resistance and gas barrier properties along with its limited solubility in water (it requires dilute acidic solutions for dissolution). All of these disadvantages are frequently not good enough for pristine CS to meet those wide ranges of applications (Wu *et al.*, 2010). A convenient and effective method to overcome this drawback is to add of a second component thereby creating new CS-based materials with the target properties appropriate for specific applications. In this work, the preparations of new CS-based materials with the target properties requirement were performed on the basis of two approaches (I) Nanocomposite by adding of clay particles and (II) Blend by adding of a flexible polymer, poly(ethylene oxide).

Chitosan/Montmorillonite (CS/MMT) Nanocomposite: There are some recent literatures that reported the enhancement of CS properties by using polymer layered silicate nanocomposites (PLSNs) technology (Han *et al.*, 2010; Katti *et al.*, 2008;

Wang *et al.*, 2005; 2008; Wu *et al.*, 2010). An appreciable increase in the stability of CS films has been obtained by coverage with organosilicate layers. An attempt in this work has been made to develop a biocompatible composites film from CS by incorporating the nanoclay, montmorillonite (MMT), particles to improve the drug controlled release efficiency. MMT layers may act as barrier as well as implantable drug reservoirs to provide on-demand release of drug molecules.

Chitosan/Poly(ethylene oxide) (CS/PEO) Blend: Blending has been promoted in this work to improve the physical and mechanical properties as well as ionic conductivity of CS thereby aiming to apply this CS-based blend as a solid polymer electrolyte. Accordingly, a conductive and flexible polymer, PEO, is the most promising candidate of the blending partner. It has been shown that blending PEO with CS does not lead to a phase separation (Mohamad *et al.*, 2007). Since CS chains are too rigid (Sakurai *et al.*, 2000), blending with flexible polymer PEO may reduce its rigidity and improve physical and mechanical properties of the films. At the same time, amorphous CS chains also facilitate a decrease of PEO crystallinity giving an appropriated material for solid polymer electrolyte application (Donoso *et al.*, 2007; Idris *et al.*, 2005; 2007).

2.2 Chitosan/Montmorillonite (CS/MMT) Nanocomposite; for Drug Controlled Release Application

2.2.1 Controlled Release Drug Delivery

Controlled drug delivery technology is one of the frontier areas of science, which involves multidisciplinary scientific approach, contributing to human health care. These delivery systems offer numerous advantages compared with conventional

dosage forms. A number of significant advances has been made in the development of the new material technologies for optimizing drug delivery. To maximize the efficacy and safety of medication treatment, drug delivery systems should be capable of regulating the rate of drug release and/or targeting the drug to a specific site. Efficient drug delivery systems should provide a desired delivery rate of the therapeutic dose at the most appropriate time and place in the body as shown in Figure 2.3 (Alvarez-Lorenzo *et al.*, 2004) to prolong the duration of pharmacological action, reduce the adverse effects, minimize the dosing frequency, and enhance the patient compliance. To control the moment at which delivery should begin as well as the appropriate drug release rate, the following three approaches have been developed.

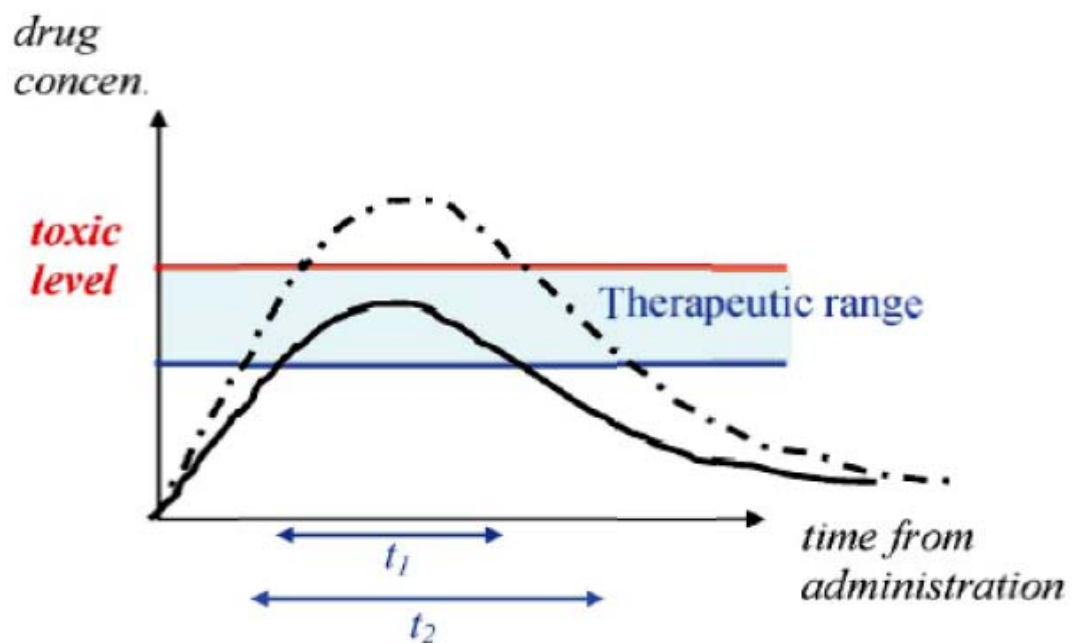


Figure 2.3 Correlation of appropriate drug concentration and time with therapeutic range (Alvarez-Lorenzo *et al.*, 2004).

- *Rate-programmed drug delivery*: the drug diffusion from the system has to follow a specific rate profile.
- *Activation-modulated drug delivery*: the drug release is activated by some physical, chemical or biochemical processes.
- *Feedback-regulated drug delivery*: the drug release rate is regulated by the concentration of a triggering agent, such as a biochemical substance, concentration of which is itself dependent on the drug concentration in the body.

2.2.2 Potential and Limitation of Chitosan for Drug Controlled Release

Application

CS has been the subject of interest for its use as a polymeric drug carrier material in dosage form design due to its appealing properties such as biocompatibility, biodegradability, low toxicity and relatively low production cost from abundant natural sources (Hamman, 2010). CS has been widely used for drug carrying devices in controlled drug delivery systems. Drug-polymer dispersion can be utilized to accomplish coating of non-pariel seeds, yielding a matrix for diffusion-mediated controlled drug release. In addition, a drug-polymer matrix film may be adaptable for transdermal drug delivery. The incorporation of drug into a CS matrix to form a monolithic device can expand the use of this biopolymer. Up to date, the studies of drug-loaded CS films focused on release behavior of the drug from CS matrix films. Depending on the amount of CS, film thickness, and dissolution medium, the liberation of drug from the CS films varied from fast release to slow release. (Puttipipatkachorn *et al.*, 2001).

Puttipipatkachorn *et al.* have studied the controlled release behavior of acidic and basic drugs by CS. Four different grades of CS varying in molecular weight (MW) and degree of deacetylation (%DD) were used to prepare CS films along with salicylic acid and theophylline that were incorporated into cast CS films as model acidic and basic drugs, respectively. The results confirmed that the occurring of the acidic drug-polymer interaction prevails to present the sustained release behavior, whereas no basic drug-polymer interaction emerged (thereby giving fast release behavior). Moreover, it was suggested that the swelling property and dissolution characteristics of the polymer films (refers to MW of CS), pK of drugs and especially drug-polymer interaction (refers to %DD of CS) were important factors governing drug release patterns from CS. The dissolution profiles of salicylic acid from drug-loaded CS films are shown in Figure 2.4. (Puttipipatkachorn *et al.*, 2001).

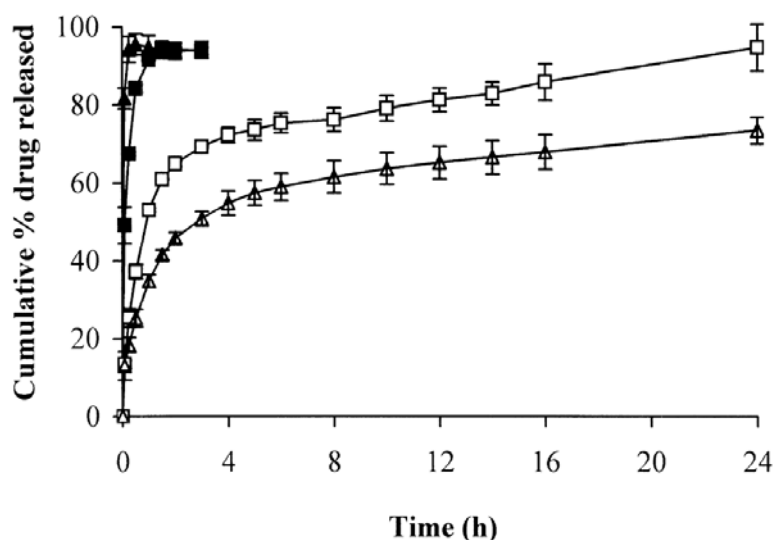


Figure 2.4 Dissolution profiles of salicylic acid from 10% drug-loaded CS films prepared from CS of different grades in distilled water, (■) VL-82%DD, (▲) VL-100%DD, (■) H-80-85%DD, and (△) H-100%DD (VL and H referred to very low and high molecular weight CS, respectively) (Puttipipatkachorn *et al.*, 2001).

However the drug incorporated CS films still has some disadvantages including poor physical and mechanical properties, high drug permeability and water uptake along with the ionic interaction between drug and CS is low and too weak to control the drug release (Boonsongrit *et al.*, 2006; Hamman, 2010). To overcome this limitation, several physical and chemical methods have been proposed to improve the CS properties and make it more suitable for drug controlled release applications, such as the functional groups modification (Le Tien *et al.*, 2003), ionic cross-linking (Shu *et al.*, 2002(a&b)), blending (Xu *et al.*, 2007) and grafting (Sokker *et al.*, 2009) with other polymers, along with using polymer/layered silicate nanotechnology (Aguzzi *et al.*, 2010; Hua *et al.*, 2010; Liu *et al.*, 2008). An improvement of CS by polymer/layered silicate nanotechnology is promising, and this method is conveniently and very effectively utilized in this work.

2.2.3 Polymer/Layered Silicate Nanocomposite

Polymer/layered silicate nanocomposite (PLSN) is the new family of composite materials frequently exhibits a remarkable improvement of the material properties as compared with the individual polymer or conventional micro- and macro-composite materials (Ray *et al.*, 2003; 2005). The improvements include a high storage modulus, both in solid and melt state, an increase in tensile and flexible properties, a decrease in gas permeability and flammability, an increase in heat distortion temperature, an increase in biodegradability rate of biodegradable polymers, and so forth (Krishnamoorti *et al.*, 1996). The main reason for these improvements is interfacial interaction between the polymer matrix and clay due to the nanodispersion of silicate layers not achieved in conventional microcomposites.

Generally, these composites are classified into three different types, depending on the relative distribution/dispersion of the stacks of clay platelets. (Alexandre *et al.*, 2000).

- *Phase separated microcomposite*: (or flocculated microcomposite) The intercalated and stacked silicate layers flocculate to some extent due to the hydroxylated edge-edge interactions of the silicate layers (Figure 2.5a).
- *Intercalated nanocomposite*: An insertion of polymer chains into a layered silicate structure occurs in a crystallographically regular fashion, with a repeating distance of few nanometers, regardless of polymer to clay ratio (Figure 2.5b).
- *Exfoliated nanocomposite*: The individual silicate layers are separated in the polymer matrix by average distances that depended only on the clay loading (Figure 2.5c).

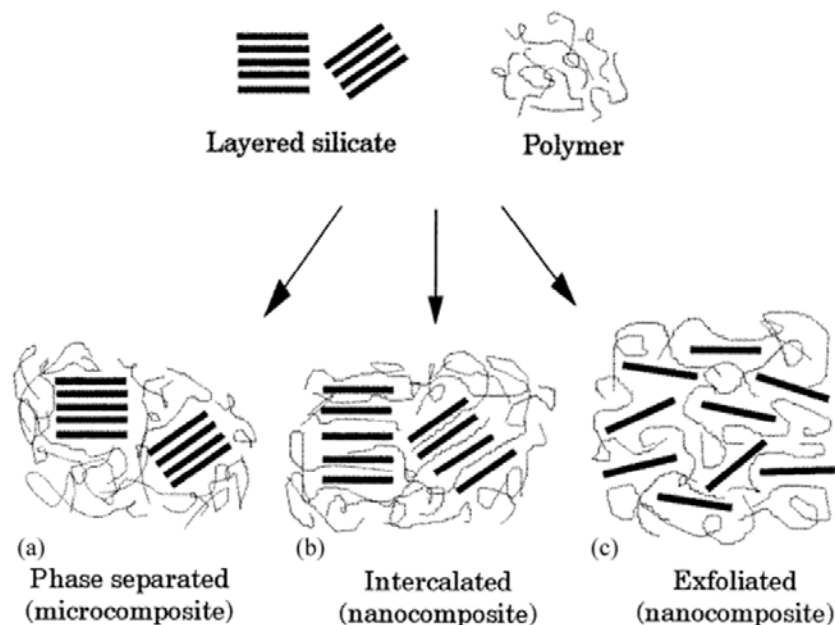


Figure 2.5 Different types of composite arising from the interaction of layered silicates and polymers: (a) phase separated microcomposite; (b) intercalated nanocomposite and (c) exfoliated nanocomposite (Alexandre *et al.*, 2000).

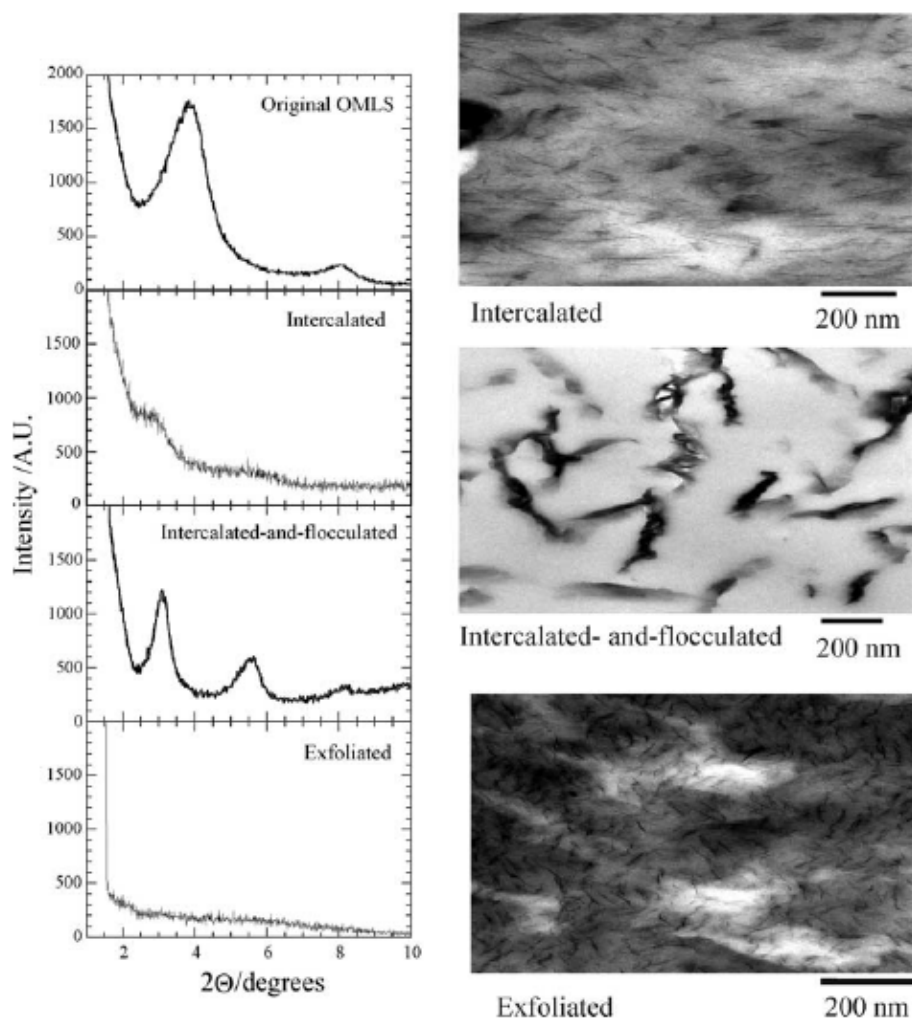


Figure 2.6 WAXD patterns and TEM images of three different types of nanocomposites (Ray *et al.*, 2003).

Montmorillonite (MMT) is one of the mostly used layered silicates for preparation of polymer/layered silicate nanocomposite (PLSN). MMT is a smectite clay and belongs to the 2:1 layered or phyllosilicates family: Its chemical formula is $(\text{Na,Ca})_{0.33}(\text{Al,Mg})_2(\text{Si}_4\text{O}_{10})(\text{OH})_2 \cdot n\text{H}_2\text{O}$. Their crystal structure consists of layers made up of two tetrahedral coordinated silicon atoms fused to an edge-shared octahedral sheet of either aluminum or magnesium hydroxide as shown in Figure 2.7. The layer thickness is around 1 nm, and the lateral dimensions of these layers may

vary from 85 nm to 150 nm (Usuki *et al.*, 2001). Stacking of the layers leads to a regular van der Waals gap between the layers called the interlayer or gallery. Isomorphic substitution within the layers (for example, Al^{3+} being replaced by Mg^{2+} or Fe^{2+} , or Mg^{2+} being replaced by Li^+) generates negative charges that are counterbalanced by alkali and alkaline earth cations situated inside the galleries. The moderate surface charge known as the cation exchange capacity (CEC) is about 110 mequiv/100 g. This charge is not locally constant, but varies from layer to layer, and must be considered as an average value over the whole crystal (Kennedy, 1990; Ray *et al.*, 2003). Layered silicates have two types of structure: tetrahedral-substituted and octahedral-substituted. In the case of tetrahedrally substituted layered silicates the negative charge is located on the surface of silicate layers, and hence, the polymer matrices can interact more readily with tetrahedrally-substituted material than with octahedrally-substituted material (Ray *et al.*, 2003; 2005).

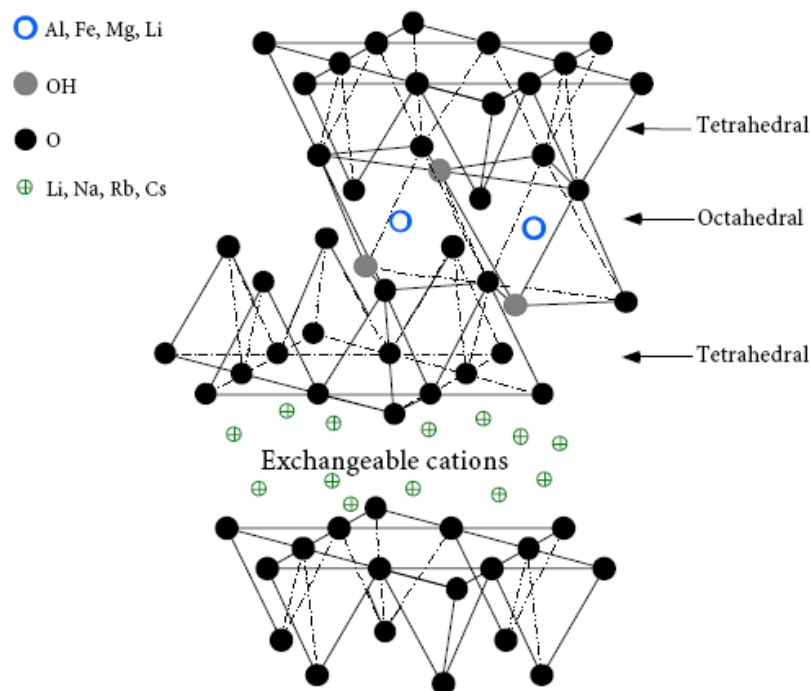


Figure 2.7 Structure of 2:1 phyllosilicates (Ray *et al.*, 2003).

The characteristics of layered silicates generally considered for the preparation of PLSN are: The first is the ability of the silicate particles to disperse into the interlayers spacing. The second is the ability to modify their surface chemistry through ion exchange reactions with organic and inorganic cations. These two characteristics are interrelated since the degree of dispersion of layered silicate in a polymer matrix depends on the interlayer cation. The MMT mineral usually contains hydrated Na^+ or K^+ ions. Obviously, in this pristine state, this layered silicate is only miscible with hydrophilic polymers, such as poly(ethylene oxide) (PEO) (Aranda *et al.*, 1992), poly(vinyl alcohol) (PVA) (Greenland, 1963), and CS (Darder *et al.*, 2003; 2005). To modify MMT to be miscible with hydrophobic polymers, one must convert the normally hydrophilic silicate surface to an organophilic one, making the intercalation of many hydrophobic polymers possible (Hussain *et al.*, 2006).

2.2.4 Chitosan/Montmorillonite (CS/MMT) Nanocomposite

CS/MMT nanocomposite is a material of increasing interest because of their structural and functional behavior. The preparation of CS/MMT nanocomposites was established by Darder *et al.* (2003) using a solution casting method with varying amounts of added clay. The research effort is made for enhancement of long-term stability of CS by intercalation of this biopolymer into the MMT interlayer gallery. Accordingly, they reported that the intercalation was made by mono- or bilayers of CS chains depending on the relative amount of CS with respect to the cationic exchange capacity of the clay. As shown in Figure 2.8, the XRD patterns of pristine MMT, pure CS film, and the corresponding nanocomposite films confirmed the intercalation of the CS polymer in the silicate galleries, showing the decrease in 2θ

values with increase in the CS/clay ratio. Table 2.2 shows the d_{001} spacings obtained from XRD patterns and an increase in d_{001} spacing of silicate galleries with the CS/clay ratio. Moreover, the intercalation of the cationic biopolymer CS in MMT gallery provided compact and robust three-dimensional nanocomposites with anion exchange capacity. (Darder *et al.*, 2003; 2005).

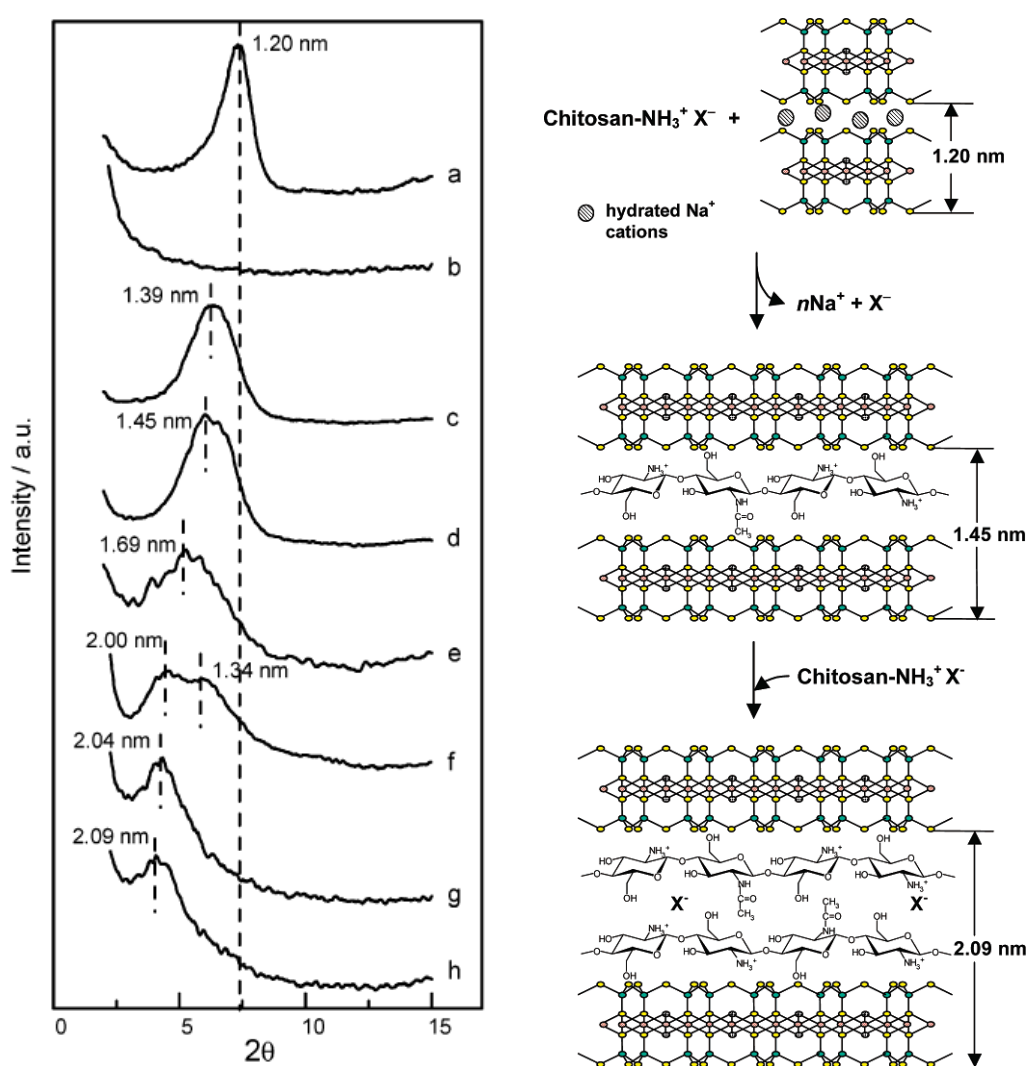


Figure 2.8 XRD patterns of (a) Na⁺-MMT, (b) CS film, and nanocomposites prepared from CS:MMT ratios of (c) 0.25:1, (d) 0.5:1, (e) 1:1, (f) 2:1, (g) 5:1, and (h) 10:1. The Scheme shows the intercalation of CS into Na⁺-MMT (Darder *et al.*, 2003).

Table 2.2 Change in d_{001} spacing of CS nanocomposite depending on the ratio of CS to MMT (Darder *et al.*, 2003).

CS : MMT ratio	d_{001} Spacings (nm)	Δd_{001} Spacings (nm)
Pristine MMT	1.20	-
0.25 : 1	1.39	0.19
0.5 : 1	1.45	0.25
1 : 1	1.69	0.49
2 : 1	2.00	0.80
5 : 1	2.04	0.84
10 : 1	2.09	0.89

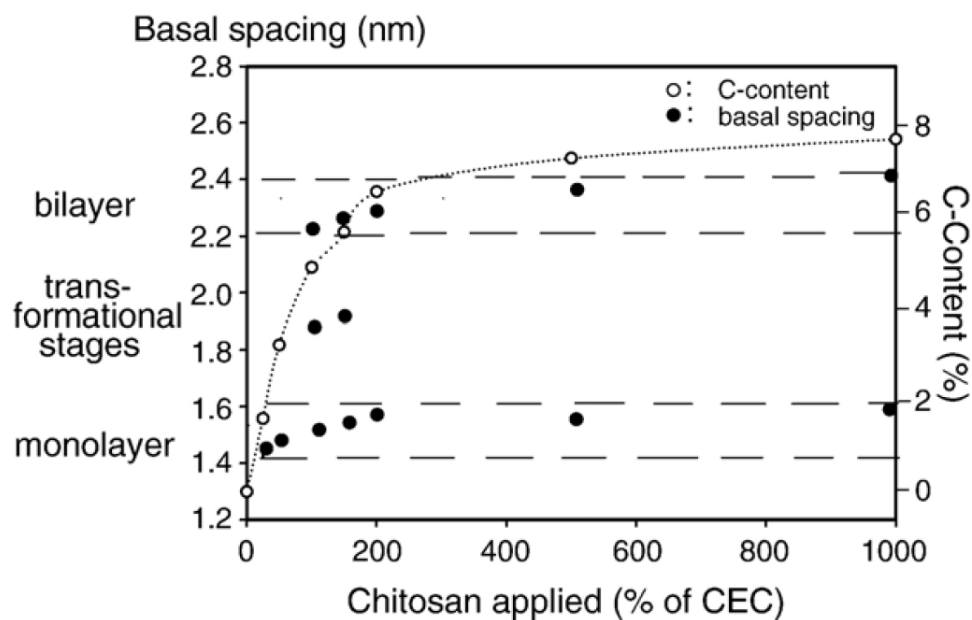


Figure 2.9 Basal spacings and Carbon content of CS-MMT of different loadings (0-1000% of the CEC applied) (An *et al.*, 2007).

An and Dultz have proposed the important key parameter expressing the correlation between the uptake content of CS and the nanocomposites structure. The results of this work showed that when the uptake of CS is up to 152% (CS unit to the CEC of MMT) resulting in occurring of anion exchange capacity of CS/MMT nanocomposites. A monolayer is formed in MMT at low CS loadings (24.7% and 49.5% uptake), for an uptake up to 96.8%, a bilayer structure is observed and becomes more dominant at higher CS loadings. The basal spacing and Carbon content of CS-MMT of different loadings were shown in Figure 2.9. Additionally, a monolayer of CS was also formed on the external surface of MMT. (An *et al.*, 2007).

Table 2.3 Mechanical property of CS/Nanoclay composites (Xu *et al.*, 2006).

Materials	Tensile strength (MPa)	Elongation at break (%)
Pure CS	40.62 ± 0.84	13.14 ± 3.85
1% MMT	54.98 ± 4.83	8.72 ± 0.97
3% MMT	65.67 ± 2.20	10.81 ± 0.52
5% MMT	44.51 ± 3.91	8.98 ± 1.21

The morphology and properties of CS/MMT nanocomposites have been reported in several literatures. Wang *et al.* found that an intercalated/exfoliated nanostructure was formed at low MMT content and an intercalated/flocculated nanostructure was formed at high MMT content (Wang *et al.*, 2005). The related result was also found by Xu *et al.* They indicated that at very low MMT content (< 5 %w/w MMT) the nanoclay was exfoliated along with the CS matrix, and the intercalation/exfoliation occurred when the MMT content is above 5 %w/w, accordingly the surface roughness increased on addition of small amount clay.

Moreover, they also reported that tensile strength of the film was enhanced and elongation at break decreased on addition of clay into the CS matrix, as shown in Table 2.3 (Xu *et al.*, 2006).

Wang *et al.* have shown that the mono-dispersed clay improved the thermal stability and enhanced the hardness and elastic modulus of the matrix systematically with an increase of clay loading. Moreover, they also established that the existence of acetic acid residue in CS matrix affects the crystallinity, thermal stability and mechanical properties of CS. The structure of CS/MMT nanocomposites with/without acetic acid were proposed as shown in Figure 2.10 (Wang *et al.*, 2005).

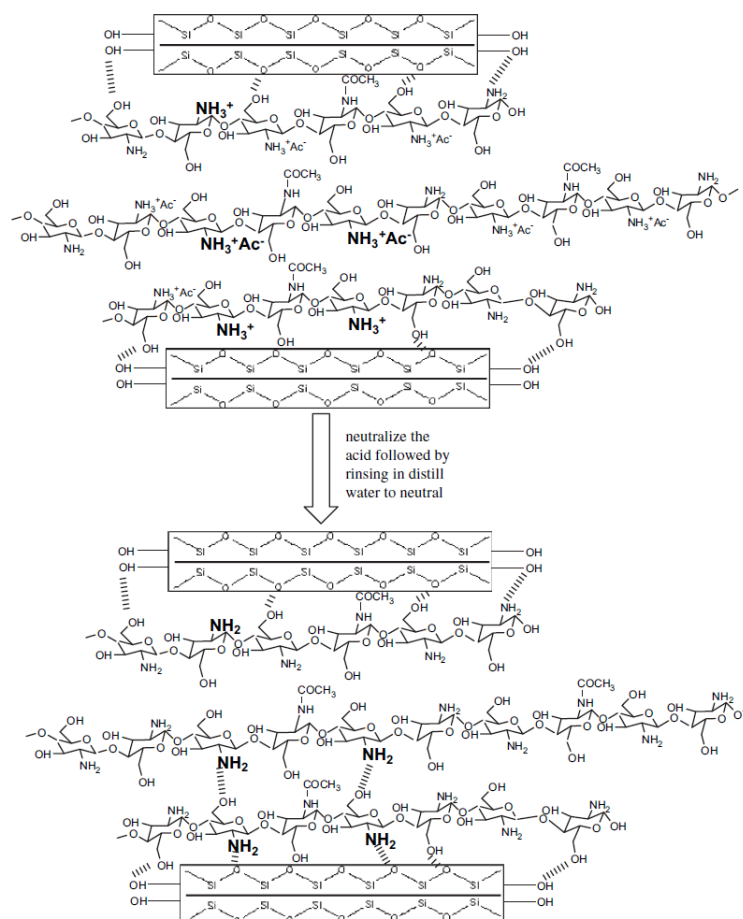


Figure 2.10 Formation of hydrogen bonds between CS and MMT (Wang *et al.*, 2005).

Rhim *et al.* has proved that the CS/MMT nanocomposite films include homogeneously dispersed of MMT particles throughout the CS polymer matrix. Consequently, mechanical and barrier properties of CS films were affected through intercalation of nanoparticles; that is the increase of tensile strength and decrease of water vapor permeability. In addition, CS/MMT nanocomposite films also showed a promising range of antimicrobial activity (Rhim *et al.*, 2006). The intercalation structure of CS/clay nanocomposite and its *in vitro* antimicrobial activity has been studied by Wang *et al.* They reported that the interlayer distance of the layered silicates in the nanocomposites enlarged as CS amount increased. Moreover, the pristine clay could not inhibit the growth of bacteria, but CS/clay nanocomposites had stronger antimicrobial activity than pure CS, particularly against Gram-positive bacteria. (Wang *et al.*, 2006b).

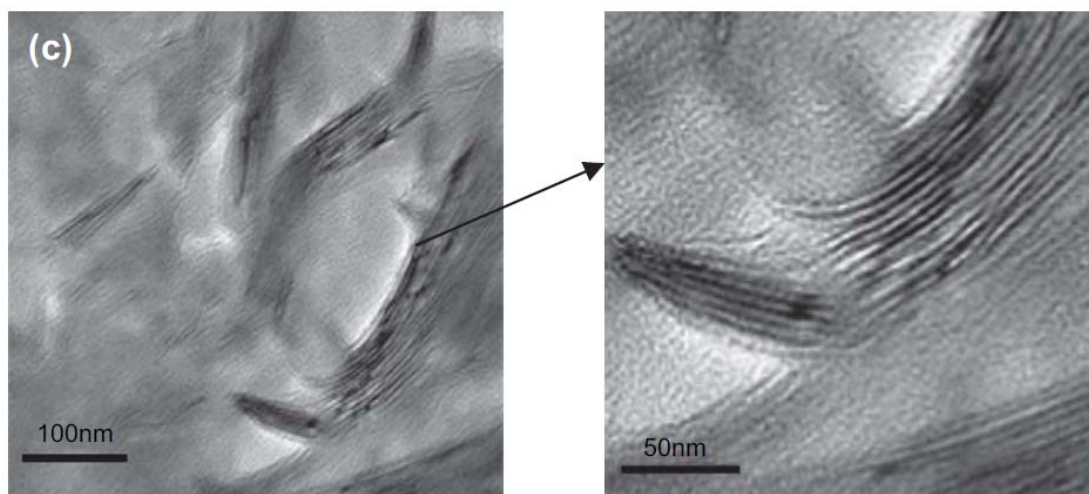


Figure 2.11 TEM micrographs of nanocomposites with CS/Clay ratios of 12:1 (Wang *et al.*, 2006b).

Accordingly, CS/MMT nanocomposite is the new composite material that frequently exhibits a remarkable improvement of the material properties as compared with the individual polymer CS or conventional micro- and macro-composite materials. The improvements can be summarized as the following.

- enhanced long-term stability
- increased surface roughness
- improved mechanical property
- enhanced tensile strength
- enhanced hardness and elastic modulus
- improved the thermal stability
- enhanced barrier property
- decreased water vapor permeability
- enhanced antimicrobial activity

The main reason for these improvements is interfacial interaction between the CS matrix and MMT particles due to the nanodispersion of silicate layers. Consequently, the nanometric scale on which the nanoclay particles, with their plate-like shape, would improve the physical and chemical properties of the polymeric materials as mentioned above. Moreover, the CS/MMT nanocomposites exhibit biocompatible and biodegradable property, antimicrobial activity, and anion exchange capacity. Therefore these materials are very popular and have been applied in diverse applications, from industrial manufacturing to medicine.

For example, Darder *et al.* proposed to use this nanocomposites material as the surface-modified sensors for anion detection. The research effort was made for improving a long-term stability through modification of the characteristics of pure CS

films. Accordingly, they tried to prepare the intercalation of the cationic biopolymer CS into the MMT gallery spacing, providing compact and robust three-dimensional nanocomposites having functional properties and low environmental impact. This material can be easily processed to construct bulk-modified electrodes suitable for the detection of anions. (Darder *et al.*, 2003; 2005).

Furthermore, An and Dultz have employed the CS/MMT nanocomposites for the adsorption of an organic pollutant, tannic acid. They have reported that because of protonation/deprotonation reactions of both CS/MMT and tannic acid, the adsorption process is strongly pH-dependent and the maximal adsorption capacity for tannic acid occurs at pH 4. (An *et al.*, 2007).

The application of CS/MMT nanocomposites for cationic dye adsorption has been designed by Monvisade and Siriphannon. They reported that the adsorption capacities of CS/MMT for all cationic dyes increased with an increase of initial dye concentration. This increase of adsorption capability was attributed to intercalate-CS in MMT gallery that could enlarge the pore structure of CS/MMT nanocomposites, facilitate the penetration of macromolecular dyes, and also electrostatically interact with the applied dyes. These results indicated the competency of CS/MMT adsorbent for cationic dye adsorption. (Monvisade *et al.*, 2009).

The mechanical strength, Young's modulus, bioactivity and controlled degradation time of CS/MMT nanocomposite material make it suitable for being utilized as a material filling bone defect, one of the most frequent problems in bone tissue reconstruction in which application of a biomaterial filling is necessary. (Paluszkiwicz *et al.*, 2011).

2.2.5 Potential of CS/MMT Nanocomposite for Drug Controlled Release

Application

CS has been extensively used for drug controlled release application. However, due to some disadvantages, the use of pure CS is still limited. For that reason, an improvement of the CS by polymer/layered silicate nanotechnology is promisingly promoted. Pharmaceutically, interesting improvements include increased mechanical and rheological properties, reduced drug permeability, and water uptake and controlled release characteristics. On the basis of these properties, CS/MMT nanocomposites are extending their applicability to the design of new drug release dosage forms with highly specific technological and biopharmaceutical properties. (Viseras *et al.*, 2008).

Liu *et al.* have systematically studied the CS/MMT nanocomposites hydrogel (nanohydrogel) for controlled release of drug (vitamin B12) following electrostimulation. The deterioration of the responsiveness and reversibility of pure CS upon repeated on-off electrostimulation switching operations are major limitations for clinical applications, as it suffers from too much structural instability for the precise control of the release of drug upon cyclic electrostimulation. To overcome these limitations, an inorganic phase, MMT, was incorporated in the CS matrix to enhance the anti-fatigue property and corresponding long-term stable release kinetics. Accordingly, they expected to obtain the exfoliated silica nanosheets which able to act as cross-linkers to form a network structure between the CS and MMT, and this difference in the cross-linking density strongly affect the release of vitamin B12 under electrostimulation, as a result the release mechanism was changed from a diffusion-controlled mode to a swelling-controlled mode with the MMT doping. In addition, the

nanohydrogel containing 2 %w/w MMT exhibited an excellent anti-fatigue behavior and better pulsatile release compared with pure CS. This new class of nanohydrogels provides an interesting alternative as a long-standing electrically induced drug delivery system with reliable drug release performance (Liu *et al.*, 2008).

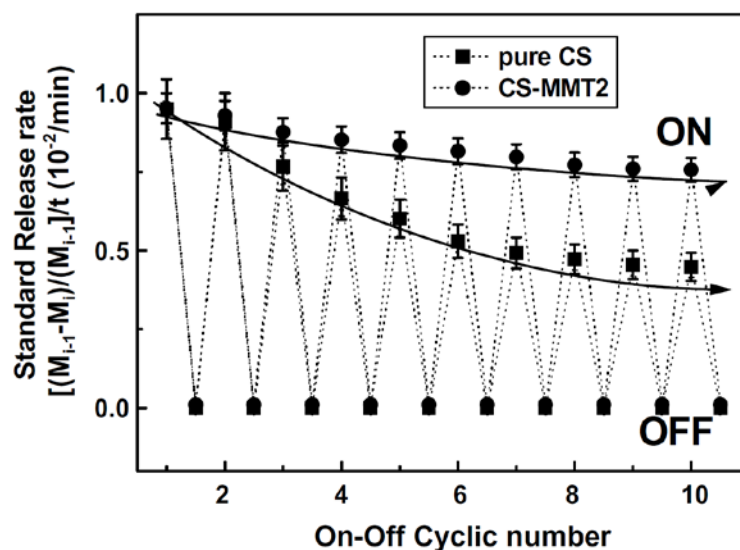


Figure 2.12 Standard release rates of drug from pure CS and CS-MMT under cyclic on-off switching of electrostimulation (Liu *et al.*, 2008).

Aguzzi *et al.* have employed CS/MMT nanocomposite to control drug release of 5-amino salicylic acid (5-ASA), to maximize the efficacy of the drug and avoid adverse effects associated with systemic absorption target release of 5-ASA to the site of action (small bowel and/or colon). The results showed that, in comparison with interaction products prepared using the drug and the individual components, there was a synergic effect between the clay mineral and the polysaccharide regarding the ability to retain drug molecules and the control of drug release in acidic medium. In particular, the 5-ASA/CS/MMT composites showed higher drug loading and slower drug release compared to both 5-ASA/MMT and 5-ASA/CS products, with almost

linear release profile throughout the test as shown in Figure 13. According to the results, biocomposites of CS and montmorillonite were a promising support for modified formulations of 5-amino salicylic acid (Aguzzi *et al.*, 2010).

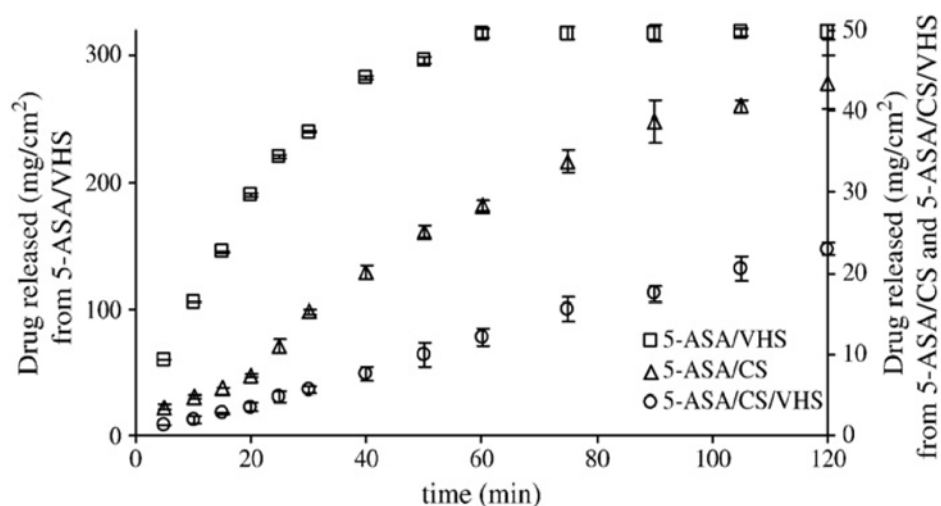


Figure 2.13 Drug release profiles from the composite and interaction products in HCl 0.1 M (mean values \pm s.d.; $n = 3$ and VHS is referred to the pharmaceutical grade MMT) (Aguzzi *et al.*, 2010).

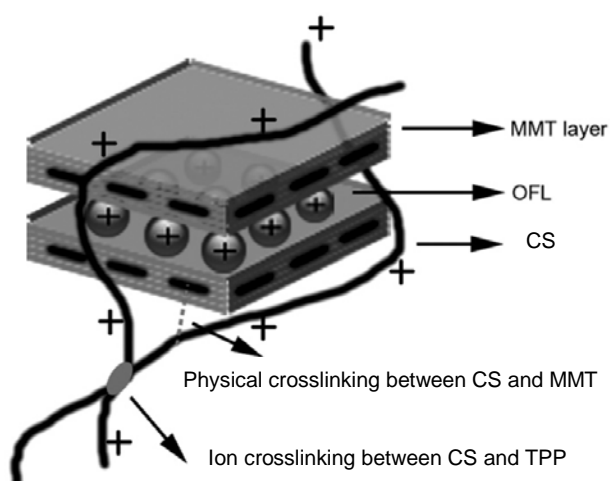


Figure 2.14 Schematic illustrations of interactions between CS, OFL and MMT (Hua *et al.*, 2010).

Hua *et al.* have studied the controlled release of ofloxacin (OFL), the fluoroquinolone antibiotic drug, from CS/MMT hydrogel. A series of OFL/CS/MMT hydrogels were prepared by solution intercalation and ionic crosslinking with sodium tripolyphosphate (TPP). Compared to pure CS beads, the incorporation of MMT enhanced the drug entrapment, improved the swelling behavior and reduced the drug release. The observations suggested that the electrostatic interaction between CS and MMT enhanced the stability of the beads and showed good potential for being used as sustained release drug carriers (Hua *et al.*, 2010).

2.3 Chitosan/Poly(ethylene oxide) (CS/PEO) Blend; for Solid Polymer Electrolyte Application

2.3.1 Solid Polymer Electrolytes

Solid polymer electrolytes (SPEs) are receiving considerable attention in several advanced applications such as rechargeable lithium ion batteries because their use allows the fabrication of safe batteries and permits the development of thin batteries and electrochemical devices with design flexibility (Yahya *et al.*, 2003). SPEs have been reported as promising materials for use in batteries due to their unique properties such as high ionic conductivity, ability to provide good electrode/electrolyte contact, physical flexibility, and good mechanical properties and film forms ability (Winie *et al.*, 2006). Besides, such electrolyte has potentially promising applications in other electrochemical devices such as fuel cells, supercapacitors, electrochromic windows and sensors (Song *et al.*, 1999). The use of SPEs can avoid problems associated with liquid electrolytes such as leakage and gas formation that arises from solvent decomposition. This leads to improvement in

battery design. Solid polymer batteries constructed with only thin-film electrodes and electrolytes can be made to be very compact, lightweight and highly reliable (Mohamed *et al.*, 2004). SPEs consist of salts dissolved in high molecular weight polymer. Polymer which can dissolve salt must be included O, N or S atom because these atoms can interact with cation, and make decompositive salt to have better conductivity (Vincent, 1995). Several polymers have been used in making of SPEs films, for example polyethylene oxide (PEO) (Ali *et al.*, 1998; Stowe, 2001; Sukeshini *et al.*, 1998), polyacrylic acid (PAA) (Bozkurt *et al.*, 2003), polyvinyl alcohol (PVA) (Agrawal *et al.*, 2004) as well as CS (Buraidah *et al.*, 2010; Khier *et al.*, 2006; Morni *et al.*, 1999; Winie *et al.*, 2006). All of these polymers can form complex with various salts to provide the ionic conduction.

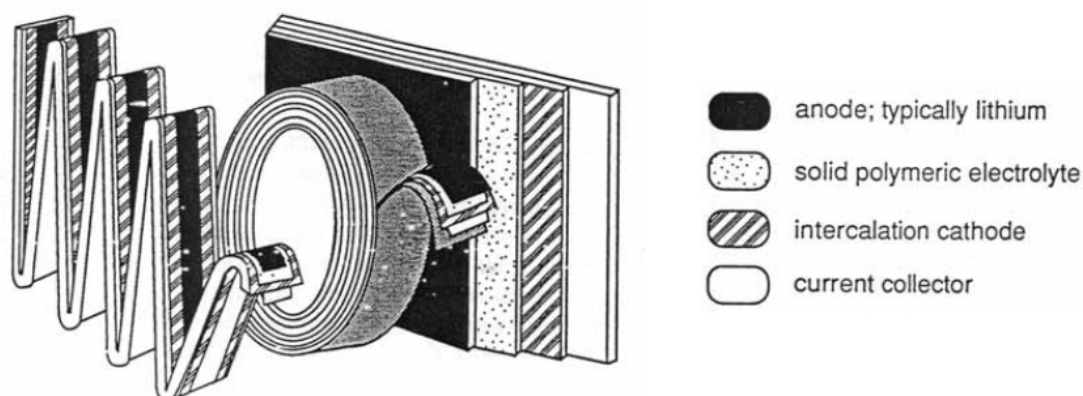


Figure 2.15 Schematic of polymer-based batteries. The thin-film composites are very flexible and can be folded or rolled into various geometries (Mendoliaa *et al.*, 1995).

2.3.2 Potential and Limitation of Chitosan for Solid Polymer Electrolyte Application

CS is one promising candidate of the polymer host for proton conducting polymer electrolyte (Buraidah *et al.*, 2010; Khair *et al.*, 2006; Mohamad *et al.*, 2007; Yahya *et al.*, 2003). The monomer of CS consists of hydroxyl and amine functional groups with lone pair electrons. The lone pair electrons enable the chelation of a proton donor, thus CS satisfies one of the criteria to act as a polymer host for the solvation of salts. In addition, it is stable in neutral conditions. Amine and hydroxyl groups on the glucosamine unit can form strong inter- and intra- molecular hydrogen bond to crystallize. Therefore, CS is a polymer which has been shown to be a promising solid electrolyte for solid state cells (Morni *et al.*, 1999). There are several researches paying attention to the use of CS as solid polymer electrolytes in the fabrication of proton batteries (Kadir *et al.*, 2009; 2010). CS is a neutral polymer; when it swells in water, its amine group may be protonated and this will lead to ionic conductivity. In an aqueous acid medium, the amine group of CS is protonated, the polymer behaves like a cationic polyelectrolyte (Kadir *et al.*, 2010). The conductance behavior of the CS polymer electrolytes is affected by the dopant that is added to make the CS a proton (H^+) conductor. The addition of ionic salt helps to increase the conduction of electrolyte as the mobile charge carrier whether in solid, liquid, or gel forms. (Du *et al.*, 2009).

However, SPE films made only from pure CS exhibit high rigidity and poor mechanical properties along with the rather low ionic conductivity at ambient temperature (Du *et al.*, 2009). All of these disadvantages frequently restrict the application of CS as a solid polymer electrolyte film. To enhance the conductivity,

several approaches were suggested in the literature, including addition of polymers (blending), addition of a ceramic filler, plasticizer, and even radiation (Ng *et al.*, 2006). Compared to other methods, blending is the simplest, lowest cost and most effective way to improve the conductivity of a CS-SPE. Besides, the rigidity and mechanical properties of this material also can be improved by blending (Alexeev *et al.*, 2000). Among a number of CS blended polymer, the mostly used is poly(ethylene oxide) to provide an suitable material for solid polymer electrolyte application (Mohamad *et al.*, 2007).

2.3.3 Poly(ethylene oxide)

Poly(ethylene oxide) (PEO) is a linear polymer consisting of a series of polyethers as:



The melting point of PEO is a function of the average molecular weight and molecular weight distribution of the sample. Usually, it varies from 60°C for lower molecular weights (~4000 g/mol) and up to 66°C for larger molecular weights (~100,000 g/mol) (Gray, 1991). The glass transition temperature (T_g) is also closely correlated with molecular weight, $T_g \cong -17^\circ\text{C}$ for a molecular weight of 6000 g/mol (Faucher *et al.*, 1966). The T_g values of -65°C and -60°C are reported for higher molecular weight polymers (Gray, 1991). PEO is a linear polymer and the regularity of the structure unit allows a high degree of crystallinity of about 70-95% (Takahashi *et al.*, 1973) usually with a density of 1.09 g/cm^3 (Roe, 1968b), and a heat of fusion of 196.8 J/g (Pielichowski *et al.*, 2004). The unit structure of crystalline PEO is monoclinic (Saruyama, 1983; Takahashi *et al.*, 1973; Zhu *et al.*, 2000). XRD analysis

confirmed that PEO molecules are well packed and the molecules are neither unreasonably close nor too far apart. The internal rotation angles are considerably distorted from the uniform helix due to the intermolecular forces. This distortion and the ability of the PEO to orient under stress show the high degree of flexibility of the PEO chains (Takahashi *et al.*, 1973). The electrostatic interactions ($\epsilon \sim 5$), electron pair donating ability (~ 22), most importantly the optimal spatial solvating oxygen units make PEO a superior solid polymer electrolytes candidate (Stowe, 2001).

2.3.4 Potential and Limitation of Poly(ethylene oxide) for Solid Polymer Electrolyte Application

PEO is one of the most widely studied host polymer matrix for potential use as an electrolyte in high energy-density batteries because of its ability to solvate a variety of inorganic salts leading to polymer electrolytes with significant values of ionic conductivity (Vincent, 1995).

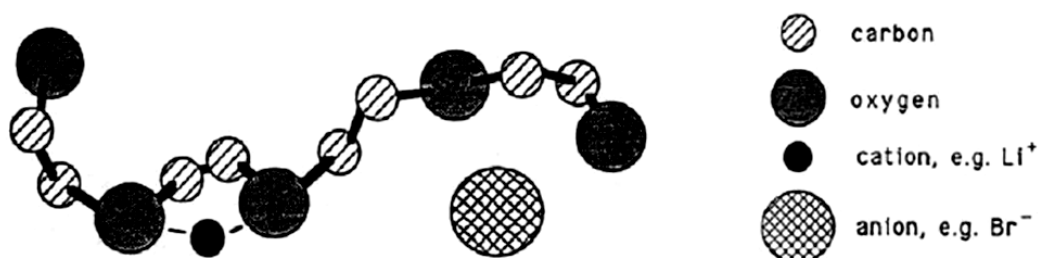


Figure 2.16 Solvation of a salt by a PEO chain. The primary interaction is between the ether oxygens and the cation (Vincent, 1995).

PEO shows sufficient thermal and chemical stability, and has spacing between the oxygen groups which is ideal for cation solvation. Since PEO has no double bonds, it displays a large flexibility and can be coordinated with many different types of cations. The solvation of salt occurs through the association of the metallic cation with the oxygen atom in the backbone as shown in Figure 2.16.

In polymer electrolyte applications, for example, ion conduction has been shown to take place in only the amorphous phase. The disadvantage of PEO as a salt host then becomes apparent, since ~70-95% of pure PEO is crystalline at room temperature, depending on its molecular weight (Takahashi *et al.*, 1973). A large degree of PEO crystallinity become a major barrier to ions transport and the polymer electrolytes always end up with an undesirably low ionic conductivity (Shuo, 2004). Moreover, the crystallinity also enhances the rigidity of the polymers and reduces the transparency of the materials (Fuentes *et al.*, 2007).

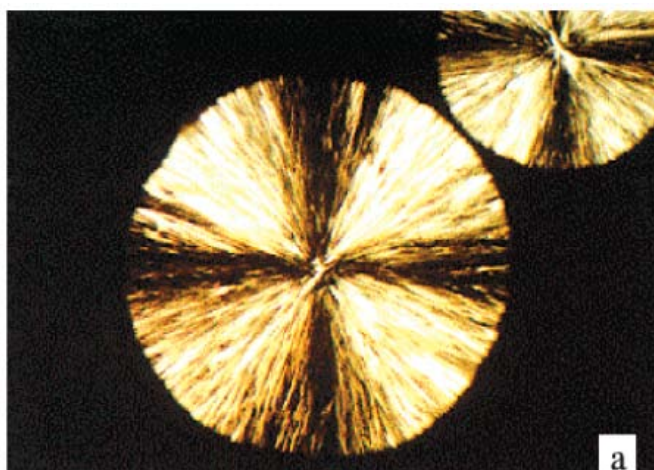


Figure 2.17 Typical polarized micrographs of spherulites of PEO (Huang *et al.*, 2001).

Acceptable improvements of the conductivity at low temperatures are afforded by the addition of low molecular electron pair donors, generally common organic solvents able to act as plasticizer that increases the solubility of inorganic salt solvating the ion and enhances the flexibility of the polymer favoring the chain movement. The use of plasticizers, limited only by the mechanical stability of the product, does not however guarantee the transparency of the composite, which is mostly determined by the chemical compatibility of the components (Fuentes *et al.*, 2007).

Therefore, homogeneous blending is the most suitable approach to prevent PEO from crystallizing. Blending with other polymers has been reported to be one of the convenient and effective methods to reduce the crystallinity of PEO (Li *et al.*, 1993). Normally, high molecular weight PEO could be blended with many types of polymers, such as polystyrenes (Gray *et al.*, 1986), polymethacrylates (Florianczyk *et al.*, 1991), and also polyacrylamides (Wieczorek *et al.*, 1992). In some cases, the conductivity of the blend can reach 10^{-4} S/cm at room temperature, which is higher than the theoretical value for a salt-doped fully amorphous PEO phase (Wieczorek *et al.*, 1995). CS, a largely amorphous polymer, is one promising candidate as the PEO blended polymer. There has been shown that blending PEO with CS does not lead to a phase separation (Mohamad *et al.*, 2007). Accordingly, amorphous CS chains may facilitate a decrease in PEO crystallinity, at the same time, a flexible PEO chains may reduced the rigidity and enhanced the mechanical properties of CS to provide suitable materials for solid polymer electrolyte application (Donoso *et al.*, 2007; Idris *et al.*, 2005; 2007).

2.3.5 Chitosan/Poly(ethylene oxide) (CS/PEO) Blend

As compared with the pure polymer film, CS/PEO blend exhibited the improvement in thermal, physical, mechanical, transparent and conductive properties and provided additional functionality because of the specific interactions between the amino groups of CS and the ether groups of PEO (Chang *et al.*, 2010; Zivanovic *et al.*, 2007). Thus, CS can act as a proton donor while PEO can act as a proton acceptor, giving rise to a homogeneous polymeric blend and the maximum interaction between CS and PEO occurs at 20 %w/w PEO content (Wang *et al.*, 1997). The polarized micrographs of CS/PEO blend films as shown in Figure 2.18 demonstrate that PEO decreases its tendency of spherulitic crystallization in the blends with a large CS content (> 50 %w/w) (Zivanovic *et al.*, 2007). Moreover, the mechanical properties of CS films are improved in blending with PEO: a six times larger elongation at break and a two times higher tensile strength for the CS/PEO blends containing 16.7 %w/w of PEO as shown in Figure 2.19 (Alexeev *et al.*, 2000). This improvement can be related to an increase in the packing density of the polymer chains in blends through filling of the cavities in the rigid structure of CS by flexible PEO (Sashina *et al.*, 2006) as well as to an attractive interaction between the polymer components. Accordingly, Blends of CS and PEO have a great potential applicability as a polymer host for the solid polymer electrolyte since both CS and PEO can dissolve the ionic salts to provide the protonic conductivity as previously discussed (Donoso *et al.*, 2007; Idris *et al.*, 2007; Mohamad *et al.*, 2007).

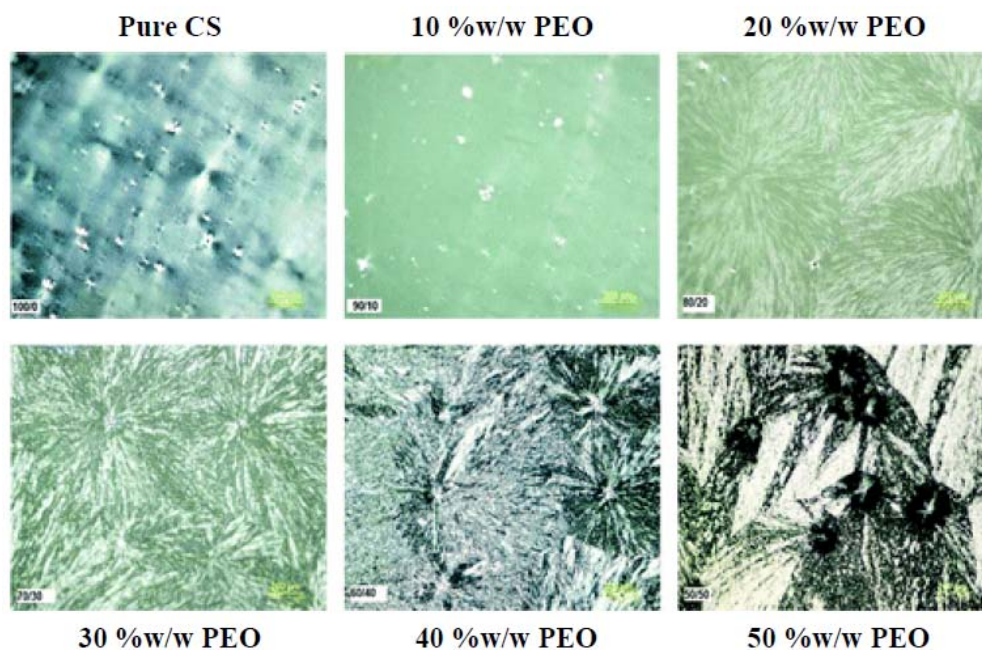


Figure 2.18 Polarized micrographs of CS/PEO blend films with difference %w/w of PEO in blends; 100 × magnification and scale bar of 200 μm (Zivanovic *et al.*, 2007).

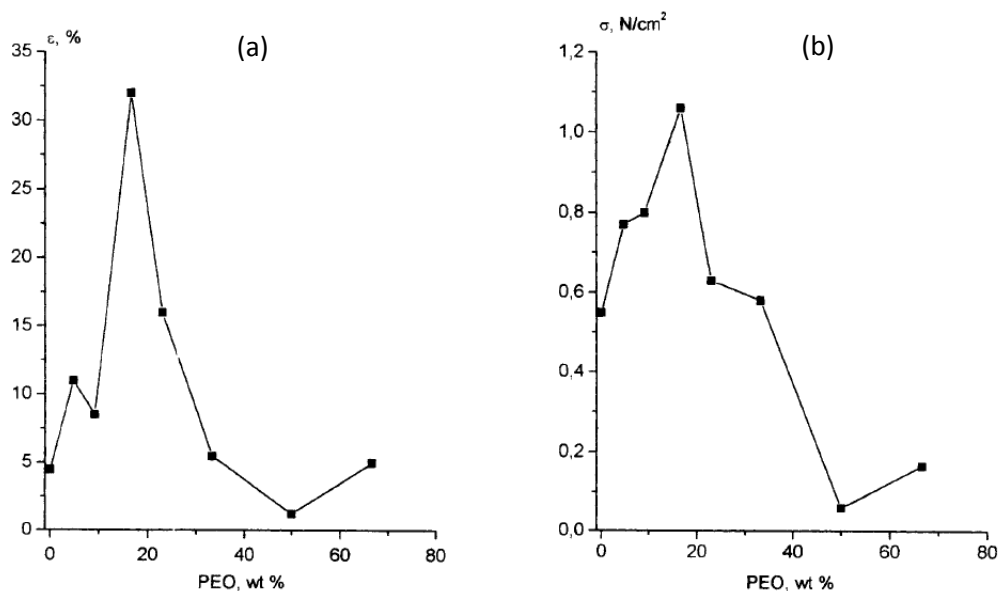


Figure 2.19 (a) The relative elongation-at-break; ϵ and (b) the tensile strength; σ of CS/PEO blends films depending on the PEO content (M_v of PEO is 600,000 g/mol) (Alexeev *et al.*, 2000).

2.3.6 Potential of Chitosan/Poly(ethylene oxide) Blend for Solid Polymer Electrolyte Application

CS/PEO blends exhibit good electrical conductivity as well as the mechanical and chemical stability there are the most important properties of materials to be used as electrolytes in solid-state devices. Thus, the flexibility needed for getting films useful in microdevices or the transparency in a given light frequency range required for electroptical applications may be also important in the development of new ion-conducting materials. Both, the adaptability to any type of spaces and the functional versatility of polymer make CS/PEO blends especially suitable in the development of solid electrolytes (Fuentes *et al.*, 2007). Therefore, several researches have been interested to use this material in various applications.

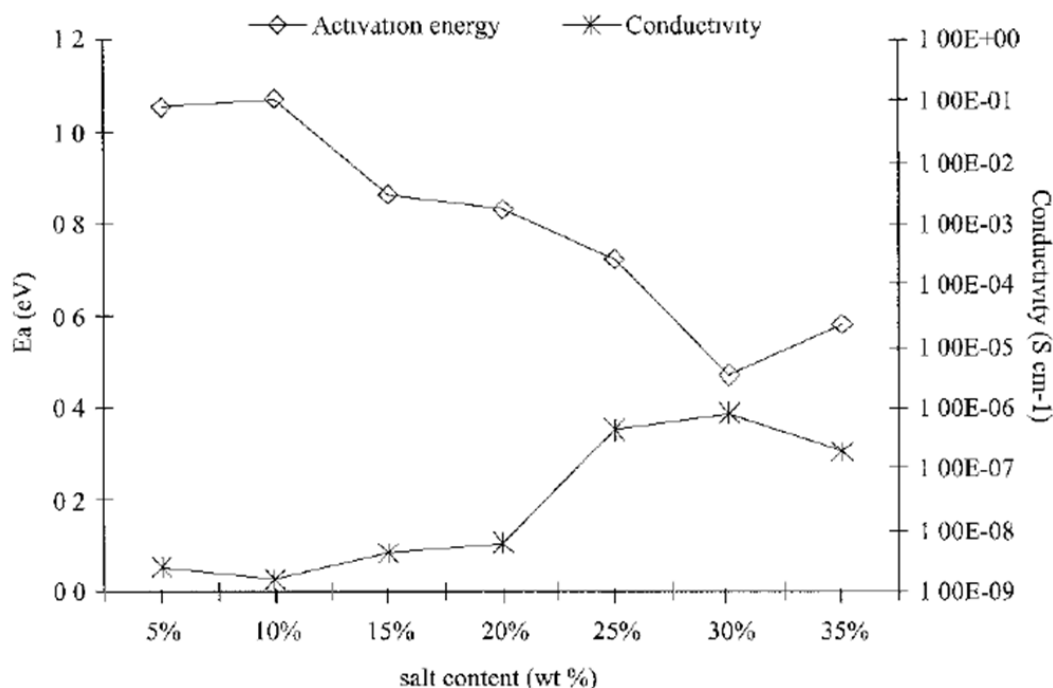


Figure 2.20 Variation of the conductivity and activation energy as a function of salt content (Idris *et al.*, 2005).

Idris *et al.* have been interested in lithium battery using CS/PEO blend as a host polymer. The ionic conductivity of CS/PEO blend (1:1 weight ratio) doped lithium trifluoromethanesulfonimide (LiTFSI) films was studied. They reported the enhancement in conductivity compared to a singly salted CS film is attributed to the segmental motion of PEO in the CS/PEO blend host (Idris *et al.*, 2007) and the conductivity of the samples is depended on the number of mobile ions. The highest conductivity at room temperature was $1.4 \times 10^{-6} \text{ S cm}^{-1}$ and the activation energy was 0.47 eV for CS/PEO blends containing 30 %w/w LiTFSI salt (Idris *et al.*, 2005).

Mohamad *et al.* have fabricated a ZnTe/polymer junction for dye-sensitized solar cells by using CS/PEO blend (1:1 weight ratio). The polymer blend was complexed with NH_4I and some iodine crystals were added to the polymer/ NH_4I solution. They have shown that a CS/PEO blend can host the redox I/I_3^- couple for the operation of a junction solar cell to provide the ionic conductivity of $4.32 \times 10^{-6} \text{ S cm}^{-1}$ at room temperature (at 15% salt). Accordingly, the conductivity is depended on the amount of doping salt as shown in Table 2.4 (Mohamad *et al.*, 2007).

Donoso *et al.* have been employed Nuclear Magnetic Resonance (^7Li and ^1H NMR) technique to study the dynamics of lithium ions (Li^+) within CS/PEO blend-based polymer electrolytes. The results suggest that the chemical functionality of CS, particularly the amine group, participate in coordinating Li^+ in the composites. The competition between CS and PEO for Li^+ is evident in the binary system. The heterogeneity, at a local microscopic scale, is revealed by a temperature-dependent equilibrium of Li^+ concentration between at least two different microphases; one dominated by the interactions with CS and the other one with polyether, PEO. (Donoso *et al.*, 2007).

Table 2.4 Amounts of polymer, salt and its conductivity at room temperature (Mohamad *et al.*, 2007).

Chitosan (g)	PEO (g)	NH ₄ I		Conductivity (S/cm)
		(g)	%	
0.25	0.25	0.000	0	4.00×10^{-10}
0.25	0.25	0.026	5	4.44×10^{-10}
0.25	0.25	0.055	10	2.24×10^{-10}
0.25	0.25	0.088	15	9.39×10^{-9}
0.25	0.25	0.125	20	7.25×10^{-9}
0.25	0.25	0.166	25	1.83×10^{-8}
0.25	0.25	0.214	30	6.72×10^{-8}
0.25	0.25	0.269	35	6.85×10^{-7}
0.25	0.25	0.333	40	4.73×10^{-7}
0.25	0.25	0.049	45	4.32×10^{-6}
0.25	0.25	0.500	50	2.69×10^{-6}

CHAPTER III

COMPUTATIONAL MOLECULAR MODELING

3.1 Computational Chemistry

Since the development of the first computers in the early 1950's, scientists have tried to explore how these machines might be used in Chemistry. From the very beginning, the field of Computational Chemistry focused either on solving complex mathematical problems, typically quantum mechanical, or has tried to model the dynamical behavior of atomic and molecular systems. The boundaries between these two areas have never been well defined and, today, we see a convergence between quantum chemistry and simulation in studying chemical reactions (Curtiss *et al.*, 2004).

With advances in computer technology leading to ever faster computers, Computational Chemistry has become an increasingly reliable tool for investigating systems where experimental techniques still provide too little information. Ultra-fast spectroscopy can be used to follow fast reactions but only at a molecular level. A variety of diffraction techniques can also give detailed information about crystalline structure, but have difficulties monitoring changes at a molecular level. This is why the exponential growth in computer power has led to a corresponding growth in the number of computational chemists and in the variety of different computational techniques available for solving chemical problems: *ab initio* Quantum Mechanics

(QM), semi-empirical methods, Density Functional Theory (DFT), Monte Carlo (MC), Molecular Mechanics (MM), Molecular Dynamics (MD), QM/MM, Car-Parrinello, *etc.*

There are two main branches within the Computational Chemistry: the computationally expensive methods which try to explore the electronic structure of small systems or systems with fixed crystal structures by quantum mechanical methods; and methods which focus on the atomic structure and dynamics of much larger systems but using less complex calculations. In this thesis, the focus is on the latter-simulating atomic and molecular interaction with the mathematics of classical mechanics.

3.2 Molecular Dynamics (MD) Simulation

3.2.1 Theory in MD Simulations

In reality, atoms and molecules in solid materials are far from static unless the temperature is low; but even at 0 K, vibrational motion remains. MD allows us to simulate the dynamics of the particles in a well defined system to gain greater insights into local structure and local dynamics, such as drug and ion transport in polymeric materials (Accelrys, 2007).

In an MD simulation, atomic motion in a chemical system is described in classical mechanics terms by solving Newton's equations of motion:

$$\vec{F}_i = m_i \vec{a}_i \quad (3.1)$$

for each atom i in a system of N atoms: m_i is their respective atomic mass; $a_i = d^2 r_i / dt^2$ is their acceleration; and F_i is the force acting upon atom i due to interactions

with all other particles in the system. The forces are generated from a universal energy potential E :

$$-\frac{dE}{d\vec{r}_i} = \vec{F}_i = m_i \frac{d^2\vec{r}_i}{dt^2} \quad (3.2)$$

The basic idea of MD goes back to classical idea in Physics that if one knows the location of the particles in the Universe, and the forces acting between them, one is able to predict the entire future. In a normal MD simulation, this Universe comprises only a few thousand atoms; in extreme cases, up to a million.

With Newton's equations, it is possible to calculate sequentially the locations and velocities of all particles in the system. This generates a sequence of snapshots which constitutes a "movie" of the simulated system on the atomic scale. Due to the massive computer time necessary to solve these equations for a large number of particles, the movies are generally fairly short (in this work is in the pico- or nanosecond regime). All that is needed to solve the equations of motion are the masses of the particles and a description of the potentials, E .

In order to solve Eq. (3.2), various kinds of numerical integration methods such as Gear, Verlet, leapfrog, and velocity Verlet have been developed.

From the Verlet algorithm, which is based on particle position at time t , $r(t)$, acceleration at time t , $a(t)$, and the position from previous time $r(t-\Delta t)$, the new position of a particle after time Δt (Δt is the time-step between two snapshots.) is given by

$$r(t + \Delta t) = 2r(t) - r(t - \Delta t) + \Delta t^2 a(t) \quad (3.3)$$

Then, the velocity at time t can be calculated by

$$v(t) = \frac{r(t + \Delta t) - r(t - \Delta t)}{2\Delta t} \quad (3.4)$$

The Verlet algorithm uses no explicit velocities. The advantages of the Verlet algorithm are, *i*) it is straightforward, and *ii*) the storage requirements are modest. The disadvantage is that the algorithm is of moderate precision. The leapfrog algorithm works stepwise by: Calculating the acceleration at time t according to Eq. (3.2). Updating the velocity at time $t + \Delta t / 2$ using

$$v(t + \Delta t / 2) = v(t - \Delta t / 2) + a(t)\Delta t \quad (3.5)$$

Calculating the atom position in the snapshot using:

$$r(t + \Delta t) = r(t) + v(t + \Delta t / 2)\Delta t \quad (3.6)$$

In this way, the velocities *leap* over the positions, and then the positions *leap* over the velocities. The advantage of this algorithm is that the velocities are explicitly calculated, however, the disadvantage is that they are not calculated at the same time as the positions. The velocity Verlet algorithm is as follows:

$$r(t + \Delta t) = r(t) + \Delta t v(t) + \frac{\Delta t^2 a(t)}{2} \quad (3.7)$$

$$a(t + \Delta t) = \frac{f(t + \Delta t)}{m} \quad (3.8)$$

$$v(t + \Delta t) = v(t) + \frac{1}{2} \Delta t [a(t) + a(t + \Delta t)] \quad (3.9)$$

This algorithm yields positions, velocities and accelerations at the same time. There is no compromise on precision.

The MD simulation method is very straightforward, but one must bear in mind that it is based on some severe approximations. At the highest level, the Born-Oppenheimer approximation is made, separating the wavefunction for the electrons from those of the nuclei. The Schrödinger equation can then be solved for every fixed nuclear arrangement, given the electronic energy contribution. Together with the nuclear-nuclear repulsion, this energy determines the potential energy surface, E . At the next level of approximation, all nuclei are treated as classical particles moving on the potential energy surface, and the Schrödinger equation is replaced by Newton's equations of motion. At the lowest level of approximation, the potential energy surface is approximated to an analytical potential energy function which gives the potential energy and interatomic forces as a function of atomic coordinates.

3.2.2 Forcefields for MD Simulations

In the context of molecular modeling, a forcefield means the energy functions and parameter sets used to calculate the potential energy of a system. The energy functions and parameter sets are either derived from quantum chemistry calculations or empirically from experimental data. Typically, classical forcefields (described here) employ two-body pairwise additive potentials and ignore multi-body dispersion and many-body polarization effects. The basic functional form of a classical forcefield can be regarded as the sum of nonbonded interactions, also called intermolecular interactions, and intramolecular interactions (bond stretch, valence angles and dihedral angles):

$$E = \sum_{i \neq j} E_{ij}^{NB}(r) + \sum_{ij} E_{ij}^s(r) + \sum_{ijk} E_{ijk}^b(\theta) + \sum_{ijkl} E_{ijkl}^t(\Phi) \quad (3.10)$$

where r is the distance between atom centers, $E_{ij}^{NB}(r)$ is the nonbonded energy associated between atom i and j , $E_{ij}^s(r)$ is the covalent bond stretching energy between atom pair i and j , $E_{ijk}^b(\theta)$ is the bond-angle bending energy that depends on the angle θ formed by atoms i , j and k , and $E_{ijkl}^t(\Phi)$ is the torsional energy arising from rotation around the dihedral angle Φ defined by atoms i , j , k and l . Nonbonded interactions $E_{ij}^{NB}(r)$, the interactions between atoms in different molecules or in the same molecules separated by two or more atoms, are composed of electrostatic interactions and van der Waals interactions as given by:

$$E_{ij}^{NB}(r) = E_{ij}^{elec}(r) + E_{ij}^{vdw}(r) \quad (3.11)$$

The summations run over all interactions of each type present in each molecule and between molecules. The bond-stretch, bond-angle and torsional-angle terms have many forms. In the vast majority of forcefields used in Molecular Dynamics simulations, bond breaking is not possible; this is also the case for the forcefields used in this work. The electrostatic energy, E_{ij}^{elec} , also called the Coulombic energy, is directly related to atomic charges by Coulombs law,

$$E_{ij}^{elec}(r) = \frac{1}{4\pi\epsilon_0} \frac{q_i q_j}{r} \quad (3.12)$$

where q_i , q_j are the charges on atoms i and j , and ϵ_0 is the permittivity of free space. There are many forms used to describe the van der Waals energy. The two most popularly used are the Lennard-Jones (LJ) potential (Lennard-Jones, 1931),

$$U(r) = \left(\frac{A}{r^{12}}\right) - \left(\frac{B}{r^6}\right) = 4\varepsilon \left[\left(\frac{\sigma}{r}\right)^{12} - \left(\frac{\sigma}{r}\right)^6 \right] \quad (3.13)$$

where $A = 4\varepsilon\sigma^{12}$ and $B = 4\varepsilon\sigma^6$ and the Buckingham potential,

$$U(r) = A' \exp(-B'r) = \frac{C'}{r^6} \quad (3.14)$$

In Eq. (3.13) and (3.14), A , B , ε , σ , A' , B' and C' are constants fitted to *ab initio* and/or experimental data. The parameters A' and B' determine the short range repulsive interaction, C' is the dispersion parameter. The parameters ε and σ have the significance of being the depth and zero point of the potential. Both the LJ and Buckingham potential include the long-range London dispersion term.

Such classical forcefields are used widely in the Molecular Dynamics simulations of polymer electrolytes, but recent Molecular Dynamics simulations by Smith and coworkers have shown that polarization effects can play a very important role for these systems and should not be ignored (Londono *et al.*, 1997).

3.2.3 Periodic Boundary Conditions and Other Requirements

Since the computation time required for calculating the trajectories of all N particles in a simulation box increases with N^2 , the simulated system cannot be made large enough to accurately represent the bulk properties of an actual crystal or amorphous material: surface effects will always be present. This problem is solved by implementing periodic boundary conditions, in which the simulation box is replicated through space in all directions; see Figure 3.1. The set of atom present in the box is thus surrounded by exact replicas of itself, *i.e.* periodic images. If an atom moves

through a boundary on one side of the simulation box, so will its replica on the other side. This keeps the number of atoms in one box constant, and if the box has constant volume the simulation then preserves the density of the system, which can affect the properties of the simulation, but much less than the surface effect would have done without the periodicity. An MD simulation should also follow the laws of thermodynamics. At equilibrium, it should have a specific temperature, volume, energy, density, pressure, heat capacity, *etc.* In statistical thermodynamics, this constitutes the state of the system; its *ensemble*. Since MD is a statistical mechanics method, an evaluation of these physical quantities can be made from the velocities and masses of the particles in the system, and MD can serve as a link between these atomic-level quantities and macroscopic properties. When performing an MD simulation model is retained. This ensemble then scales the velocities of the particles. Three different ensembles have been used here:

- **The Microcanonical Ensemble (NVE)**; which maintains the system under constant energy (E) and with constant number of particles (N) in a well-defined box with volume (V). This is appropriate during the initial equilibration phase of a simulation.
- **The Isothermal-Isobaric Ensemble (NPT)**; where number of particles (N), temperature (T), and pressure (P) are kept constant. This is normally the best model of the experimental conditions.
- **The Canonical Ensemble (NVT)**; where number of particles (N), volume (V), and temperature (T) are kept constant. This ensemble has been used for most simulations, so that comparisons can be made with experimental data from structures with fixed dimensions.

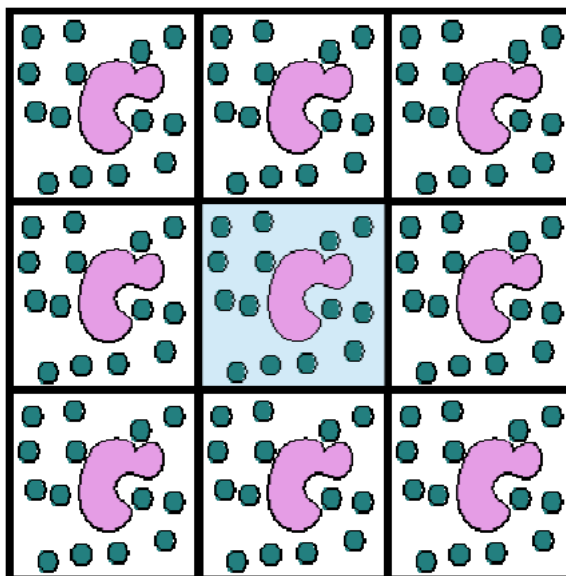


Figure 3.1 Periodic boundary conditions in Molecular Dynamics (CCL.NET, 1996).

One factor that impacts total CPU time required by a simulation is the size of the integration time-step (Δt). This is the time length between evaluations of the potential. The time-step must be chosen small enough to avoid discretization errors (*i.e.* smaller than the fastest vibrational frequency in the system). Typical time-step for classical MD is in the order of 1 femtosecond (10-15 s). This value may be extended by using algorithms such as *SHAKE*, which fix the vibrations of the fastest atoms (*e.g.* hydrogens) into place (Wikipedia, 2010). The *SHAKE* algorithm, a modification of the Verlet algorithm, has become the standard approach for doing Molecular Dynamics with fixed bond lengths. It can also be used to hold angles fixed, but this is less common. It works well for time-step up to 5 fs, thereby enabling a fivefold speedup in computational time as long as the process of iteratively solving the constraint equations does not consume too much time (Mathiowetz, 1994).

3.2.4 Structure and Dynamics from MD Simulation

The statistics provided by the MD simulations have been used to calculate different properties relating to structural and dynamical behavior of the materials.

3.2.4.1 Radial Distribution Function

One of the most important properties extracted from the MD simulation is the pair radial distribution function (RDF). It is a function, usually written $g_{a...b}(r)$, which presents the probability of finding a particle of type b at a distance r from particle of type a . In a perfect crystal without thermal motion, the RDF would appear as periodically sharp peaks, which gives information about the short-range order in the system.

The RDF can be calculated by counting the number of atom pairs within some distance range, and averaging this over a number of time-steps and particle pairs:

$$g_{ab}(r) = \frac{\sum_{k=1}^M N_k(r_{ab}, \Delta r)}{M \left(\frac{1}{2} N\right) \rho V(r_{ab}, \Delta r)} \quad (3.15)$$

where N_k is the number of atoms found at time k in a spherical shell of radius r and thickness Δr , and ρ is the average system density, N/V , of a given atom type.

Integrating this RDF over r gives the coordination number function (CNF), which is the average coordination number of particle type a to particle type b at distance r . The RDF can be compared directly with experimental data from X-ray or neutron diffraction, and can thus be used as a check on the reliability of the potentials in many systems.

3.2.4.2 Density Profile

A local density profile, $\rho(z)$ is defined as the average number of atoms in a slice of width Δz , which is parallel to the solid substrate. The proper choice of the width Δz of a slice is a trade-off between two factors. First, a very small width results in too few particles in each slice, and therefore one observes large statistical errors and data scattering. Second, a very large width of a slice will not show the actual dependence of the properties on the distance from the surface. Hence, a balance between those two requirements must be achieved (Sorkin, 2003).

3.2.4.3 Mean Square Displacement and Diffusion Coefficient

The self diffusion coefficient, D of an atom undergoing random Brownian motion in three dimensions can be evaluated from the limiting slope of the mean square displacement as a function of time, that is:

$$D_\alpha = \frac{1}{6N_\alpha} \lim_{t \rightarrow \infty} \frac{d}{dt} \sum_{i=1}^{N_\alpha} \langle [r_i(t) - r_i(0)]^2 \rangle \quad (3.16)$$

where r_i denotes the position vector of atom α , and the angular brackets denote averaging over all choices of time origin within a dynamics trajectory.

An alternative method for obtaining the self diffusion coefficient involves making use of the velocity autocorrelation function. In this case, D is given by:

$$D = \frac{1}{3} \int_0^\infty \langle v_i(t) \cdot v_i(0) \rangle dt \quad (3.17)$$

where $v_i(t)$ denotes the velocity of atom i at time t . Again, averaging is performed over all time origins in the trajectory. This equation is an example of the Green-Kubo

formalism for calculating transport coefficients from time correlation functions measured on an *equilibrium* system.

3.2.4.4 MD vs. Experiment

It has been argued that Computational Chemistry is both “theory” and “experiment”: “theory” since clearly no measurements are made on a real system, and “experiment” since the potentials used are often based on experimental data on simple systems. MD is indeed often referred to as a “computer experiment”.

Today, most computational chemists would probably say that computation is neither theory nor experiment, but rather a third leg on the chemical body-both to test theory and to interpret experiment; alternatively, to perform “experiments” on systems inaccessible to normal experimental techniques.

This discussion puts focus on the relationship between MD and experiment. Experimentalists interpret their data using theories and models-they do not anticipate reality. Experimental data can often be interpreted in several ways, sometimes even within the same theoretical context. Not rarely are data interpreted on the basis of incorrect or inappropriate theory for the system under study. The interpretation of experimental results is not a search for biblical “truth”, just like the computational chemist, the experimentalists use models to make their interpretation, thereby creating a gap between themselves and reality. MD can indeed sometimes be as good (or bad) a method as experiment for modeling this reality.

3.3 Mesoscopic Dynamic (MesoDyn) Simulation

MesoDyn Simulation (Fraaije, 1993; Fraaije *et al.*, 1997) is a dynamic simulation method for studying the long length and time behavior of complex fluid systems, including polymer melts and blends. It has gained wide respect in literature and commercial circles with scientifically astute algorithms aimed at elucidating industrially important mesoscale structure and kinetics. Such structures are found to critically affect the bulk properties of a material and are often frozen in by processing, where timescales may be of the same order as relaxations. The dynamics of the system is described by a set of so-called functional Langevin equations. In simple terms, these are diffusion equations in the component densities which take account of the noise in the system. By means of numerical inversions, the evolution of the component densities is simulated, starting from an initially homogeneous mixture in a cube of typical size 100-1000 nm (with periodic boundary conditions) which can be found for example in polymer blends, block-copolymer systems, surfactant aggregates in detergent materials, latex particles, or drug delivery systems (Accelrys, 2007).

MesoDyn takes a coarse-grained description of a complex fluid and performs time-evolution dynamics of the density and potential fields of the system. The free energy seeks a minimum which may be achieved by demixing if intermolecular forces are sufficiently disfavored. The coarse-graining of the system involves replacing polymer chains by a Gaussian representation with the same response functions and including non-ideality of the system via effective external potentials, the magnitude of which is determined by the Flory-Huggins interaction parameters of the various binary pairs in the system. Electrostatics may be included via the Flory-Huggins parameter, or may be explicitly included for each bead in the system (Accelrys, 2007).

3.3.1 Theory in MesoDyn Simulation

MesoDyn is based on a dynamic variant of mean-field density functional theory. The latter is based on a theorem which basically states that there is one-to-one mapping between the distribution functions of the system, the densities and an external potential field. Furthermore, a real system, *i.e.* a system with interactions, can be equated to an *ideal* system, *i.e.* without interactions, via an effective external potential (Fan *et al.*, 1994; Fraaije *et al.*, 1997).

The reason for this is that with the above theorem an external potential can always be found such that the distribution of the ideal system equals that of the real system at the same density. This theory can be used to great effect in the description of polymer fluids. We take the polymer chain as the fundamental building blocks of the model. In this description, the intrachain correlations can in principle be treated by any suitable model. In practice, a Gaussian chain model is used because it allows a factorization of the interactions, hence is computationally very efficient, and because it can be shown that the Gaussian chain may be used as a statistical model for a real chain, *i.e.* for each real, atomistic force-field model, a Gaussian chain representation with the same response function can be found.

The non-interacting Gaussian chains are hence the *ideal* system. Any interchain, *i.e.* non-bonded interactions are treated as *non-ideal*, that is, they enter into the effective external potential. Hence, the molecular ensemble is represented by a number n of Gaussian chains, made up of a number of different beads of types I , with a total number of N beads per chain. At an instant of time there will be a certain distribution ψ of bead positions in space, resulting in three-dimensional concentration fields $\rho_I(r)$. The evolution of these fields is the result of the dynamics outlined in the

following section, in combination with the thermodynamic driving force described in the section thereafter. For simplicity of presentation, in the following we are going to limit the number of bead types to two, named A and B , but the theory will equally apply to any number of bead types (Fraaije, 1993).

3.3.2 Dynamics of MesoDyn Simulation

The derivation of the diffusive dynamics of the molecular ensemble is based on the assumption that for each type of bead I the local flux is proportional to the local bead concentration and the local thermodynamic driving force:

$$J_I = -M\rho_I\nabla\mu_I + \tilde{J}_I \quad (3.18)$$

where \tilde{J}_I is a stochastic flux (related to thermal noise). Together with the continuity equation

$$\frac{\partial\rho_I}{\partial t} + \nabla \cdot J_I = 0 \quad (3.19)$$

this leads to simple diagonal functional Langevin equations (stochastic diffusion equations) in the density fields:

$$\frac{\partial\rho_I}{\partial t} = M\nabla \cdot \rho_I\nabla\mu_I + \eta_I \quad (3.20)$$

with a Gaussian distribution of the noise.

However, the fluctuations in the total density of this simple system are not realistic since finite compressibility is not enforced by the mean-field potential chosen (see below). Therefore, total density fluctuations are simply removed by introducing an incompressibility constraint:

$$(\rho_A(r,t) + \rho_B(r,t)) = \frac{1}{v_B} \quad (3.21)$$

where v_B is the average bead volume. This condition then leads to “exchange”

Langevin equations:

$$\frac{\partial \rho_A}{\partial t} = M v_B \nabla \cdot \rho_A \rho_B \nabla [\mu_A - \mu_B] + \eta \quad (3.22)$$

and

$$\frac{\partial \rho_B}{\partial t} = M v_B \nabla \cdot \rho_A \rho_B \nabla [\mu_B - \mu_A] - \eta \quad (3.23)$$

Here M is a bead mobility parameter. The kinetic coefficient $M v_B \rho_A \rho_B$ models a local exchange mechanism. Hence the model is strictly valid only for Rouse dynamics (Effects such as reptation lead to kinetic coefficients which extend over a range of roughly the coil size. They lead to computationally expensive non-local operators which in addition, are very complex in the non-linear regime).

The distribution of the Gaussian noise satisfies the fluctuation-dissipation theorem:

$$\langle \eta(r,t) \rangle = 0 \quad (3.24)$$

and

$$\langle \eta(r,t) \eta(r',t') \rangle = -\frac{2M v_B}{\beta} \delta(t-t') \nabla_r \cdot \delta(r-r') \rho_A \rho_B \nabla_{r'} \quad (3.25)$$

and ensures that the time-integration of the Langevin equations generates an ensemble of density fields with Boltzmann distributions.

3.3.3 Thermodynamics of MesoDyn Simulation

The above Langevin equations contain the bead chemical potential as the thermodynamic driving force of the diffusive dynamics. These chemical potentials can be derived from the thermodynamics of the molecular ensemble.

The first step is to derive an expression for the free energy of the system in terms of the bead distribution functions ψ . Since the positions of the beads are correlated to each other this amounts to a multi-dimensional many-body problem. To overcome this, any interchain correlations are neglected, and the system is approximated by a set of independent Gaussian chains embedded in a mean-field.

The distribution functions of the independent Gaussian chains factorize exactly, and hence the density functional can be simplified to a product of single-chain density functionals. In this approximation, the free energy functional can be written as

$$F[\psi] = \frac{1}{Q} \int dR (\psi H^{id} + \beta^{-1} \psi \ln \psi) + F^{nid}[\psi] \quad (3.26)$$

The first term is the average value of the Hamiltonian for the ideal system, comprising the internal Gaussian chain interactions:

$$H^{id} = \sum_{\gamma=1}^n H_{\gamma}^G \quad (3.27)$$

where H_{γ}^G is the Gaussian chain Hamiltonian

$$\beta H_{\gamma}^G = \frac{3}{2a^2} \sum_{s=2}^N (R_{\gamma,s} - R_{\gamma,s-1})^2 \quad (3.28)$$

here a is the Gaussian bond length parameter and the index s goes over all N segments of the chain. The second term in the free energy functional stems from the Gibbs entropy of the distribution. The third term is the non-ideal contribution related to the interchain interactions.

In the present mean-field approximation, the latter is independent of the particular distribution ψ . In the spirit of the particular application of density functional theory taken here, namely treating the chains as the ideal system, the correlations between the chains are neglected, and the density functional method applies to the correlations within the Gaussian chain only.

The key rudiment of dynamic density functional theory is now that on a coarse-grained time-scale the distribution function ψ is such that the free energy functional $F[\psi]$ is minimized. Hence ψ is independent of the history of the system, and is fully characterized by the constraints that it represents the density distribution and minimizes the free energy functional (Jawalkar *et al.*, 2005). This constraint on the density fields is realized by means of an external potential U_I .

The constraint minimization of the free energy functional leads to an optimal distribution, which in turn, and by the one-to-one relation between densities, distributions and external potential can be written as:

$$\beta F[\rho] = n \ln \Phi + \beta^{-1} \ln n! - \sum_I \int U_I(r) \rho_I(r) dr + \beta F^{nid}[\rho] \quad (3.29)$$

Finally, in order to account for the interchain (non-ideal) interactions, a Flory-Huggins type interaction is introduced:

$$\begin{aligned}
F^{nid}[\rho] = & \frac{1}{2} \iint \varepsilon_{AA}(|r-r'|) \rho_A(r) \rho_A(r') + \varepsilon_{AB}(|r-r'|) \rho_A(r) \rho_B(r') \\
& + \varepsilon_{BA}(|r-r'|) \rho_B(r) \rho_A(r') + \varepsilon_{BB}(|r-r'|) \rho_B(r) \rho_B(r') dr dr' \quad (3.30)
\end{aligned}$$

where $\varepsilon_{ij}(|r-r'|)$ is a mean-field energetic interaction between beads of type i at r and type j at r' . This interaction is defined by the same Gaussian kernel as in the ideal chain Hamiltonian:

$$\varepsilon_{ij}(|r-r'|) = \varepsilon_{ij}^0 \left(\frac{3}{2\pi a^2} \right)^{\frac{3}{2}} e^{-\frac{3}{2a^2}(|r-r'|)^2} \quad (3.31)$$

3.3.4 Parameterization: Mapping of Atomistic Level to Mesoscale Molecular Architecture

As a result of the model of the mesoscopic molecular ensemble dynamics outlined above, the following parameters arise as characterizing the system. The molecular architecture of the Gaussian chain in terms of a number of different beads. This includes the chain or block lengths of each bead type, as well as the possibility of branching.

The Gaussian bond length parameter. The self-diffusion coefficient of each bead type. The Flory-Huggins interaction parameters between the different bead types. Fortunately, the theory does not end here, but actually tells us how to interpret these parameters in terms of atomistic information. The crucial theorem which helps at this point was already mentioned above. It says that for each atomistic, force field model, a Gaussian chain representation can be found, such that this Gaussian chain has the same response function (or correlation functions) as the real system.

At this point it is important to emphasize, that this Gaussian chain might differ considerably from the real chain. For example, the Gaussian chain may be branched

while the real chain is not. This, however, does not need to concern us. We only need to know what the mapping is, and in particular what each bead represents in terms of bonded atoms. In conclusion, MesoDyn offers a complete path from the atomistic level through to the simulation of mesoscale phase morphologies.

3.3.5 Numerics of MesoDyn Simulation

The Gaussian chain density functional constitutes a one-to-one relation between the external potential fields and the density fields for each bead type. In addition, the intrinsic chemical potentials μ are functionals of the external potentials and the density fields. The coupled Langevin equations constitute a relation between the time derivatives and the intrinsic chemical potentials. Finally, the noise source is related to the exchange kinetic coefficients.

CHAPTER IV

STRUCTURE, PROPERTIES AND DRUG CONTROLLED RELEASE EFFICIENCY OF CHITOSAN/MONTMORILLONITE NANOCOMPOSITE

4.1 Introduction

Chitosan/Montmorillonite (CS/MMT) nanocomposite is a CS-based material that might improve the drug controlled release efficiency of pristine CS. Preparation of this nanocomposite is based on the convenient method by direct mixing of clay particles (*i.e.* MMT) into CS matrix. The cationic biopolymer CS can be directly intercalated into the MMT interlayer through the cationic exchange and hydrogen bonding processes to initiate the novel CS/MMT nanocomposite material with fascinating properties (Darder *et al.*, 2003; 2005). Hence, this nanocomposite is expected to have novel properties because of the nanometric scale on which the nanoclay particles, with their plate-like shape, would alter the physical and chemical properties and may improve drug controlled release efficiency of pristine polymer, CS. Accordingly, the MMT particles may act as barrier as well as implantable drug reservoir to provide on-demand release of drug molecules. Moreover, another significant potential of this CS/MMT nanocomposite for using as a drug controlled release material is biocompatible, biodegradable and low cost

(Liu *et al.*, 2008; Wang *et al.*, 2009). To design the CS/MMT nanocomposite for drug controlled release application, a clue for choosing the proper drug type, to provide the highest controlled release efficiency, is very important. Accordingly, two types of drug, acidic and basic drug, were investigated in this work; consequently, salicylic acid and theophylline were considered as the representative models of acidic and basic drug, respectively.

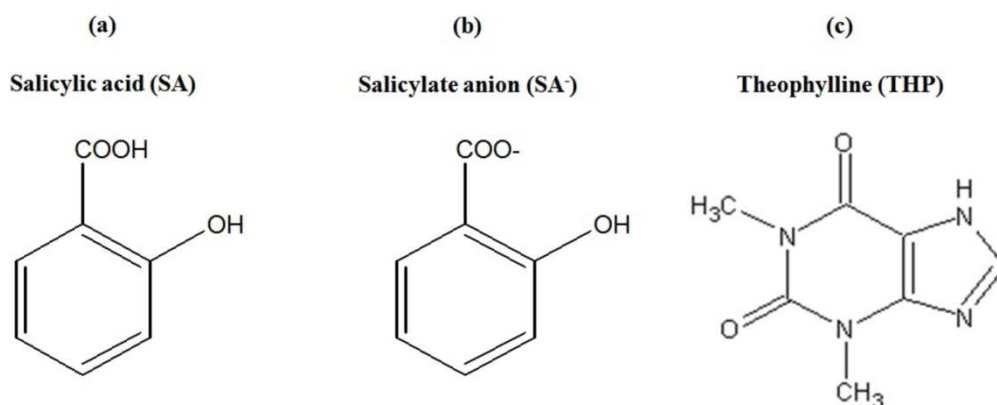


Figure 4.1 Chemical structures of (a) salicylic acid, (b) salicylate anion and (c) theophylline.

Several techniques were employed to study the structure and morphology of the CS/MMT nanocomposites, *i.e.* X-ray spectroscopy and electron microscopy. The thermal property and stability of these materials were studied by TGA technique while the interaction between CS-drugs was studied by FTIR spectroscopy. The *in-vitro* drugs controlled release efficiency was also studied by the dissolution apparatus V that was most suitable for transdermal drug delivery.

The computational molecular simulation technique was also employed to fulfill the experimental findings and gain a comprehensive understanding in atomistic

level of these materials. Molecular modeling has been performed at atomistic level of CS and its complex with salicylic acid (SA), intends to study the structure, interaction and diffusion of drug molecule in bulk CS matrix. The results provided a detailed description of a disordered state of CS chains as well as an interaction with the model drug. Moreover, MD simulation was also employed to study the intercalation structure of SA/CS/MMT nanocomposite to investigate the basal spacing and probe the layering behavior and interlayer structure of the SA/CS/MMT nanocomposite.

Technologically, this work has been driven by an interest in understanding of the correlation between the structure and property of CS/MMT nanocomposites and the drug diffusion-controlled phenomena. Overall of this work provide us with a clue for developing of a novel CS/MMT nanocomposite suitable for controlled release drug delivery application.

4.2 Research Methodology

4.2.1 Experimental Section

4.2.1.1 Materials and Apparatus

- Magnetic stirrers and magnetic bars
- Glass *Petri* dish for sample casting
- Chitosan (CS; $M_v = 6.58 \times 10^5$ g/mol, %DD = 73%), Aquatic Nutrition Lab
- Sodium Montmorillonite (Na^+ -MMT; CEC = 102.8 mequiv/100 g) refined from Bentonite, Vittayasom Co.
- Salicylic acid (SA; $\text{C}_7\text{H}_6\text{O}_3$), Aldrich
- Theophylline (THP; $\text{C}_7\text{H}_8\text{N}_4\text{O}_2$), Aldrich
- Acetic acid (CH_3COOH), Analytical Reagent, Merck

4.2.1.2 Sample Preparation

Drug-loaded CS: In case of acidic drug, salicylic acid (SA) and CS powder were mixed together to obtain chitosonium salicylate (SA/CS) salt with 10-100 %w/w drug loaded by using water as a solvent. While, in case of basic drug, theophylline (THP) was dissolved in 1 %w/v chitosan acidic solution at 10-100 %w/w drug loaded by using 1 %v/v acetic acid as a solvent. The drug containing solutions in all cases were then cast in a glass *Petri* dish and air-dried at 60°C, the in vitro drug-controlled delivery behavior and physical properties were studied.

Drug-loaded MMT: 0.03 %w/v SA and 2.0 %w/v THP aqueous solutions were prepared. Aliquots were taken from these stocks and diluted with water to obtain 25 ml of several drug concentrations. For sorption experiments, 25 ml of each drug solution was added to a flask containing 0.25 g of MMT. A control sample containing MMT in 25 ml of water was run in parallel. All flasks were shaken at 150 rpm for 48 h. Samples were then centrifuged (7,000 rpm, 10 min, 25°C) and the supernatant solutions decanted for subsequent analysis with UV-VIS spectroscopy at wavelength 297 and 272 nm for SA and THP, respectively. The solid samples were allowed to air-dry at room temperature and then used for subsequent intercalation analysis.

SA/CS/MMT nanocomposites: SA loaded CS/MMT nanocomposite films with different mass ratios of CS to Na⁺-MMT were prepared by a casting/solvent evaporation method. Starting by the preparation of the 70 %w/w chitosonium salicylate (SA/CS) solutions containing 322.0 mg of CS and 225.4 mg of SA in 50 ml of distilled water and then the SA/CS solutions were stirred until obtained the clear homogeneous solutions. To prepare SA/CS/MMT nanocomposites with initial

CS:MMT molecular ratios of 0.5:1, 1:1, and 2:1, several amounts of SA/CS solution (6.25 ml, 12.5 ml, and 25 ml, respectively) were taken from this stock and then diluted with water to 25 ml. The resulting SA/CS solutions were stirred for 4 h before being mixed with the MMT suspension. Preparation of SA/CS/MMT nanocomposite, 25 ml of each SA/CS concentration was slowly added to 25 ml of 2 %w/v clay suspension with stirring at 50°C and the resulting mixtures were continually stirred for 2 days. The nanocomposites were air-dried at 60°C, in vitro drug-controlled delivery behavior and structural properties were then studied.

4.2.1.3 Characterization

Fourier Transform Infrared (FTIR) Spectroscopy

FTIR spectroscopy was employed to study the interaction between CS-drugs. FTIR measurements were performed on a Perkin Elmer model: spectrum GX. The number of scans was 4 at the resolution of 4 cm⁻¹. The range of measurement was between 4000-400 cm⁻¹. The infrared spectra of the thin film samples were obtained with ATR-FTIR method, whereas, the spectra of the powder samples were obtained with KBr method. The spectra were averaged/co-added and converted to absorbance using Spectrum v.3.01 software.

Powder X-ray Diffraction (XRD)

XRD technique was employed to verify the intercalation structure of CS chains within MMT interlayer. XRD measurements were conducted for specimens at room temperature with an X-ray diffractometer (Bruker axs D5005). A monochromic CuK α (1.54 Å) X-ray source was operated at 40 kV and 40 mA, and the diffraction intensity was measured at a scattering angle 2 θ scanned from 2° to 30°.

Scanning Electron Microscopy (SEM)

SEM was employed to study the drug crystallization within CS matrix. The measurements were conducted on a JEOL JSM-6400 with an operating voltage at 10 kV. The sample films were mounted onto stubs, sputter coated with gold in a vacuum evaporator in order to make them conductive.

Transmission Electron Microscopy (TEM)

TEM was employed to verify the intercalation structure of CS chains within MMT interlayer. The measurements were conducted on a JEOL JEM-2010 microscope with an operating voltage at 200 kV. For the TEM investigations a drop of the sample (water suspension) was taken on a carbon-coated copper grid which was then dried at room temperature.

Thermogravimetric Analysis (TGA)

TGA was employed to study the thermal property and stability of SA/CS/MMT nanocomposites. The measurements were conducted on a TGA-DTA Analyzer, TA Instrument SDT 2960. The samples were heated in the temperature range 30-900°C using heating rates of 10°C/min, under a nitrogen atmosphere. The temperature and the weight scales were calibrated using high-purity standards (indium, nickel, zinc, aluminum and gold) over a specific range of heating rates with a calibration parameter of their respective melting points.

Dissolution Apparatus

Dissolution apparatus was employed to study the drug controlled release efficiency. The releasing profiles of SA and THP from drug-loaded CS films and

drug-loaded CS/MMT nanocomposites were studied. The measurements were performed on the USP dissolution apparatus V (paddle over disk, Pharma Test, PTW S3) in 900 ml distilled water. The paddles were rotated at 50 rpm at 32°C for transdermal drug delivery. Drug concentration was analyzed by using a UV/VIS spectrometer (Perkin Elmer, Lambda Bio 20) at wavelength 297 and 272 nm for SA and THP, respectively. All the experiments were done in triplicate and mean values were reported.

4.2.2 Computational Section

4.2.2.1 Molecular Dynamics Simulation of Bulk Amorphous Chitosan and Salicylic Acid/Theophylline in Chitosan Matrix

All simulations were carried out at 25°C (298 K) with Discover module in Materials Studio (MS version 4.2) (Accelrys, 2007). The COMPASS (Rigby *et al.*, 1997; Sun, 1998(a&b)) force field was employed for all calculations. Each simulation system was minimized using Discover module. The amorphous phase of pure CS and its complex with SA and THP, *i.e.* a model of drug control-release systems, were constructed inside the simulation box with periodic boundary conditions. The 5 oligomers with 10 monomer units constitute the amorphous cell for the neat CS system. Density data for CS was taken from the literature: $\rho_{CS} = 0.67 \text{ g/cm}^3$ (Gulke, 1999; Prathab *et al.*, 2007) and the box sizes was $23.7 \times 23.7 \times 23.7 \text{ \AA}^3$. In general, the initial amorphous structure is in a relatively high-energy state. Therefore, before performing MD calculations, we had to perform the energy minimization by using smart minimization method (Accelrys, 2007) (with a convergence level of 0.01

kcal/mol/Å). The Smart minimizer starts with the steepest descent method, followed by the conjugate gradient method and ends with a Newton method. Atom-based cutoff of 9.5 Å and a switching function with the spline and buffer widths of 5 and 2 Å, respectively, were applied to evaluate non-bonded interactions. The MD simulations under constant temperature and volume (NVT ensemble) were performed for each configuration. A time step of 1 fs was used, and temperature was controlled by the Anderson thermostat. Short NVT simulations were run for 0.2 ns at 900 K to relax the structures to obtain the equilibrium density. Then another NVT simulation was performed for 1 ns at 25°C. The energy of the system was monitored to ensure that it fluctuated around the average value, and this was considered as a criterion for having “equilibrated” system to the desired temperature, wherein trajectories were stored periodically for later processing. The solubility parameters (δ) and X-Ray scattering function of pure CS were calculated in this equilibrated state, to match these values with the reported literature data as a reliable test protocol.

Bulks amorphous states of drugs incorporated CS were built in similar manner by adding of 10 molecules of salicylic acid or theophylline into the periodic simulation box containing 5 oligomers with 10 monomer units of CS. NPT MD was run to equilibrate structure and density. The amorphous assembly was energy-minimized using the Smart minimization method (Accelrys, 2007) with a convergence level of 0.01 kcal/mol/Å. The Smart minimizer starts with the steepest descent method, followed by the conjugate gradient method and ends with a Newton method. Atom-based cutoff of 9.5 Å and a switching function with the spline and buffer widths of 5 and 2 Å, respectively, were applied to evaluate non-bonded interactions. Since the density of the amorphous CS/drug is different from those of the

crystalline structures of the starting pure polymers, the simulations were carried out with isothermal-isobaric (NPT) ensemble based on Andersen-Berendsen method (Andersen, 1980;1983; Berendsen *et al.*, 1984). These NPT simulations were performed at atmospheric pressure as previously described (Rigby, 2004). Subsequently, short NVT simulations were run for 0.05 ns at 900 K, 700 K, 500 K and 300 K to relax the structures to obtain the equilibrium density. Then another NVT simulation was performed for 1 ns at 298 K with a time step of 1 fs. Hildebrand solubility parameter (δ), the diffusion coefficients of drugs within CS along with the radial distribution functions (RDFs), $g(r)$, were calculated in this equilibrated state.

4.2.2.2 Molecular Dynamics Simulation of SA/CS/MMT Nanocomposite

One of the most commonly used layer silicate in the preparation of polymer/layer silicate nanocomposites is montmorillonite (MMT) belong to the 2:1 type swelling clays (smectite). The thickness of a layer is ~ 0.97 nm. Because of isomorphic substitutions within the layers (for example, Al^{3+} replaced by Mg^{2+} or Fe^{2+} , or Mg^{2+} replaced by Li^+ in the octahedral sheet; Si^{4+} replaced by Al^{3+} in the tetrahedral sheet), the clay layer is negatively charged, which is counterbalanced by cations within the galleries. These cations are exchangeable and the sum of their charges is the cation exchange capacity (CEC). This CEC value determines the number of cationic molecules that can be intercalated into the galleries by ion exchange. Clay minerals are hydrophilic and are only miscible with hydrophilic polymers. In this work, the clay mineral surface was modified by cationic polymer and model drug (salicylic acid; SA), where alkali cations in the galleries are replaced by the protonated CS ($-\text{NH}_3^+$). As seen from XRD results (will be discussed later),

there were two different values of interlayer spacings as a function of initial CS:MMT ratio. In addition, when SA was mixed with CS and MMT at several ratios, the gallery spacing was varied depending on the amount of CS adsorbed. It is implied that the magnitude of interlayer spacing should be related to an imbalance between an attractive interaction between charge groups of CS and SA with MMT surface.

Due to the fine particle, the low crystallizability, and the complicated chemical components of clays, detailed information about the interlayer structure and the atomic local environment in polymer-clay nanocomposite is rarely available from experimental measurements. More recently, molecular simulation has been proved to be a powerful technique to probe the detailed information about molecular arrangements and layering structure. The simulated results provide not only the complementary evidence for the experimental results but also new insights for the microstructure of polymer nanocomposites. With the application of molecular simulation in the study of polymer nanocomposite, more and more detailed information on structure and physical-chemical characteristics will be provided. This is of great importance in the design and application of clay-based nanocomposite materials.

In this study, we employed the polymer consistent force field (PCFF) with recent parameters by Heinz and coworkers (Heinz *et al.*, 2005) for layered silicates and the Discover program from Accelrys, Inc (Accelrys, 2007). The semiempirical energy model for layered silicates takes surface energies accurately into account, and thus reproduces crystal structures, surface energies, and approximate vibrational frequencies of phyllosilicates in very good agreement with experiment. Moreover, the

PCFF parameters allow the quantitative reproduction of densities, vaporization energies, and rotational energy barriers of various polymers.

Montmorillonite models have been prepared according to the X-ray crystal structure. The spatial distribution of $\text{Al}^{3+} \rightarrow \text{Mg}^{2+}$ charge defects in the octahedral sheet is modeled in agreement with solid-state NMR data and the assignment of charges at the defect sites has been previously discussed in detail. Montmorillonite structure with a cation exchange capacity (CEC) of 144 meq/100 g is considered. The cation exchange capacity (CEC, milliequivalent of positive charge per 100 g of clay, or meq/100 g), which is defined as the amount of the exchangeable cations retained by the clay to neutralize the negative charge, can be calculated from the layer charge. The chemical composition of the corresponding montmorillonite models is $\text{Na}_{0.533}[\text{Si}_4\text{O}_8][\text{Al}_{1.467}\text{Mg}_{0.533}\text{O}_2(\text{OH})_2]$, the net charge per unit cell is -0.533 and the calculated formula weight per unit cell of a Na clay is 371 g. Thus, the CEC of this montmorillonite is 144 meq/100 g. The models closely resemble natural montmorillonite. An uncertainty in $\text{CEC} \pm 5\%$ and additional isomorphous substitution, *e.g.*, $\text{Al}^{3+} \rightarrow \text{Fe}^{3+}$ can be found in the corresponding natural minerals.

The model of CS and SA were sketched using Material Studio (MS), Version 4.2. Since chitosan is usually insoluble in water, it is necessary to protonate its NH_2 groups to obtain the soluble acidic models of protonated chitosan of the type R-NH_3^+ with chain lengths $n = 4$ was prepared using Sketcher. For NH_3^+ head groups, the assigned partial charges are -0.50 for N and +0.4 for each H. SA was also represented in the anionic form according to the experimental condition. All systems are contained in a cubic box of $2.596 \times 2.705 \times 10 \text{ nm}^3$ size, based on a $5 \times 3 \times 1$ unit cell of montmorillonite. Periodic boundary conditions are effective in the x and y

directions while the systems remain open in the z direction to allow free equilibration of the gallery spacing. These unit cells contain 16 cations inside the gallery and were removed when the protonated chitosans and SA were added. Four systems were investigated containing 16, 20, 24 and 28 chitosan units with 0, 4, 8 and 12 of SA molecules in the ionic forms to balance the charge inside the gallery. The initial structure for each SA/CS system was generated using the Amorphous Cell module with the slab mode option at the appropriated thickness. Then it was inserted inside the interlayer spacing of montmorillonite. Two additional mixtures of SA/CS were also placed at the top and bottom of the clay surface according to the technique to predict the d -spacing described previously by Heinz.

Several structures with different orientation distribution of the CS chains and salicylate anion were built for each system, subjected to a short energy minimization (1000 steps conjugate gradient method), and subsequent 0.5 ns NVT dynamics. The equilibration of different start structures for a given CS surface density converged to very similar end structures. The structure of lowest energy was further equilibrated between 0.5 and 1.0 ns, in proportion to number of molecule loadings. Next, two snapshots of equilibrated, single-layer chitosonium-montmorillonite were combined by uniformly offsetting coordinates within the simulation cell and subsequently decreasing the separation distance until CS chains were within a several hundred picometer distance. The duplicate assemblies were subjected to further molecular dynamics simulation (NVT ensemble) about 1 ns. Structures and energies were equilibrated after 0.5-1.0 ns, and snapshots were recorded during the second half of the trajectory to analyze structural and dynamic properties, using 1 ps intervals. In all molecular dynamics simulations, the NVT ensemble, the Verlet integrator, a time step

of 1 fs, a temperature of 298 K (maintained through velocity scaling), and summation of Coulomb and van der Waals interactions using the cell multipole method (fourth order, two layers of cells) were employed, using the Discover program from Accelrys, Inc.

4.3 Results and Discussion

4.3.1 Experimental Section

4.3.1.1 Solubility of Acidic and Basic Drug in Chitosan Matrix

The morphology of CS films loaded with salicylic acid or theophylline at various concentrations was investigated under SEM and XRD technique to determine the drug crystalline in bulk CS that directly indicates the solubility limit of acidic and basic drug in CS matrix.

For acidic drug loading, the XRD patterns of 30-100 %w/w SA loaded CS films are shown in Figure 4.2a. The diffraction peaks at $2\theta \approx 11^\circ$ associated to the drug crystalline are observed at ≥ 90 %w/w drug loading. The result indicates that SA molecules exist in an amorphous form or molecularly dispersed state in the CS matrix at only less than 90 %w/w drug loading. However, at ≤ 60 %w/w SA loading, the chitosan flake was still visually observed associated to the incomplete protonation of CS. Accordingly, the homogeneous SA/CS solution obtained only at 70-80 %w/w SA loading. This result is consistent with the SEM photomicrographs as illustrated in Figure 4.2b.

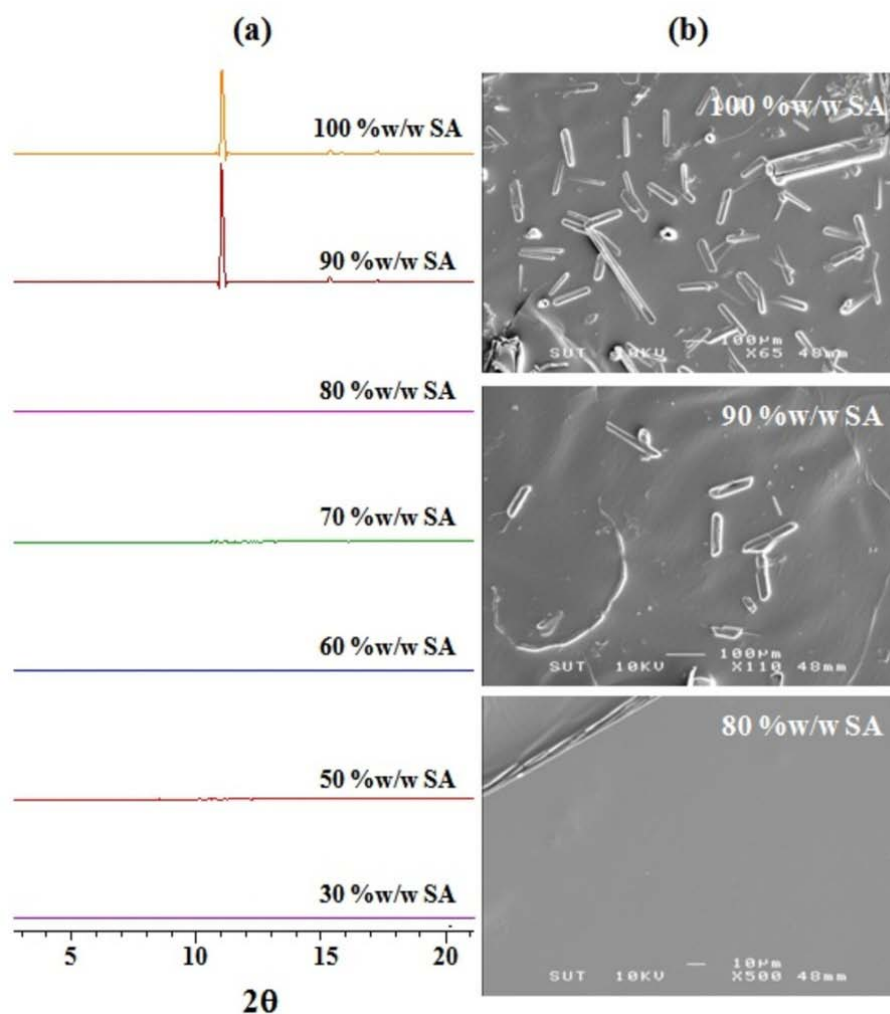


Figure 4.2 (a) XRD patterns and (b) scanning electron photomicrographs of CS films with different %w/w of salicylic acid loading.

FTIR spectra of (a) SA powder, (b) SA containing CS films, and (c) CS flake are shown in Figure 4.3. FTIR results can verify the interaction between CS and SA drug molecule. FTIR spectrum of SA (Figure 4.3a) displays the characteristic bands at around 1670 and 1445 cm^{-1} that due to C=O stretching and C=C stretching of aromatic ring, respectively. Typical C-O carboxylic stretching vibration can also be observed in the spectrum of SA at 1240 cm^{-1} (Sanli *et al.*, 2009). When SA was

loaded into CS (70 % w/w SA in CS), changes in the IR spectrum were observed. The carbonyl stretching peak of pristine CS at 1637 cm^{-1} (amide I peak) (Figure 4.3c), representing the *N*-acetyl functional group of CS, was shifted to an asymmetric NH_3^+ bending at 1633 cm^{-1} (Figure 4.3b). Therefore, salicylate anions (SA^-) might interact CS at the position of amino groups (NH_3^+) to form chitosonium salicylate ($\text{NH}_3^+/\text{SA}^-$).

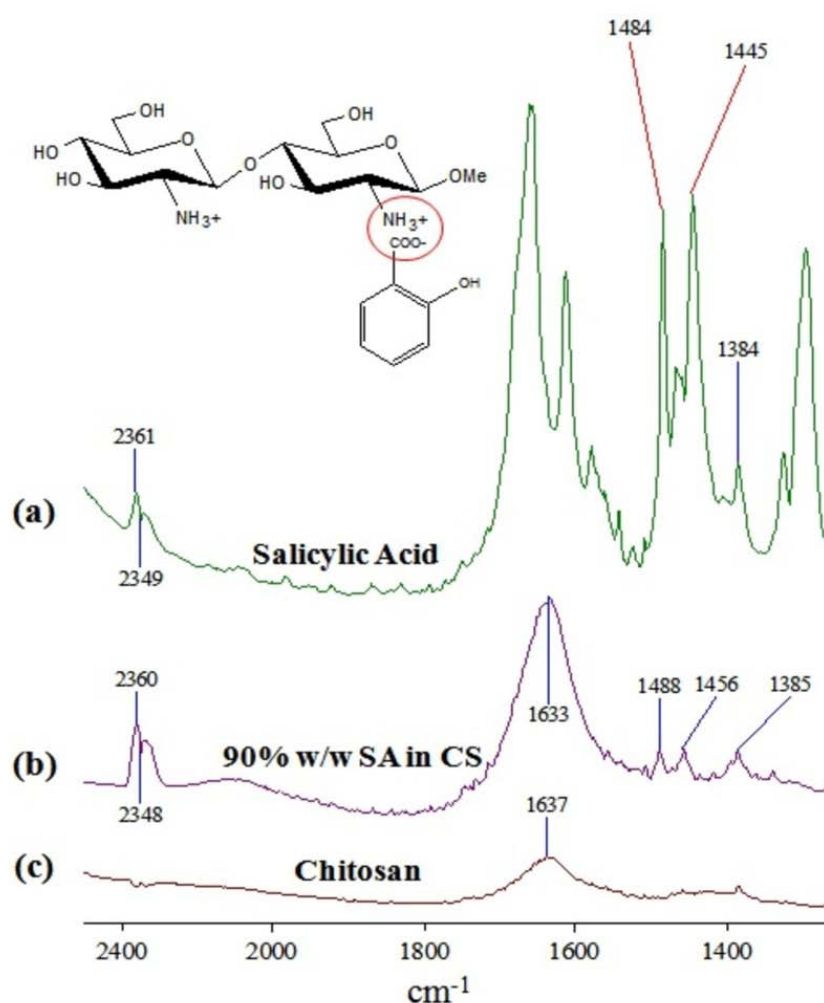


Figure 4.3 FTIR spectra of (a) salicylic acid powder, (b) 70 %w/w salicylic acid loaded chitosan film, and (c) pristine chitosan flake.

The protonation degree of CS in the chitosonium salicylate solution can be calculated from pH (An *et al.*, 2007; Wang *et al.*, 2006a). The protonation reaction of the amino group in CS chain is



where R-NH₂ is the unit of glucosamine in CS and R-NH₃⁺ is the protonated one. The relation between the equilibrium constant (pKa) in Eq. (4.1) and the protonation degree (*P*) is derived from Eqs. (4.2), (4.3):

$$\text{pKa} = \text{pH} - \log(\text{C}_{\text{NH}_2}/\text{C}_{\text{NH}_3^+}) \quad (4.2)$$

$$P = \text{C}_{\text{NH}_3^+}/C \quad (4.3)$$

$$\text{pKa} = \text{pH} - \log((1 - P)/P) \quad (4.4)$$

where the value for pKa is 6.3 (Wang *et al.*, 2006a), C_{NH₂} is the concentration of the non protonated amino group in solution, C_{NH₃⁺} is the concentration of the protonated amino group at a given pH and C is the total concentration of CS solution. According to pH of chitosonium salicylate solution, *P* values of CS were calculated by Eq. (4.4). The *P* values and the corresponding chitosonium salicylate concentration are demonstrated in Figure 4.4. Accordingly, *P* values increase while the corresponding pH of chitosonium salicylate solutions decrease, with increase of SA concentration and reach ~100% protonation at 70 %w/w drug loading (pH = 3.64). These *P* values agree well with XRD and SEM results as previously discussed. Therefore, the chitosonium salicylate with concentration of 70 %w/w SA/CS was selected for the preparation of SA/CS/MMT nanocomposites.

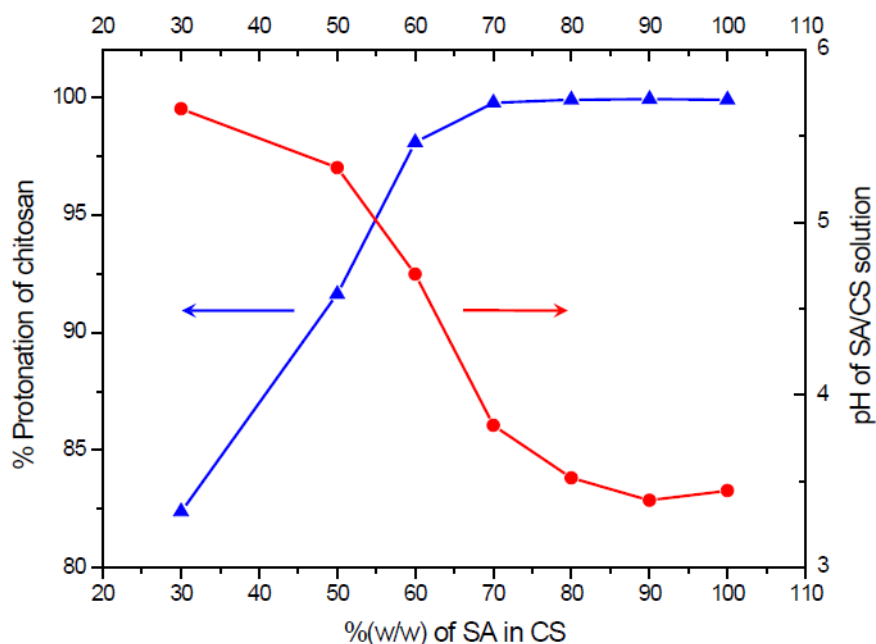


Figure 4.4 Correlation of the protonation degree (P) of chitosan and pH of the solution versus the chitosonium salicylate concentration.

For basic drug loading, the XRD patterns of 10-60 %w/w anhydrous THP loaded CS films are shown in Figure 4.5a. The drug crystalline peaks were observed at only 10 %w/w drug loading and higher. The diffraction peaks associated with both anhydrous and monohydrate THP were observed in CS films loaded with anhydrous THP. THP in CS films seems to exist in both anhydrous and monohydrate crystalline forms. There have been many studies reporting the phase transition of hydrate and anhydrous THP. Rodríguez-Hornedo and Wu reported that the transformation of anhydrous THP to monohydrate form took place when being recrystallized from an aqueous buffer supersaturated solution or processed during wet granulation or even stored at high humidity condition (Rodríguez-Hornedo *et al.*, 1991). The phase transformation of THP monohydrate to anhydrous THP was about 60-70°C (Suihko *et al.*, 1997). It was suggested that the crystallization below the phase transformation

point would provide the monohydrate crystal. In this study, the CS films were dried at 60°C, which was closed to the transformation point. This may result in the crystallization of both anhydrous and monohydrate THP in the films.

From SEM micrographs, two crystal forms of THP, needle-like and plate-like crystals, were observed in all films. Rodríguez-Hornedo *et al.* reported that the plate-like crystal was anhydrous crystal of THP, which would change to the needle-like crystal of monohydrate form in the presence of water or high humidity (Rodríguez-Hornedo *et al.*, 1991). THP can crystallize in anhydrous or monohydrate crystal forms in CS films.

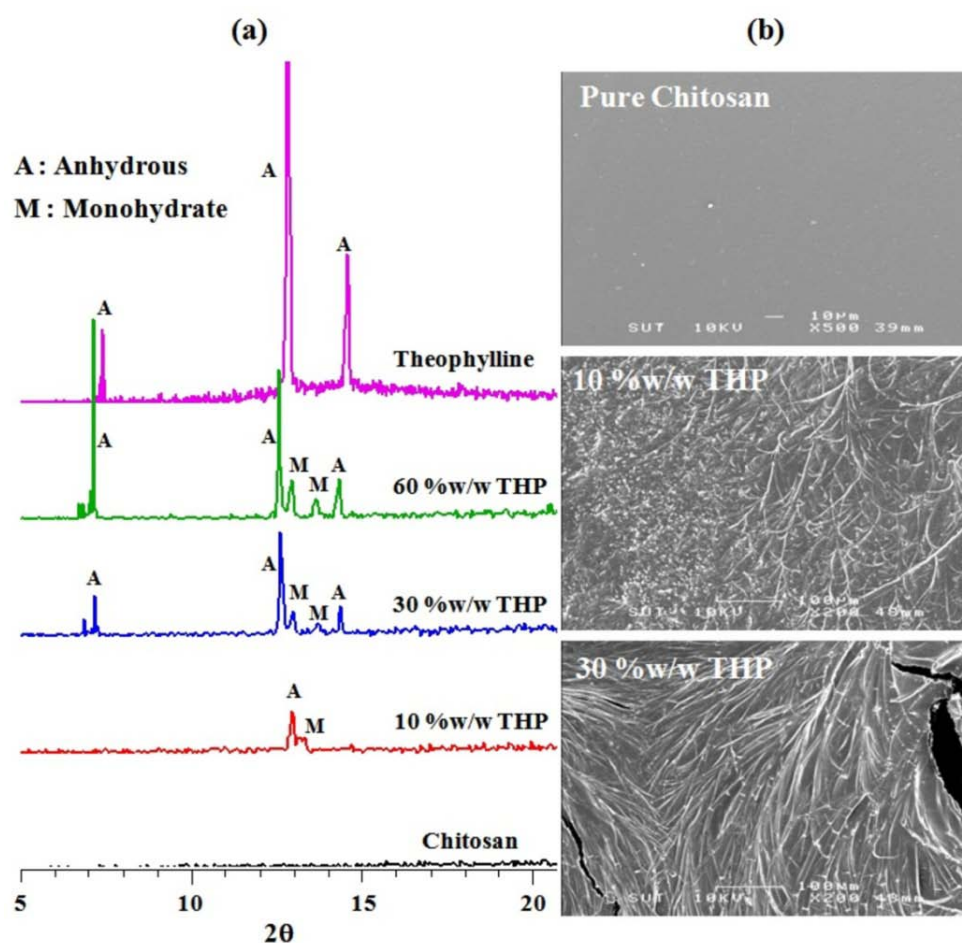


Figure 4.5 (a) XRD patterns and (b) scanning electron micrographs of CS films with different %w/w of theophylline loading.

Accordingly, can be concluded that the basic drug or THP cannot dissolve in CS acidic solution, although at very low drug concentration. There should be no drug-polymer interaction occurring for the case of basic drug loading.

4.3.1.2 Sorption of Acidic and Basic Drug by Na⁺-Montmorillonite

XRD technique was employed to study the intercalation structure of model drugs, SA and THP, into the MMT interlayer. In Figure 4.6, the XRD pattern of pristine MMT shows the *d*-spacing (1.25 nm) does not increased with SA loading. Therefore, salicylate anions (SA⁻; from dissociation of SA) cannot exchange with Na⁺ to intercalate into the MMT interlayer.

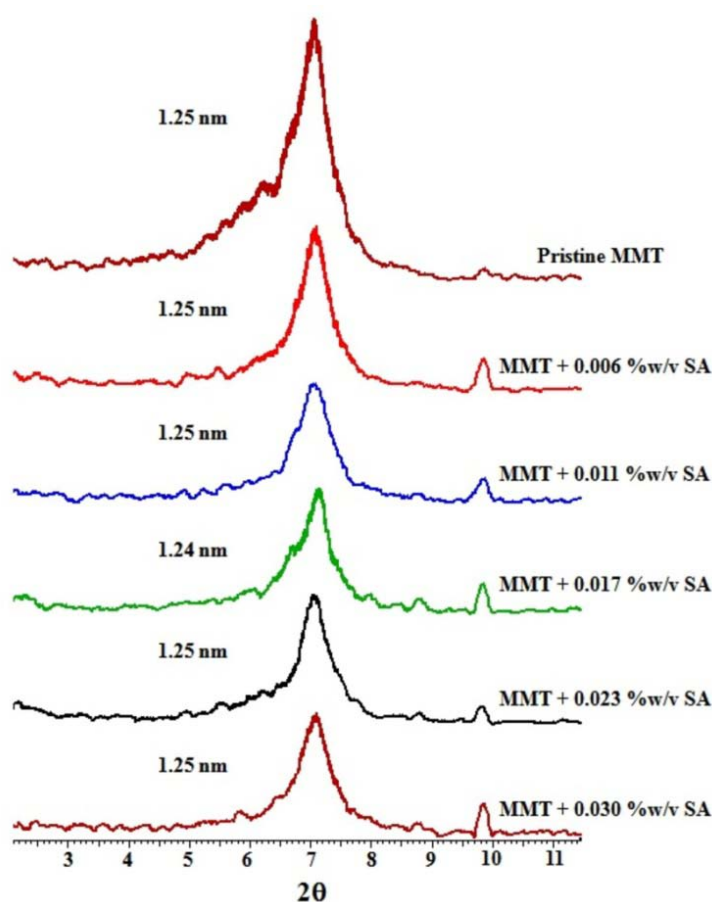


Figure 4.6 XRD patterns of pristine Na⁺-MMT and Na⁺-MMT with different %w/v of salicylic acid loading.

In contrast, for the sorption of basic drug, THP, by MMT, the *d*-spacing of MMT increases with drug concentration as demonstrated in Figure 4.7, and the drug concentration decreases after this sorption. This can be designated to the direct intercalation of protonated theophylline (THP⁺) into the MMT interlayer via the cation exchange process.

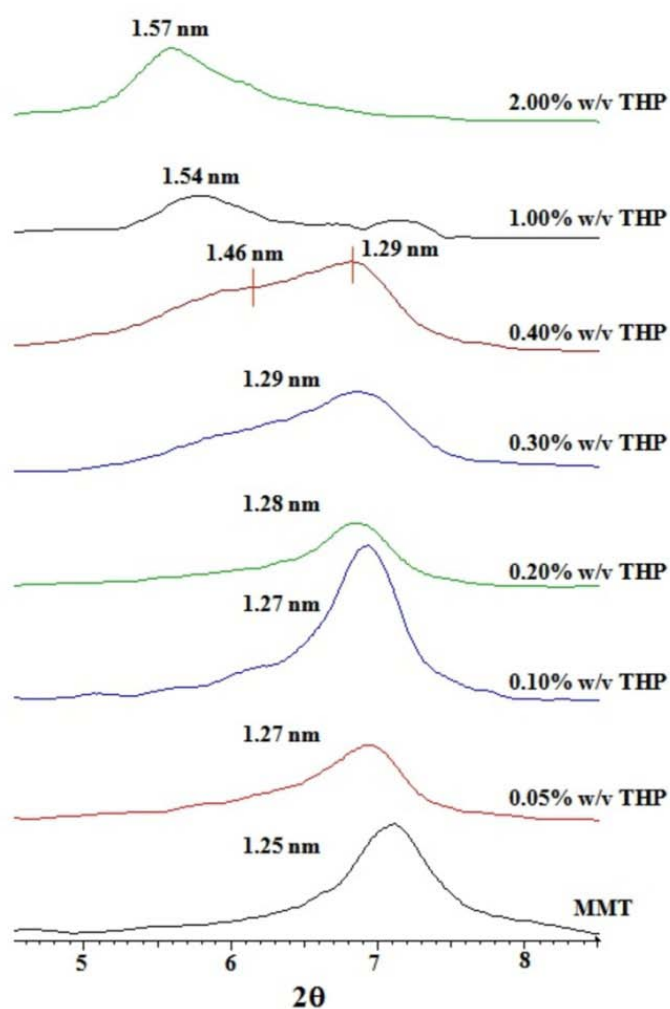


Figure 4.7 XRD patterns of pristine Na⁺-MMT and Na⁺-MMT with different % w/v of theophylline loading.

4.3.1.3 Structure, Morphology and Thermal Stability of SA/CS/MMT Nanocomposites

XRD technique was employed to verify the intercalation structure of SA/CS/MMT. Figure 4.8 displays XRD patterns of pristine MMT and SA/CS/MMT nanocomposites with different initial CS:MMT molar ratios (0.5:1, 1:1, and 2:1). Accordingly, the *d*-spacing of MMT increases with increase of the initial CS:MMT molar ratio associated to the loaded amount of chitosonium salicylate in the MMT interlayer. Hence, chitosonium salicylate (SA/CS) should have an extended structure to facilitate the intercalation process.

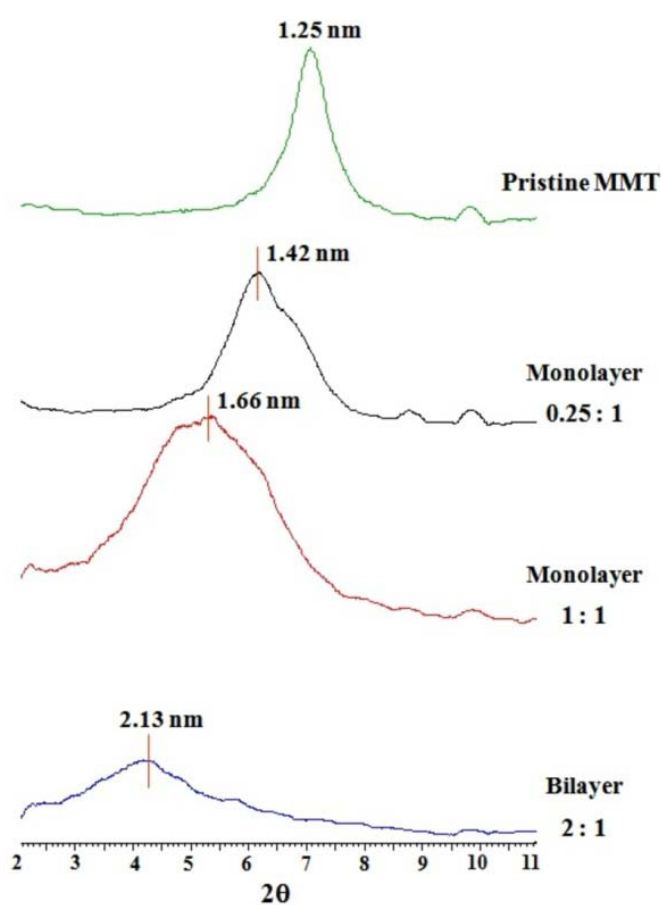


Figure 4.8 XRD patterns of pristine MMT and SA/CS/MMT nanocomposites with different initial CS:MMT molar ratios.

From Figure 4.8, should be noted that the broad distribution of d -spacing is mainly attributed to a magnitude of CS intercalation. Accordingly, the d -spacings of SA/CS/MMT nanocomposites with CS:MMT molar ratios of 0.5:1 and 1:1 are increased to 1.42 and 1.66 nm, respectively, as compared with that of pristine MMT (1.25 nm). These increases are associated to the width of one CS monolayer covering the interlayer surface, as shown in Figure 4.9a. However, incomplete monolayer covering might be occurred for the system with low CS concentration (*i.e.* 0.5:1).

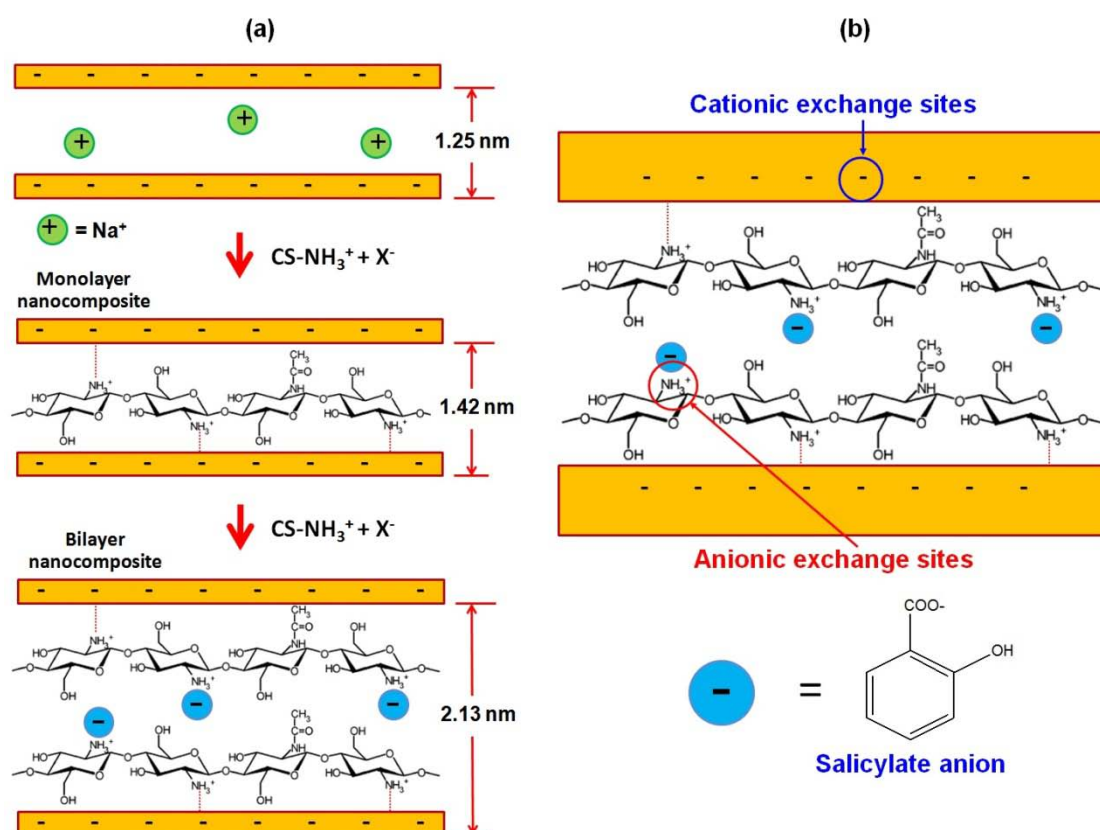


Figure 4.9 (a) Intercalation of CS into the interlayer of Na⁺-MMT through the cationic exchange process and (b) schematic representation of CS intercalated into the interlayer of Na⁺-MMT as a bilayer.

Compared with the pristine MMT, d -spacing are increased to 2.13 nm for the nanocomposites with CS:MMT of 2:1. This can be explained as the uptake of two CS layers covering the interlayer surface of MMT. The second polymer layer should correspond to the adsorption of CS in its salicylate salt (chitosonium salicylate), with the Δd_L value corresponding to the thickness of two CS layers together with the thickness of salicylate anion. The second layer of biopolymer is absorbed by means of the hydrogen bonding mechanism, since the CEC of clay has been already balanced by $-\text{NH}_3^+$ groups of the first CS layer. Thus, $-\text{NH}_3^+$ groups of the second CS layer interact electrostatically with salicylate anion (SA^-) from the starting chitosonium salicylate solution, as shown in Figure 4.9b.

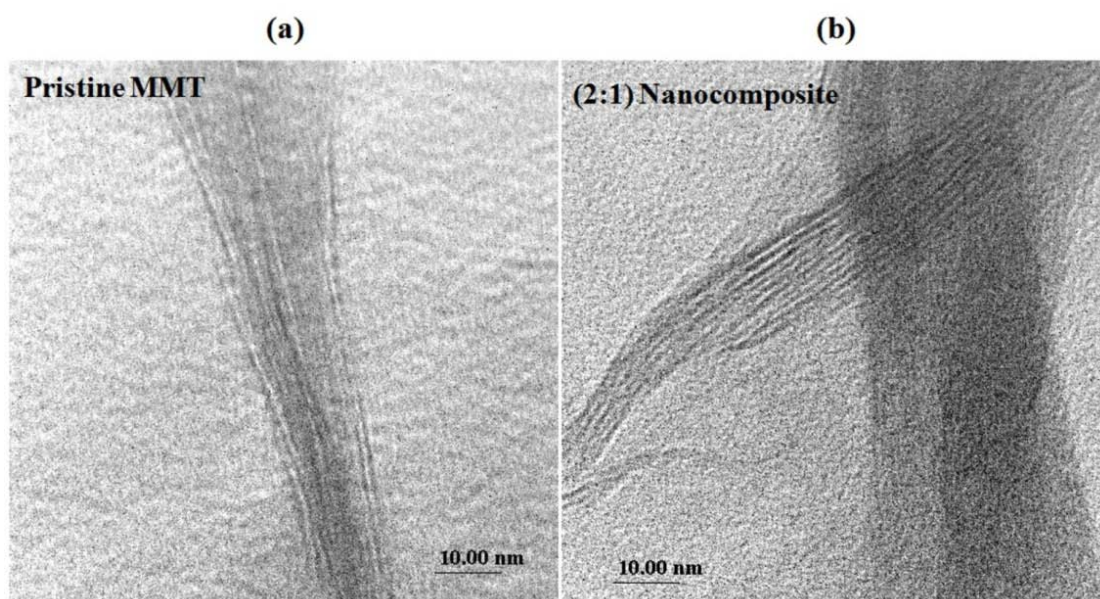


Figure 4.10 TEM images of (a) pristine MMT and (b) SA/CS/MMT nanocomposites with initial CS:MMT molar ratio of 2:1.

Increase of the *d*-spacing of MMT interlayer by CS intercalation also can be verified by TEM images. The TEM images of pristine MMT and SA/CS/MMT nanocomposites with initial CS:MMT of 2:1 are displayed in Figures 4.10a and 4.10b, respectively. Accordingly, the *d*-spacing of MMT interlayer increases when chitosonium salicylate is loaded and the nanocomposite consists essentially of well-intercalated phases. Corrugations in the MMT layers are indicative of the constrained action of the polymer interacting with MMT substrate. Therefore, from TEM and XRD results, it can be summarized that the chitosonium salicylate loaded into MMT should have both mono- and bilayer intercalation structures depended on the initial CS:MMT molar ratio.

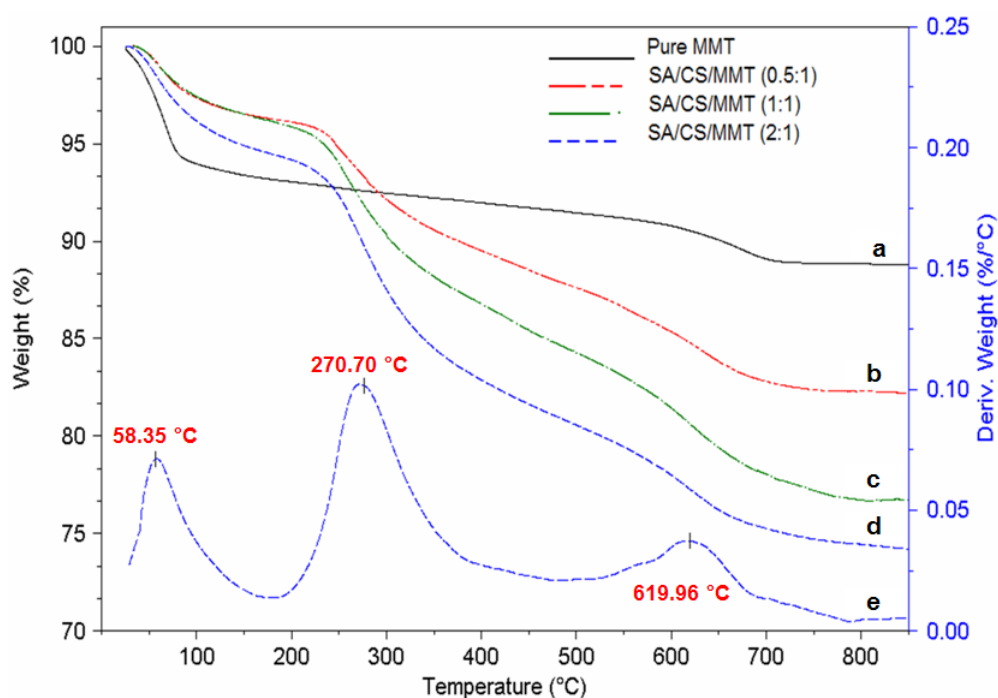


Figure 4.11 TGA curves in the temperature range of 30-900°C (under a nitrogen atmosphere) of (a) pure Na⁺-MMT and SA/CS/MMT nanocomposites with different initial CS:MMT molar ratios of (b) 0.5:1, (c) 1:1, and (d) 2:1. The DTA curve corresponding to the CS:MMT of 2:1 (e).

Thermal stability of these nanocomposites was investigated by DTA and TGA recorded in the temperature range of 30-900°C under nitrogen flow condition, as shown in Figure 4.11. Accordingly, the weight loss associated to the adsorbed water molecules at ~90°C for pristine MMT increases to ~120°C for SA/CS/MMT nanocomposites. This is due to H-bonding between water molecules and active functional groups of CS.

According to TGA results, the combustion of bulk chitosonium salicylate film was found at 262.7°C. From Figure 4.11, higher thermal stability of SA/CS/MMT nanocomposites is evidenced by the elevated temperature required to eliminate the organic matter associated with MMT. This elimination occurs at ~271°C corresponding to the combustion of the intercalated CS, with weight loss of 6.0%, 8.3% and 10.4% for SA/CS/MMT nanocomposites with initial CS:MMT molar ratio of 0.5:1, 1:1, and 2:1, respectively. The weight losses at 600-700°C are referred to the combustion of some MMT residues.

4.3.1.4 *In vitro* Drugs-Released Study of SA/CS/MMT Nanocomposites

The dissolution profiles of SA released from SA/CS/MMT nanocomposites, with different initial CS:MMT molar ratios of 0.5:1, 1:1, and 2:1, are displayed in Figure 4.12. The dissolution profile of SA from bulk chitosonium salicylate film (the concentration similar to CS solution used to prepare 2:1 nanocomposites) is also shown for comparison.

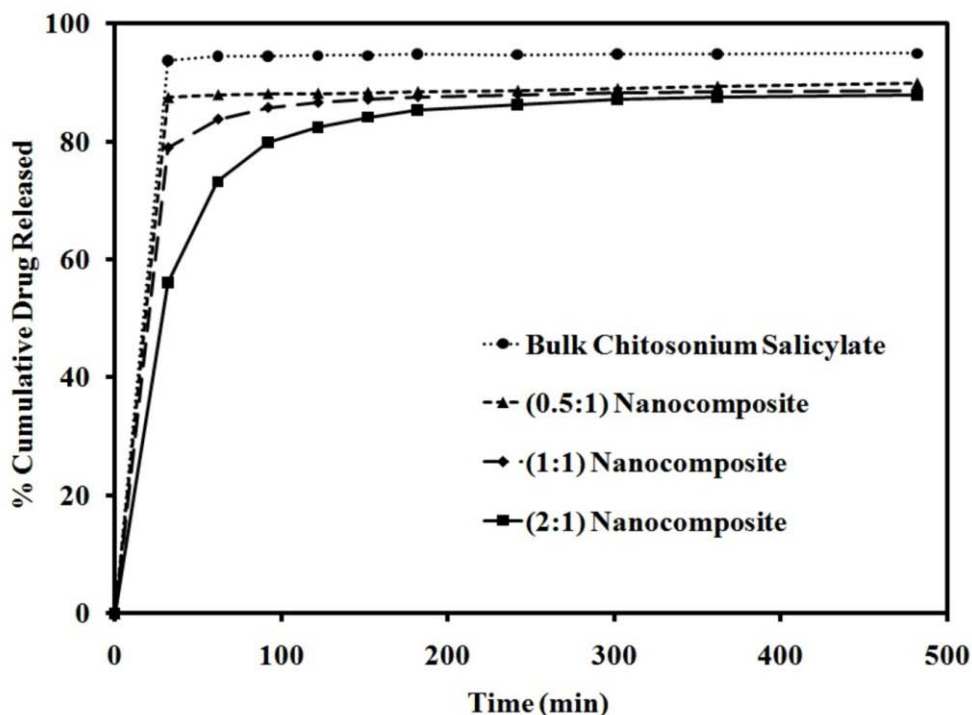


Figure 4.12 Dissolution profiles of salicylic acid from bulk chitosonium salicylate film and SA/CS/MMT nanocomposites with different initial CS:MMT molecular ratios of 0.5:1, 1:1, and 2:1.

From Figure 4.12, the monolayer intercalation (in 0.5:1 and 1:1 nanocomposites) gives the fast release behavior, whereas the bilayer intercalation (in 2:1 nanocomposite) gives the gradual release behavior. The correlation between the intercalation structures and the drug released behavior of SA/CS/MMT nanocomposites as explained below in more detail.

Generally, it is assumed that the cationic exchange sites in the MMT interlayer adsorb the same number of $-\text{NH}_3^+$ equivalents of the biopolymer. The excess of CS should not interact electrostatically with the MMT surface because the CEC has already been balanced. Such an amount of CS may be adsorbed by interactions

through the amino and the hydroxyl groups in the chain. Therefore, the protonated amino groups in the glucosamine units would be balanced with the salicylate anions (SA^-) of the starting solution because they do not compensate the electrical charge in the MMT interlayer. This suggests that the excess CS intercalates as a bilayer with one of CS chains as salicylate salt, as illustrated in Figure 4.9b. The presence of NH_3^+SA^- species in the bilayer SA/CS/MMT nanocomposite turns this material into the potential acidic drug controlled release material that MMT particle acts as a barrier and also an implantable drug reservoir.

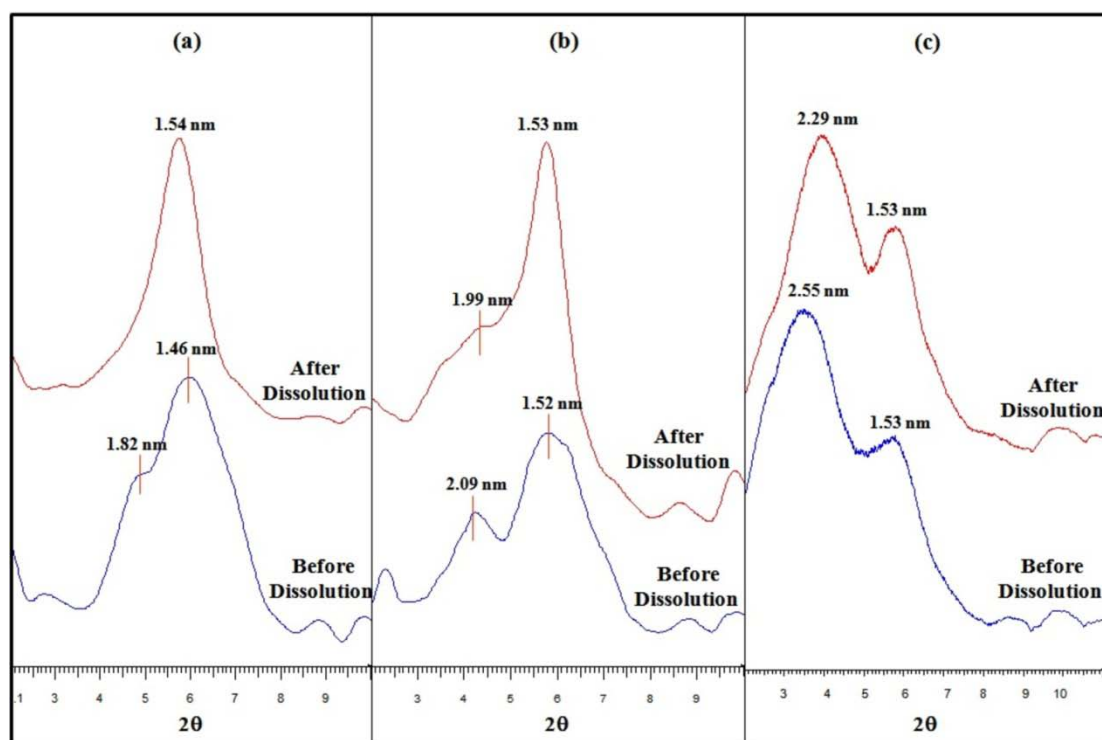


Figure 4.13 Comparison of XRD patterns before and after dissolution of SA/CS/MMT nanocomposites with different initial CS:MMT molar ratios; (a) 0.5:1, (b) 1:1, and (c) 2:1.

XRD technique was employed to verify this explanation. The comparison of XRD patterns before and after dissolution (for 24 h) of SA/CS/MMT nanocomposites with different initial CS:MMT molar ratios of 0.5:1, 1:1, and 2:1 is shown in Figures 4.13a, 4.13b, and 4.13c, respectively. The decrease of MMT interlayer d -spacing after the dissolution due to the release of SA^- is observed only for the bilayer structure (associated to XRD peaks at 1.82-2.55 nm). Whereas, the monolayer intercalation releasing no SA^- , gave the same d -spacing at 1.46-1.54 nm after the dissolution. Thus, only the bilayer structure has the excess numbers of $-\text{NH}_3^+$ and balanced by SA^- which can be released from MMT interlayer during the dissolution process. After this process, this controlled-release material can be reused by re-saturation with SA^- solution.

4.3.1.5 Structure, Morphology and *In vitro* Drugs-Released Study of Theophylline/Chitosan/Montmorillonite Materials

For the basic drug (THP/CS/MMT) system, CS only acts as a matrix with no drug-polymer interaction, whereas, the directly intercalation of THP^+ into the MMT interlayer via cationic exchange process was found as previously discussed. From XRD data (Figure 4.14), addition of MMT into the THP/CS matrix associated with drug crystals ($2\theta \approx 7$ and 14°) decreases the drug crystallinity. This can be attributed to the interaction between THP and MMT, specifically, the intercalation of THP^+ into the MMT interlayer along with sorption of THP^+ onto the MMT surfaces.

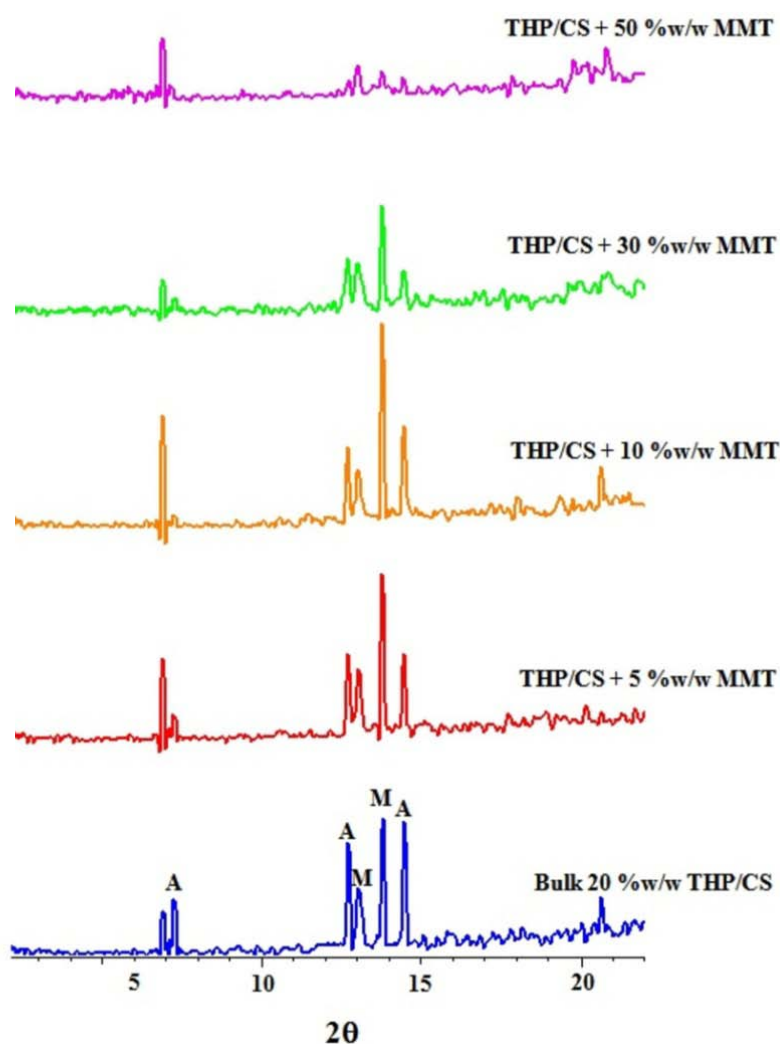


Figure 4.14 XRD patterns bulk 30 %w/w THP/CS and THP/CS/MMT materials with different %w/w of MMT/CS (A: Anhydrous THP, M: Monohydrate THP).

The dissolution profiles of THP released from 30 %w/w THP/CS bulk film and THP/CS/MMT materials, with different amount of MMT (50 and 100 %w/w of MMT/CS), are displayed in Figure 4.15. Fast release behavior is observed for both THP/CS film and THP/CS/MMT materials, probably because there is the drug-polymer interaction is weak and the interaction between drug and MMT is also rather weak.

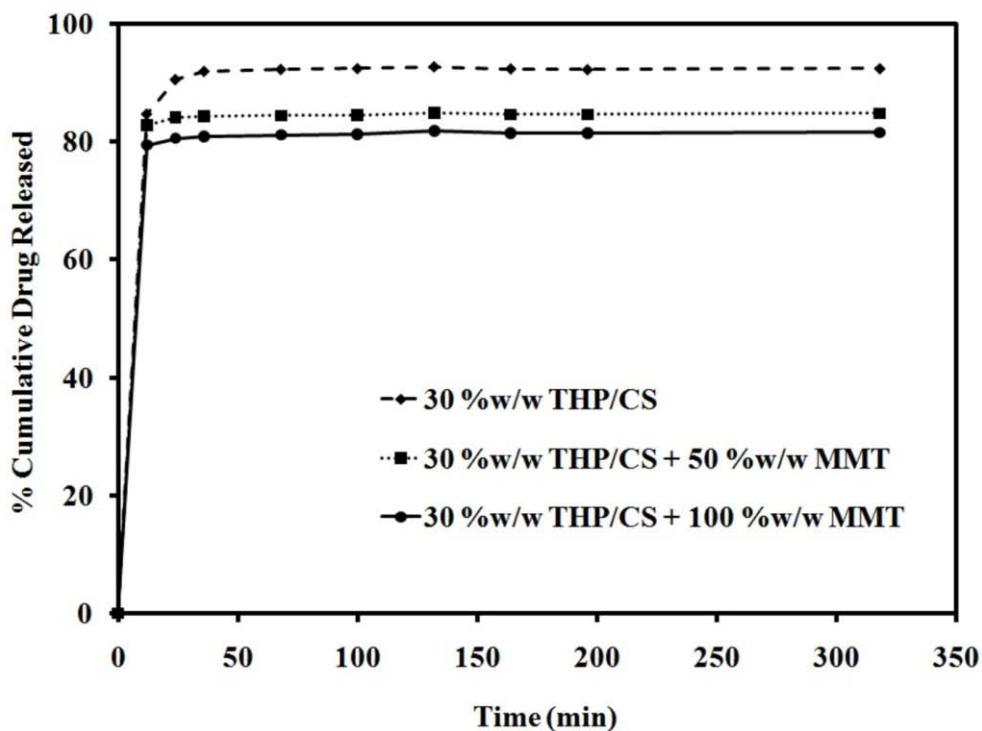


Figure 4.15 Dissolution profiles of theophylline from bulk THP/CS film and THP/CS/MMT materials with different amount of MMT.

4.3.2 Computational Section

4.3.2.1 Molecular Dynamics Simulation of Bulk Amorphous Chitosan and Salicylic Acid/Theophylline in Chitosan Matrix

Recent advances in controlled drug delivery systems are largely based on the advances in polymer chemistry, *e.g.* the ability to fabricate different polymeric materials for controlling the diffusion of drug molecules. Measurements of the diffusion coefficients and the knowledge about the interaction between drug and polymeric matrices are important in this respect. Accordingly, the computational molecular simulations were also employed in this work to provide deeper understanding at the microscopic level not achieved by experimental techniques.

Molecular modeling technique was employed to investigate the structure, interaction and diffusion of model acidic and basic drugs (SA and THP, respectively) in CS matrix. The atomistic models of CS/SA and CS/THP complexes are shown in Figure 4.16.

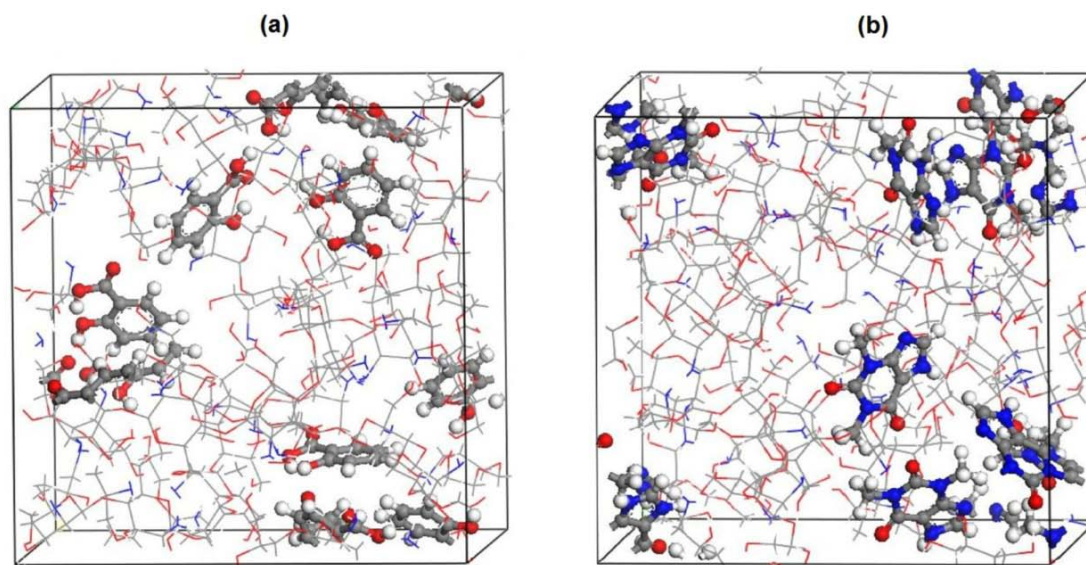


Figure 4.16 The atomistic models of (a) chitosan/salicylic acid and (b) chitosan/theophylline complexes.

Bulk Amorphous Chitosan

The equilibration of CS microstructure is validated by calculating its cohesive energy density (CED). In molecular simulation studies, cohesive energy (E_{coh}) is defined as an increase in energy per mole of polymer if all the intermolecular forces are eliminated. On the other hand, cohesive energy density corresponds to cohesive energy per unit volume. If V_{mol} is the molar volume of polymer, then CED is defined as $CED = (E_{coh}/V_{mol})$.

The Hildebrand solubility parameter (δ) is given by: $\delta = \text{CED}^{1/2}$. The cohesive energy (CED) and Hildebrand's solubility (δ) parameter derived from the ensemble average of the intermolecular part of the internal energy per mole of substance are then calculated for checking the accuracy of the simulation. The δ value of pure CS was calculated in the equilibrated state, to match the δ value with reported literature data as a reliable test protocol. The δ values of pure CS, CS/SA and CS/THP are given in Table 4.1.

Table 4.1 Solubility parameters of CS, CS/SA and CS/THP.

Sample	Solubility Parameter (cal/cm ³) ^{1/2}	
	Simulation	Experiment
Bulk CS	10.0 ± 0.2	10.3 ^a
CS/SA	11.2 ± 0.1	-
CS/THP	14.3 ± 0.1	-

^a (Ravindra *et al.*, 1998)

Another parameter to validate the equilibration of CS microstructure is X-Ray scattering intensity, as shown in Figure 4.17, which is to be matched with the experimental data. Two peaks are found at the scattering vector $Q = 1.3$ and 2.8 \AA^{-1} , where $Q = \frac{4\pi \sin \theta}{\lambda}$ with $\lambda = 1.54 \text{ \AA}$. These scattering vectors are corresponded to the scattering angle $2\theta = 18.4^\circ$ and 40.2° of pure CS. These data agree well with the experimental data $2\theta = 19.4^\circ$; as shown in Figure 4.18, thus authenticating the validity of the simulation model.

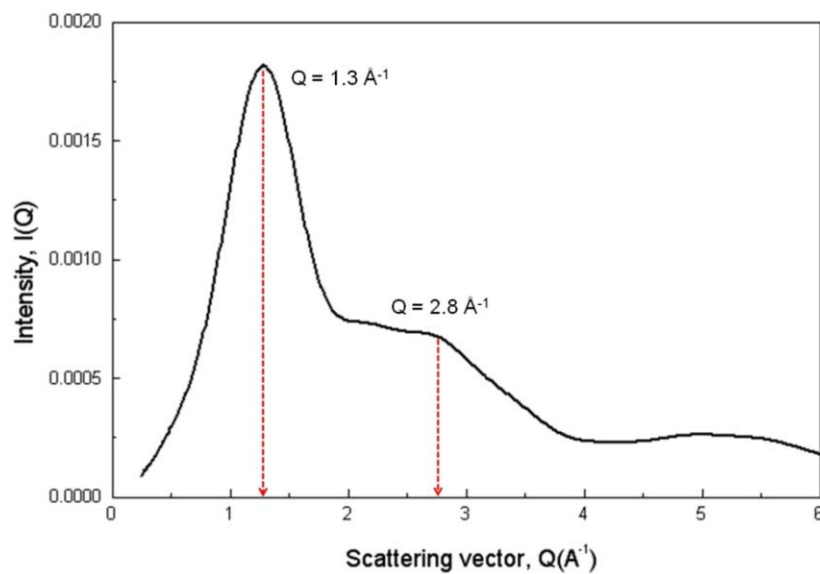


Figure 4.17 X-Ray scattering function of chitosan.

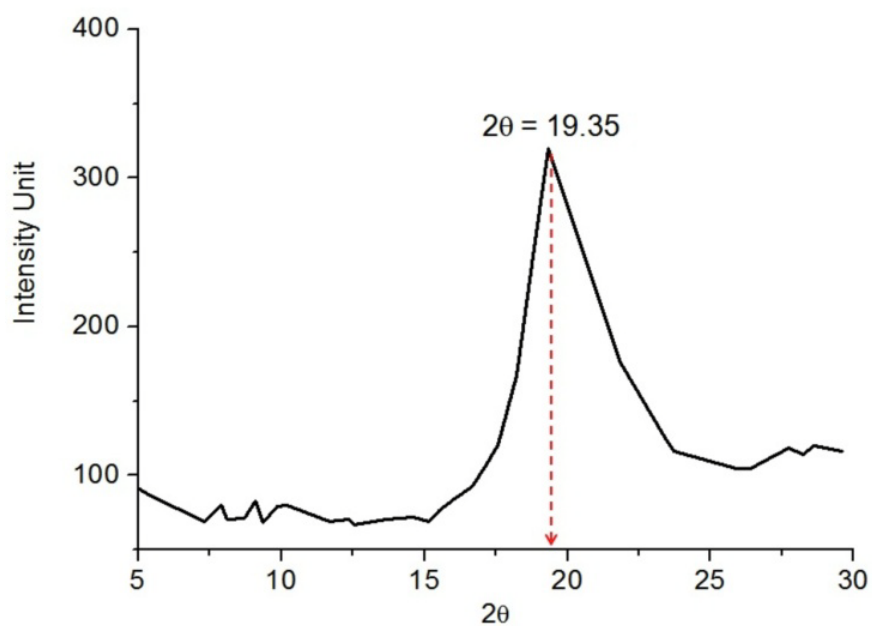


Figure 4.18 X-Ray diffraction pattern of chitosan.

The RDF also referred to as pair correlation function; $g(r)$, demonstrates the average density of atoms at a distance from a specified atom. The $g(r)$ peaks indicate the presence of definite correlation between atoms within that radius, while the

absence of any peaks beyond 4 Å distance indicates that there is no long-range interaction in the systems. At longer distances, $g(r)$ approaches the unity, which is quite probable for a purely amorphous system. The peaks observed at $r < 4$ Å are assigned to a specific distance of the closely coupled atoms.

The atomic pair distribution function, $g(r)$ giving a measure of the order in the CS system, was calculated from the spatial orientation of the atoms as shown in Figure 4.19. The peaks at 1.1 and 1.5 Å are assigned to covalently bond of hydrogen and carbon atoms, respectively. Peaks at a distance $r > 2$ Å are due to nonbond atoms separated by two, three, and/or four bonds on the chain. This structural order due to intramolecular connections disappears and the structure is random at longer distances ($r \geq 4.5$ Å).

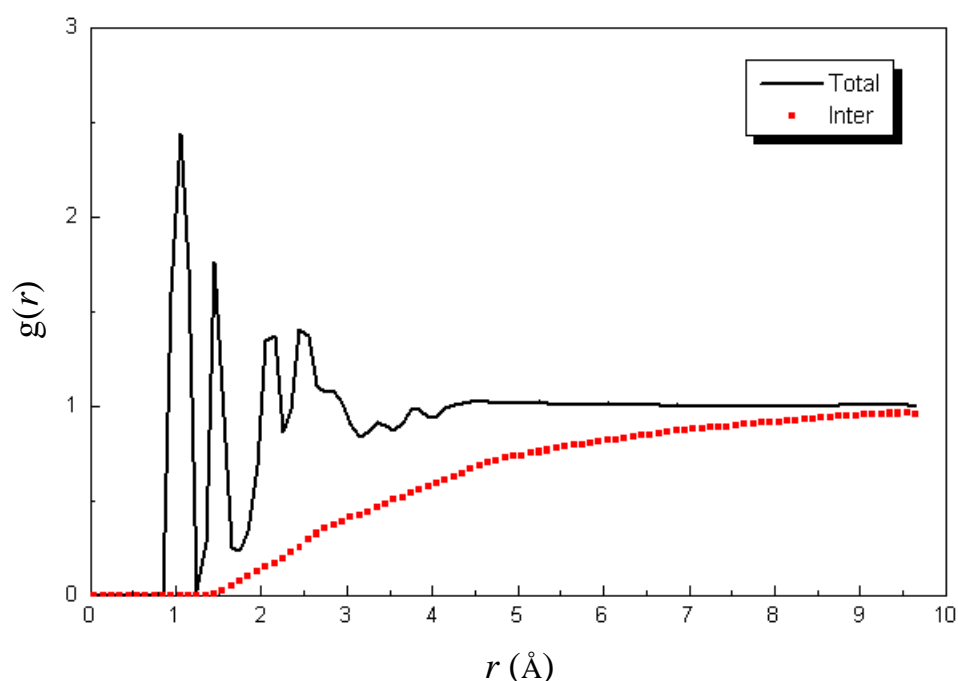


Figure 4.19 Radial distribution function of chitosan.

Hydrogen bonds have greater influence on the molecular structure of CS as in most polysaccharides. Hydrogen bond is defined with the geometrical criteria, whenever the distance between donors (H connected to O or N) and acceptors (O or N) is smaller than 2.5 Å and the absolute angle for “donor-hydrogen...acceptor” larger than 120°. MD simulations suggest several intermolecular H-bonding can be occurred between active functional groups of CS as shown in Figure 4.20. The main contribution comes from the hydrogen and oxygen atoms of C6-OH groups due to they have more room to interact with the other active functional groups of CS. Further, CS is more hydrophilic because of its polar amino group, thus it swells in aqueous media and offers an active site for hydrogen bonding formation.

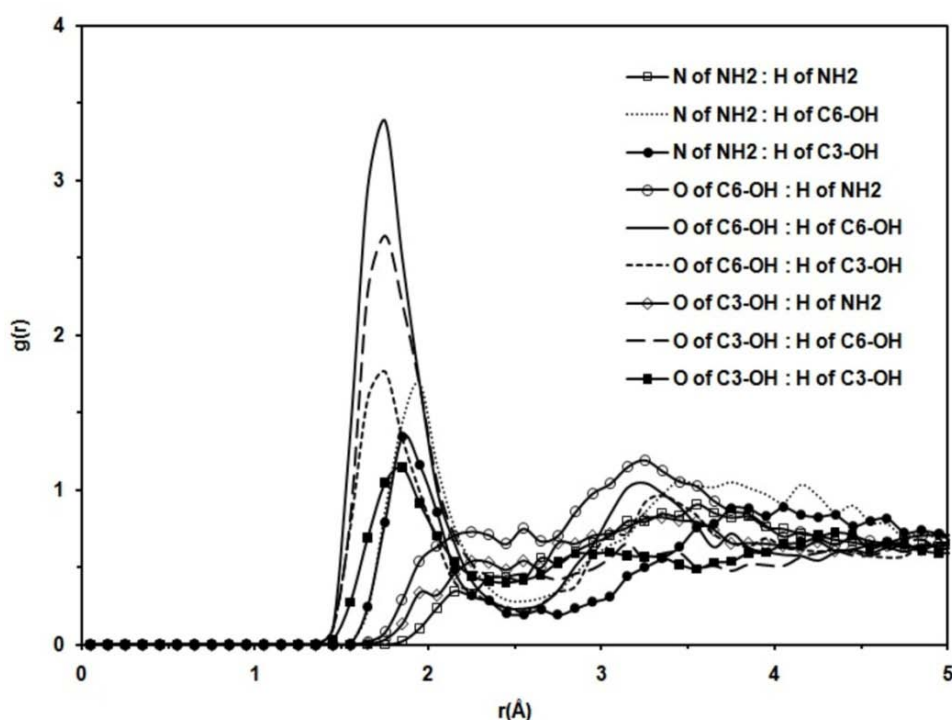


Figure 4.20 Radial distribution functions of intermolecular interaction between active functional groups of chitosan; representing the hydrogen atom of NH₂, C3-OH and C6-OH relative to the distance of nitrogen atom of NH₂ and oxygen atom of C3-OH and C6-OH.

Interaction and Mobility of Drugs within Chitosan Matrix

The miscibility between drugs and CS can be considered from the δ values given in Table 4.1 for bulk CS ($\delta_{\text{CS}} = 10.0 \pm 0.2 \text{ (cal/cm}^3)^{1/2}$), CS/SA ($\delta_{\text{CS/SA}} = 11.2 \pm 0.1 \text{ (cal/cm}^3)^{1/2}$) and CS/THP ($\delta_{\text{CS/THP}} = 14.3 \pm 0.1 \text{ (cal/cm}^3)^{1/2}$) complexes. Compared with bulk CS, the drug loading seems to give larger δ values. The slightly larger $\delta_{\text{CS/SA}}$ value is still within the miscibility window of CS. On the other hand, the much larger $\delta_{\text{CS/THP}}$ value indicates the immiscibility between THP and CS which arise to phase separation. This result agrees well with the experimental observation that only SA can be dissolved in CS, whereas THP cannot.

Molecular dynamics simulations and subsequent the calculations of drugs diffusion coefficient (D) along with the radial distribution functions (RDFs) were performed in the last 1 ns where the simulations showed stable behavior as illustrated in Figure 4.21 for the CS/SA system.

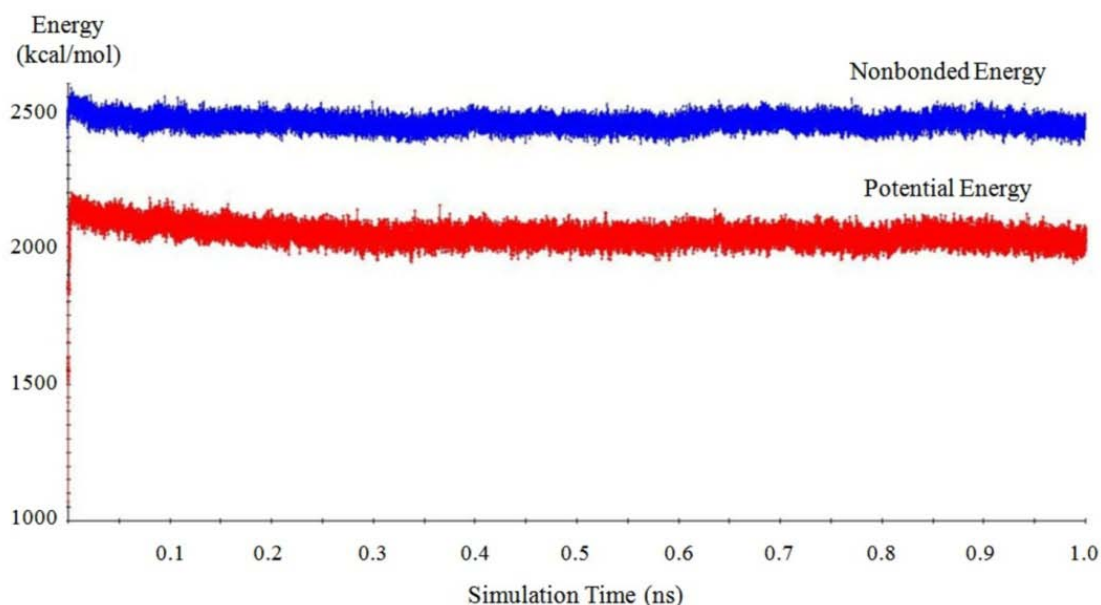


Figure 4.21 Potential and nonbonded energy vs simulation time of the CS/SA system.

Once the molecular dynamics simulation was done, diffusion behavior can be studied from the trajectory files. The displacement of penetrants can be plotted as a function of time and the diffusion coefficient can be calculated from the trajectory of atoms. The diffusion coefficient is defined as: $D = \frac{1}{6} \lim_{t \rightarrow \infty} \langle r(t) - r(0) \rangle^2 / t$, the bracket denotes an ensemble average. The result, shown in Figure 4.22, gives $D = 1.2 \times 10^{-9}$ cm²/s for salicylic acid, and $D = 4.6 \times 10^{-9}$ cm²/s for theophylline, which fall in the same order of magnitude of drug molecule diffusion in CS matrix. This result indicates a faster diffusion rate of THP within CS matrix than SA, which is in harmony with the experimental finding that THP shows fast release while SA shows gradual release behavior thus reflects a stronger interaction between SA and CS.

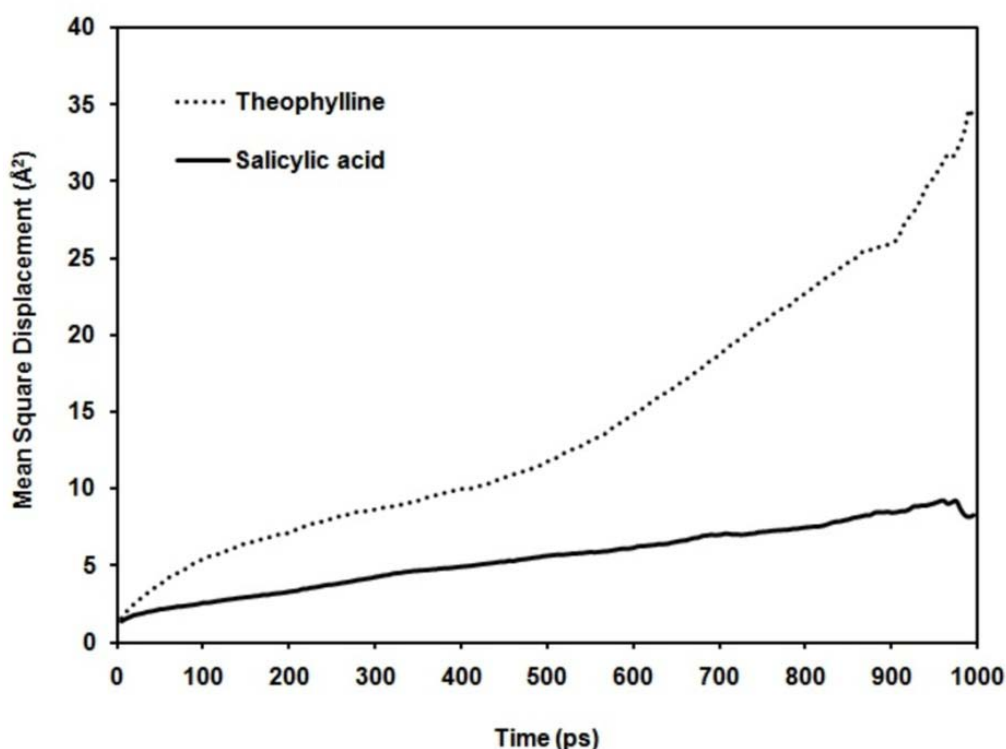


Figure 4.22 Mean-square displacements of salicylic acid and theophylline in chitosan matrix.

The diffusion capability of drug in CS matrix governing the controlled release efficiency is mainly attributed to the drug/polymer interaction. Therefore, the radial distribution function (RDF) was calculated to investigate the specific interaction between CS and SA. The atoms in CS and SA are indexed as shown in Figure 4.23.

The interaction between CS-SA is very difficult to analyze by FTIR technique, since the peaks due to the presence of SA are overlapped with the characteristic bands of pure CS film (Sanli *et al.*, 2009). Therefore this interaction still remains inconclusive. There are some literatures reporting that the interaction between CS and SA might be attributed to the hydrogen bonding between amino groups (NH₂) of CS and carboxyl groups (COOH) of SA (Puttipipatkachorn *et al.*, 2001). However, the experimental information was not enough to specify the active atoms that play the main role in this interaction and the contribution of the functional groups of CS (NH₂, C3-OH, C6-OH) and SA (C=O, C1-OH, C3-OH) on this interaction. Therefore, RDFs of CS/SA system were calculated to specify the active atoms and contribution of the functional groups. For this specification (for a case that CS behaves as the H-donor), the $g(r)$ between the hydrogen atom of NH₂, C3-OH and C6-OH of CS relative to the oxygen atom of C=O, C1-OH and C3-OH groups of SA are analyzed and displayed in Figure 4.24. For the other case that SA behaves as the H-donor, the $g(r)$ between the hydrogen atom of COOH and C3-OH of SA relative to the oxygen atom of C3-OH and C6-OH and nitrogen atom of NH₂ of CS are analyzed and displayed in Figure 4.25.

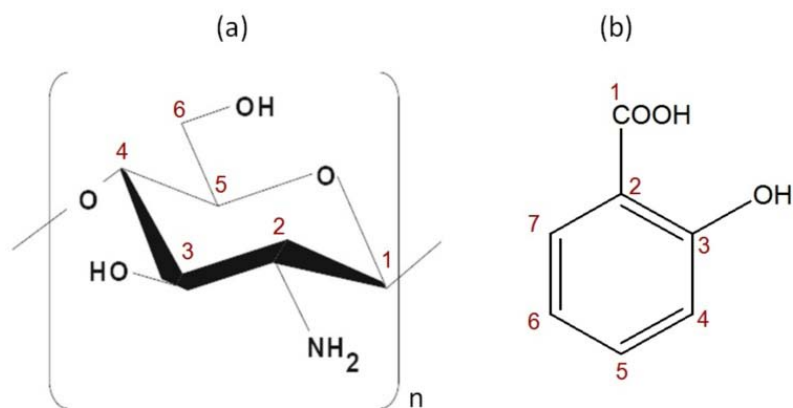


Figure 4.23 Chemical structures of (a) chitosan and (b) salicylic acid.

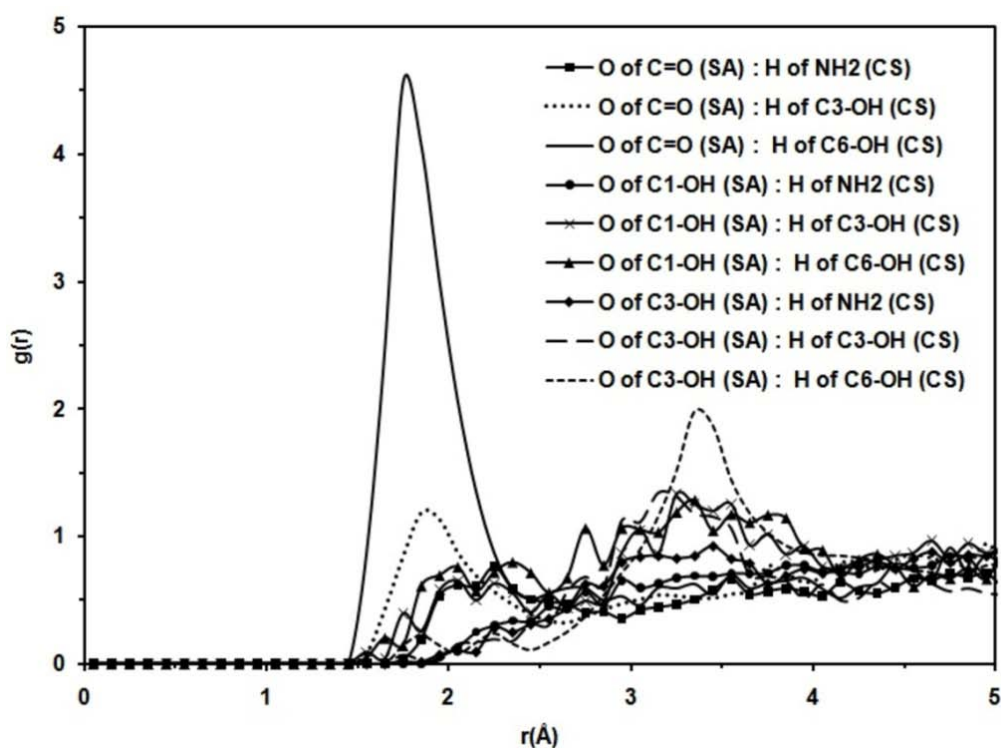


Figure 4.24 Radial distribution functions for CS/SA complex when considered CS as a H-donor; representing the hydrogen atom of NH₂, C3-OH and C6-OH of CS relative to the distance of oxygen atom of C=O, C1-OH and C3-OH of SA.

In Figure 4.24, a pronounced peak at $r = 1.75 \text{ \AA}$ (where $g(r) = 4.55$) corresponds to the hydrogen bonding between the H atom of C6-OH of CS and O atom of C=O of SA. Meanwhile, the peak at $r = 1.85 \text{ \AA}$ ($g(r) = 1.19$) is observed for H atom of C3-OH of CS and O atom of C=O of SA. This result indicates that H atom of C6-OH form stronger hydrogen bonds with C=O of SA than H atom of C3-OH. The stronger interaction is possibly because of the free rotation of C6-OH group compared to C3-OH, and consequently there is more accessibility to interact with oxygen atoms in SA. This computational result is the first result that distinguishes the proton donor capacity between C6-OH and C3-OH of CS interacting with drug molecule. Moreover, weak hydrogen bonds between H atom of C6-OH of CS and O atom of C3-OH of SA is also observed at $r = 3.35 \text{ \AA}$ ($g(r) = 1.98$).

Figure 4.24 also shows that there is no $g(r)$ peak for pairs of H atom of NH_2 of CS and the O atom of SA (C=O, C1-OH, C3-OH). Therefore, the intermolecular hydrogen bond involving the amino group of CS as a proton donor is totally insignificant. This may be due to the fact that the N-H bond has less polarity than an O-H bond. Thus the $\text{N-H}\cdots\text{O}=\text{C}$ hydrogen bond is rather weak and not significant as compared with the $\text{O-H}\cdots\text{O}=\text{C}$ counterpart. Some distinction between the results from simulation and experiment should be mainly due to the different in form of CS amino groups. Simulations were performed in neutral amino ($-\text{NH}_2$), whereas FTIR data indicating the occurring of protonated amino ($-\text{NH}_3^+$) therefore it can stronger interact with SA to form $-\text{NH}_3^+\text{SA}^-$ complex as previously discussed.

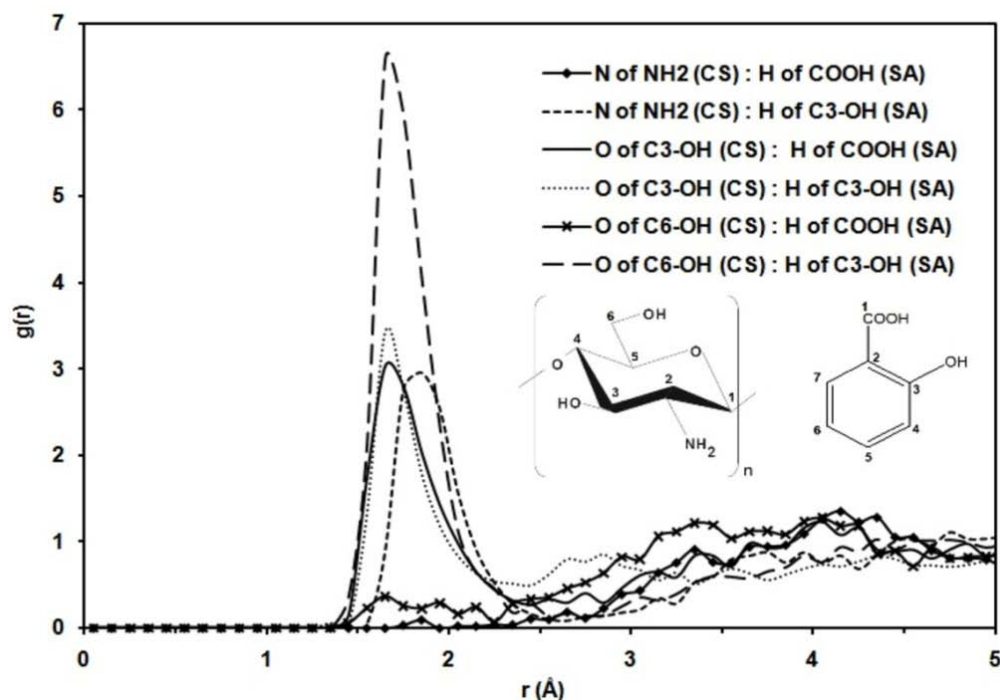


Figure 4.25 Radial distribution functions for CS/SA complex when considered SA as a H-donor; representing the hydrogen atom of COOH and C3-OH of SA relative to the distance of nitrogen atom of NH₂ along with oxygen atom of C3-OH and C6-OH of CS.

Figure 4.25 displays the RDFs for the proton donor groups of SA relative to the proton acceptor groups of CS. This clearly indicates that all functional groups (NH₂, C3-OH and C6-OH) of CS behave as H-acceptors, while all functional groups (COOH and C3-OH) of SA, H-donors, thereby facilitating the H-bond formation in CS/SA complex. As shown in Figure 4.25, a pronounced peak at $r = 1.75 \text{ \AA}$ ($g(r) = 6.57$) corresponds to the hydrogen bonding between the H atom of C3-OH of SA and the O atom of C6-OH of CS. Meanwhile the peak at $r = 1.75 \text{ \AA}$ ($g(r) = 3.43$) was observed for H atom of C3-OH of SA and O atom of C3-OH of CS and the peak at $r = 1.90 \text{ \AA}$ ($g(r) = 2.95$) was observed for H atom of C3-OH of SA and N atom of NH₂ of CS.

It can be observed that, as compared with the O atom from hydroxyl groups, the CS amide N atom is less likely to function as a proton acceptor. This may be attributable to larger steric effect from two H atoms connecting to N which results in larger distance available for interaction with H atom of SA. Therefore, when the proton donors of SA interact with CS, they would form a bond with the O atom of CS in preference to the N atom. However, in the real system where CS amino groups are in protonated form ($-\text{NH}_3^+$) this may increase its activity to interact with SA.

Among all H-acceptors of CS, C6-OH has the highest activity to form H-bonding with SA hydrogen atoms of C3-OH as noted from the rather higher $g(r)$ peak (at a shorter radial distance as compared to NH_2), probably because C6-OH group can freely rotate and has more room to interact with the H-donors from SA.

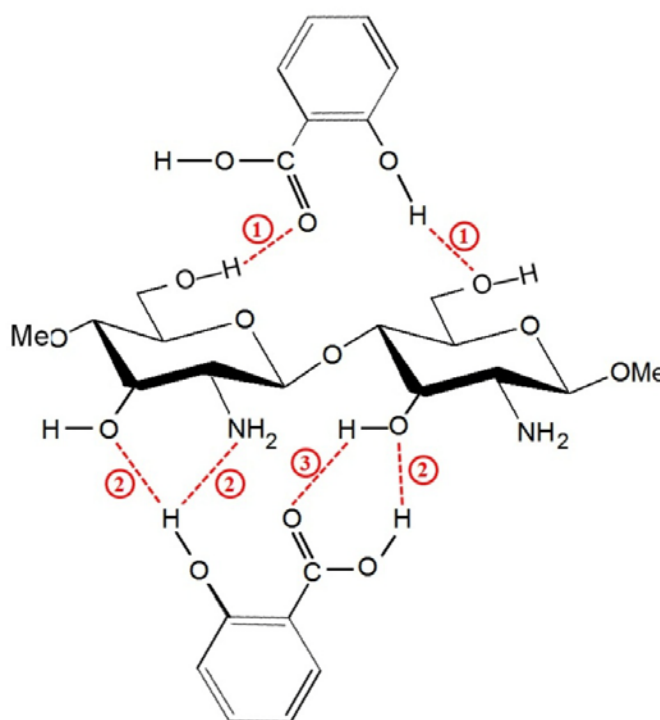


Figure 4.26 Intermolecular hydrogen bonding between active functional groups of salicylic acid and chitosan proposed from RDFs analysis. The numbers adjacent to the bonds respect to the priority of H-bond formation.

All of RDFs analysis revealed several types of intermolecular hydrogen bonding between active functional groups of CS and SA as illustrated in Figure 4.26. The gradual release of SA from CS matrix is mainly attributed to those hydrogen bonds.

4.3.2.2 Molecular Dynamics Simulation of SA/CS/MMT Nanocomposites: Intercalation Structure

Molecular simulation was employed to find the basal spacing (on the basis of the molecular dynamics) and probe the layering behavior and interlayer structure of Salicylic acid/Chitosan/Montmorillonite (SA/CS/MMT) nanocomposites at an atomic scale. Basal plane spacing was computed as the mean center to center distance between the planes formed by octahedral Al atoms in the upper and lower layers of the clay mineral in duplicate structures, as an average over 100 independent snapshots. Interlayer densities were calculated as the quotient of the mass of chitosonium (NH_3^+) and salicylate ions (SA^-) between the silicate layers and the associated interlayer volume. The interlayer volume was calculated according to $V_i = A_i h_i$, where A_i is the cross-sectional area of the box and h_i the interlayer height. The latter is obtained from the basal plane spacing by subtracting the constant value 0.919 nm, which corresponds to the mean gallery height of aluminosilicate layers without charge defects and interlayer material. Diffusion coefficients (D) for chitosonium and salicylate ions on the MMT surface were calculated from the mean squared displacement of the head group nitrogen atoms ($\langle r^2(t) \rangle$) over the entire trajectory time (t) in equilibrium, applying the Einstein relation ($\langle r^2(t) \rangle = 2dDt$) for two-dimensional diffusion ($d = 2$).

This section describes the simulated structure and dynamics of chitosonium and salicylate ions in montmorillonite, including the structure of the inorganic-organic interface, basal plane spacings, the interlayer density, and diffusion on the surfaces. The outside surface of the clay mineral is especially important because it builds the interface when dispersed in polymer media. The simulation was made for cation exchange capacities (CEC) of 144 mequiv/100 g, R-NH₃⁺ head groups, and polymer and drug loadings ranging from 16 to 28 CS units. As a visual guide in the analysis, representative snapshots of the systems are displayed in Figure 4.27.

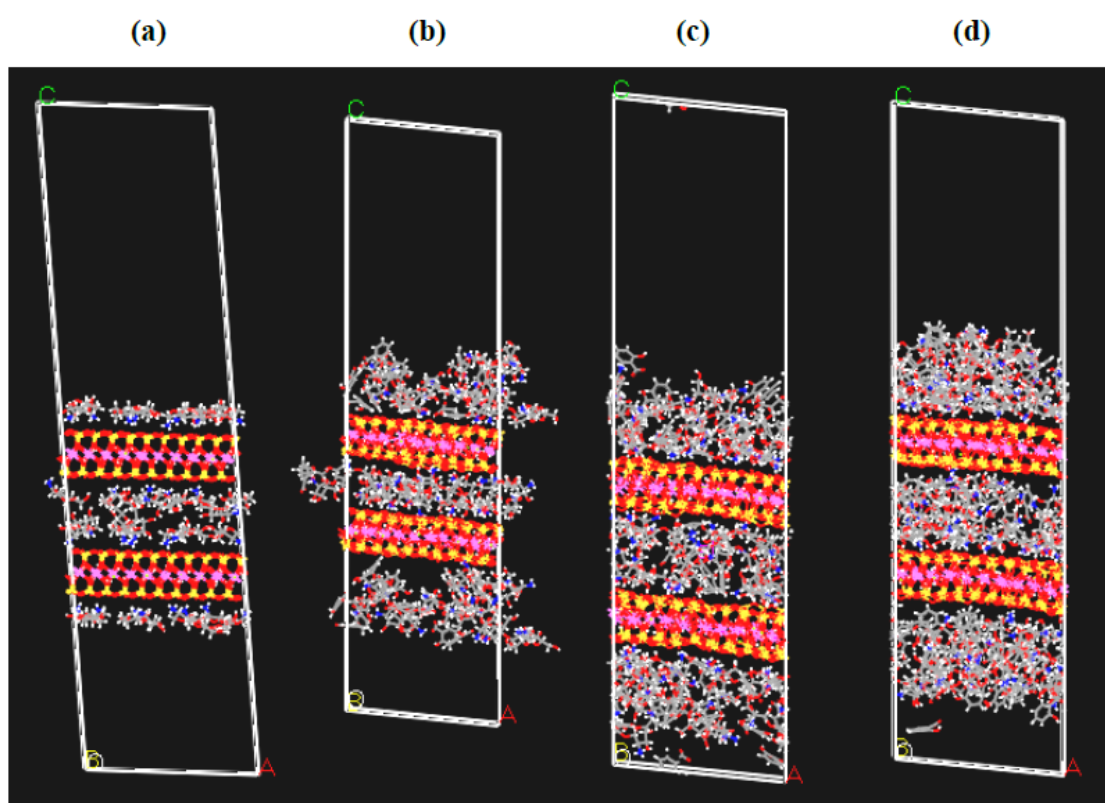


Figure 4.27 Representative MD snapshots (pictures not scale) of Salicylate anion/Chitosonium/Montmorillonite, viewed along the y direction (a) SA₀/CS₁₆/MMT (b) SA₄/CS₂₀/MMT (c) SA₈/CS₂₄/MMT (d) SA₁₂/CS₂₈/MMT.

Location of Adsorption Sites

As illustrated in Figure 4.27, the NH_3^+ head groups are positioned preferentially in cavities of (Si,O) 6-rings on the montmorillonite surface and ionically bonded to negatively charged ($\text{Al}^{3+} \rightarrow \text{Mg}^{2+}$) defects in the octahedral sheet of the silicate layer. The interaction of the head group with MMT surface should impact the structure and dynamics of the chitosonium ions on the surface of clay mineral. In addition to electrostatic bonding, the R-NH_3^+ head groups form $\text{N-H}\cdots\text{O-Si}$ hydrogen bonds to oxygen in the silicate surface with an average $\text{O}\cdots\text{H}$ distance of 1.5 nm. Each of the three H atoms can approach an oxygen atom in the superficial cavity so that the N-terminal part of the CS shows a preference for an upright orientation relative to the surface as shown in Figure 4.28. The energetic gain from H-bonding is typically 1-4 kcal/mol per H bond so that this leads to a stiff orientation of R-NH_3^+ head group on the surface and less lateral mobility, including rearrangements across cavities and lower rate of diffusion.

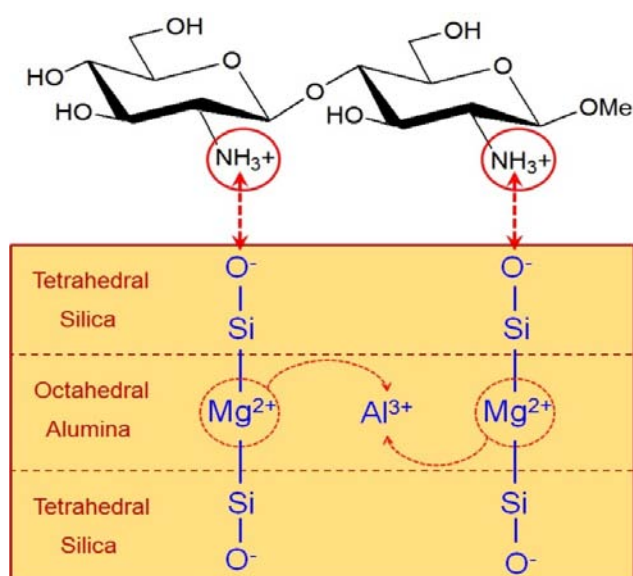


Figure 4.28 The electrostatic hydrogen bonding between R-NH_3^+ head groups of chitosan and oxygen of the MMT surface proposed from MD simulation.

Basal Plane Spacing

At CEC = 144 mequiv/100 g, MMT exhibits a step-wise change in gallery spacing with increasing loading. When salicylate anions are loaded with chitosonium ions, gallery height is first decreased for the SA₄/CS₂₀ system and then increased for other systems relative to unloaded systems as shown in Figures 4.29 and 4.30.

This verifies in a quantitative manner what has been observed in XRD results in experimental section. A densely packed bilayer is formed at CS loading. The negative charges from salicylate anions were compensated with the positive charge from the extra protonated group of CS. These extra units are located far from the clay surface and cause the interlayer to expand.

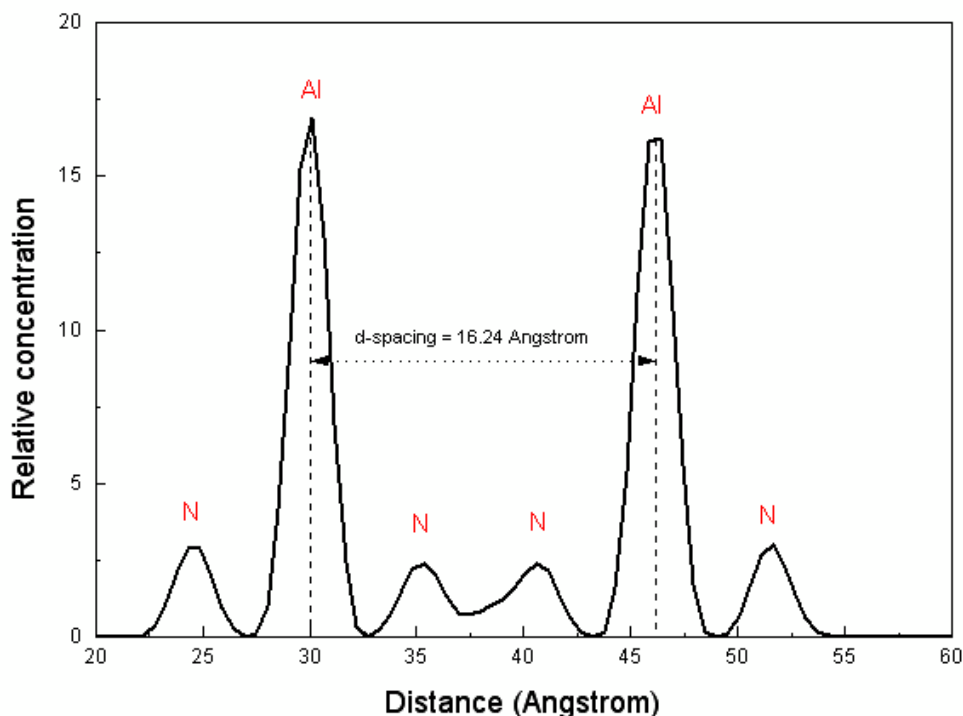


Figure 4.29 Density profile of the SA₀/CS₁₆/MMT system at 298 K (only nitrogen and aluminium atoms); the interlayer spacing is 16.24 Å.

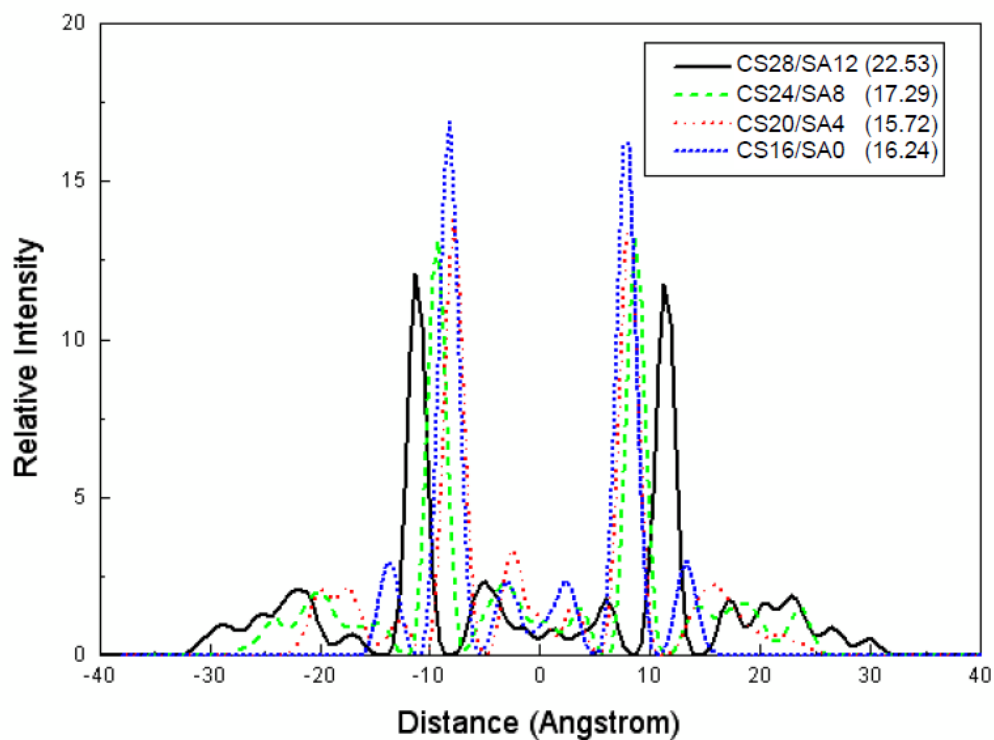


Figure 4.30 Density profiles of different SA/CS/MMT systems at 298 K.

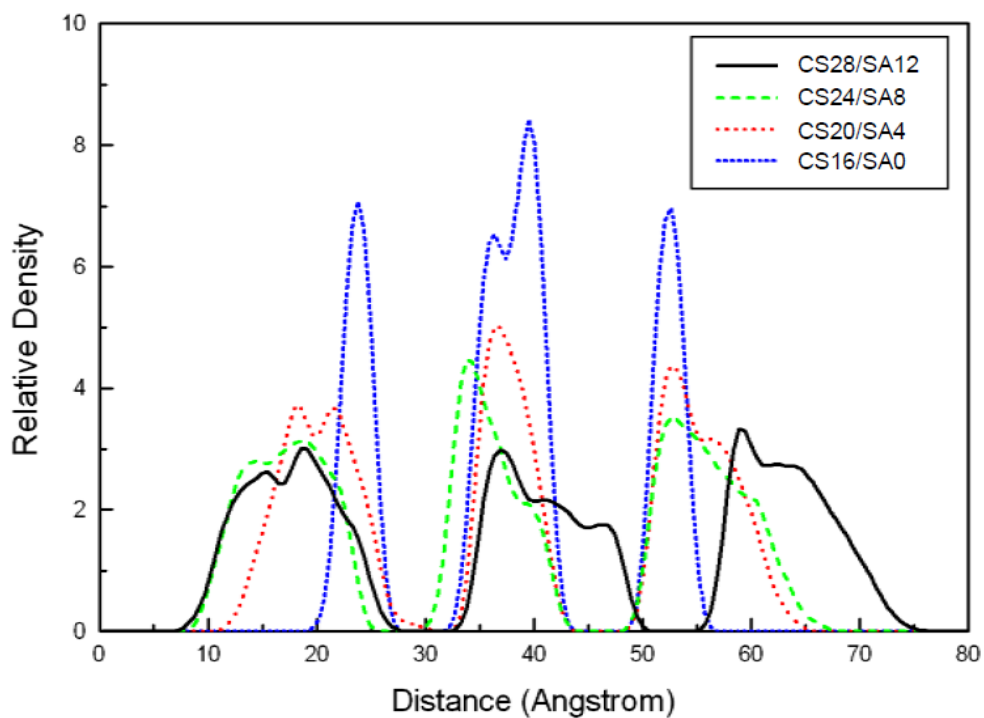


Figure 4.31 Density profiles of the SA/CS/MMT systems at 298 K (only SA and CS).

Interlayer Density

The confinement of gallery spacing for a range of SA/CS loading causes periodic fluctuations in interlayer density as shown in Figure 4.31. The interlayer density is minimal for a partially formed layer and maximal at a loading yielding a “complete” layer. The formation of new layers is accompanied by periodic fluctuations in interlayer density. However, due to the higher surface density of protonated group from CS, the chains must adopt conformations that favor perpendicular orientation to the aluminosilicate surface. Thus, the “layers” are less distinctly formed; the amplitude of fluctuations in interlayer density is smaller and decreases with the formation of increasingly homogeneous multilayered structures.

Diffusion

Diffusion of CS and SA on MMT surface can have two possible causes: (1) hopping across the cavities due to Brownian motion or (2) concentration gradients of defect sites (only possible if ion exchange with surfactants would be incomplete). For CS ions, the simulation showed self-diffusion was observed by Brownian motion only, *i.e.*, the exchange rate between adjacent molecules. Because of desire to remain close to the charge group, the motion of CS chains is characterized by the correlation between the protonated amino group and either the clay surface or negative charge on SA molecule. The CS chains in the interlayer space between two silicate layers show virtually no lateral mobility in simulation, independent of SA loading. Diffusion constants of CS and SA in the direction parallel to the clay surface at room temperature are less than 10^{-9} cm²/s, related to close packing of the chains. Self-diffusion is activated conformational changes in the backbone cooperative with

movements of chitosonium ions (Figure 4.27), which is associated with high-energy barriers. Qualitatively, the lowest diffusion constants (and highest net energy barriers) was expected for high loading and H-bonded NH_3^+ head groups. As a result, significant diffusion can be only found on single surfaces, *i.e.*, on the outside of the duplicate structures. The order of magnitude of the rate of diffusion is still sensitive to CEC and the amount of extra chitosonium groups that are balanced by the negative from drug molecules.

4.4 Concluding Remark

Physicochemical characterization of CS films loaded with SA and THP (models of acidic and basic drug) could reveal the drug physical state and drug-polymer interaction. The experimental data demonstrate that SA molecules exist in a molecularly dispersed state in CS matrix at only < 90 %w/w drug loading. The SA-CS interaction occurring at CS amino group resulted in chitosonium salicylate ($-\text{NH}_3^+/\text{SA}^-$) formation, whereas, no drug-polymer interaction was observed in THP-loaded CS films. The CS protonation degree increases with increase of SA concentration and reaches ~100% protonation at 70 %w/w drug loading. Accordingly, this concentration was selected as that of the initial chitosonium salicylate solution for the preparation of SA/CS/MMT nanocomposites.

CS/MMT nanocomposites with different initial molar ratios of CS:MMT as well as corresponding SA incorporated into CS/MMT nanocomposites were successfully obtained by solvent casting and evaporation method. The results from XRD and TEM techniques verify the intercalation of CS with MMT interlayer to form mono- and bi-layer intercalated nanocomposites and the interlayer distance enlarged

when the initial CS:MMT molar ratio increased. Moreover, the intercalated CS exhibits higher thermal stability compared to the pristine polymer as noted from TGA thermogram. The *in vitro* SA-controlled release study demonstrates the gradual release behavior occurring only for the bilayer nanocomposite. According to the bilayer structure intercalation presents the excess -NH_3^+ ($\text{-NH}_3^+ > \text{CEC of clay}$) that would be balanced and interact electrostatically with salicylate anions (SA^-). A presence of NH_3^+SA^- species turns this material to acidic drug controlled release material where MMT particle acts as both a barrier and an implantable drug reservoir.

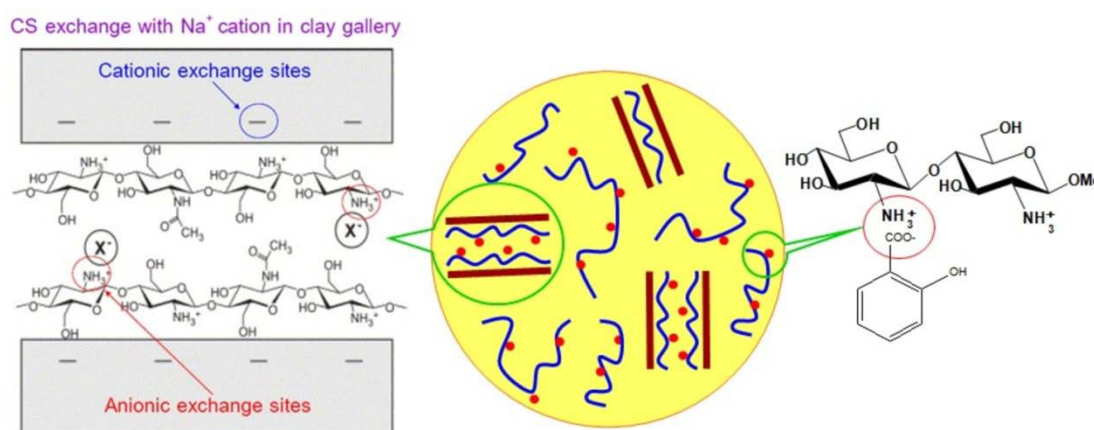


Figure 4.32 The schematic representation of SA/CS/MMT system.

Conversely, for basic drug THP/CS/MMT system, CS merely acts as a matrix with no drug-polymer interaction, whereas, direct intercalation of THP^+ into MMT interlayer via cationic exchange process was monitored. The drug-MMT interaction can be verified from the decrease of THP crystallinity on addition of MMT particles. However, no gradual release behavior for THP/CS/MMT material was observed as monitored from *in vitro* THP-controlled release study, probably because the

interaction between THP and MMT is rather weak. The schematic representations of SA/CS/MMT and THP/CS/MMT systems are demonstrated in Figures 4.32 and 4.33, respectively.

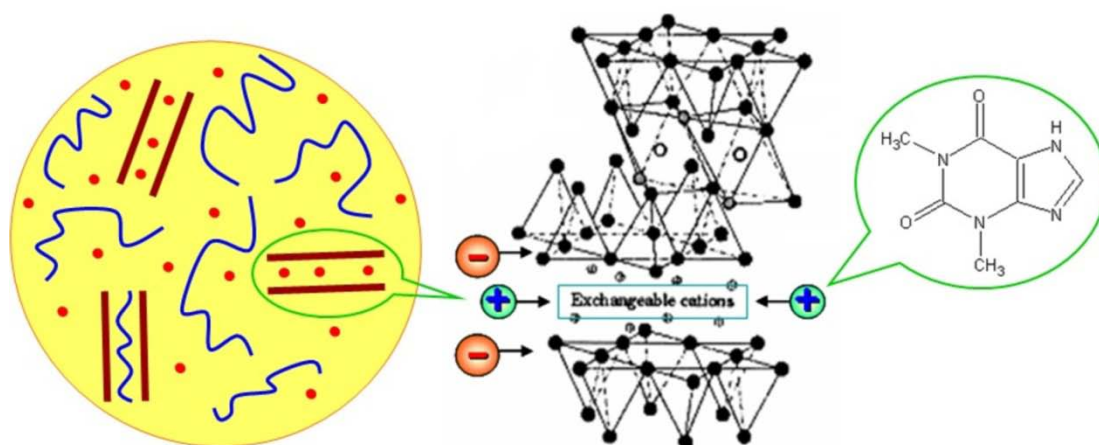


Figure 4.33 The schematic representation of THP/CS/MMT system.

Atomistic MD simulations were performed to study structure and property of bulk amorphous CS and its complex with SA and THP. Solubility of incorporated drugs in CS denotes that CS-SA mixture is miscible whereas CS-THP is immiscible and tends to phase separate. Due to weaker interaction between CS-THP, the diffusion coefficient of THP within CS is faster than SA about 4 times. This data agree well with experimental observation as noted from drugs release behavior. The RDFs analysis revealed that the gradual release of SA from CS matrix is mainly attributed to hydrogen bond formation of both CS amino and hydroxyl groups which form H-bonds with SA carboxyl and hydroxyl groups.

MD simulation was also employed to investigate the basal spacing, the layering behavior, and the intercalation structure of SA/CS/MMT nanocomposites at

an atomic scale. The influences of CS chain length (number of extra positive charge groups) and the amount of polymer/drug loading on the self-assembly of these molecules on MMT were analyzed. The simulation was conducted for typical systems with CEC of 144 mequiv/100 g, NH_3^+ side groups, a series of chain length or drug loading from 16 to 28 units, in attempt to link XRD, FTIR, and TGA data to the molecular structure. While NH_3^+ head groups of CS are ionically bonded to the MMT surface, they can also form three additional N-H \cdots O-Si hydrogen bonds closely attached to the surface associates to a lower lateral mobility. Formation of successive molecular layers between the MMT layers with increase of drug-polymer loading causes periodic fluctuations in interlayer density. Minimum was found for partially layers formation, maximum was found for fully packed layers, and convergence to almost a homogeneous interlayer structure and density can be obtained for a high enough loading. Formation of molecular layers also proceeds on the outer surface of MMT. The relationship between computational and experimental data was found to be very complementary. Basal plane spacings from X-ray diffraction are comparable with from simulation data. DSC, FTIR, and TGA measurements gave qualitative insight into molecular packing and interaction, which agree well with the simulation data.

CHAPTER V

STRUCTURE AND DYNAMICS OF ALKALI AND ALKALI EARTH METAL IONS DOPED CHITOSAN/POLY(ETHYLENE OXIDE) BLEND

5.1 Introduction

Chitosan/Poly(ethylene oxide) (CS/PEO) blend is a CS-based material that may improve the physical and mechanical properties along with enhancement of the conductive efficiency of pristine CS film (Mucha *et al.*, 2005; Zivanovic *et al.*, 2007). Preparation of this blend is based on an uncomplicated method by solution mixing of a flexible polymer, PEO, into acidic solution of CS. Due to the existence of the ether oxygen in PEO structure, this polymer can interact with CS to provide a homogeneous polymeric blend (Donoso *et al.*, 2007; Li *et al.*, 2010; 2011; Neto *et al.*, 2005; Zivanovic *et al.*, 2007).

CS/PEO blend films provide additional functionality compared to the individual polymer films of CS and PEO. PEO may contribute to the formation of colorless and more flexible film, while CS may improve mechanical property and transparency as well as decrease water solubility of PEO (Neto *et al.*, 2005). Moreover, blending with amorphous CS may facilitate a decrease of PEO crystallinity

(Zivanovic *et al.*, 2007), a major barrier for ion transportation, providing an ideal material appropriated for solid polymer electrolyte application, because both CS and PEO are able to dissolve the ionic salts to provide the ionic conductivity (Donoso *et al.*, 2007; Idris *et al.*, 2005; 2007).

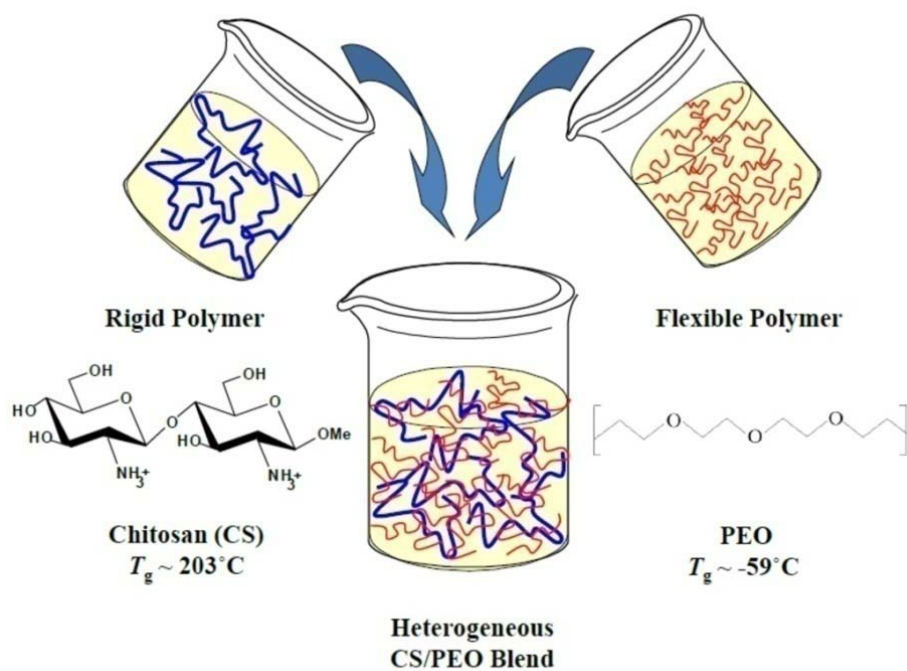


Figure 5.1 Solution blending of chitosan and poly(ethylene oxide).

To design the CS/PEO blend suitable for solid polymer electrolyte application, a choice of the doping ion is very important for achieving the highest ionic conductivity. Accordingly, two types of metal ions, alkali and alkali earth, were investigated as the doping ions into CS/PEO blend. In this respect, K^+ and Ca^{2+} were considered as the representative model of alkali and alkali earth ions, respectively, due to their similarity in both size and mass ($Z_{\text{K}} = 19$, $M_{\text{K}} = 39$ g/mol; $Z_{\text{Ca}} = 20$, $M_{\text{Ca}} = 40$ g/mol). The miscibility of CS/PEO blends and the effects of doping the alkali and alkali earth metal ions on the structure/property of the blends were studied intent to discuss a role of the ion valency in the interaction between the metal ions and each

polymer component. In addition, the effect of the CS:PEO composition on the ionic conductivity of the blends was also discussed in this work.

There are several techniques employed in this work. DSC technique was employed to study the miscibility and thermal property of CS/PEO blends. X-Ray technique was employed to verify the decrease of PEO crystallinity on blending with CS and also employed to study the crystallinity of ionic salts doped in CS/PEO blends matrix, while interactions between CS-PEO, CS-Ions, PEO-Ions and CS-PEO-Ions were elucidated by FTIR spectroscopy. The ionic conductivity and dielectric property, correlated with the diffusion behavior of ions within the CS/PEO blend matrix, were investigated by the dielectric/conductive Measurement. To subtract the effect of acetic acid (used as solvent) which interfere the ionic conductivity, NMR spectroscopy was employed to investigate the remaining amount of acetic acid in the samples.

The computational molecular simulation techniques were also employed to fulfill the experimental findings and gain an inclusive understanding in atomistic and mesoscopic level of these materials. The simulation techniques employed in this study consist of two parts: (1) the calculation via Molecular Dynamic (MD), (2) Mesoscopic Dynamic (MesoDyn) simulations. MD simulation was conducted for a series of CS/PEO blends with/without doped K^+ and Ca^{2+} , to study the miscibility of CS/PEO blends as well as the diffusion behavior and/or complex formation of ions within the blend matrix. Since the length scale in MD simulation is not possible to detect the phase separation in blends, it is necessary to combine MD technique with the mesoscopic simulation technique to study the phase morphology in this CS/PEO blend.

Technologically, this work has been driven by an interest in understanding the correlation between the structure and property of CS/PEO blends and the ions diffusion phenomena. Overall of this work provides us with a clue for developing a novel CS/PEO blend film suitable for solid polymer electrolyte application.

5.2 Research Methodology

5.2.1 Experimental Section

5.2.1.1 Materials and Apparatus

- Magnetic stirrers and magnetic bars
- Vacuum oven
- Polystyrene *Petri* dish for sample casting
- CS ($M_v = 1.13 \times 10^6$ g/mol, %DD = 75%), Aquatic Nutrition Lab
- Poly(ethylene oxide) ($M_w = 2 \times 10^5$ g/mol), Aldrich
- Potassium Sulfate (K_2SO_4), Aldrich
- Calcium Sulfate Dihydrate ($CaSO_4 \cdot 2H_2O$), Aldrich
- Acetic acid (CH_3COOH), Analytical Reagent, Merck
- Diethyl Ether ($C_4H_{10}O$), Analytical Reagent, Merck

5.2.1.2 Sample Preparation

CS and PEO were used without further purification. In preparation of a series of CS/PEO blends of different PEO content (total mass = 0.6 g for each blend), prescribed masses of CS and PEO were dissolved in 40 ml of 0.1 M aqueous acetic acid to obtain clear homogeneous solutions. For preparation of K^+ and Ca^{2+} doped blends, 0.0495 g of K_2SO_4 and 0.0978 g of $CaSO_4 \cdot 2H_2O$, respectively, were added to

each CS/PEO blend solution to obtain the constant amount of metal ions (9.47×10^{-4} mol ions/g of polymer mixture). The solutions were stirred overnight at room temperature to achieve complete dissolution, cast onto polystyrene *Petri* dish, and dried at room temperature in a dust free chamber. The resulting dry films were peeled off, rinsed with diethyl ether and dried again under reduced pressure at room temperature for 24 h. The samples for dielectric/conductive measurement were further dried at 110°C for 2 days to reduce the remaining amount of acetic acid (casting solvent) that interfered accurate determination of the conductivity of doped ions. The films were then stored in a desiccator for continuous drying before use.

5.2.1.3 Characterization

Differential Scanning Calorimetry (DSC)

DSC technique was employed to study the miscibility and thermal property of CS/PEO with/without doped metal ions. The measurements were performed with a calorimeter (TA instrument DSC-Q20). Accurately weighed specimens (~10 mg) were placed in aluminum pans and sealed. An empty pan was used as a reference and all measurements were performed under nitrogen atmosphere (purge flow = 50 ml/min). The specimen was firstly heated to 100°C and then annealed at 100°C for 7 min, thereby allowing the PEO crystallines therein to fully melt. Then the specimen was quenched to/annealed at a given crystallization temperature for 60 min. On the successive heating to 100°C, the thermal behavior including the PEO melting was examined at a scanning rate of 5°C/min. The cycles of heating and quenching at several crystallization temperatures (T_c) were used to obtain the information about equilibrium PEO melting temperature (T_m°). In the other type of thermal test, the

specimen was first heated to 100°C and annealed at 100°C for 7 min to erase its thermal history, quenched to -80°C and held for 10 min, and then heated at a scanning rate of 2°C/min (up to -20°C) to examine the glass transition temperature T_g of PEO. The specimen was further heated to 350°C at a scanning rate of 5°C/min, and the dehydration behavior as well as the degradation temperature (T_d) of CS were examined.

Wide-Angle X-ray Diffraction (WAXD)

WAXD technique was employed to verify the decrease of PEO crystallinity on blending with CS and also employed to study the crystallinity of ionic salts such doped in CS/PEO blends matrix. The measurements were conducted for specimens at room temperature with an X-ray diffractometer (Rigaku, RINT 2002). A monochromic $\text{CuK}\alpha$ (1.54 Å) X-ray source was operated at 40 kV and 50 mA, and the scattering intensity was measured at a scattering angle 2θ scanned from 5° to 30°.

Fourier Transform Infrared (FTIR) Spectroscopy

FTIR spectroscopy was employed to elucidate interaction between CS-PEO, CS-Ions, PEO-Ions as well as CS-PEO-Ions. The measurements were performed at Synchrotron Light Research Institute (SLRI) of Thailand on a Bruker Vertex 70 Fourier Transform Infrared spectrometer with a resolution of 4 cm^{-1} in a measurement range of 4000-800 cm^{-1} using a MCT (HgCdTe) detector cooled with liquid nitrogen. The infrared spectra of all sample films were obtained with ATR-FTIR method (PIKE MIRacle Crystal Plate: Single Reflection Ge Crystal Plate) and recorded by scanning for 32 times. The spectra were co-added and converted to absorbance using OPUS 5.0 software (Bruker Optics Ltd, Ettlingen, Germany).

Nuclear Magnetic Resonance (NMR) Spectroscopy

NMR measurements were conducted to determine the amount of the remaining acetic acid (casting solvent) in the samples, with the proton in PEO being utilized as the internal standard. JEOL JNM-AL400 spectrometer operating with a ^1H resonance frequency of 395.75 MHz was utilized to make the measurements at 70°C. The blend samples of a known mass were placed into a 5 mm NMR tube and sealed, and were dissolved by 1 ml of D_2O with gentle agitation. The sample tubes were kept at 70°C ($> T_m$ of PEO) overnight before the measurement in order to obtain the complete dissolution of the sample.

Dielectric/Conductive Measurement

Dielectric/Conductive measurement was employed to study the dielectric property and ionic conductivity correlated with the diffusion behavior of ions within the CS/PEO blend matrix. The measurements were performed at several temperatures and at frequencies between 0.01 Hz to 1 MHz with an impedance analyzer/dielectric interface system (1260 and 1296, Solartron) that was interfaced to a computer. The sample films were cut into small discs of 2 cm diameter, coated with gold by sputtering (to ensure good electrical contact to the sample). In the measurements, the sample films with accurately known thickness were sandwiched between two stainless steel electrodes and mounted in a dielectric cell having a guard electrode. For temperature controlling, the cell was placed in an oven and kept at the measuring temperature for 30 min before the measurement.

5.2.2 Computational Section

5.2.2.1 Molecular Dynamics Simulation of CS/PEO Blends

All simulations were carried out at 298 K with Discover module in Materials Studio (MS version 4.2) (Accelrys, 2007). The COMPASS (Rigby *et al.*, 1997; Sun, 1998(a&b)) force field was employed for all calculations. Each simulation system was minimized using Discover module. The amorphous phase of pure CS, pure PEO, and CS/PEO blends were constructed inside the simulation box with periodic boundary conditions. The oligomer of 40 monomer units for CS and 146 monomer units for PEO constitutes the amorphous cell for the neat polymers systems in order to obtain the equivalent molecular weight of both polymers. Density data for the chosen polymers were taken from the literature: $\rho_{\text{CS}} = 0.67 \text{ g/cm}^3$ (Gulke, 1999; Prathab *et al.*, 2007) and $\rho_{\text{PEO}} = 1.125 \text{ g/cm}^3$ (Eilmes, 2003). The box sizes were $20.6 \times 20.6 \times 20.6 \text{ \AA}^3$ and $21.2 \times 21.2 \times 21.2 \text{ \AA}^3$ for bulk CS and PEO, respectively. In general, the initial amorphous structure is in a relatively high-energy state. Therefore, before performing MD calculations, we had to perform the energy minimization by using smart minimization method (Accelrys, 2007) (with a convergence level of 0.01 kcal/mol/Å). The Smart minimizer starts with the steepest descent method, followed by the conjugate gradient method and ends with a Newton method. Atom-based cutoff of 9.5 Å and a switching function with the spline and buffer widths of 5 and 2 Å, respectively, were applied to evaluate non-bonded interactions. The MD simulations under constant temperature and volume (NVT ensemble) were performed for each configuration. A time step of 1 fs was used, and temperature was controlled by the Anderson thermostat. Short NVT simulations were run for 0.2 ns at 800 K to relax the structures to obtain the equilibrium density. Then another NVT simulation was

performed for 1 ns at 298 K. The energy of the system was monitored to ensure that it fluctuated around the average value, and this was considered as a criterion for having “equilibrated” system at the desired temperature, wherein trajectories were stored periodically for later processing. The solubility parameters (δ) of pure CS and pure PEO were calculated in this equilibrated state, to match these δ values with the reported literature data as a reliable test protocol.

Table 5.1 Atomistic simulation details of CS/PEO blends.

Composition w_{PEO}	Number of repeat unit		Density* (g/cm^3)
	CS	PEO	
0.0	40	0	0.670
0.2	32	29	0.760
0.4	24	58	0.851
0.6	16	88	0.943
0.8	8	117	1.034
1.0	0	146	1.125

* Densities of CS/PEO blends were calculated from the density of the individual polymers and volume fraction of each polymer component.

Bulk amorphous states of the CS/PEO blends were built in similar manner. The detailed model construction procedure corresponds to use of different ratios of the number of CS repeating units to the number of PEO repeating units in the unit cells. The details of the simulation condition for the pure polymers, CS and PEO, as well as the CS/PEO blends with difference weight fraction of PEO (w_{PEO}) are summarized in Table 5.1.

NPT MD was run to equilibrate the structure and the blend density. The amorphous assembly was energy-minimized using the Smart minimization method (Accelrys, 2007) with a convergence level of 0.01 kcal/mol/Å. The Smart minimizer starts with the steepest descent method, followed by the conjugate gradient method and ends with a Newton method. Atom-based cutoff of 9.5 Å and a switching function with the spline and buffer widths of 5 and 2 Å, respectively, were applied to evaluate non-bonded interactions. Since the density of the amorphous CS/PEO blend is different from those of the crystalline structures of the starting pure polymers, the simulations were carried out with isothermal-isobaric (NPT) ensemble based on Andersen-Berendsen method (Andersen, 1980;1983; Berendsen *et al.*, 1984). These NPT simulations were performed at atmospheric pressure as previously described (Rigby, 2004). Subsequently, short NVT simulations were run for 0.2 ns at 800 K to relax the structures to obtain the equilibrium density. Then another NVT simulation was performed for 1 ns at 298 K with a time step of 1 fs. Hildebrand solubility parameter (δ), defined as the square root of cohesive energy density (CED), and the radial distribution functions (RDFs), $g(r)$, were calculated in this equilibrated state.

5.2.2.2 Mesoscopic Dynamics Simulation of CS/PEO Blends

As a further proof, the Mesoscopic Dynamics (MesoDyn) simulation was employed to simulate the phase separation dynamics of the blends. This approach is based on the dynamic variant of mean-field density functional theory (Fraaije *et al.*, 1997), which is similar to classical dynamic random phase approximation (RPA) (Fan *et al.*, 1994). Here, the polymer chains are modeled as ideal Gaussian chains consisting of beads, each representing the monomer of polymer (Kuhn statistical

segments). Free energy of the system was then calculated in terms of bead distribution functions. Positions of the beads were then correlated to each other by converting it to a many-body problem. To overcome this problem, interchain correlations were neglected and the system is approximated by a set of independent Gaussian chains embedded in the mean-field. A key rudiment of the dynamic density functional theory is that on a coarse grained time scale, the free energy function is minimized. Details of these derivations were given earlier (Jawalkar *et al.*, 2005).

Parametrization: The expression for MesoDyn chain length (N_{meso}) is given by

$$N_{meso} = \frac{M_p}{M_m C_n} = \frac{n}{C_n} \quad (5.1)$$

where M_p is polymer molecular weight, M_m is monomer molecular weight, C_n is characteristic ratio of polymers (Flory, 1989) ($C_n = 14.2$ for CS (Kienzle-Sterzer, 1984) and $C_n = 5.2$ for PEO (Kawaguchi *et al.*, 1997), obtained from the experimental data) and n is the number of repeating units employed earlier in MD simulation. MesoDyn inputs are related to Flory-Huggins interaction parameter through the following relation:

$$\nu^{-1} \epsilon_{ij} = \chi_{ij} RT \quad (5.2)$$

where χ_{ij} is taken from atomistic simulations carried out for each blend at each composition, R is molar gas constant (8.314 J/mol.K) and T is 298 K. The N_{meso} and interacting energies between pair of interacting bead types ($\nu^{-1} \epsilon_{ij}$) are summarized in Table 5.2.

Table 5.2 Input parameters of CS/PEO blends for MesoDyn calculations.

Composition w_{PEO}	$\nu^{-1} \epsilon_{ij}$ (kJ/mol)	N_{meso}	
		CS	PEO
0.2	-0.36	2	6
0.4	-0.19	2	11
0.6	0.21	1	17
0.8	0.72	1	23

To account for numerical stability, the time step was chosen in such a way that dimensionless time step (τ) was 0.5 and bond length was 1.154 nm. A constant noise parameter of 75.002 was maintained during the entire simulation. The grid dimensions were $32 \times 32 \times 32$ nm and size of the mesh over which density variations are plotted in MesoDyn length units using the grid spacing field is 1 nm. The temperature of 25°C (298 K) corresponds to the temperature at which χ parameter was calculated for a total simulation of 250 μs . After setting up the initial configurations, systems were let to evolve toward equilibrium (phase separation or mixing). The initially homogeneous phases were cooled in the two phase region by tuning on interactions at time, $t = 0$. Then, blend compatibility was deduced from the final equilibrium morphologies. During the simulation steps, free energy should asymptotically approach a stable value as the system attains dynamic equilibrium.

5.2.2.3 Molecular Dynamics Simulation of Ions Incorporated CS/PEO Blend

For the CS/PEO blend of the PEO content $w_{\text{PEO}} = 20$ %w/w and with/without doped by K^+ and Ca^{2+} , molecular dynamics (MD) simulations were

conducted using Materials Studio 4.2 (Accelrys, 2007). The COMPASS (Rigby *et al.*, 1997; Sun, 1998(a&b)) force field was employed for all calculations. Each simulation system was minimized using Discover module. The amorphous phase of CS/PEO blend as well as the blend with doped by K^+ and Ca^{2+} were constructed inside the simulation box with periodic boundary conditions. For the neat CS/PEO blend with $w_{PEO} = 20\%$ w/w, 1 chain with 32 monomer units of CS and 1 chain with 29 monomer units of PEO were constructed in the periodic box with the dimensions of $20.62 \times 20.62 \times 20.62 \text{ \AA}^3$. Density of the blend was first estimated from the average density of individual pure polymers. Then, NPT MD was run to equilibrate the structure and the blend density was simulated to be 0.760 g/cm^3 . The amorphous assembly was energy-minimized using the Smart minimization method (Accelrys, 2007) with a convergence level of $0.01 \text{ kcal/mol/\AA}$. Atom-based cutoff of 9.5 \AA and a switching function with the spline and buffer widths of 5 and 2 \AA , respectively, were applied to evaluate non-bonded interactions. Since the density of the amorphous CS/PEO blend is different from those of the crystalline structures of the starting pure polymers, the simulations were carried out with isothermal-isobaric (NPT) ensemble based on Andersen-Berendsen method (Andersen, 1980;1983; Berendsen *et al.*, 1984). These NPT simulations were performed at atmospheric pressure. Subsequently, short NVT simulations were run for 0.2 ns at 800 K to relax the structures to obtain the equilibrium density. Then another NVT simulation was successively performed for 1 ns at 298 K with a time step of 1 fs. The radial distribution functions (RDFs), $g(r)$, were calculated in this equilibrated state.

For ion doped systems, ten K^+ units and five SO_4^{2-} units were added into the periodic simulation box of the equilibrated CS/PEO blend for the simulation of the K^+ -doped blend, while ten Ca^{2+} units and ten SO_4^{2-} units were added for the simulation of the Ca^{2+} -doped blend. These systems were allowed to relax in a manner similar to that for the neat CS/PEO blend mention above. The NVT simulation was then performed in this equilibrated state for 1 ns at high temperature (800 K) with a time step of 1 fs to examine the dynamics of ions in the CS/PEO blend matrix. The radial distribution functions (RDFs), $g(r)$, were calculated after another NVT simulation performed for 1 ns at 298 K.

5.3 Results and Discussion

5.3.1 Experimental Section

5.3.1.1 Thermodynamics of Polymer Blend

For polymer blends, the melting point depression is usually discussed on the basis of the work of Nishi and Wang (1975) who derived the expression for A/B polymer blends as:

$$\frac{1}{T_m} - \frac{1}{T_m^0} = -\frac{RV_{Bu}}{\Delta H_{Bu}V_{Au}} \chi_{AB}v_A^2 \quad (5.3)$$

where T_m and T_m^0 are the melting point of the crystallizable polymer component B (PEO for our case) in the blends and in pure bulk, respectively, and R is the gas constant. ΔH_{Bu} and V_{Bu} are the molar enthalpy of fusion and molar volume of the repeating unit of B. V_{Au} and v_A are the molar volume of the repeating unit of the non-crystallizable component A (amorphous CS in our case) and the volume fraction of

this component in the blends, respectively. Finally, χ_{AB} is the Flory-Huggins interaction parameter between the components A and B.

Equation (5.3) allows us to estimate the interaction parameter χ_{AB} from the measured melting point depression, $\Delta T_m = T_m^0 - T_m$. If $\Delta T_m/T_m^0$ ratio is much smaller than unity (with ΔT_m and T_m^0 expressed in K unit), Eq. (5.3) is rewritten as:

$$\Delta T_m = -T_m^0 \left(\frac{V_{Bu}}{\Delta H_{Bu}} \right) v_A^2 B \quad (5.4)$$

with

$$B = \left(\frac{RT_m^0}{V_{Au}} \right) \chi_{AB} \quad (5.5)$$

It follows from Eqs. (5.4) and (5.5) that ΔT_m is proportional to v_A^2 and χ_{AB} is obtained from the proportionality constant.

5.3.1.2 Miscibility of CS/PEO Blends Containing no Salt

WAXD measurements were conducted for pure PEO and CS/PEO blends (containing no salt) to verify the decrease of PEO crystallinity upon blending with CS. Decrease in PEO crystallinity is associated with the miscibility/compatibility between CS and PEO; therefore, the specific interaction between CS and PEO chains may suppress the crystallization of PEO. For CS/PEO blends, as CS is the fully amorphous component, only the semi-crystalline PEO portion exhibits the unique X-ray diffraction pattern.

Figure 5.2 shows WAXD patterns of CS/PEO blends films. In all CS/PEO mixtures, there are two main peaks at the scattering angle $2\theta = 19.2^\circ$ and 23.4° corresponding to *120* and *112/004* reflections, respectively, from PEO crystallites

(Radhakrishnan *et al.*, 1996). The relative intensities of two main diffraction peaks decrease monotonically with w_{CS} in the range of 0-40 % w/w. For $w_{CS} \geq 60$ % w/w, the relative intensities between these two peaks are deviated from the dilution behavior as expected from a simple law of mixtures, as discussed by Radhakrishnan for PEO/PMMA blends (Radhakrishnan *et al.*, 1996). Namely, the variation of WAXD intensity of certain reflection may be caused by an inhibition for the growth of PEO crystallites along particular directions and distortion from the general monoclinic unit cell. For CS/PEO blends, the deviation seen at $w_{CS} \geq 60$ % w/w is possibly due to strong hydrogen bond formation between PEO ether groups and CS amino groups (Sashina *et al.*, 2006; Zivanovic *et al.*, 2007). At high CS content, the interaction between CS and PEO is stronger than that between PEO and PEO.

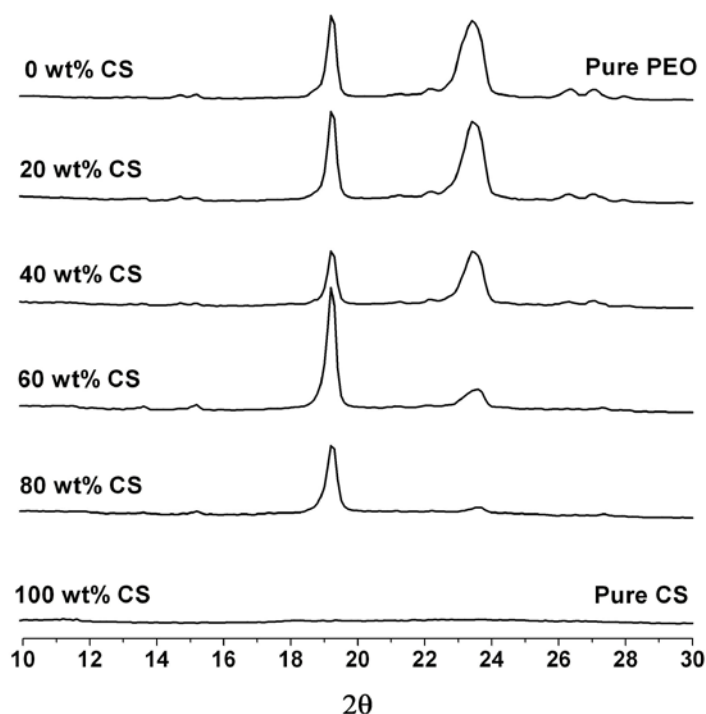


Figure 5.2 WAXD patterns for CS/PEO blends. The numbers adjacent indicate the CS content, w_{CS} (in % w/w).

DSC measurements were conducted to determine the melting temperatures, T_m^0 and T_m for pure PEO and the PEO in CS/PEO blends, respectively. The measurements also gave the PEO crystallinity (defined as the mass unit of PEO crystalline per mass unit of PEO in blends) as:

$$X_c^m = \frac{\Delta H_m}{f_w \Delta H_m^0} \quad (5.6)$$

Here, ΔH_m is the enthalpy of PEO fusion measured for the unit mass of sample, while ΔH_m^0 is the enthalpy of fusion for perfectly PEO crystalline ($\Delta H_m^0 = 196.8$ J/g (Pielichowski *et al.*, 2004)) and f_w is the weight fraction of PEO in the blends. The X_c^m values obtained for a series of CS/PEO blends are shown in Table 5.3, and the plots as a function of PEO weight fraction (w_{PEO}) shown in Figure 5.5.

In DSC measurements, T_m measured for pure PEO and PEO in CS/PEO blends are not necessarily identical to the melting temperature T_m^e of fully equilibrated/developed PEO crystalline. T_m is smaller than T_m^e due to insufficient crystalline growth (giving thin crystalline lamellae) and a consequent high surface energy of lamellae and/or of defects. Thus, the Hoffman and Weeks method was utilized (Hoffman *et al.*, 1962) to evaluate T_m^e . The PEO component in bulk and blends were allowed to crystallize at different temperatures T_c , and then melting temperature T_m was measured upon heating as shown in Figure 5.3. T_m , T_c , and T_m^e can be related by:

$$T_m = \phi T_c + (1 - \phi) T_m^e \quad (5.7)$$

where ϕ is the slope of T_m vs. T_c plot. The crystalline is perfectly stable if $\phi = 0$, while it is inherently unstable if $\phi = 1$.

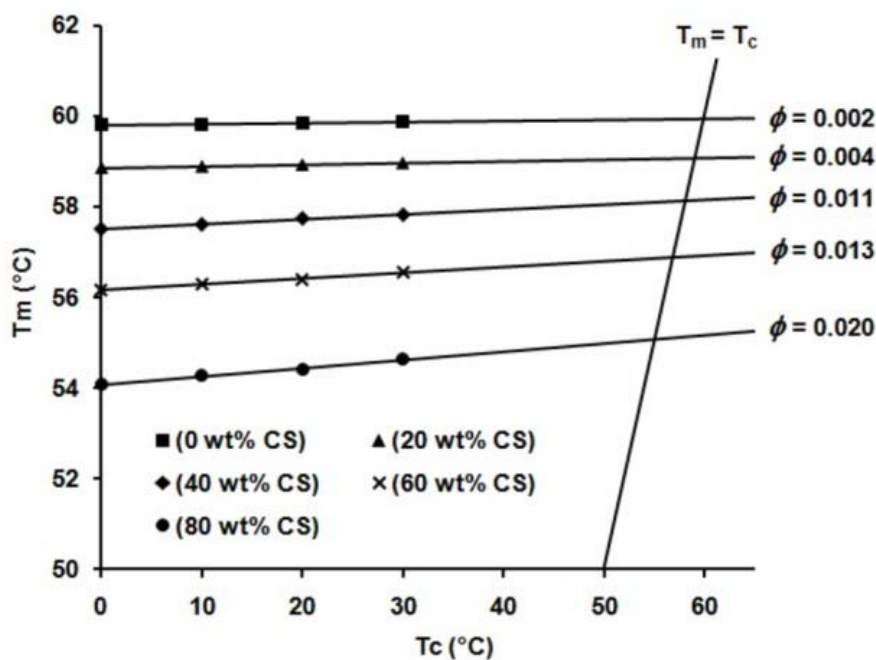


Figure 5.3 Hoffman-Weeks plots of the melting temperature (T_m) and crystallisation temperature (T_c), for CS/PEO blends with different w_{CS} .

Table 5.3 Equilibrium melting temperatures (T_m^e), degree of crystallinity (X_c^m) and stability parameters (ϕ) of PEO crystal for pure PEO and CS/PEO blends.

% w/w of CS in blends (w_{CS})	Mole fraction of CS in blends	T_m^e (K)	% X_c^m	ϕ ($\times 10^{-3}$)
0 % w/w	0.00	333.1	77	2
20 % w/w	0.06	332.2	71	4
40 % w/w	0.15	331.3	71	11
60 % w/w	0.28	330.0	72	13
80 % w/w	0.51	328.3	62	20

From Eq. (5.7), T_m^e is evaluated from a crossing point of Hoffman-Weeks plots with the $T_m = T_c$ line. T_m^e and ϕ values are shown in Table 5.3. $T_m^{0,e}$ for neat PEO is 333.1 K. From Table 5.3, ϕ for neat PEO is close to 0 and thus the crystallines are highly stable. In contrast, ϕ for CS/PEO blends is considerably larger than 0 and increases with increasing w_{CS} , which suggests that PEO crystallines are destabilized by CS. Correspondingly, both T_m^e and X_c^m also decrease with w_{CS} . All these results suggest that PEO-PEO interaction is interrupted by CS because of hydrogen bond formation between PEO ether groups and the CS amino groups. These interactions also lead to an increase of the degradation temperature (T_d) of CS component (as shown in Figure 5.8).

From Table 5.3, can be noted that X_c^m changes little with increasing w_{CS} up to 60 %w/w and is close to that in pure PEO. The optimum stoichiometric composition of the hydrogen bond formation appears at $w_{CS} \cong 80$ %w/w. Thus, the PEO crystalline content seems to decrease significantly when the stoichiometric amount of CS significantly retards a large scale motion of PEO thereby reducing PEO crystalline growth rate. Since PEO crystalline growth should be faster than the diffusion of amorphous CS chains located away from the PEO crystalline surface, the growth front always faces to CS chains (Lisowski *et al.*, 2000). Therefore, when ϕ increases significantly with increasing w_{CS} upon 80 %w/w, both T_m and ΔH_m (or crystallinity X_c^m) of PEO decreases.

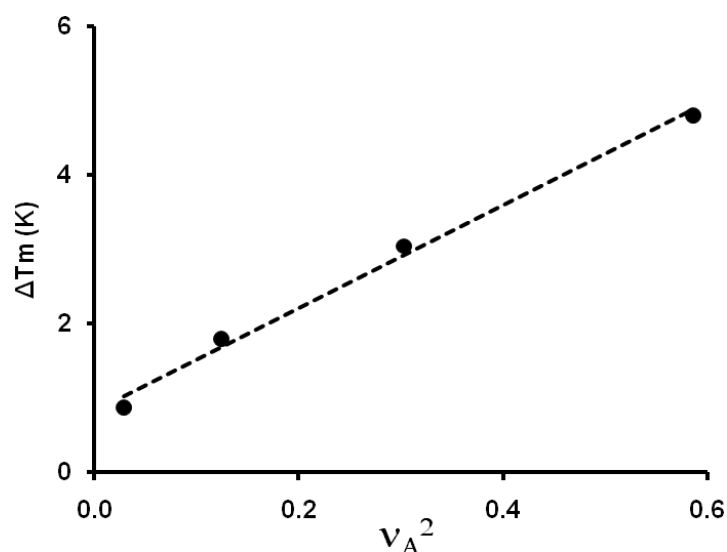


Figure 5.4 Melting point depression analysis for CS/PEO blends. The interaction energy density $B = -1.06 \text{ cal/cm}^3$, obtained from the slope of the plot.

In Figure 5.4, the melting point depression (ΔT_m), evaluated from T_m^e data shown in Table 5.3, is plotted against the square of CS volume fraction in blends (v_A^2). (v_A was estimated from the density of amorphous CS and PEO melt as 1.33 g/cm^3 (Deepak *et al.*, 2000) and 1.09 g/cm^3 (Roe, 1968), respectively, under an assumption of volume additivity. The density of PEO melt was utilized because the interaction parameter was estimated at the melting point.

The melting point depression reflects a favorable interaction between PEO and CS. The least-squares fit of ΔT_m against v_A^2 as shown in Figure 5.4 gives a straight line with its intercept close to zero in accord with Eq. (5.4). A tiny positive intercept is insignificant and within a typical range for compatible polymers that is attributed to the effect of morphological changes (Walsh *et al.*, 1985) and/or the result of a residual entropic effect (Paul *et al.*, 1984; Ziska *et al.*, 1981). Eq. (5.4) was utilized together

with $T_m^{0,e} = 333.1$ K (Table 5.3) to estimate the CS-PEO interaction parameter (χ_{AB}). The other parameters utilized in this estimation are: $\Delta H_{Bu} = 196.8$ J/g for perfectly crystalline PEO (Pielichowski *et al.*, 2004), $V_{Au} = 128.57$ cm³/mol and $V_{Bu} = 40.37$ cm³/mol for amorphous CS and PEO, respectively. (The method of calculating V_{Au} and V_{Bu} is explained in the appendix). This estimation gives $\chi_{AB} = -0.21$. The negative χ_{AB} value suggests a considerable attractive interaction between CS and PEO due to hydrogen bonding formation and dipolar interaction (Sashina *et al.*, 2006; Zivanovic *et al.*, 2007).

Figure 5.5 shows FTIR spectra of CS, PEO, and CS/PEO blend films. For CS film ($w_{PEO} = 0$) (Pawlak *et al.*, 2003; Zivanovic *et al.*, 2007), the main characteristic peaks of amino groups and amide groups (O=CR-NH attributed to chitin unit) are seen at 1568 cm⁻¹ and 1655 cm⁻¹, respectively. The broad bands for stretching vibration of OH and NH₂ group are observed at 3429 (O-H stretching) and 3346 cm⁻¹ (N-H stretching), respectively, and this hydroxyl band is responsible for the vibration of both C3-OH and C6-OH in CS structure. The bands at 2931 and 1410 cm⁻¹, attributed to the vibration of pyranose ring, are assigned to CH₂ stretching and OH/CH vibrations, respectively. The other bands at 1153, 1072 and 1028 cm⁻¹ are assigned to the vibration of C-O-C in CS glycosidic linkage. For PEO film ($w_{PEO} = 1$) (Ramesh *et al.*, 2008; Su *et al.*, 2002; Zivanovic *et al.*, 2007), the vibrations are the CH stretching (2895 cm⁻¹), CH₂ scissoring (1475 cm⁻¹), CH₂ wagging (1367, 1350 and 968 cm⁻¹) and CH₂ twisting (1288, 1250 and 847 cm⁻¹). The main characteristic peaks due to C-O-C stretching are seen at 1157 (C-C stretching), 1111 and 1086 cm⁻¹ (CH₂ rocking). FTIR spectra of CS/PEO blends change considerably from that of neat CS. The vibration bands of amino (1568 cm⁻¹), amide (1655 cm⁻¹) and hydroxyl

(3429 cm^{-1}) of CS are shifted to 1555 cm^{-1} , 1643 cm^{-1} and 3385 cm^{-1} , respectively, at $w_{\text{PEO}} = 0.2$. For $w_{\text{PEO}} = 0.8$, C-O-C stretching at 1157 , 1111 , 1086 cm^{-1} are shifted to 1148 , 1101 , 1061 cm^{-1} , respectively. Moreover, the vibration bands of PEO CH_2 groups are also shifted to lower frequency. These results suggest the specific interaction between the PEO ether groups and the amino, amide, and hydroxyl groups of CS. For the blends with $w_{\text{PEO}} > 0.2$, the vibration bands of amino, amide and hydroxyl groups are slightly shifted to higher frequency. The optimum interaction (the maximum change of the spectrum) is observed at $w_{\text{PEO}} = 0.2$ where the molar ratio between PEO ether oxygen and amino/hydroxyl groups of CS is 1:1. These results support a discussion for DSC and WAXD data in Figures 5.2-5.4.

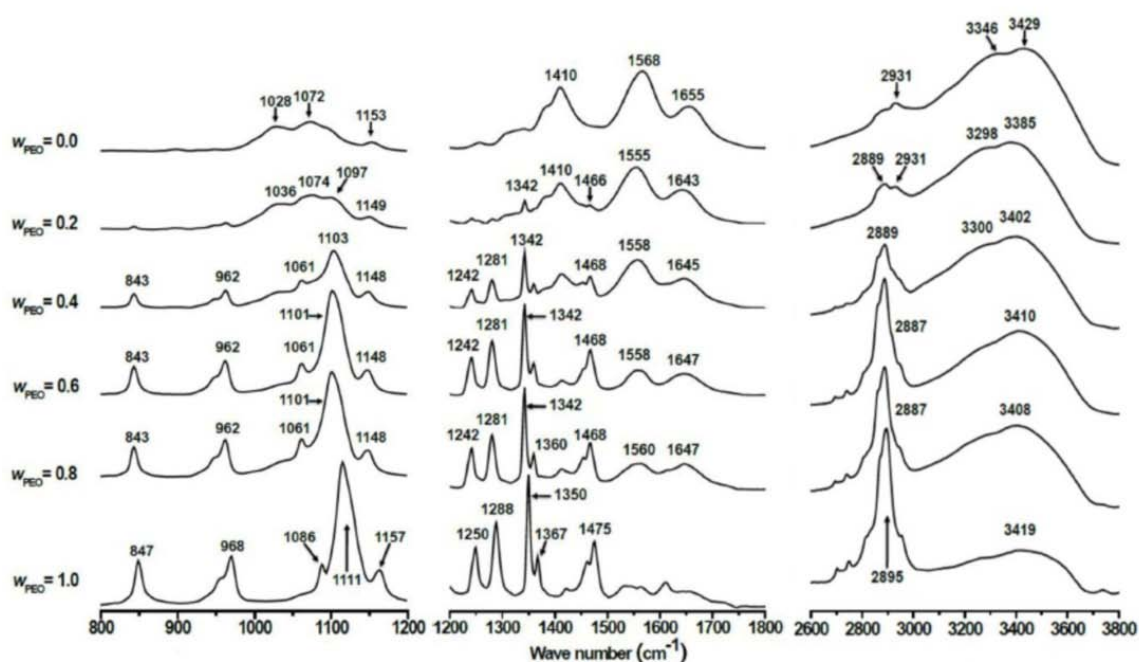


Figure 5.5 FTIR spectra of CS, PEO and CS/PEO blend.

5.3.1.3 CS and PEO Doped with Metal Ions

Krajewska (Krajewska, 2001) studied the interaction and complex formation behavior of CS doped with metal ions. He reported that K^+ does not strongly interact with CS while Ca^{2+} interacts with CS amino groups to form chelation network. These features are consistent with our observation for the degradation temperature of CS (data shown later in Figure 5.8): $T_d = 273.6^\circ\text{C}$, 280.0°C and 278.4°C for neat CS, Ca^{2+}/CS and K^+/CS , respectively. The highest T_d for Ca^{2+}/CS reflects the stabilization due to the network formation. In addition, Ca^{2+}/CS film was more brittle than neat CS and K^+/CS films. This network formation occurs primarily at the amino and hydroxyl groups that behave as the complex-forming ligand for metal ions. The complex formation is more significant for Ca^{2+} than K^+ , which reflects a difference in cation valency. Di-valence metal ions strongly interact with amino groups to form inclusion complex (Krajewska, 2001), while the mono-valence metal ions are bound only peripherally with amino groups and have a minimal effect on the thermal degradation behavior (Sreenivasan, 1996; Trimukhe *et al.*, 2009).

For ion-doped PEO, DSC measurements indicate a decrease in PEO crystallinity (X_c^m) in the order of $Ca^{2+}/\text{PEO} < K^+/\text{PEO} < \text{PEO}$ (data shown in Figure 5.7). This decrease is attributed to weak coulombic interaction between metal ions and PEO ether groups (Reddy *et al.*, 2002). Weak coordination of metal ions on ether groups could also reduce X_c^m . The glass transition temperatures (T_g) of K^+/PEO (-62.3°C) and Ca^{2+}/PEO (-57.6°C) were lower and higher than that of neat PEO (-59.4°C), respectively. Thus, Ca^{2+} interacts more strongly with ether groups than K^+ . This complex formation naturally reduces the segmental mobility and increases T_g of Ca^{2+}/PEO .

Figures 5.9 and 5.10, respectively, show FTIR spectra of K^+ /CS and Ca^+ /CS. We note changes in the vibration bands of amino, amide, and hydroxyl groups of CS due to metal ion doping. The amino, amide, and hydroxyl bands in K^+ /CS are shifted to 1555 cm^{-1} , 1643 cm^{-1} and 3403 cm^{-1} , respectively, and those in Ca^{2+} /CS are shifted to 1551 cm^{-1} , 1639 cm^{-1} and 3378 cm^{-1} , respectively. As noted from these shifts, the interaction between metal ions and CS mainly occurs at the amino, amide, and hydroxyl groups, and the interaction is more significant for Ca^{2+} than K^+ . Addition of K^+ and Ca^{2+} into bulk PEO also changed the infrared spectrum compared to unmixed PEO (cf. Figures 5.9 and 5.10). For K^+ /PEO and Ca^{2+} /PEO, the C-O-C stretching vibration at 1157 , 1111 , 1086 cm^{-1} shifted to 1149 , 1103 , 1063 cm^{-1} and 1148 , 1099 , 1061 cm^{-1} , respectively, indicating that the interaction with metal ions mainly occurs at the ether group of PEO and the interaction is more significant for Ca^{2+} than K^+ .

5.3.1.4 CS/PEO Blends Doped with Metal Ions

DSC measurement was conducted for K^+ - and Ca^{2+} -doped CS/PEO blends to determine T_m and X_c^m of PEO as well as T_d of CS. From Hoffman-Weeks plots, the melting temperature of well equilibrated PEO crystalline (T_m^e) was obtained. In Figures 5.6, 5.7, and 5.8, T_m^e , X_c^m , and T_d are plotted as a function of w_{PEO} , respectively. The data for the ion-doped PEO ($w_{PEO} = 1$) and ion-doped CS ($w_{PEO} = 0$) are also shown.

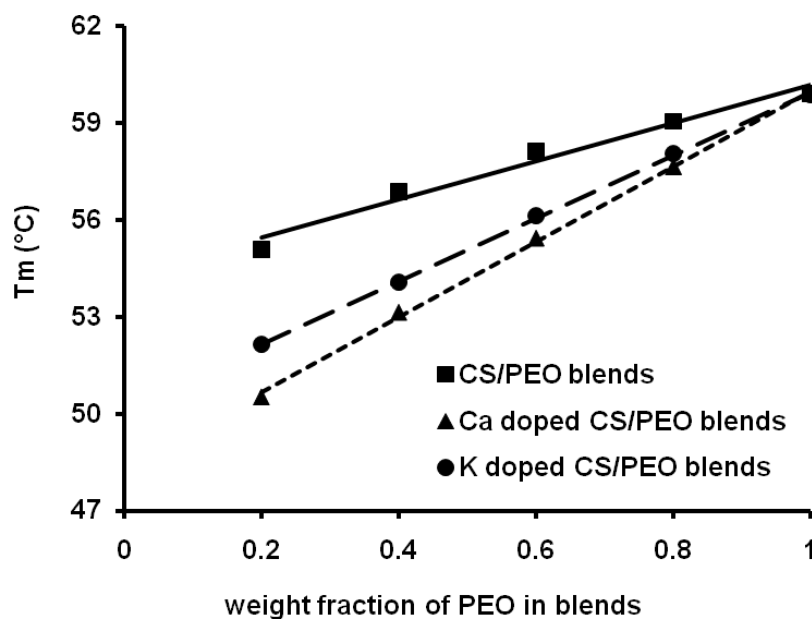


Figure 5.6 Depression of the melting temperature of fully equilibrated PEO crystalline (T_m) in undoped and ion-doped CS/PEO blends.

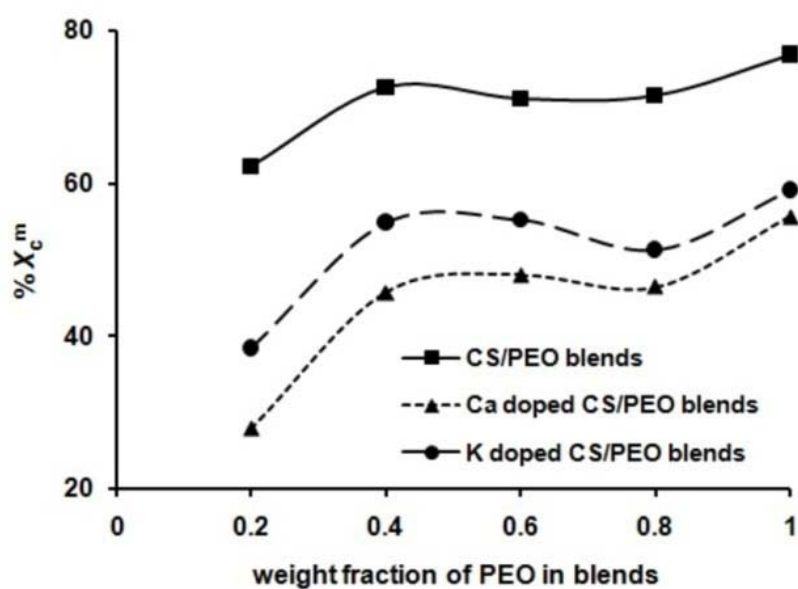


Figure 5.7 Degree of crystallinity (X_c^m) of PEO in undoped and ion-doped blends.

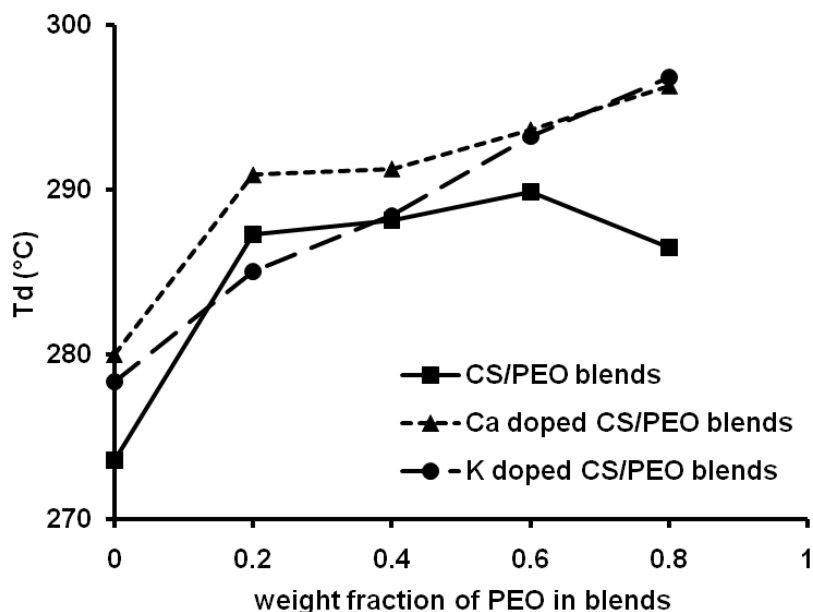


Figure 5.8 Degradation temperature of CS in undoped and ion-doped CS/PEO blends.

From Figures 5.6 and 5.7, T_m^e and X_c^m of PEO decrease upon ion doping, and this decrease is larger for Ca^{2+} -doped than for K^+ -doped. This decrease is more significant for larger w_{CS} . These results suggest that ions favorably interact with PEO ether groups to form the complex (Reddy *et al.*, 2002). This ion-polymer interaction is cooperatively enhanced in the presence of CS as suggested from larger decrease of T_m^e and X_c^m at high CS content. This molecular picture of cooperative interaction is consistent with an increase in T_d of CS with increasing w_{PEO} as shown in Figure 5.8.

FTIR spectra of K^+ - and Ca^{2+} -doped CS ($w_{\text{PEO}} = 0.0$), PEO ($w_{\text{PEO}} = 1.0$), and CS/PEO blends ($w_{\text{PEO}} = 0.2, 0.4, 0.6, 0.8$) films are shown in Figures 5.9 and 5.10. For K^+ doped blends, DSC and WAXD data indicated that the doped salt, K_2SO_4 , was fully dissolved in blends (no residual K_2SO_4 crystals) and fully dissociated into K^+ and SO_4^{2-} at all w_{PEO} . In contrast, CaSO_4 was just partially dissolved in particular for

large w_{PEO} . Complete dissolution to Ca^{2+} was confirmed only for pure CS, suggesting a favorable interaction between Ca^{2+} with CS more than that of PEO.

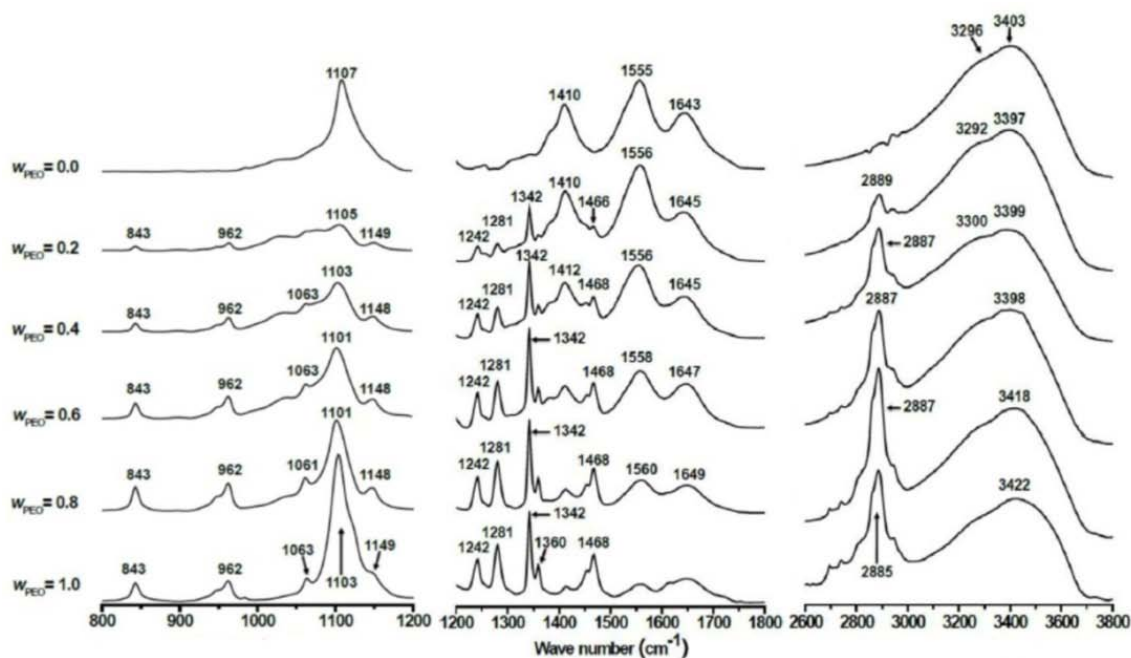


Figure 5.9 FTIR spectra of K^+ doped into CS, PEO and CS/PEO blends.

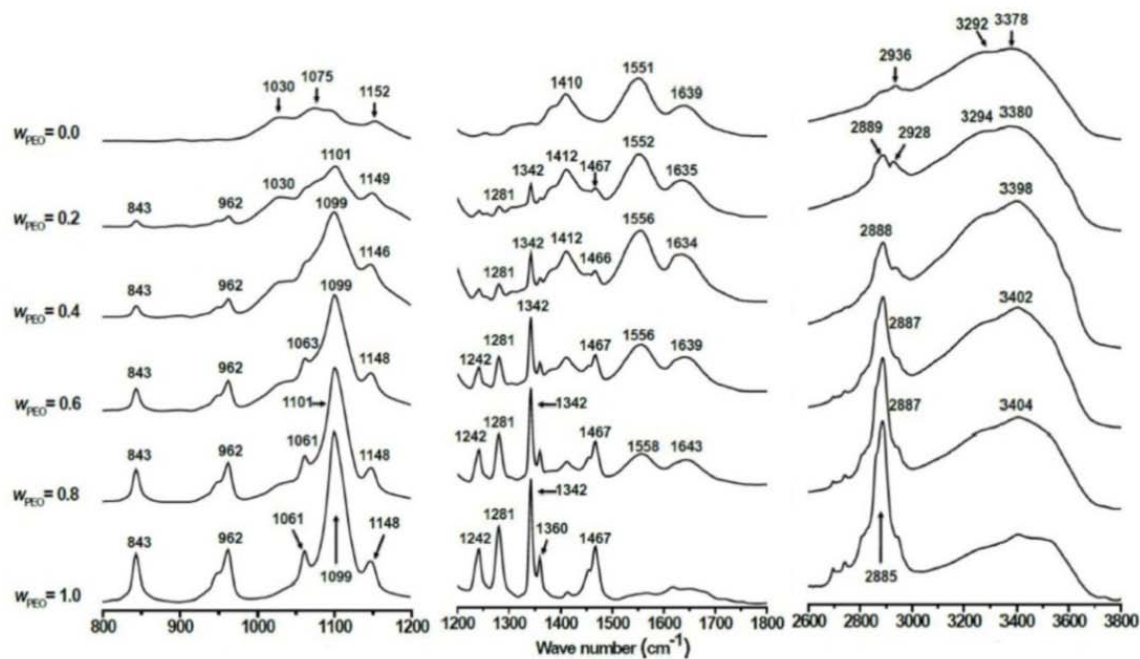


Figure 5.10 FTIR spectra of Ca^{2+} doped into CS, PEO and CS/PEO blends.

As noted in Figures 5.9 and 5.10, the vibration modes of K^+ -doped blends do not change significantly, which implies weaker interaction between K^+ and both polymers. In contrast, the spectra of Ca^{2+} -doped blends substantially changed the vibration bands of amino, amide, and hydroxyl groups of CS (at 1568, 1655, and 3429 cm^{-1} , respectively) along with PEO ether groups (at 1157, 1111, 1086 cm^{-1}), despite the fact that the doped salt, $CaSO_4$, was only partially dissolved/dissociated in the CS/PEO blends. In the presence of Ca^{2+} , the vibration bands of the blends corresponding to the CS and PEO functional groups shifted slightly to lower frequencies. These results suggest that Ca^{2+} interacts specifically with the amino, amide, and hydroxyl groups of CS as well as with the PEO ether groups. Ca^{2+} seems to serve as a transient cross-linker to form a stable CS/ Ca^{2+} /PEO complex, while less significant complex formation occurs for the case of K^+ . The hydrogen bonding between CS and PEO in the undoped CS/PEO blend was replaced by ion-dipole interaction between Ca^{2+} and polymers. Specifically, the vibrational frequencies of amino, amide, and hydroxyl groups are the lowest at $w_{PEO} = 0.2$ (CS:PEO molar ratio 1:1) and increase for $w_{PEO} > 0.2$, suggesting that ion-dipole interaction is the strongest at $w_{PEO} = 0.2$.

5.3.1.5 Mobility of Ions in CS/PEO Blends

It is interesting to examine dynamic characteristics of ion/CS/PEO blends in addition to the structural and thermodynamic aspects. Thus, dielectric/conductive behavior of these blends was focused to examine ion motion in relation to the blend structure. To subtract the effect of acetic acid (casting solvent) that interfere the ionic conductivity, NMR spectroscopy was employed to evaluate the

remaining amount of acetic acid in the samples, in which the proton in PEO utilized as the internal standard. The assignment of $^1\text{H-NMR}$ signal was based on the previous literatures: In fact, the resonance lines were observed exactly at the reported chemical shift (δ), $\delta = 1.9$ ppm for 3 equivalent protons of CH_3OOH (Alger *et al.*, 1979) and $\delta = 3.7$ ppm for 4 equivalent protons of $(\text{CH}_2)_2$ unit of EO segment (Ma *et al.*, 2006). The remaining amount of acetic acid was evaluated from the ratio of signal intensities of those protons. Table 5.4 summarizes the molar ratio of acetic acid to EO unit obtained for CS/PEO blends with $w_{\text{PEO}} = 0.2$ with/without doped K^+ and Ca^{2+} . A small amount of the acetic acid remained in the sample even after drying process because of the strong attractive interaction of acetic acid with CS and PEO.

Table 5.4 Content of acetic acid remaining in 0.6 g of CS/PEO blends at $w_{\text{PEO}} = 0.2$ with/without doped metal ions.

CS/PEO blend ($w_{\text{PEO}} = 0.2$)	Mole ($\times 10^{-3}$)		Acetic acid/EO molar ratio
	Acetic acid	Ethylene Oxide	
Neat blend	0.31	2.73	0.11
K^+ -doped	0.27	2.73	0.10
Ca^{2+} -doped	0.43	2.73	0.16

Overview of Dielectric Data

For representative CS/PEO blends at $w_{\text{PEO}} = 0.2$ (stoichiometric composition) with/without doped metal ions, Figure 5.11 shows the dynamic dielectric constant (ϵ') and dielectric loss (ϵ'') measured at several temperatures T . These data are plotted against frequency f (in Hz) in double-logarithmic format. The dielectric behavior can be classified into two regimes, as explained below.

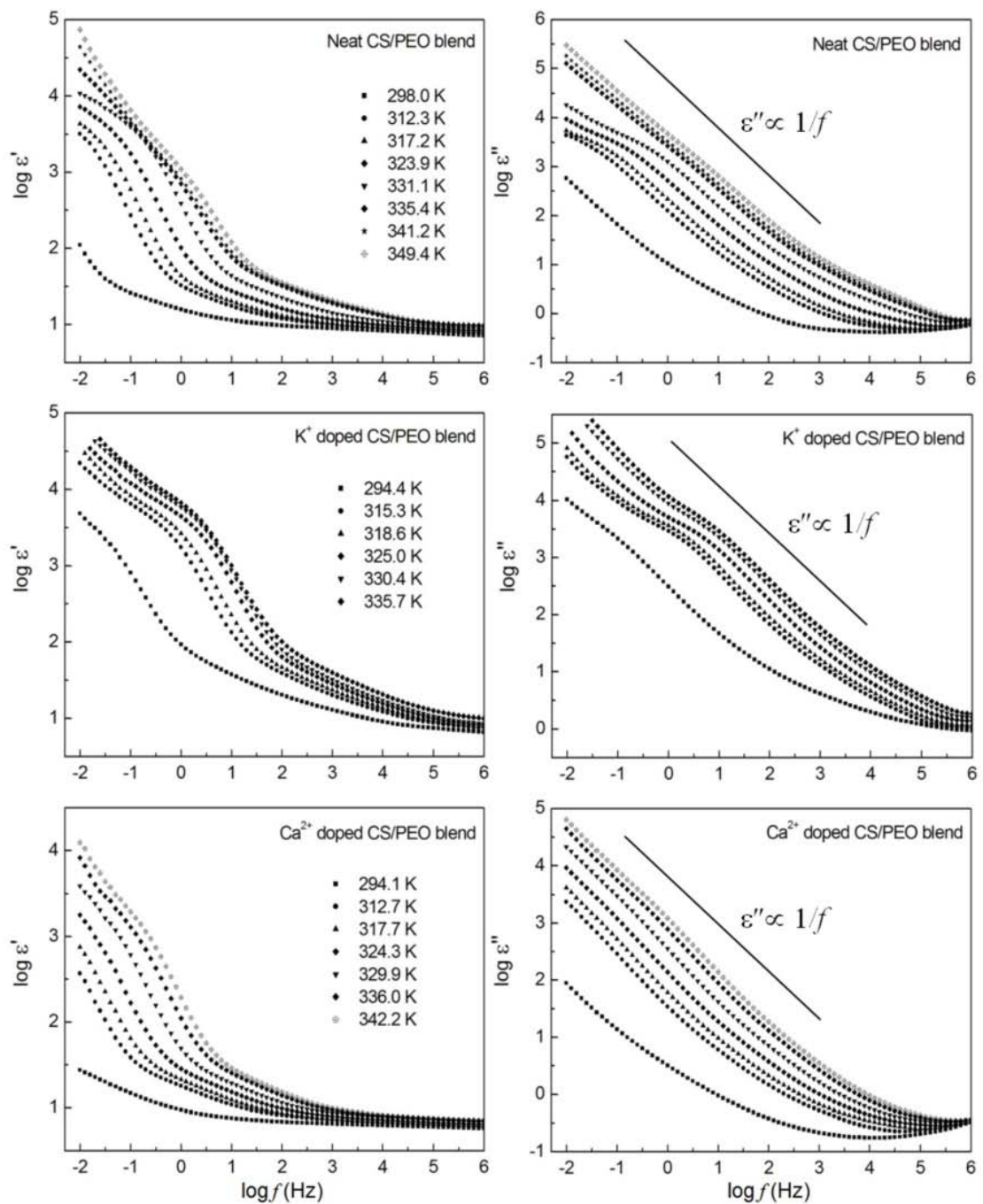


Figure 5.11 Frequency (f) dependence of dynamic dielectric constant (ϵ') and dielectric loss (ϵ'') of CS/PEO blend ($w_{\text{PEO}} = 0.2$) with/without doped metals. The ϵ' and ϵ'' data at various temperatures are double-logarithmically plotted against f .

(1) Low f regime, ε'' is essentially proportional to $1/f$ and ε' increases drastically with decreasing f . This behavior is attributed to the electrode polarization (EP) effect (Fragiadakis *et al.*, 2008; Lee *et al.*, 2010; Macdonald, 1953; Matsumiya *et al.*, 2003). Charge carrying ions, including doped K^+ and Ca^{2+} as well as H^+ from the remaining acetic acid (casting solvent; cf. Table 5.4), can move between the electrodes but they cannot discharge themselves at the electrodes (made of stainless steel). Thus, ions should be concentrated near the electrodes at low f to store a huge electrostatic energy reflected in a large increase of ε' (up to 10^4 or above). In an ideal case of EP polarization, a single-Maxwell type dispersion associated with ε'' -peak and ε' -plateau is observed at low f (Fragiadakis *et al.*, 2008; Lee *et al.*, 2010; Matsumiya *et al.*, 2003). The blend data do not exhibit this ideal behavior but they appear to associate with an extra, slower dispersion; cf. the inflection of ε' and ε'' followed by upturn seen for the K^+ -doped blend ($T \geq 315K$) on a decrease of $f < 1$ Hz. This extra slow dispersion, seen as the low- f upturn, can be assigned as a parasitic dispersion due to thin oxide layer on electrodes. (Matsumiya *et al.*, 2003)

(2) Intermediate to high f regime, ε' weakens its f dependence and approaches a high- f dielectric constant ε_∞ ($= \varepsilon_\infty$ of CS/PEO), and ε'' also weakens its f dependence accordingly; see, for example, the data of the K^+ -doped blend ($T \geq 315K$) at $f > 100$ Hz. This behavior is attributable to ion-hopping process. It should be noted the real direct current (dc) conduction is accompanied by full discharge at the electrodes and no real dc conduction occurs in the blend at low f where EP effect start to emerge. The static conductivity (σ_0) can be still estimated from an analysis of ε' and ε'' data in the ion-hopping regime.

Before making further analysis for ε' and ε'' data, Figure 5.11 is noted that ε'' data in the EP regime is larger in the order: K^+ -doped blend $>$ neat blend \gg Ca^{2+} -doped blend. Thus, the conductivity (σ_0) reflected in these data is also larger in the same order. Since all blends with $w_{\text{PEO}} = 0.2$ contained nearly the same amount of H^+ (from the acetic acid; cf. Table 5.4), $\sigma_{0,\text{neat}} \gg \sigma_{0,\text{Ca}^{2+}\text{-doped}}$ unequivocally tells us that Ca^{2+} ions are not only strongly bound with PEO and CS chains (in particular to CS chains as judged from the Ca^{2+} -CS affinity explained earlier) but also constraining the motion of H^+ . Since $\sigma_{0,\text{K}^+\text{-doped}} > \sigma_{0,\text{neat}}$, K^+ appears to hardly bound to PEO and CS chains and give no synergetic constraint on H^+ . These features were observed for all examined blends (including those with $w_{\text{PEO}} \neq 0.2$). ε' and ε'' data of these blends are analyzed below to quantitatively examine the molecular picture for ion mobility.

The complex permittivity (ε^*) can be equivalent to the complex impedance (Z^* ; $Z^* = Z' - jZ''$) of dielectric materials and described by: (Abdul-Jawad *et al.*, 1997)

$$\varepsilon' = -Z'' / (Z'^2 + Z''^2) \omega C_0 \quad \text{and} \quad \varepsilon'' = -Z' / (Z'^2 + Z''^2) \omega C_0 \quad (5.8)$$

Here, C_0 is the vacuum capacitance of the cell. Z^* characterized fundamental electrical properties of the materials: induction and capacitance. The Cole-Cole plot between Z'' and Z' may specify the relaxation assigned to bulk material and grain boundaries (dipole and structure). The main contribution to the relaxation in our materials is expected to be local motion of ions.

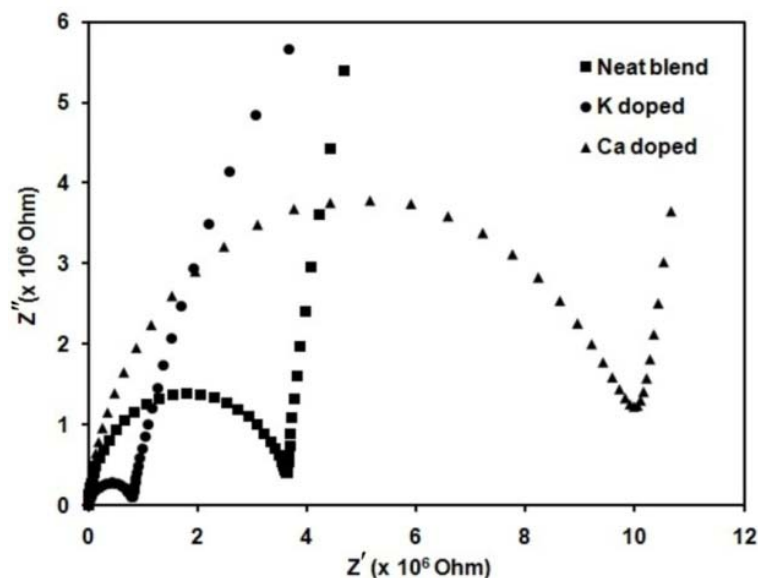


Figure 5.12 The Cole-Cole plots of CS/PEO blends ($w_{\text{PEO}} = 0.8$), with/without doped K^+ and Ca^{2+} (at 318 K).

The Cole-Cole plots of CS/PEO blends ($w_{\text{PEO}} = 0.8$), with/without doped K^+ and Ca^{2+} are shown in Figure 5.12. From these plots, these samples are partially resistive and capacitive in nature and the capacitances are frequency-dependence. These high frequency intercepts give the sample resistances. A semicircle diameter gives electrical resistivity of sample and the maximum value corresponds to relaxation frequency, $\omega = 1/RC$ with R = resistance and C = capacitance.

The Cole-Cole plots for neat CS/PEO blends at any composition as well as K^+ - and Ca^{2+} -doped blends also gives the high-frequency semi-circle in the Cole-Cole plot, as similar to that in Figure 5.12. This behavior can be due to the parallel combination of bulk resistance (due to migration of ions) and bulk capacitance (due to immobile polymer chains) (Hema *et al.*, 2009). The bulk resistance R_b can be evaluated from the intercept of the high-frequency semi-circle, and the ionic conductivity (σ) of samples were calculated from R_b as (Idris *et al.*, 2007)

$$\sigma = \frac{d}{R_b A} \quad (5.9)$$

where A is the area of film-electrode contact and, d is the thickness of sample film.

The ionic conductivity (σ), evaluated from Cole-Cole plots for a series of CS/PEO blends with/without doped K^+ and Ca^{2+} , was measured at 318 K where some PEO fraction was in the crystalline state (318 K, $T_{m,PEO} = 333$ K). In Figure 5.13, σ are normalized by the content of amorphous PEO and CS as well as the degree of $CaSO_4$ dissociation evaluated from DSC data. These normalized conductivities increase, at any w_{PEO} , in the order of K^+ -doped blends $>$ neat blends (containing H^+) $>$ Ca^{2+} -doped blends and the conductivity are largest at $w_{PEO} = 0.2$.

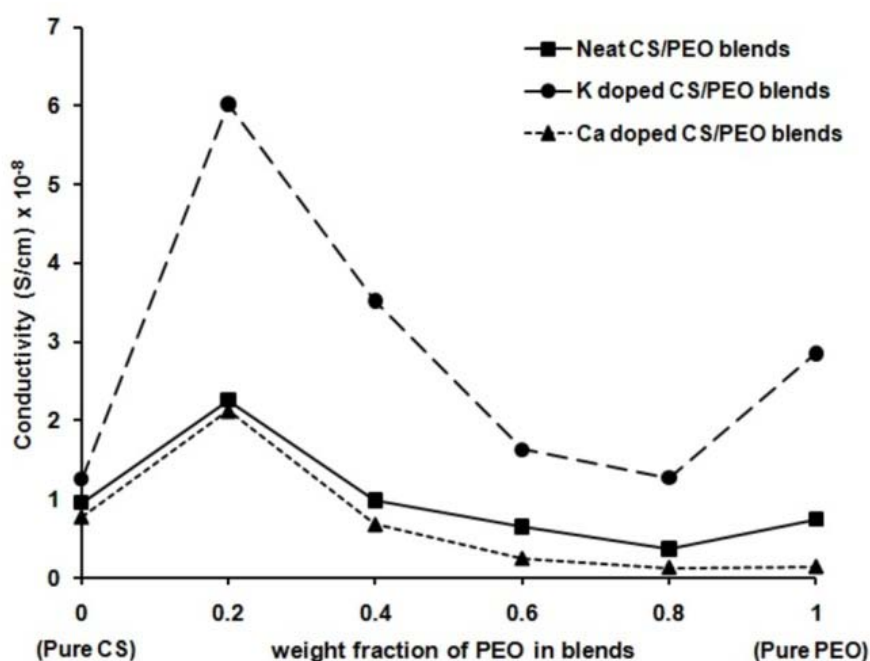


Figure 5.13 The normalized conductivity (at 318 K) for a series of CS/PEO blends with different weight fraction of PEO (w_{PEO}), with/without doped K^+ and Ca^{2+} .

In the neat CS/PEO blends, the conductivity is mainly due to H^+ supplied from the remaining casting solvent, *i.e.* acetic acid. A tiny decrease of the conductivity on Ca^{2+} addition into neat blends suggests that Ca^{2+} can act as a crosslinker to form a chelation network structure between CS and PEO and it retards polymer chain motion. This retardation would have suppressed the H^+ motion aided/activated by the polymer chain motion. In addition, Ca^{2+} ions were possibly attached within the chelation structure. The Ca^{2+} doped blends contained more ions (*i.e.*, both Ca^{2+} and H^+) compared to non-doped blends but they exhibit smaller conductivity, probably because of this CS/ Ca^{2+} /PEO interaction. In contrast, K^+ seems to be bound to both polymers chains more weakly than Ca^{2+} thereby moving by itself (without the aid of polymer motion) and allows H^+ to move. This behavior possibly provided the K^+ -doped blends with the highest conductivity for the entire range of w_{PEO} .

At $w_{PEO} = 0.2$, CS and PEO chains interact most strongly by forming H-bonds stoichiometrically (molar ratio of 1:1) thereby achieving the highest magnitude of miscibility as suggested by DSC and FTIR data. Thus, the ions binding to polymer chains possibly became the weakest at $w_{PEO} = 0.2$ thereby giving the highest conductivity at this w_{PEO} .

Analysis of High-Frequencies Regime

The complex conductivity (σ^*) is actually equivalent to ε^* ($\sigma^* = i\omega\varepsilon_0\varepsilon^*$) but it is more convenient to use σ^* to discuss the ion-hopping process. For sinusoidal electrical fields, the conductivity (σ) and the dielectric function (ε) can be related by (Kremer *et al.*, 2003).

$$\sigma'(\omega) = \omega \varepsilon_0 \varepsilon''(\omega) \quad \text{and} \quad \sigma''(\omega) = \omega \varepsilon_0 \varepsilon'(\omega) \quad (5.10)$$

Both quantities σ^* and ε^* characterize semi-conductivity disordered materials. From dielectric functions shown in Figure 5.11, the real (σ') and imaginary (σ'') parts of the complex conductivity were evaluated by Eq. (5.10) and the variation of σ' as a function of frequency at different temperatures are shown in Figure 5.14.

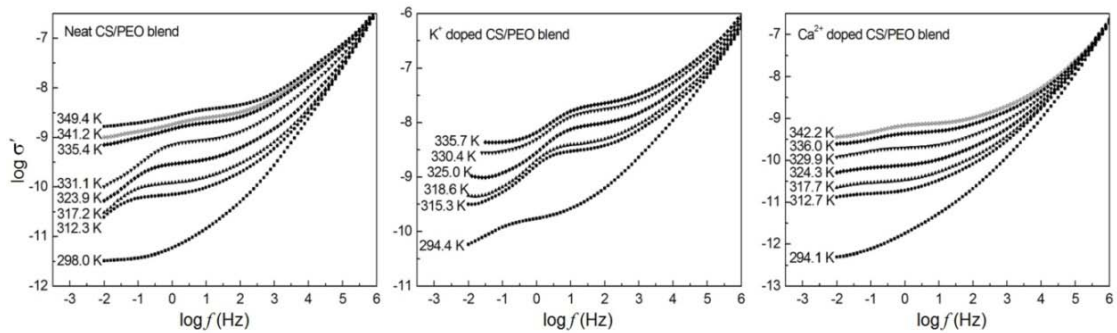


Figure 5.14 Variation of the real part of conductivity (σ') as a function of frequency at indicated temperatures for CS/PEO blend ($w_{\text{PEO}} = 0.2$) with/without doped K^+ and Ca^{2+} .

The microscopic model is required to describe the dispersion of complex conductivity at high frequencies above the critical value (ω_c ; the frequency such ion start to hop) which respects the diffusion of charge carriers in the system. For the microscopic hopping conduction mechanism, a variety of models has been proposed. The simplest is the random free-energy barrier model developed by Dyre (Dyre, 1988; Dyre *et al.*, 2000). This model assumes that conduction takes place by charge carriers hopping which are subjected to energy barriers that vary randomly in space. This model can be solved within the Continuous-Time-Random Walk (CTRW) approximation (Montroll *et al.*, 1965) to give

$$\sigma^*(\omega) = \sigma_0 \left[\frac{i\omega\tau_e}{\ln(1+i\omega\tau_e)} \right] \quad (5.11)$$

where τ_e is the attempt frequency to overcome the largest barrier determining the dc-conductivity. Eq. (5.11) is split into real and imaginary parts as

$$\sigma'(\omega) = \frac{\sigma_0 \omega \tau_e \arctan(\omega \tau_e)}{\frac{1}{4} \ln^2(1 + \omega^2 \tau_e^2) + (\arctan \omega \tau_e)^2} \quad (5.12)$$

$$\sigma''(\omega) = \frac{\sigma_0 \omega \tau_e \ln(1 + \omega^2 \tau_e^2)}{\frac{1}{2} \ln^2(1 + \omega^2 \tau_e^2) + 2(\arctan \omega \tau_e)^2} \quad (5.13)$$

For study the diffusion behavior of mobile charge carriers in CS/PEO blend ($w_{\text{PEO}} = 0.2$) matrix, the complex conductivity was analyzed with aid of CTRW model. At temperatures lower than the melting point of PEO (333.1 K) where the mobility of PEO does not disturb the analysis, the real (σ') and imaginary (σ'') parts of complex conductivity were fitted with Eqs. (5.12) and (5.13). The results are shown in Figure 5.15.

Figure 5.15 shows that σ' and σ'' data are well described by CTRW model at high frequencies. At low frequencies, the electrode polarization effect dominates the dielectric behavior to give the upturn/peak of σ'' , as shown in Figure 5.15, that deviate from CTRW curves. From CTRW fitting, the dc-conductivity (σ_0) and electrical relaxation time (τ_e) can be obtained.

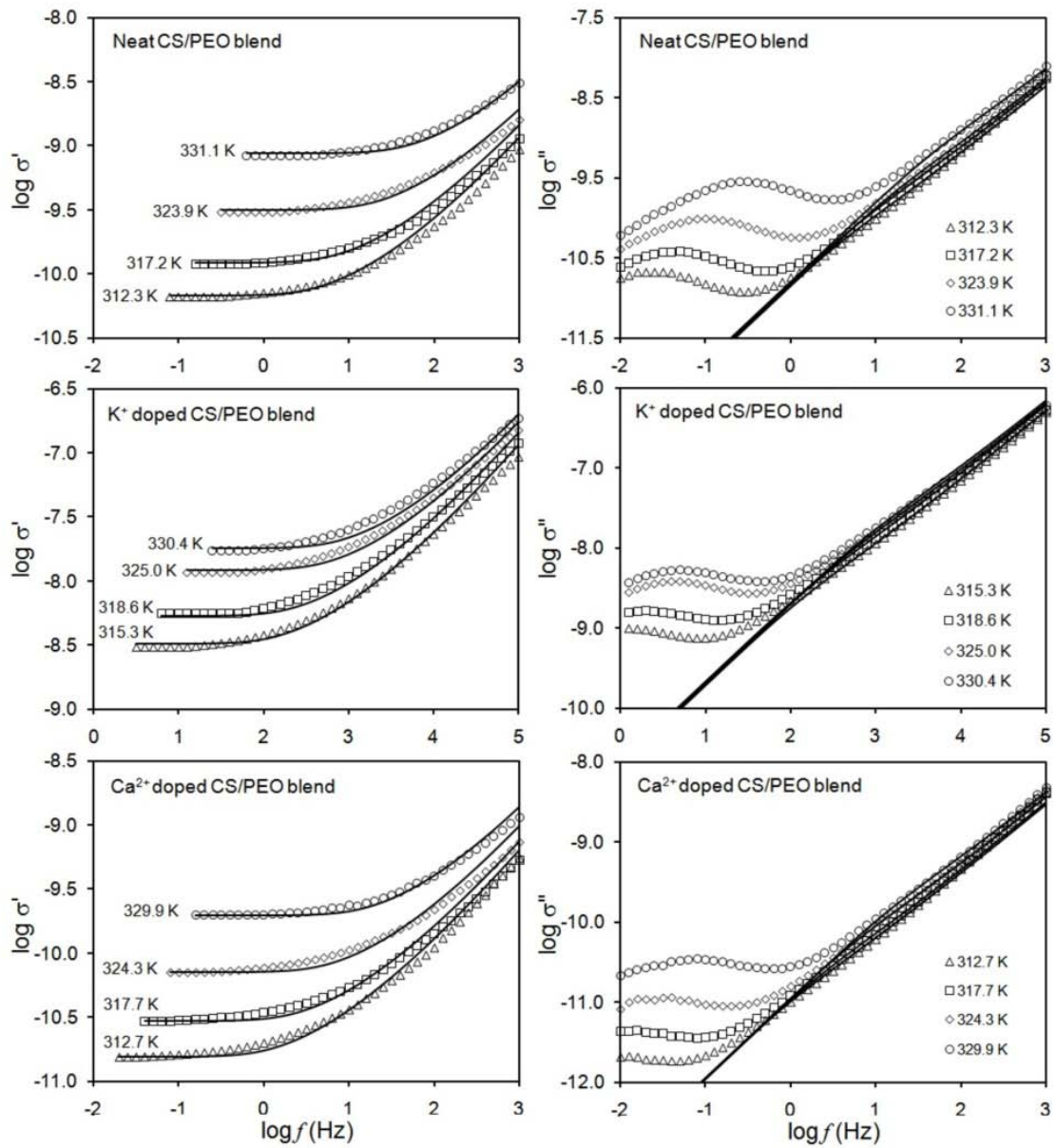


Figure 5.15 Real (σ') and imaginary (σ'') parts of complex conductivity for neat CS/PEO blend ($w_{\text{PEO}} = 0.2$) with/without doped K⁺ and Ca²⁺ at indicated temperatures. The solid lines are fits of Eqs. (5.12) and (5.13) to the data.

Figure 5.16 shows plots of the normalized conductivity $\sigma'(\omega)/\sigma_0$ against the normalized frequency $\omega\tau_e$, good superposition seen here confirms Barton-Nakajima-Namikawa (BNN) relationship (Dyre *et al.*, 2000). Furthermore, in Figure 5.17, the

BNN plots of $\log \sigma_0$ versus $\log (1/\tau_e)$ show good correlation between ac- and dc-conductivity that are based on the same mechanism of charge transport. Thus, BNN relation is fulfilled by CTRW model, suggesting that the frequency- and temperature-dependence of the conductivity are determined by the weakest link (the bottleneck) in the conductive path, irrespective of the nature of charge carriers in the systems.

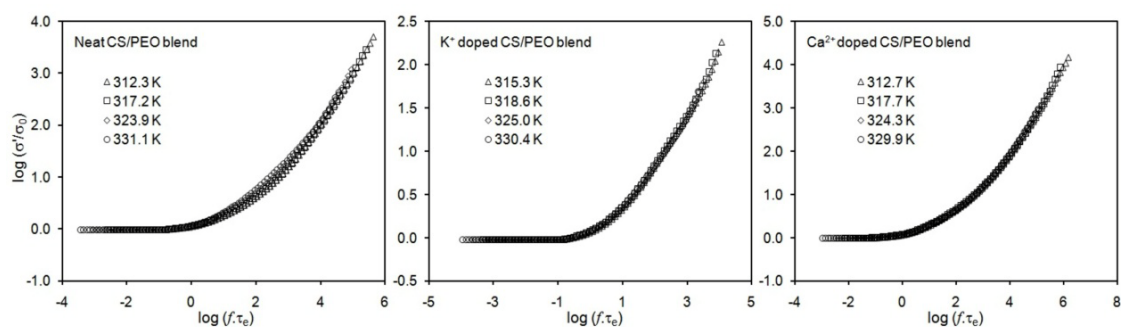


Figure 5.16 Ac conductivity master plots at different temperatures for CS/PEO blend ($w_{\text{PEO}} = 0.2$) with/without doped K^+ and Ca^{2+} .

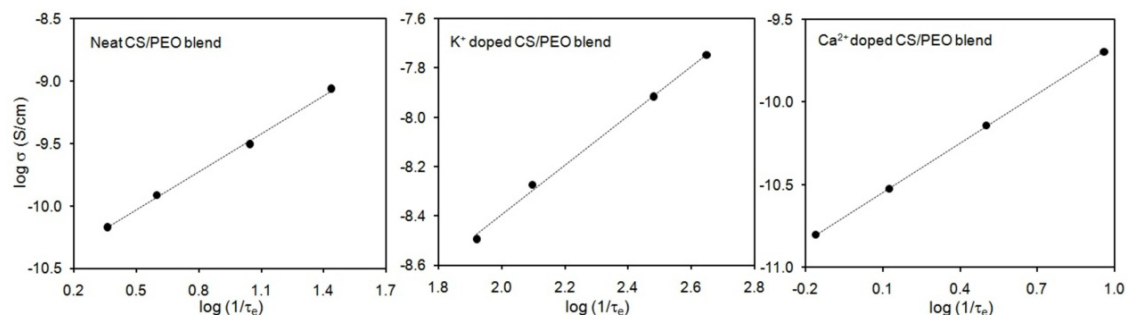


Figure 5.17 BNN plots: $\log \sigma_0$ vs. $\log (1/\tau_e)$ for CS/PEO blend ($w_{\text{PEO}} = 0.2$) with/without doped K^+ and Ca^{2+} .

Activation Energy for Ionic Conduction Process

Dielectric data for all systems were well described by CTRW model assuming the conductivity is due to the charge carriers hopping in polymer matrix with a variety of energetic barriers. The variation of $1/\tau_e$, ω_c and σ_0 with temperature is shown in

Figure 5.18 clearly $1/\tau_e$, ω_c and σ_0 exhibit a simple Arrhenius type of temperature dependence,

$$1/\tau_e, \omega_c, \sigma_0 = A \exp(-E_a / RT) \quad (5.14)$$

where A is the pre-exponential factor, E_a is the activation energy, and R is the ideal gas constant. E_a represents the bottleneck and/or the largest barrier for hopping of ions in the matrix. The activation energy E_a for hopping of ions in the CS/PEO blend matrix were estimated from slope of the plots and listed in Table 5.5.

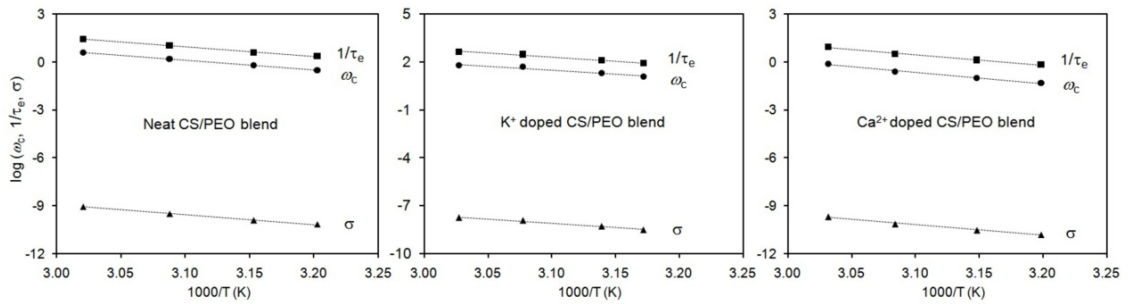


Figure 5.18 Arrhenius plots for CS/PEO blend ($w_{\text{PEO}} = 0.2$) with/without doped K^+ and Ca^{2+} ; ω_c evaluated from the maximum in $\partial^2 \sigma' / \partial \omega^2$, while σ_0 and τ_e obtained from the fitting with Eqs. (5.12) and (5.13).

Table 5.5 Activation energy (kJ/mol) evaluated from Arrhenius plots for CS/PEO blend ($w_{\text{PEO}} = 0.2$) with/without doped K^+ and Ca^{2+} .

CS/PEO blend ($w_{\text{PEO}} = 0.2$)	Activation Energy (kJ/mol)			
	$1/\tau_e$	ω_c	σ_0	Average
Neat blend	50.2	50.4	51.0	50.5
K^+ doped	42.9	41.7	43.2	42.6
Ca^{2+} doped	55.0	58.9	54.6	56.1

Table 5.5 clearly seen that E_a for ion hopping appeared to increase in the order of K^+ -doped < neat blend (for H^+) < Ca^{2+} -doped, which possibly reflects the order of the strength of the interaction between metal ions and polymer matrix.

For neat CS/PEO blends, E_a is mainly due to the energy barrier for H^+ hopping remained from casting solvent, acetic acid. According to the weakest interaction between K^+ and polymers, K^+ -doped system provides the lowest E_a mainly attributes to the energy barrier for K^+ hopping in CS/PEO blend. Conversely for Ca^{2+} -doped system, Ca^{2+} cannot diffuse due to the stronger interaction between Ca^{2+} and polymers. Accordingly, Ca^{2+} should act like a transient crosslinking center and are possibly attached to the chelation structure between CS and PEO, thereby retarding the polymer chain motion. For that reason, the E_a for Ca^{2+} -doped system does not seem to reflect the barrier for hopping of the immobilized Ca^{2+} but mainly attributed to the barrier for hopping of the remaining H^+ in the CS/PEO matrix. The increase of E_a on addition of Ca^{2+} to the neat blend suggests a chelation network formation of CS/ Ca^{2+} /PEO which suppresses the polymer-aided H^+ motion. These results agree well with the conductivity (σ) evaluated from the impedance data (shown in Figure 5.13) reflecting the ion motion as previously discussed.

5.3.2 Computational Section

Molecular Modeling of CS/PEO Blends: Despite the above-mentioned experimental studies, miscibility of CS/PEO blends still remains elusive. With an ever-growing computational power and resource, molecular simulations have played increasingly important role in material modeling and subsequent technology development, as they can reveal microscopic pictures of underlying mechanisms that

are experimentally inaccessible or difficult to obtain. The simulation techniques employed to study the miscibility of CS/PEO blends with different compositions (w_{PEO} of 0.2, 0.4, 0.6, and 0.8) consist of two parts: (1) the molecular dynamic (MD) simulation, (2) the mesoscopic dynamic (MesoDyn) simulation. The bridge connecting them is the Flory-Huggins interaction parameter (χ). MD simulation is used to study bulk properties, which is difficult to do experimentally. Since the length scale in MD simulation is not possible to detect the phase separation in blends, it is necessary to combine MD with MesoDyn method to study the phase morphology of CS/PEO blends.

5.3.2.1 Molecular Dynamic Simulation of CS/PEO Blends

The simulation results (CED and δ) of CS, PEO as well as CS/PEO blends with different compositions (w_{PEO}) are summarized in Table 5.6.

Table 5.6 Atomistic simulation details and results of CS/PEO blends.

Composition w_{PEO}	Number of repeat unit		Density* (g/cm ³)	CED (cal/cm ³)	Solubility Parameter
	CS	PEO			
0.0	40	0	0.670	104 ± 0.02	10.2 ± 0.1
0.2	32	29	0.760	119 ± 0.02	10.9 ± 0.1
0.4	24	58	0.851	113 ± 0.02	10.6 ± 0.1
0.6	16	88	0.943	98 ± 0.02	9.8 ± 0.1
0.8	8	117	1.034	79 ± 0.03	8.9 ± 0.2
1.0	0	146	1.125	109 ± 0.02	10.4 ± 0.1

* Initial densities of CS/PEO blends were calculated from the density of individual polymer and the volume fraction of each polymer component.

To study the miscibility between CS and PEO, Flory-Huggins interaction parameter (χ) was calculated by (Case *et al.*, 1994; Flory, 1953)

$$\chi = \frac{z\Delta E_{mix}}{RT} \quad (5.15)$$

where z is a coordination number (= 6 taken from cubic lattice), R is the molar gas constant (cal/mol), and T is the absolute temperature (in K) at which simulation was performed. The energy of mixing, ΔE_{mix} , needed to compute χ was calculated as (Case *et al.*, 1994)

$$\Delta E_{mix} = \phi_A CED_{pureA} + \phi_B CED_{pureB} - CED_{mix} \quad (5.16)$$

where ϕ is volume fraction and $CED = E_{coh}/V$ (Table 5.6), with subscripts A , B , and mix standing for CS, PEO, and their blends, respectively. From theory, the critical value of χ can be found as

$$\chi_{critical} = \frac{1}{2} \left(\frac{1}{\sqrt{m_A}} + \frac{1}{\sqrt{m_B}} \right)^2 \quad (5.17)$$

where m_A and m_B represent the degree of polymerization (actual number of repeating units) of A and B . In general, blends are miscible if $\chi < \chi_{critical}$. If χ is considerably greater than $\chi_{critical}$, the component polymers are totally immiscible. If χ is slightly greater than $\chi_{critical}$, the blends are partially miscible, in which each phase contains both components. Since the measured χ and the corresponding critical values are calculated on the basis of the same reference volume, comparison of the measured χ with critical values would provide a good indication about the degree of miscibility of the blend (Krause, 1978).

Figure 5.19 shows Flory-Huggins interaction parameters (χ) and the critical values ($\chi_{critical}$) plotted as a function of PEO weight fraction (w_{PEO}) in blends. Comparing the calculated χ with $\chi_{critical}$, can be note that the CS and PEO are miscible only for $w_{PEO} < 0.58$. Moreover, the miscibility between CS and PEO increases (χ decreases) with increase of CS content. The highest magnitude of miscibility is observed for the blend with 1:1 stoichiometric ratio of CS and PEO functional group (at $w_{PEO} = 0.2$).

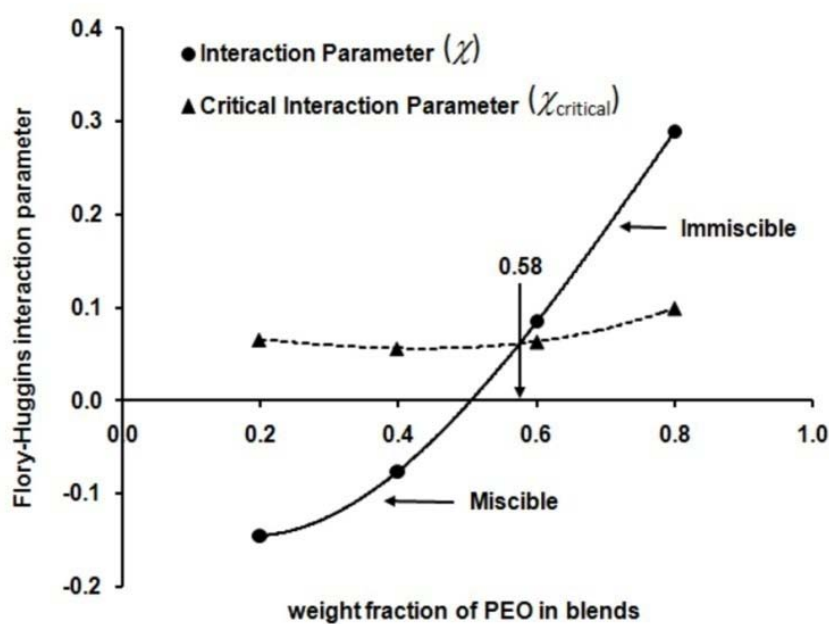


Figure 5.19 Flory-Huggins interaction parameters (χ) as a function of the PEO weight fraction (w_{PEO}) in CS/PEO blends.

Enthalpy of mixing, (ΔH_m) is another important parameter characterizing the magnitude of miscibility of the blend. It can be calculated as

$$\Delta H_m = \chi RT \phi_A \phi_B \quad (5.18)$$

where χ and T were taken from MD simulation. The plot of ΔH_m as a function of w_{PEO} is shown in Figure 5.20. Only for the blends with w_{PEO} of 0.2 and 0.4 give $\Delta H_m < 0$, clearly indicating that the miscibility occurs only for the blend which PEO is a minor component and the miscibility significantly increases with CS content.

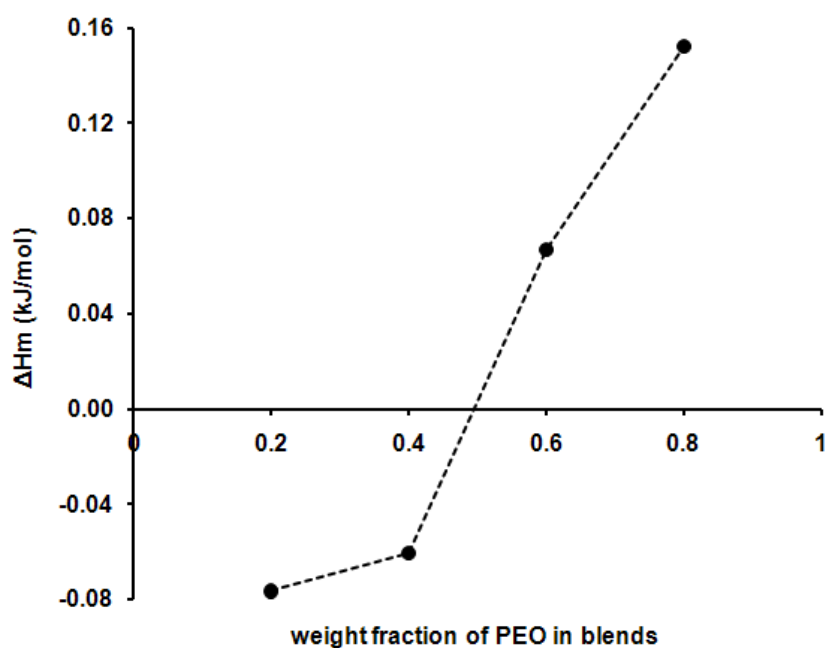


Figure 5.20 Change in the enthalpy of mixing (ΔH_m) as a function of PEO weight fraction (w_{PEO}) in CS/PEO blends.

In MD simulation, the total energy (E_T) of the system is considered as a sum of bonding and nonbonding interactions given by

$$E_T = E_b + E_\theta + E_\phi + E_{oop} + E_{vdw} + E_q \quad (5.19)$$

In Eq. (5.19), the first four terms represent the bonded interactions, which correspond to energies associated with bond stretching (E_b), bond angle bending (E_θ), torsion angle rotations (E_ϕ), and out of loop (E_{oop}). The last two terms represent nonbonded interactions, which consist of van der Waals term (E_{vdw}) and electrostatic term (E_q). E_{vdw} is invariably described by Lennard-Jones 6-12 potential, whereas E_q is calculated from partial charges of atoms in the system estimated by charge equilibration method (Rappe *et al.*, 1991). Electrostatic interaction was calculated according to Ewald summation method (Ewald, 1921), that enables accurate calculation of long-range interactions. Minimization was done in the refinement option automatically during the cell construction. Subsequent minimization after cell construction gives miscibility (which was fairly insensitive to this option).

Table 5.7 Energy components for CS/PEO Blends.

Composition w_{PEO}	Energy (kcal/mol)					
	E_b	E_θ	E_ϕ	E_{oop}	E_{vdw}	E_q
0.0	367.57	684.96	-1175.75	0.00	-11.36	2346.68
0.2	328.82	695.46	-1064.48	0.00	-140.60	1488.87
0.4	324.12	714.56	-987.45	0.00	-228.84	1649.78
0.6	321.46	666.30	-880.39	0.00	-298.64	1320.97
0.8	295.65	711.13	-812.11	0.00	-288.20	1014.05
1.0	294.56	707.22	-675.43	0.00	-432.98	630.44

The simulation energies, calculated by Eq. (5.19), for the systems of pure polymers and blends are summarized in Table 5.7. The E_ϕ , E_{vdw} and E_q terms appear to largely contribute to the miscibility of the CS and PEO.

Pair correlation function $g(r)$ is probability of an atom located at a distance r from the reference atom at the origin. This concept also embraces the idea that the atom at the origin and the atom at distance r may be of different chemical species, A and B . The resulting function is given by the symbol, $g_{AB}(r)$, referred to as the radial distribution function (RDF), which can be calculated by the average of static relationship of every given pair of particles as follows:

$$g_{AB}(r) = \frac{\langle n_{AB}(r) \rangle}{4\pi r^2 \Delta\rho_{AB}} \quad (5.20)$$

where $\langle n_{AB}(r) \rangle$ is average number of A - B atom pairs between distance r and $r + \Delta r$ and ρ_{AB} is density of atom pairs of type AB . The total pair distribution function, $g(r)$, gives a measure of spatial organization of atoms about the central atom. RDF was calculated for various pairs of atoms in molecules, since it gives an insight how the atoms pack in an amorphous structure. The $g(r)$ peaks indicate the presence of definite correlation between atoms within that radius. In particular, the peaks observed at $r < 4$ Å are assigned to a specific distance of the closely coupled atoms. In contrast, the absence of any peaks beyond 4 Å distance indicates that there is no long-range interaction in the systems. At longer distances, $g(r)$ approaches the unity (for an amorphous system).

There are some literatures reporting that the miscibility of CS and PEO might be attributed to the hydrogen bond formation. However, the experimental information was not enough to know which functional groups of CS (NH_2 , C3-OH or C6-OH) are

responsible to interact with the PEO ether group (-O-). The $g(r)$ between O atom of C3-OH and C6-OH groups and N atom of NH₂ groups of CS with -O- atom of PEO are analyzed and displayed in Figure 5.21.

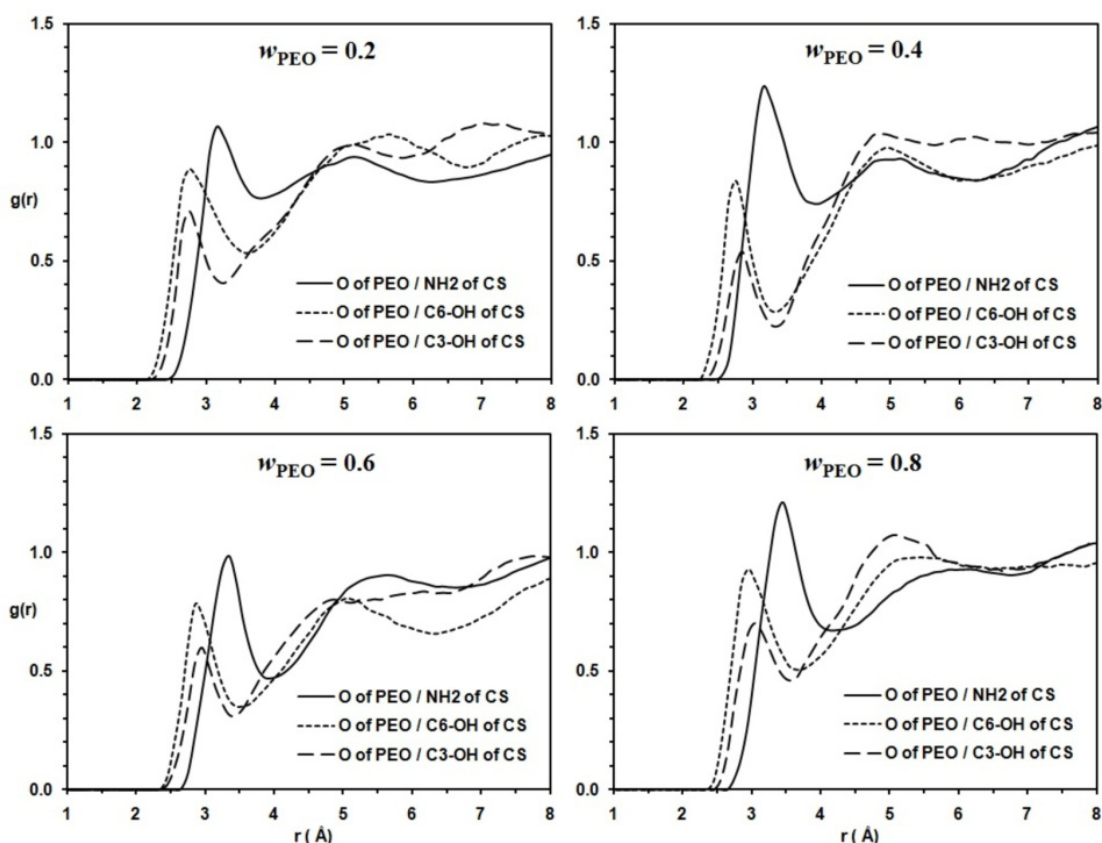


Figure 5.21 Radial distribution functions (RDFs) of the CS/PEO blends with different PEO weight fraction (w_{PEO}).

It is clearly indicated that all CS functional groups (NH₂, C3-OH and C6-OH) interact with PEO ether groups for the whole compositions. Among all CS functional groups, NH₂ has the highest activity to interact with PEO ether groups as indicated by a large height of the first RDF peaks observed at $r < 4 \text{ \AA}$. Although the radial distances of C3-OH and C6-OH groups in the vicinity of PEO ether groups are shorter than those of NH₂ groups (cf. Table 5.8), suggesting a weaker interaction between

NH₂ groups and PEO ether oxygens. The longer radial distance of NH₂ groups is mainly attributed to a larger steric effect from two hydrogen atoms connecting to nitrogen, resulting in larger distances available to interact with PEO ether groups.

Table 5.8 Correlation between FTIR data and the radial distance (r) from radial distribution functions (RDFs) analysis of CS/PEO blends.

w_{PEO}	Vibrations Assignment of FTIR spectra (cm ⁻¹)			Radial distance (r) from RDF analysis (Å)		
	PEO	CS		O of PEO	O of PEO	O of PEO
	C-O-C stretching	NH stretching	OH stretching	NH ₂ of CS	C3-OH of CS	C6-OH of CS
0.0	-	1568	3429	-	-	-
0.2	1097	1555	3385	3.15	2.75	2.75
0.4	1103	1558	3402	3.15	2.75	2.85
0.6	1101	1558	3410	3.35	2.85	2.95
0.8	1101	1560	3408	3.45	2.95	3.05
1.0	1111	-	-	-	-	-

Focusing, more closely, on their difference between C3-OH groups and C6-OH groups of CS, the radial distance (r) of C6-OH groups are slightly shorter and the $g(r)$ peaks are rather higher and broader than those of C3-OH groups at all compositions. This observation indicates a significant contribution of C6-OH groups to interact with PEO ether groups. Hence, C6-OH groups have more tendencies to interact with PEO ether groups.

In addition, for all CS functional groups, an increase of PEO component in blends affects a slightly larger of radial distance and this change is more significant for the blends with $w_{\text{PEO}} > 0.4$ as summarized in Table 5.8. This observation suggests a decrease of interaction between CS and PEO with an increase of PEO component

and a tendency of phase separation for the blends with high PEO content ($w_{\text{PEO}} > 0.4$). This observation thoroughly agrees well with FTIR result discussed previously and confirmed the reliability of MD simulations for evaluation of the miscibility of CS/PEO blends.

5.3.2.2 Mesoscopic Dynamics Simulation of CS/PEO Blends

As a further proof, Mesoscopic Dynamics (MesoDyn) simulation (Fraaije, 1993; Fraaije *et al.*, 1997) was employed to simulate the phase separation dynamics of CS/PEO blends.

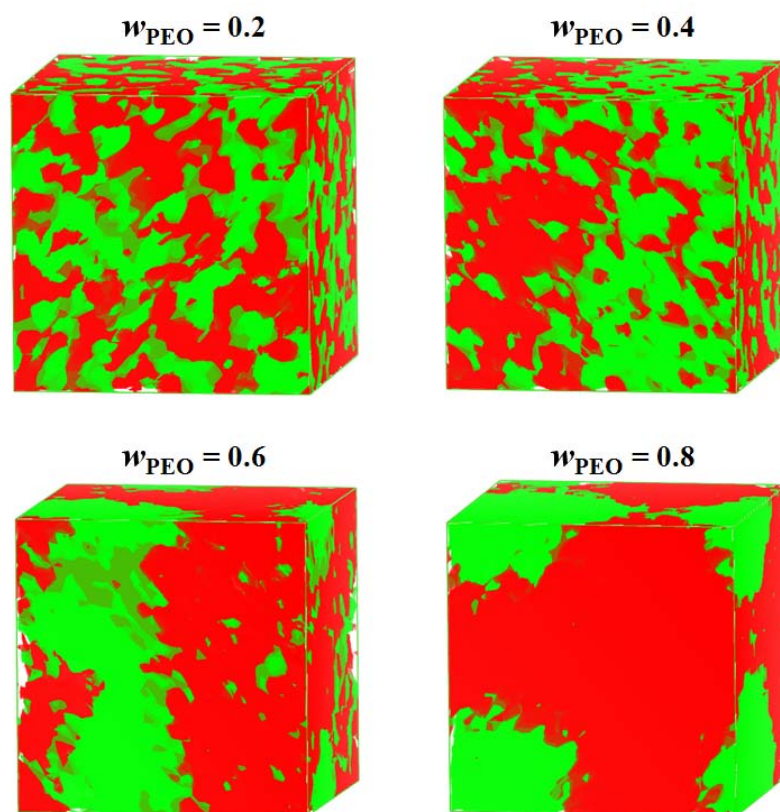


Figure 5.22 Iso-density profiles for CS/PEO blends with different PEO weight fractions (w_{PEO}). Green (light) and red (dark) color represent CS and PEO component, respectively.

Figure 5.22 displays mesoscopic simulation results of CS/PEO blends with different compositions. The iso-density profiles clearly show a transition in the phase morphology. The phase separation tends to proceed with increasing PEO content and the phase transition (from completely miscible to microphase isolation) may occur in the range of w_{PEO} between 0.4-0.6. This result agrees well with MD simulation that CS/PEO blends are completely miscible only for low w_{PEO} .

Order Parameter (P_i) defined as the volume average of the difference between local density squared and the overall density squared, is given by the following integral:

$$P_i = \frac{1}{V} \int_V [\eta_i^2(r) - \eta_i^2] dr \quad (5.21)$$

where η_i is dimensionless average density (volume fraction) for species, i . The larger value of P_i indicates the stronger tendency of phase separation. When P_i values exceed 0.1, macrophase separation is judged to occur.

Figure 5.23 shows the order parameters (P_i) considered in both CS and PEO portion as a function of w_{PEO} . The $P_{\text{CS}} < P_{\text{PEO}} < 0.1$, suggesting no strong macrophase separation occurring for entire compositions of CS/PEO blends. The P_{PEO} values increase with increase of PEO content in blends and a microphase segregation can be observed in the PEO-rich phase. The strongest heterogeneity is found at $w_{\text{PEO}} = 0.8$. In Figure 5.23, P_{CS} values are very low and quite constant at all blend compositions, whereas P_{PEO} values are largely decreased with increase of CS content. This phenomenon is agreed well with an assumption that CS is fully amorphous polymer therefore adding PEO into CS has not much effect in the order arrangement of CS portion. Conversely, addition of CS into the semicrystalline polymer, PEO, shows

significant decrease of the order arrangement of PEO portion. Compared with CS, the PEO monomeric unit is smaller and PEO chain is more flexible due to free flip of ether oxygen bond. The presence of an intra-molecular interaction of PEO-PEO occurring via ether oxygen possibly results in a larger order of PEO portion. In the blends with large CS content, the interaction of CS-PEO is rather stronger than PEO-PEO interaction and possibly results in a decrease of PEO order parameters with an increase of CS content.

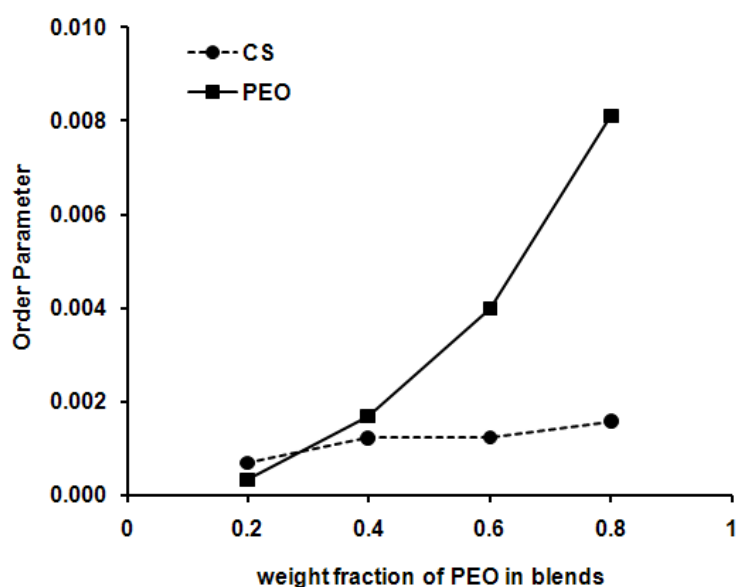


Figure 5.23 Mesophase order parameters (P_i) of both CS and PEO portion as a function of the PEO weight fractions (w_{PEO}) in the CS/PEO blends.

5.3.2.3 Molecular Dynamics Simulation of Ion Doped CS/PEO Blend

Molecular dynamics (MD) simulations of CS/PEO blend were carried out to investigate the molecular picture of CS/PEO blends and their complex with metal ions. In the simulation, the CS hydroxyl groups were separated into C3-OH and

C6-OH for the radial distribution function (RDF) analysis. Miscibility between CS and PEO was mainly attributed to CS functional groups: amino (NH_2), hydroxyl (C3-OH) and hydroxymethyl (C6-OH), interacting with the PEO ether groups (-O-). Among all CS functional groups, NH_2 had the highest tendency to interact with PEO ether groups, although the interaction was rather weaker than those of C3-OH and C6-OH groups.

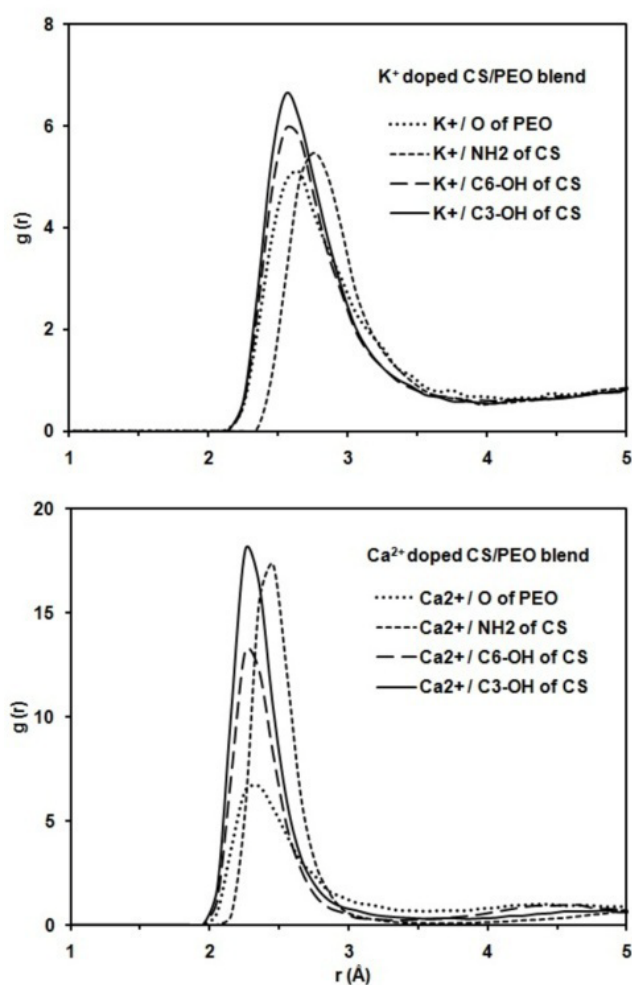


Figure 5.24 Radial distribution functions (RDFs) for the system of K^+ - and Ca^{2+} -doped CS/PEO blends with $w_{\text{PEO}} = 0.2$. RDF represents the relative distances between metal ions (K^+ and Ca^{2+}) and N atom in amino (NH_2) group, O atom in hydroxyl (C3-OH) and hydroxymethyl (C6-OH) groups of CS as well as PEO ether oxygen atom.

The interaction between CS and PEO in cation-doped blends was also investigated. RDFs were analyzed in the interval where MD simulation gave a stable behavior. Figure 5.24 displays total pair correlation $g(r)$ as a function of radial distance (r) for K^+ - and Ca^{2+} -doped blends at $w_{PEO} = 0.2$. $g(r)$ peaks seen at $r = 2.3$ - 2.9 Å indicate the presence of definite correlation between atoms and are correlated with the specific distance of closely coupled atoms. An absence of peaks at $r > 4$ Å indicates that there is no long-range correlation in the systems.

The coordination number (CN) stands for the number of CS or PEO functional groups located around the probed ions (K^+ and Ca^{2+}). $g(r)$ data obtained from simulation were utilized to evaluate CN through integration up to the first minimum distance r_{min} (Bujnicka *et al.*, 2006):

$$CN = 4\pi \frac{N}{V} \int_0^{r_{min}} g(r)r^2 dr \quad (5.22)$$

Here, N is the total number of corresponding functional group and V is the volume of simulation box. N/V denotes the number density of solvation component. CN and radial distance (r) of functional groups in the first coordination shell of K^+ and Ca^{2+} , both obtained from MD simulations, are listed in Table 5.9.

The results shown in Table 5.9 suggest that NH_2 , C3-OH and C6-OH of CS as well as PEO ether groups are responsible for the interaction between CS and PEO. These groups are also located within the first solvation shell of the cations in mixed salt systems. The radial distances of all functional groups in the first coordination shell are shorter whereas CN are larger for Ca^{2+} -doped than K^+ -doped system. As judged from these results, the number of active sites available for the interaction with polymers functional groups is possibly larger for bivalent metal ion (Ca^{2+}) and more

stable CS/Ca²⁺/PEO complex was formed accordingly. Both Ca²⁺ and K⁺ seem to interact more strongly with CS than with PEO because CS has a larger number of interacting functional groups.

Table 5.9 Coordination number (*CN*) and radial distance (*r*) of CS and PEO functional groups in the first coordination shell of K⁺ and Ca²⁺.

Metal ions	Vicinity functional groups	<i>r</i> (Å)	<i>CN</i>
K ⁺	O of PEO	2.77	1.2
	NH ₂ of CS	2.84	1.3
	C3-OH of CS	2.68	1.5
	C6-OH of CS	2.69	1.3
Ca ²⁺	O of PEO	2.43	1.2
	NH ₂ of CS	2.46	1.8
	C3-OH of CS	2.33	1.9
	C6-OH of CS	2.34	1.4

The radial distances and CN of C3-OH and C6-OH groups in the vicinity of K⁺ and Ca²⁺ are shorter and smaller than those of NH₂ groups, suggesting a stronger interaction between OH groups and metal ions compared to that between NH₂ groups and ions. The longer radial distance of NH₂ groups is mainly attributed to larger steric effect from two hydrogen atoms connected to nitrogen. The distance of the first peak in *g(r)* for C3-OH groups are slightly shorter whereas *CN* is larger than those of C6-OH groups for both cases of K⁺ and Ca²⁺ doping. Thus, the C3-OH group appears to interact with these metal ions more significantly compared to C6-OH group. This difference may be attributed to the fact that the C3-OH and NH₂ groups are located at the same side of the pyranose ring while C6-OH groups are at the other side. This

configuration possibly allows the metal ions to interact with both of C3-OH and NH₂ groups more easily compared to the interaction with C6-OH groups. C6-OH groups seem to prefer to interact with PEO ether oxygen more than C3-OH groups. Therefore, C6-OH groups are less likely to form the complex with metal ions.

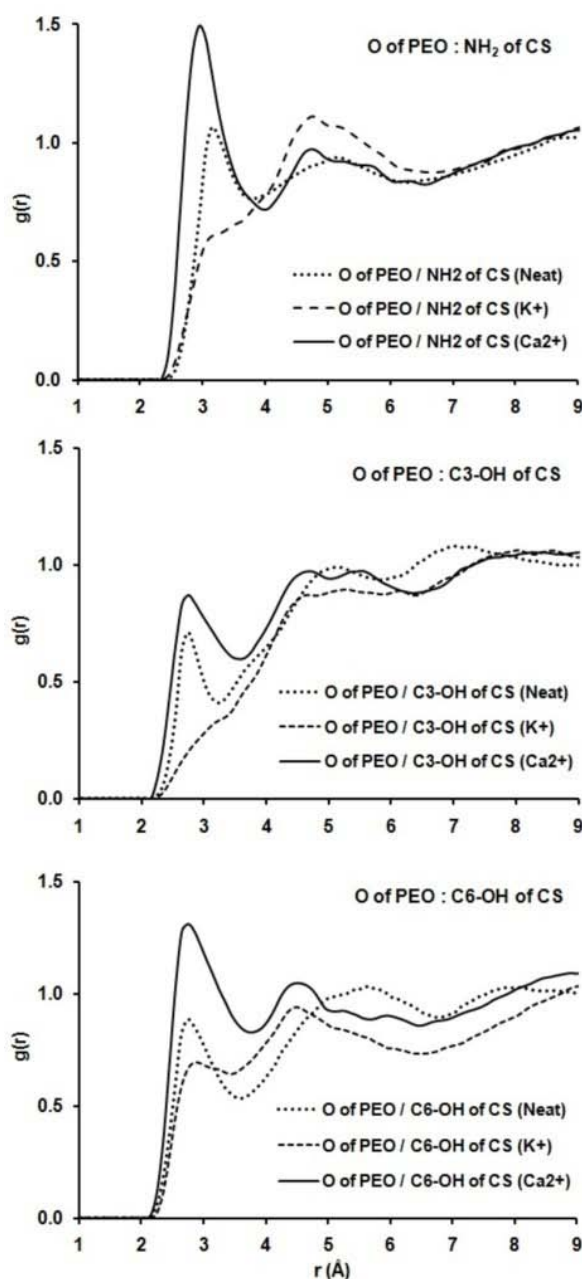


Figure 5.25 Radial distribution functions (RDFs) for undoped CS/PEO blends at $w_{\text{PEO}} = 0.2$ and for CS/K⁺/PEO and CS/Ca²⁺/PEO blends.

Figure 5.25 displays RDFs evaluated from NVT simulation at 298 K for neat CS/PEO blends in comparison with K^+ - and Ca^{2+} -doped systems. The correlation between PEO ether groups with C3-OH, C6-OH and NH_2 groups of CS are larger in the presence of Ca^{2+} . Ca^{2+} appears to enhance the interaction between PEO ether groups and all CS functional groups, as suggested from a slight decrease in radial distances of these groups (in particular of NH_2 group) compared to those in neat blend. This result offers a comprehensive picture of CS/ Ca^{2+} /PEO complex. Due to stronger interaction between Ca^{2+} and polymers, Ca^{2+} should act as a transient cross-linker to enlarge the interaction of all neighborhood CS and PEO functional groups and enhance the correlation of all these groups. In contrast, K^+ weakens the correlation between PEO ether groups and all CS functional groups compared to that in the neat blend. This observation reflects an insignificant and unstable complex formation for CS/ K^+ /PEO. As a result, K^+ appears to interact separately with CS and/or PEO functional groups.

Dynamic characteristics of K^+ and Ca^{2+} in CS/PEO matrix were also studied by MD simulation. Snapshots of Ca^{2+} doped system clearly indicated that Ca^{2+} cannot diffuse even at very high simulation temperature ($T = 800$ K). In contrast, K^+ was found to diffuse freely through hopping mechanism within CS/PEO matrix with the estimated diffusion coefficient of 1.70×10^{-6} cm^2/s . These results reflect a weaker interaction between K^+ with CS and PEO.

5.4 Concluding Remark

CS/PEO blends show partial/full miscibility, as characterized by depression of PEO melting temperature (T_m) in a series of neat CS/PEO blends. DSC data gave a

negative interaction parameter for CS and PEO blends, $\chi_{\text{CS-PEO}} = -0.21$, that imply an attractive interaction between CS and PEO. Correspondingly, CS tends to suppress the crystallization of PEO chain, as suggested by DSC and WAXD. The highest magnitude of miscibility was obtained at $w_{\text{PEO}} = 0.2$ that corresponded to the stoichiometric 1:1 molar interaction between the PEO ether oxygen with amino and hydroxyl groups of CS noted from the FTIR spectra.

Crystallinity (X_c^m) and T_m^e of PEO decrease and thermal degradation temperature (T_d) of CS increase when Ca^{2+} and K^+ were doped into CS/PEO blends. Decrease in T_m^e and X_c^m are more significant for high CS content. Therefore ions favorably interact with the PEO ether groups and this interaction is cooperatively enhanced in the presence of CS. Metal ions specifically interact with the amino and hydroxyl groups of CS as well as PEO ether groups, as revealed from FTIR spectra. Ca^{2+} seem to behave as a transient cross-linker to form the stable CS/ Ca^{2+} /PEO complex. On the other hand, there was less significant interaction between K^+ and polymers.

Dielectric permittivity and conductivity reflecting the motion of metal ions as well as H^+ ion (from the remaining casting solvent, acetic acid) are increased in the order of K^+ -doped > neat blends > Ca^{2+} -doped. This behavior should be related to the chelation network structure of CS/ Ca^{2+} /PEO that retards polymer chain motion and associating H^+ motion. Accordingly, Ca^{2+} acts as a transient crosslinking center and it is possibly attached within the chelation structure of CS and PEO. The conductivity in each series of blends is the highest at $w_{\text{PEO}} = 0.2$ (stoichiometric 1:1 ratio of CS and PEO active functional groups), which possibly reflected the strongest CS-PEO interaction and the weakest ion binding at this content. The ionic conductivity is due

to the hopping of charge carriers. The energy barrier for ion hopping increase in order of K^+ -doped < neat blend (containing H^+) < Ca^{2+} -doped. Larger energy barrier on addition of Ca^{2+} to the blend confirms the occurring of chelation network formation of CS/ Ca^{2+} /PEO which have suppressed the polymer-aided H^+ motion.

The miscibility of CS/PEO blends was investigated by both atomistic molecular dynamics (MD) and mesoscopic dynamics (MesoDyn) simulations. Flory-Huggins interaction parameters (χ_{CS-PEO}) determined from cohesive energy densities suggests that CS/PEO blends are miscible only for the system with $w_{PEO} < 0.58$. The miscibility increases with CS content and the highest magnitude of miscibility is observed at $w_{PEO} = 0.2$. Radial distribution functions (RDFs) for CS/PEO blends suggest the interaction between CS and PEO is attributed to PEO ether groups and all functional groups (NH_2 , C3-OH and C6-OH) of CS. These results are correlated well with FTIR data. However, the interactions attribute to C3-OH and C6-OH groups seem stronger than that of NH_2 groups. Compared to C3-OH groups, C6-OH groups have ability to interact with the PEO ether groups. Phase behavior in CS/PEO blends was also investigated by MesoDyn technique. The iso-density profiles confirm that phase separation tends to increase with increasing PEO content and the miscible blend was observed only at $w_{PEO} < 0.6$ that agrees well with MD simulation.

MD simulations was also used to examine the structure of metal ions doped CS/PEO blends to see the correlation between dynamic behavior and the interaction between ions and polymers in CS/PEO blend. At the simulated temperature of 800 K, Ca^{2+} could not diffuse but are only involved in the chelation structure between CS and PEO, which is in harmony with the result from FTIR spectra. In contrast, K^+ was found to diffuse freely in CS/PEO blend matrix.

CHAPTER VI

SUMMARY

According to the disadvantage properties of pristine CS are frequently not good enough to meet those wide ranges of its applications and limited its uses. One uncomplicated and effective method to overcome these limitations is adding of a second component (filler or second polymer); therefore to create a new CS-based material with the target properties appropriated for specific applications is the gold of this work. Accordingly, the CS/MMT Nanocomposites, suitable for drug controlled release application, and CS/PEO Blends, suitable for used as a solid polymer electrolyte, were initiated and developed in this study. The structure, morphology, thermal property of these CS-based materials along with drug controlled release efficiency of CS/MMT nanocomposites and ionic conductive efficiency of CS/PEO blends were studied. The theoretical modeling and molecular simulation were also employed to fulfill the experimental findings and gain a comprehensive understanding in atomistic level of these materials. Overall of this research can be summarized and established below.

CS/MMT nanocomposites with different intercalation structures of CS into MMT gallery were prepared and proposed to apply as a drug controlled release material. Accordingly, salicylic acid (SA) and theophylline (THP) were incorporated as the representative models of acidic and basic drug, respectively. The experimental data reveal that the SA-CS interaction occurring at amino groups of CS, resulting in

chitosonium salicylate ($-\text{NH}_3^+\text{SA}^-$) formation, whereas no THP-CS interaction occurring. Therefore, the application of CS/MMT nanocomposite as a controlled release material is limited for using in only acidic drug. Both mono- and bi-layer intercalation structure of CS into MMT interlayer can be observed in the SA/CS/MMT nanocomposites. However, only the bilayer nanocomposite presents the gradual release behavior, associated to the existence of excess $-\text{NH}_3^+$ ($-\text{NH}_3^+ > \text{CEC}$ of clay) that will be balanced and interact electrostatically with the salicylate anions (SA^-). The presence of $-\text{NH}_3^+\text{SA}^-$ species turns this material into a potential to develop the acidic drug controlled release material that MMT particle acts as a barrier and also an implantable drug reservoir. Conversely, fast release behavior of THP/CS/MMT material was observed, probably because no drug-polymer interaction and the interaction between THP and MMT is rather weak.

Atomistic MD simulations were performed to study the bulk amorphous CS and its complex with SA and THP. The solubility parameters of drugs incorporated CS denote that the CS-SA is miscible but CS-THP is immiscible and tend to phase separate. Due to the weaker interaction between CS-THP, therefore the diffusion coefficient of THP within CS seems to be faster than SA about 4 times; this data agrees well with the experimental observation. The RDFs analysis reveals that the gradual release of SA from CS matrix mainly attributes to the hydrogen bonding formation, accordingly, both amino and hydroxyl groups of CS can form the H-bonds with carboxyl and hydroxyl groups of SA to provide the CS/SA complex. MD simulation was also employed to investigate the intercalation structure of the SA/CS/MMT nanocomposites. The results also agree well with the experimental

finding that the MMT interlayer density is periodically fluctuated depends on the drug-polymer loading amount.

CS/PEO blend was developed for applying as a solid polymer electrolyte. Accordingly, alkali and alkali earth metal ions were utilized as doping ions. The effects of ions doping on the structure/property of the CS/PEO blends were studied intent to discuss a role of the ion valency in the interaction between the metal ions and each polymers component. In this respect, K^+ and Ca^{2+} were selected as the ions due to their similarity in both size and mass ($Z_K = 19$, $M_K = 39$ g/mol; $Z_{Ca} = 20$, $M_{Ca} = 40$ g/mol). CS/PEO blends is partial/full miscible and the highest magnitude of miscibility was obtained at the stoichiometric interaction between the ether oxygen of PEO with amino and hydroxyl groups of CS (at $w_{PEO} = 0.2$). The presence of ions in CS/PEO blends causes in a decrease of cryatallinity and melting temperature of PEO along with an increase of degradation temperature of CS. The difference between Ca^{2+} and K^+ possibly reflects a stronger multi-valence interaction of Ca^{2+} with amino and hydroxyl groups of CS as well as ether groups of PEO. Accordingly, Ca^{2+} acts as a transient crosslinking center and it is possibly attached within the chelation structure of CS and PEO, whereas less significant interaction occurring between K^+ and polymers. Therefore, the CS/ Ca^{2+} /PEO complex formation has suppressed the polymer-aided H^+ motion (from remaining casting solvent, acetic acid), while K^+ was found to diffuse freely within CS/PEO matrix. The conductivity is due to the hopping of charge carriers and the energy barrier for hopping appeared to increase in the order of K^+ -doped < neat blend (containing H^+) < Ca^{2+} -doped, which was possibly affected by the interaction between metal ions and polymer matrix. The conductivity in each series of blends was the highest at the stoichiometric ratio of CS and PEO, which

reflected the strongest CS-PEO interaction and the weakest binding of ions. This can be concluded that the alkali metal ion is more suitable for use as a doping ion in the CS/PEO blend solid polymer electrolyte than the alkali earth metal ion. Additionally, the optimum blend composition that provides the highest ionic conductivity is occurring at the stoichiometric ratio of CS:PEO.

Atomistic MD simulation and MesoDyn simulation were employed to study the miscibility of CS/PEO blends and reported that the CS/PEO blends are miscible only for the system with $w_{\text{PEO}} < 0.58$. The miscibility increases with increase of CS content and the highest magnitude of miscibility was obtained at $w_{\text{PEO}} = 0.2$ and the miscibility is attributed to the interaction between ether groups of PEO and amino/hydroxyl groups of CS. The diffusion behavior of K^+ and Ca^{2+} within CS/PEO blend matrix were also elucidate via MD simulations. At the simulated temperature of 800 K, Ca^{2+} could not diffuse but were involved in the chelation structure of CS and PEO, which was accorded to the stable complex formation of CS/ Ca^{2+} /PEO, in contrast, K^+ was found to diffuse freely in the blend matrix. Accordingly, all simulation data seem to be agreeing well with the experimental inspection.

REFERENCES

REFERENCES

- Abdul-Jawad, S., Alnajjar, A., and Abdallah, M. H. (1997). AC impedance, permittivity and modulus spectroscopy of lead chloride single crystal. **Applied Physics A: Materials Science & Processing**. 64: 199.
- Accelrys. (2007). **Materials studio 4.2**. San Diego.
- Agrawal, S. and Awadhia, A. (2004). DSC and conductivity studies on PVA based proton conducting gel electrolytes. **Bulletin of Materials Science**. 27: 523.
- Aguzzi, C., Capra, P., Bonferoni, C., Cerezo, P., Salcedo, I., Sánchez, R., Caramella, C., and Viseras, C. (2010). Chitosan-silicate biocomposites to be used in modified drug release of 5-aminosalicylic acid (5-ASA). **Applied Clay Science**. 50: 106.
- Ahmad, A. L., Sumathi, S., and Hameed, B. H. (2004). Chitosan: A natural biopolymer for the adsorption of residue oil from oily wastewater. **Adsorption Science & Technology**. 22(1): 75.
- Alexandre, M. and Dubois, P. (2000). Polymer-layered silicate nanocomposites: Preparation, properties and uses of a new class of materials. **Materials Science and Engineering: R: Reports**. 28: 1.
- Alexeev, V. L., Kelberg, E. A., Evmenenko, G. A., and Bronnikov, S. V. (2000). Improvement of the mechanical properties of chitosan films by the addition of poly(ethylene oxide). **Polymer Engineering & Science**. 40: 1211.

- Alger, J. R. and Prestegard, J. H. (1979). Nuclear magnetic resonance study of acetic acid permeation of large unilamellar vesicle membranes. **Biophysical Journal**. 28: 1.
- Ali, A. M. M., Mohamed, N. S., and Arof, A. K. (1998). Polyethylene oxide (PEO)-ammonium sulfate ((NH₄)₂SO₄) complexes and electrochemical cell performance. **Journal of Power Sources**. 74: 135.
- Alvarez-Lorenzo, C. and Concheiro, A. (2004). Molecularly imprinted polymers for drug delivery. **Journal of Chromatography B**. 804: 231.
- An, J. H. and Dultz, S. (2007). Adsorption of tannic acid on chitosan-montmorillonite as a function of pH and surface charge properties. **Applied Clay Science**. 36: 256.
- Andersen, H. C. (1980). Molecular dynamics simulations at constant pressure and/or temperature. **The Journal of Chemical Physics**. 72: 2384.
- Andersen, H. C. (1983). Rattle: A velocity version of the shake algorithm for molecular dynamics calculations. **Journal of Computational Physics**. 52: 24.
- Aranaz, I., Harris, R., and Heras, A. (2010). Chitosan amphiphilic derivatives: Chemistry and applications. **Current Organic Chemistry**. 14: 308.
- Aranda, P. and Ruiz-Hitzky, E. (1992). Poly(ethylene oxide)-silicate intercalation materials. **Chemistry of Materials**. 4: 1395.
- Berendsen, H. J. C., Postma, J. P. M., van Gunsteren, W. F., DiNola, A., and Haak, J. R. (1984). Molecular dynamics with coupling to an external bath. **The Journal of Chemical Physics**. 81: 3684.
- Bhupendra, P. (2009). Chitosan: A marine medical polymer and its lipid lowering capacity. **The Internet Journal of Health**. 9: 25.

- Boonsongrit, Y., Mitrevej, A., and Mueller, B. W. (2006). Chitosan drug binding by ionic interaction. **European Journal of Pharmaceutics and Biopharmaceutics**. 62: 267.
- Bozkurt, A., Meyer, W. H., and Wegner, G. (2003). PAA/imidazol-based proton conducting polymer electrolytes. **Journal of Power Sources**. 123: 126.
- Bujnicka, K. and Hawlicka, E. (2006). Solvation of Ca^{2+} in aqueous methanol-MD simulation studies. **Journal of Molecular Liquids**. 125: 151.
- Buraidah, M. H., Teo, L. P., Majid, S. R., Yahya, R., Taha, R. M., and Arof, A. K. (2010). Characterizations of chitosan-based polymer electrolyte photovoltaic cells. **International Journal of Photoenergy**. 7: 5.
- Case, F. H. and Honeycutt, J. D. (1994). **Trends in Polymer Science**. 2: 259.
- Castro, C., Gargallo, L., Radic, D., Kortaberria, G., and Mondragon, I. (2011). Blends containing chitosan and poly(sodium-4-styrene sulphonate): Compatibility behavior. **Carbohydrate Polymers**. 83: 81.
- CCL.NET. (1996). **Molecular Dynamics and Monte Carlo**. [On-line]. Available: <http://www.ccl.net/cca/documents/molecular-modeling/node9.html>.
- Chang, K. L. B. and Tsai, G. (1997). Response surface optimization and kinetics of isolating chitin from pink shrimp (*Solenocera Melantho*) shell waste. **Journal of Agricultural and Food Chemistry**. 45: 1900.
- Chang, W., Ma, G., Yang, D., Su, D., Song, G., and Nie, J. (2010). Electrospun ultrafine composite fibers from organic-soluble chitosan and poly(ethylene oxide). **Journal of Applied Polymer Science**. 117: 2113.

- Cheung, I. W., Chin, K. B., Greene, E. R., Smart, M. C., Abbrent, S., Greenbaum, S. G., Prakash, G. K. S., and Surampudi, S. (2003). Electrochemical and solid state NMR characterization of composite PEO-based polymer electrolytes. **Electrochimica Acta**. 48: 2149.
- Curtiss, L. A. and Gordon, M. S. (2004). **Computational Materials Chemistry: Methods and Applications**. London, Springer.
- Darder, M., Colilla, M., and Ruiz-Hitzky, E. (2003). Biopolymer-clay nanocomposites based on chitosan intercalated in montmorillonite. **Chemistry of Materials**. 15: 3774.
- Darder, M., Colilla, M., and Ruiz-Hitzky, E. (2005). Chitosan-clay nanocomposites: Application as electrochemical sensors. **Applied Clay Science**. 28: 199.
- Deepak, A. M. and Ashwani, K. (2000). Solvent and pH resistance of surface crosslinked chitosan/poly(acrylonitrile) composite nanofiltration membranes. **Journal of Applied Polymer Science**. 77: 1782.
- Dodane, V. and Vilivalam, V. D. (1998). Pharmaceutical applications of chitosan. **Pharmaceutical Science & Technology Today**. 1: 246.
- Donoso, J. P., Lopes, L. V. S., Pawlicka, A., Fuentes, S., Retuert, P. J., and González, G. (2007). Nuclear magnetic resonance study of PEO-chitosan based polymer electrolytes. **Electrochimica Acta**. 53: 1455.
- Du, J. F., Bai, Y., Pan, D. A., Chu, W. Y., and Qiao, L. J. (2009). Characteristics of proton conducting polymer electrolyte based on chitosan acetate complexed with CH₃COONH₄. **Journal of Polymer Science Part B: Polymer Physics**. 47: 549.

- Ducrotte, P., Dapoigny, M., Bonaz, B., and Siproudhis, L. (2005). Symptomatic efficacy of beidellitic montmorillonite in irritable bowel syndrome: A randomized, controlled trial. **Alimentary Pharmacology & Therapeutics**. 21: 435.
- Dyre, J. C. (1988). The random free-energy barrier model for ac conduction in disordered solids. **Journal of Applied Physics**. 64: 2456.
- Dyre, J. C. and Schrøder, T. B. (2000). Universality of ac conduction in disordered solids. **Reviews of Modern Physics**. 72: 873.
- Eilmes, A. (2003). Segment polarizabilities for microelectrostatic calculations in poly(ethylene oxide). **Chemical Physics Letters**. 382: 258.
- Ewald, P. P. (1921). Die berechnung optischer und elektrostatischer gitterpotentiale. **Annalen der Physik**. 369: 253.
- Fan, C. F., Cagin, T., Chen, Z. M., and Smith, K. A. (1994). Molecular modeling of polycarbonate. 1. force field, static structure, and mechanical properties. **Macromolecules**. 27: 2383.
- Faucher, J. A., Koleske, J. V., Santee, E. R., Stratta, J. J., and Wilson, C. W. (1966). Glass transitions of ethylene oxide polymers. **Journal of Applied Physics**. 37: 3962.
- Florianczyk, Z., Such, K., Wieczorek, W., and Wasiucioneck, M. (1991). Highly conductive poly(ethylene oxide)-poly(methyl methacrylate) blends complexed with alkali metal salts. **Polymer**. 32: 3422.
- Flory, P. J. (1953). **Principles of Polymer Chemistry**. Ithaca, New York, Cornell University Press.
- Flory, P. J. (1989). **Statistical Mechanics of Chain Molecules**. Hanser, Munich.

- Fraaije, J. G. E. M. (1993). Dynamic density functional theory for microphase separation kinetics of block copolymer melts. **The Journal of Chemical Physics**. 99: 9202.
- Fraaije, J. G. E. M., van Vlimmeren, B. A. C., Maurits, N. M., Postma, M., Evers, O. A., Hoffmann, C., Altevogt, P., and Goldbeck-Wood, G. (1997). The dynamic mean-field density functional method and its application to the mesoscopic dynamics of quenched block copolymer melts. **The Journal of Chemical Physics**. 106: 4260.
- Fragiadakis, D., Dou, S., Colby, R. H., and Runt, J. (2008). Molecular mobility, ion mobility, and mobile ion concentration in poly(ethylene oxide)-based polyurethane ionomers. **Macromolecules**. 41: 5723.
- Fuentes, S., Retuert, P. J., and González, G. (2007). Lithium ion conductivity of molecularly compatibilized chitosan-poly(aminopropyltriethoxysilane)-poly(ethylene oxide) nanocomposites. **Electrochimica Acta**. 53: 1417.
- Gadjourova, Z., Andreev, Y. G., Tunstall, D. P., and Bruce, P. G. (2001). Ionic conductivity in crystalline polymer electrolytes. **Nature**. 412: 520.
- Gray, F. M. (1991). **Solid Polymer Electrolytes: Fundamentals and Technological Applications**. New York, Wiley.
- Gray, F. M., MacCallum, J. R., and Vincent, C. A. (1986). Poly(ethylene oxide)-LiCF₃SO₃-polystyrene electrolyte systems. **Solid State Ionics**. 18-19: 282.
- Greenland, D. J. (1963). Adsorption of polyvinyl alcohols by montmorillonite. **Journal of Colloid Science**. 18: 647.
- Grulke, E. A. (1999). **Polymer Handbook**. New York, Wiley.

- Hamman, J. H. (2010). Chitosan based polyelectrolyte complexes as potential carrier materials in drug delivery systems. **Marine Drugs**. 8: 1305.
- Han, Y. S., Lee, S. H., Choi, K. H., and Park, I. (2010). Preparation and characterization of chitosan-clay nanocomposites with antimicrobial activity. **Journal of Physics and Chemistry of Solids**. 71: 464.
- Heinz, H., Koerner, H., Anderson, K. L., Vaia, R. A., and Farmer, B. L. (2005). Force field for mica-type silicates and dynamics of octadecylammonium chains grafted to montmorillonite. **Chemistry of Materials**. 17: 5658.
- Hema, M., Selvasekarapandian, S., Nithya, H., Sakunthala, A., and Arunkumar, D. (2009). Structural and ionic conductivity studies on proton conducting polymer electrolyte based on polyvinyl alcohol. **Ionics**. 15: 487.
- Hoffman, J. D. and Weeks, J. J. (1962). Melting process and the equilibrium melting temperature of polychlorotrifluoroethylene. **Journal of research of the National Bureau of Standards. Section A. Physics and chemistry**. 66: 13.
- Hua, S., Yang, H., Wang, W., and Wang, A. (2010). Controlled release of ofloxacin from chitosan-montmorillonite hydrogel. **Applied Clay Science**. 50: 112.
- Huang, X. D. and Goh, S. H. (2001). Crystallization of C₆₀-end-capped poly(ethylene oxide)s. **Macromolecules**. 34: 3302.
- Hussain, F., Hojjati, M., Okamoto, M., and Gorga, R. (2006). Review article: polymer-matrix nanocomposites, processing, manufacturing, and application: an overview. **Journal of Composite Materials**. 40: 1511.
- Idris, N., Majid, S., Khiar, A., Hassan, M., and Arof, A. (2005). Conductivity studies on chitosan/PEO blends with LiTFSI salt. **Ionics**. 11: 375.

- Idris, N., Senin, H., and Arof, A. (2007). Dielectric spectra of LiTFSI-doped chitosan/PEO blends. ***Ionics***. 13: 213.
- Jawalkar, S. S., Adoor, S. G., Sairam, M., Nadagouda, M. N., and Aminabhavi, T. M. (2005). Molecular modeling on the binary blend compatibility of poly(vinyl alcohol) and poly(methyl methacrylate): An atomistic simulation and thermodynamic approach. ***The Journal of Physical Chemistry B***. 109: 15611.
- Kadir, M. F. Z., Majid, S. R., and Arof, A. K. (2010). Plasticized chitosan-PVA blend polymer electrolyte based proton battery. ***Electrochimica Acta***. 55: 1475.
- Kadir, M. F. Z., Teo, L. P., Majid, S. R., and Arof, A. K. (2009). Conductivity studies on plasticised PEO/chitosan proton conducting polymer electrolyte. ***Materials Research Innovations***. 13: 259.
- Kang, Y., Kim, H. J., Kim, E., Oh, B., and Cho, J. H. (2001). Photocured PEO-based solid polymer electrolyte and its application to lithium-polymer batteries. ***Journal of Power Sources***. 92: 255.
- Katti, K. S., Katti, R. D., and Dash, R. (2008). Synthesis and characterization of a novel chitosan/montmorillonite/hydroxyapatite nanocomposite for bone tissue engineering. ***Biomedical Materials***. 3: 034122.
- Kawaguchi, S., Imai, G., Suzuki, J., Miyahara, A., Kitano, T., and Ito, K. (1997). Aqueous solution properties of oligo- and poly(ethylene oxide) by static light scattering and intrinsic viscosity. ***Polymer***. 38: 2885.
- Kennedy, B. A. (1990). ***Surface Mining***. Society for Mining, Metallurgy, and Exploration.

- Khlar, A. S. A., Majid, S. R., Idris, N. H., Hassan, M. F., Puteh, R., and Arof, A. K. (2006). Ionic hopping transport in chitosan-based polymer electrolytes **Journal Materials Science Forum**. 517: 237.
- Khoo, C. G. L., Frantzich, S., Rosinski, A., Sjöström, M., and Hoogstraate, J. (2003). Oral gingival delivery systems from chitosan blends with hydrophilic polymers. **European Journal of Pharmaceutics and Biopharmaceutics**. 55: 47.
- Kienzle-Sterzer, C. A. (1984). **Transport Properties of a Cationic Polyelectrolyte in Dilute and Concentrated Solutions: Chitosan**. Ph.D. Thesis, Massachusetts Institute of Technology, USA.
- Krajewska, B. (2001). Diffusion of metal ions through gel chitosan membranes. **Reactive and Functional Polymers**. 47: 37.
- Krause, S. (1978). **Polymer-Polymer Compatibility in Polymer Blends**. Academic Press, New York.
- Kremer, F. and Schönhals, A. (2003). **Broadband Dielectric Spectroscopy**. Berlin, Heidelberg, New York, Springer-Verlag.
- Krishnamoorti, R., Vaia, R. A., and Giannelis, E. P. (1996). Structure and dynamics of polymer-layered silicate nanocomposites. **Chemistry of Materials**. 8: 1728.
- Le Tien, C., Lacroix, M., Ispas-Szabo, P., and Mateescu, M. A. (2003). *N*-acylated chitosan: Hydrophobic matrices for controlled drug release. **Journal of Controlled Release**. 93: 1.

- Lee, A., Matsumiya, Y., Watanabe, H., Hyun Ahn, K., and Jong Lee, S. (2010). Multiple representation of linear dielectric response. **Journal of the Society of Rheology , Japan**. 38: 149.
- Lennard-Jones, J. E. (1931). Cohesion. **Proceedings of the Physical Society**. 43: 461.
- Li, J. and Khan, I. M. (1993). Highly conductive solid polymer electrolytes prepared by blending high molecular weight poly(ethylene oxide), poly(2- or 4-vinylpyridine), and lithium perchlorate. **Macromolecules**. 26: 4544.
- Li, J., Zivanovic, S., Davidson, P. M., and Kit, K. (2010). Characterization and comparison of chitosan/PVP and chitosan/PEO blend films. **Carbohydrate Polymers**. 79: 786.
- Li, J., Zivanovic, S., Davidson, P. M., and Kit, K. (2011). Production and characterization of thick, thin and ultra-thin chitosan/PEO films. **Carbohydrate Polymers**. 83: 375.
- Lin, F. H., Chen, C. H., Cheng, W. T. K., and Kuo, T. F. (2006). Modified montmorillonite as vector for gene delivery. **Biomaterials**. 27: 3333.
- Lin, F. H., Lee, Y. H., Jian, C. H., Wong, J. M., Shieh, M. J., and Wang, C. Y. (2002). A study of purified montmorillonite intercalated with 5-fluorouracil as drug carrier. **Biomaterials**. 23: 1981.
- Lisowski, M. S., Liu, Q., Cho, J., Runt, J., Yeh, F., and Hsiao, B. S. (2000). Crystallization behavior of poly(ethylene oxide) and its blends using time-resolved wide- and small-angle X-ray scattering. **Macromolecules**. 33: 4842.
- Liu, K. H., Liu, T. Y., Chen, S. Y., and Liu, D. M. (2008). Drug release behavior of chitosan-montmorillonite nanocomposite hydrogels following electrostimulation. **Acta Biomaterialia**. 4: 1038.

- Londono, J. D., Annis, B. K., Habenschuss, A., Borodin, O., Smith, G. D., Turner, J. Z., and Soper, A. K. (1997). Cation environment in molten lithium iodide doped poly(ethylene oxide). **Macromolecules**. 30: 7151.
- Ma, J., Guo, C., Tang, Y., Wang, J., Zheng, L., Liang, X., Chen, S., and Liu, H. (2006). Microenvironmental and conformational structure of triblock copolymers in aqueous solution by ^1H and ^{13}C NMR spectroscopy. **Journal of Colloid and Interface Science**. 299: 953.
- Macdonald, J. R. (1953). Theory of ac space-charge polarization effects in photoconductors, semiconductors, and electrolytes. **Physical Review**. 92: 4.
- Mao, S., Shuai, X., Unger, F., Simon, M., Bi, D., and Kissel, T. (2004). The depolymerization of chitosan: Effects on physicochemical and biological properties. **International Journal of Pharmaceutics**. 281: 45.
- Martinou, A., Kafetzopoulos, D., and Bouriotis, V. (1995). Chitin deacetylation by enzymatic means: Monitoring of deacetylation processes. **Carbohydrate Research**. 273: 235.
- Mathiowetz, A. M. (1994). **Introduction**. [On-line]. Available: http://www.wag.caltech.edu/publications/theses/alan/section1_6_0_1.html.
- Matoba, Y., Matsui, S., Tabuchi, M., and Sakai, T. (2004). Electrochemical properties of composite polymer electrolyte applied to rechargeable lithium polymer battery. **Journal of Power Sources**. 137: 284.
- Matsumiya, Y., Balsara, N. P., Kerr, J. B., Inoue, T., and Watanabe, H. (2003). In situ dielectric characterization of poly(ethylene oxide) melts containing lithium perchlorate under steady shear flow. **Macromolecules**. 37: 544.

- Mendoliaa, M. S. and Farringtona, G. C. (1995). **High-Conductivity, Solid Polymeric Electrolytes**. Materials Chemistry: An Emerging Discipline. Washington DC, American Chemical Society.
- Mia, S. (2003). **Biopharmaceutical Evaluation of Microcrystalline Chitosan as Release-Rate-Controlling Hydrophilic Polymer in Granules for Gastro-Retentive Drug Delivery**. Ph. D. Thesis, University of Helsinki, Finland.
- Mohamad, S. A., Yahya, R., Ibrahim, Z. A., and Arof, A. K. (2007). Photovoltaic activity in a ZnTe/PEO-chitosan blend electrolyte junction. **Solar Energy Materials and Solar Cells**. 91: 1194.
- Mohamed, N. S. and Arof, A. K. (2004). Investigation of electrical and electrochemical properties of PVDF-based polymer electrolytes. **Journal of Power Sources**. 132: 229.
- Montroll, E. W. and Weiss, G. H. (1965). Random walks on lattices II. **Journal of Mathematical Physics**. 6: 167.
- Monvisade, P. and Siriphannon, P. (2009). Chitosan intercalated montmorillonite: Preparation, characterization and cationic dye adsorption. **Applied Clay Science**. 42: 427.
- Morni, N. M. and Arof, A. K. (1999). Chitosan-lithium triflate electrolyte in secondary lithium cells. **Journal of Power Sources**. 77: 42.
- Mucha, M. and Pawlak, A. (2005). Thermal analysis of chitosan and its blends. **Thermochimica Acta**. 427: 69.
- Neto, C. G. T., Giacometti, J. A., Job, A. E., Ferreira, F. C., Fonseca, J. L. C., and Pereira, M. R. (2005). Thermal analysis of chitosan based networks. **Carbohydrate Polymers**. 62: 97.

- Ng, L. S. and Mohamad, A. A. (2006). Protonic battery based on a plasticized chitosan-NH₄NO₃ solid polymer electrolyte. **Journal of Power Sources**. 163: 382.
- Nishi, T. and Wang, T. T. (1975). Melting point depression and kinetic effects of cooling on crystallization in poly(vinylidene fluoride)-poly(methyl methacrylate) mixtures. **Macromolecules**. 8: 909.
- Ogawa, K., Oka, K., and Yui, T. (1993). X-ray study of chitosan-transition metal complexes. **Chemistry of Materials**. 5: 726.
- Paluszkiewicz, C., Stodolak, E., Hasik, M., and Blazewicz, M. (2011). FT-IR study of montmorillonite-chitosan nanocomposite materials. **Spectrochimica Acta Part A: Molecular and Biomolecular Spectroscopy**. *in press*.
- Park, J. W., Jeong, E. D., Won, M. S., and Shim, Y. B. (2006). Effect of organic acids and nano-sized ceramic doping on PEO-based solid polymer electrolytes. **Journal of Power Sources**. 160: 674.
- Patel, S. S. (2006). **Pharmaceutical Significance Of Chitosan: A Review**. [On-line]. Available: <http://www.pharmainfo.net/reviews/pharmaceutical-significance-chitosan-review>.
- Patel, V. R. and Amiji, M. M. (1996). pH-sensitive swelling and drug-release properties of chitosan/poly(ethylene oxide) semi-interpenetrating polymer network, hydrogels and biodegradable polymers for bioapplications. **American Chemical Society**. 627: 209.
- Paul, D. R. and Barlow, J. W. (1984). A binary interaction model for miscibility of copolymers in blends. **Polymer**. 25: 487.

- Pawlak, A. and Mucha, M. (2003). Thermogravimetric and FTIR studies of chitosan blends. **Thermochimica Acta**. 396: 153.
- Peniston, Q. P. and Johnson, E. L. (1970). **Method for Treating an Aqueous Medium with Chitosan and Derivatives of Chitin to Remove an Impurity**. United States.
- Pielichowski, K., Flejtuch, K., and Pielichowski, J. (2004). Step-scan alternating DSC study of melting and crystallisation in poly(ethylene oxide). **Polymer** 45: 1235.
- Pitawala, H. M. J. C., Dissanayake, M. A. K. L., and Seneviratne, V. A. (2007). Combined effect of Al₂O₃ nano-fillers and EC plasticizer on ionic conductivity enhancement in the solid polymer electrolyte (PEO)₉LiTf. **Solid State Ionics**. 178: 885.
- Prathab, B. and Aminabhavi, T. M. (2007). Atomistic simulations to compute surface properties of poly(N-vinyl-2-pyrrolidone) (PVP) and blends of PVP/chitosan **Langmuir**. 23: 5439.
- Puttipatkhachorn, S., Nunthanid, J., Yamamoto, K., and Peck, G. E. (2001). Drug physical state and drug-polymer interaction on drug release from chitosan matrix films. **Journal of Controlled Release**. 75: 143.
- Radhakrishnan, S. and Venkatachalapathy, P. D. (1996). Effect of casting solvent on the crystallization in PEO/PMMA blends. **Polymer**. 37: 3749.
- Rakkapao, N., Vao-soongnern, V., Masubuchi, Y., and Watanabe, H. (2011). Miscibility of Chitosan/Poly(ethylene oxide) Blends and Effect of Doping Alkali and Alkali Earth Metal Ions on Chitosan/PEO Interaction. **Polymer**. *in press*.

- Ramesh, S., Yuen, T. F., and Shen, C. J. (2008). Conductivity and FTIR studies on PEO-LiX [X: $\text{CF}_3\text{SO}^{3-}$, SO_4^{2-}] polymer electrolytes. **Spectrochimica Acta Part A: Molecular and Biomolecular Spectroscopy**. 69: 670.
- Rappe, A. K. and Goddard, W. A. (1991). Charge equilibration for molecular dynamics simulations. **The Journal of Physical Chemistry**. 95: 3358.
- Ravi Kumar, M. N. V. (2000). A review of chitin and chitosan applications. **Reactive and Functional Polymers**. 46: 1.
- Ravindra, R., Krovvidi, K. R., and Khan, A. A. (1998). Solubility parameter of chitin and chitosan. **Carbohydrate Polymers**. 36: 121.
- Ray, S. S. and Bousmina, M. (2005). Biodegradable polymers and their layered silicate nanocomposites: In greening the 21st century materials world. **Progress in Materials Science**. 50: 962.
- Ray, S. S. and Okamoto, M. (2003). Polymer/layered silicate nanocomposites: A review from preparation to processing. **Progress in Polymer Science**. 28: 1539.
- Reddy, M. J. and Chu, P. P. (2002). Effect of Mg^{2+} on PEO morphology and conductivity. **Solid State Ionics**. 149: 115.
- Reddy, M. J., Siva Kumar, J., Subba Rao, U. V., and Chu, P. P. (2006). Structural and ionic conductivity of PEO blend PEG solid polymer electrolyte. **Solid State Ionics**. 177: 253.
- Rhim, J. W., Hong, S. I., Park, H. M., and Ng, P. K. W. (2006). Preparation and characterization of chitosan-based nanocomposite films with antimicrobial activity. **Journal of Agricultural and Food Chemistry**. 54: 5814.

- Rigby, D. (2004). Fluid density predictions using the COMPASS force field. **Fluid Phase Equilibria**. 217: 77.
- Rigby, D., Sun, H., and Eichinger, B. E. (1997). Computer simulations of poly(ethylene oxide): Force field, PVT diagram and cyclization behaviour. **Polymer International**. 44: 311.
- Rinaudo, M. (2006). Chitin and chitosan: Properties and applications. **Progress in Polymer Science**. 31: 603.
- Rodríguez-Hornedo, N. and Wu, H. J. (1991). Crystal growth kinetics of theophylline monohydrate. **Pharmaceutical Research**. 8: 643.
- Roe, R. J. (1968). Surface tension of polymer liquids. **The Journal of Physical Chemistry**. 72: 2013.
- Sahoo, S., Sasmal, A., Nanda, R., Phani, A. R., and Nayak, P. L. (2010). Synthesis of chitosan-polycaprolactone blend for control delivery of ofloxacin drug. **Carbohydrate Polymers**. 79: 106.
- Sakurai, K., Maegawa, T., and Takahashi, T. (2000). Glass transition temperature of chitosan and miscibility of chitosan/poly(*N*-vinyl pyrrolidone) blends. **Polymer**. 41: 7051.
- Sanli, O., Karaca, I., and Isiklan, N. (2009). Preparation, characterization, and salicylic acid release behavior of chitosan/poly(vinyl alcohol) blend microspheres. **Journal of Applied Polymer Science**. 111: 2731.
- Saruyama, Y. (1983). Temperature dependence of distortion in poly(ethylene oxide) crystals. **Polymer**. 24: 135.

- Sashina, E., Vnuchkin, A., and Novoselov, N. (2006). A study of the thermodynamics of chitosan interaction with polyvinyl alcohol and polyethylene oxide by differential scanning calorimetry. **Russian Journal of Applied Chemistry**. 79: 1643.
- Sato, H., Mizutani, S., Tsuge, S., Ohtani, H., Aoi, K., Takasu, A., Okada, M., Kobayashi, S., Kiyosada, T., and Shoda, S. (1998). Determination of the degree of acetylation of chitin/chitosan by pyrolysis-gas chromatography in the presence of oxalic acid. **Analytical Chemistry**. 70: 7.
- Satpathy, T. K. (2008). **Chitosan Used in Pharmaceutical Formulations: A Review**. [On-line]. Available: <http://www.pharmainfo.net/reviews/chitosan-used-pharmaceutical-formulations-review>.
- Shu, X. Z. and Zhu, K. J. (2002a). Controlled drug release properties of ionically cross-linked chitosan beads: the influence of anion structure. **International Journal of Pharmaceutics**. 233: 217.
- Shu, X. Z. and Zhu, K. J. (2002b). The influence of multivalent phosphate structure on the properties of ionically cross-linked chitosan films for controlled drug release. **European Journal of Pharmaceutics and Biopharmaceutics**. 54: 235.
- Shuo, Z. (2004). **Poly(ethylene oxide)-Based Composite Polymer Electrolytes for The Secondary Lithium Batteries**. Master Thesis, National University of Singapore, Singapore.
- Singh, P. K., Kim, K. W., and Rhee, H. W. (2008). Electrical, optical and photoelectrochemical studies on a solid PEO-polymer electrolyte doped with low viscosity ionic liquid. **Electrochemistry Communications**. 10: 1769.

- Sokker, H. H., Abdel Ghaffar, A. M., Gad, Y. H., and Aly, A. S. (2009). Synthesis and characterization of hydrogels based on grafted chitosan for the controlled drug release. **Carbohydrate Polymers**. 75: 222.
- Song, J. Y., Wang, Y. Y., and Wan, C. C. (1999). Review of gel-type polymer electrolytes for lithium-ion batteries. **Journal of Power Sources**. 77: 183.
- Sorkin, V. (2003). **Local Density Profile**. [On-line]. Available: <http://phycomp.technion.ac.il/~phsorkin/thesis/node34.html>.
- Sreenivasan, K. (1996). Thermal stability studies of some chitosanmetal ion complexes using differential scanning calorimetry. **Polymer Degradation and Stability**. 52: 85.
- Stowe, M. K. (2001). **PEO-Based Polymer Electrolytes for Secondary Lithium Batteries**. Ph.D. Thesis, Michigan State University, USA.
- Su, Y. L., Wang, J., and Liu, H. Z. (2002). Melt, hydration, and micellization of the PEO-PPO-PEO block copolymer studied by FTIR spectroscopy. **Journal of Colloid and Interface Science**. 251: 417.
- Sukeshini, A. M., Kulkarni, A. R., and Sharma, A. (1998). PEO based solid polymer electrolyte plasticized by dibutyl phthalate. **Solid State Ionics**. 113: 179.
- Sun, H. (1998a). Compass: An ab initio force-field optimized for condensed-phase applications - Overview with details on alkane and benzene compounds. **Journal of Physical Chemistry B**. 102: 7338.
- Sun, H. (1998b). The COMPASS force field: Parameterization and validation for phosphazenes. **Computational and Theoretical Polymer Science**. 8: 229.

- Takahashi, Y. and Tadokoro, H. (1973). Structural studies of polyethers, $(-(\text{CH}_2)_m-\text{O}-)_n$. X. Crystal structure of poly(ethylene oxide). **Macromolecules**. 6: 672.
- Tan, W., Zhang, Y., Szeto, Y. S., and Liao, L. (2008). A novel method to prepare chitosan/montmorillonite nanocomposites in the presence of hydroxy-aluminum oligomeric cations. **Composites Science and Technology**. 68: 2917.
- Thanpitcha, T., Sirivat, A., Jamieson, A. M., and Rujiravanit, R. (2006). Preparation and characterization of polyaniline/chitosan blend film. **Carbohydrate Polymers**. 64: 560.
- Trimukhe, K. D. and Varma, A. J. (2009). Metal complexes of crosslinked chitosans: Correlations between metal ion complexation values and thermal properties. **Carbohydrate Polymers**. 75: 63.
- Usuki, A., Hasegawa, N., Kadoura, H., and Okamoto, T. (2001). Three-dimensional observation of structure and morphology in nylon-6/clay nanocomposite. **Nano Letters**. 1: 271.
- Varma, K. S. (2010). **Chitosan as a Polymer for Macromolecular Drug Delivery**. [On-line]. Available: <http://www.pharmabiz.com>.
- Vincent, C. A. (1995). Ion transport in polymer electrolytes. **Electrochimica Acta**. 40: 2035.
- Viseras, C., Aguzzi, C., Cerezo, P., and Bedmar, M. C. (2008). Biopolymer-clay nanocomposites for controlled drug delivery. **Materials Science and Technology**. 24: 1020.

- Wai, K. N., Dekay, H. G., and Banker, G. S. (1966). Applications of the montmorillonites in tablet making. **Journal of Pharmaceutical Sciences**. 55: 1244.
- Walsh, D. and Rostami, S. (1985). The miscibility of high polymers: The role of specific interactions. **Key Polymers Properties and Performance**. 1: 119.
- Wang, Q. Z., Chen, X. G., Liu, N., Wang, S. X., Liu, C. S., Meng, X. H., and Liu, C. G. (2006a). Protonation constants of chitosan with different molecular weight and degree of deacetylation. **Carbohydrate Polymers**. 65: 194.
- Wang, S. F., Shen, L., Tong, Y. J., Chen, L., Phang, I. Y., Lim, P. Q., and Liu, T. X. (2005). Biopolymer chitosan/montmorillonite nanocomposites: Preparation and characterization. **Polymer Degradation and Stability**. 90: 123.
- Wang, W. and Roberts, G. A. F. (1997). Effect of acetyl group content on the miscibility of blends of chitosan with poly(ethylene oxide) **Advances in Chitin Science**. 2: 561.
- Wang, X., Du, Y., Luo, J., Yang, J., Wang, W., and Kennedy, J. F. (2009). A novel biopolymer/rectorite nanocomposite with antimicrobial activity. **Carbohydrate Polymers**. 77: 449.
- Wang, X., Du, Y., Yang, J., Wang, X., Shi, X., and Hu, Y. (2006b). Preparation, characterization and antimicrobial activity of chitosan/layered silicate nanocomposites. **Polymer**. 47: 6738.
- Wang, X., Du, Y., and Luo, J. (2008). Biopolymer/montmorillonite nanocomposite: preparation, drug-controlled release property and cytotoxicity. **Nanotechnology**. 19: 065707.

- Wieczorek, W., Such, K., Florjanczyk, Z., and Przyluski, J. (1992). Application of acrylic polymers in blend-based polymeric electrolytes. **Electrochimica Acta**. 37: 1565.
- Wieczorek, W., Such, K., Florjanczyk, Z., and Stevens, J. R. (1995). Polyacrylamide based composite polymeric electrolytes. **Electrochimica Acta**. 40: 2417.
- Wikipedia. (2010). **Molecular Dynamics**. [On-line]. Available: http://en.wikipedia.org/wiki/Molecular_dynamics.
- Winie, T. and Arof, A. (2006). Transport properties of hexanoyl chitosan-based gel electrolyte. **Ionics**. 12: 149.
- Wu, H., Liu, C., Chen, J., Yang, Y., and Chen, Y. (2010). Preparation and characterization of chitosan/ α -zirconium phosphate nanocomposite films. **Polymer International**. 59: 923.
- Xu, Y., Ren, X., and Hanna, M. A. (2006). Chitosan/clay nanocomposite film preparation and characterization. **Journal of Applied Polymer Science**. 99: 1684.
- Xu, Y., Zhan, C., Fan, L., Wang, L., and Zheng, H. (2007). Preparation of dual crosslinked alginate-chitosan blend gel beads and in vitro controlled release in oral site-specific drug delivery system. **International Journal of Pharmaceutics**. 336: 329.
- Yahya, M. Z. A. and Arof, A. K. (2003). Effect of oleic acid plasticizer on chitosan-lithium acetate solid polymer electrolytes. **European Polymer Journal**. 39: 897.

- Yin, J., Luo, K., Chen, X., and Khutoryanskiy, V. V. (2006). Miscibility studies of the blends of chitosan with some cellulose ethers. **Carbohydrate Polymers**. 63: 238.
- Zhu, L., Cheng, S. Z. D., Calhoun, B. H., Ge, Q., Quirk, R. P., Thomas, E. L., Hsiao, B. S., Yeh, F., and Lotz, B. (2000). Crystallization temperature-dependent crystal orientations within nanoscale confined lamellae of a self-assembled crystalline-amorphous diblock copolymer. **Journal of the American Chemical Society**. 122: 5957.
- Ziska, J. J., Barlow, J. W., and Paul, D. R. (1981). Miscibility in PVC-polyester blends. **Polymer**. 22: 918.
- Zivanovic, S., Li, J., Davidson, P. M., and Kit, K. (2007). Physical, mechanical, and antibacterial properties of chitosan/PEO blend films. **Biomacromolecules**. 8: 1505.

APPENDICES

APPENDIX A

CALCULATION OF MOLAR VOLUME OF CHITOSAN AND POLY(ETHYLENE OXIDE) REPEATING UNIT

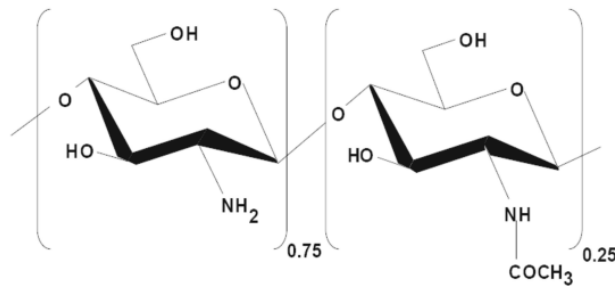
Calculation of Molar Volume of Chitosan and PEO Repeating Unit

PEO: MW of repeat unit of PEO = 44 g/mol

Density of PEO is 1.09 g/cm³ (Roe, 1968)

Molar volume of PEO repeat unit, $V_{Au} = MW/d = 44/1.09 = 40.37 \text{ cm}^3/\text{mol}$

Chitosan: The degree of deacetylation of 75%



MW of repeat unit of CS = $(161 \times 0.75) + (203 \times 0.25) = 171.5 \text{ g/mol}$

Density of CS is 1.33 g/cm³ (Deepak *et al.*, 2000)

Molar volume of CS repeat unit, $V_{Au} = MW/d = 171.5/1.33 = 128.57 \text{ cm}^3/\text{mol}$

APPENDIX B
PAPER PUBLICATION

Miscibility of Chitosan/Poly(ethylene oxide) Blends and Effect of Doping Alkali and Alkali Earth Metal Ions on Chitosan/PEO Interaction

Natthida Rakkapao¹, Visit Vao-soongnern^{1*}, Yuichi Masubuchi² and Hiroshi Watanabe²

¹ Laboratory of Computational and Applied Polymer Science (LCAPS), School of Chemistry, Institute of Science, Suranaree University of Technology, Thailand, 30000

² Institute for Chemical Research, Kyoto University, Uji, Kyoto 611-0011, Japan

Keyword: Chitosan, Poly(ethylene oxide) (PEO), Blends, Metal Ions

Abstract: The miscibility of Chitosan (CS) and poly(ethylene oxide) (PEO) and their blends and the effect of K⁺ and Ca²⁺ doping on the CS/PEO interaction have been investigated in this work. CS and PEO appeared to be miscible and the DSC analysis suggested the Flory-Huggins interaction parameter χ_{AB} to be -0.21. Doping of K⁺ and Ca²⁺ into the CS/PEO blend matrix enhanced the cooperative interaction between CS and PEO and this enhancement was larger for Ca²⁺ than for K⁺. The difference between Ca²⁺ and K⁺ possibly reflects a stronger multi-valence interaction of Ca²⁺ with the amino and hydroxyl groups of CS as well as the ether groups of PEO to form a stable CS/Ca²⁺/PEO complex and a less significant interaction of K⁺, as suggested by DSC, WAXD and FTIR results. MD simulations clearly indicated the correlation between the dynamic behavior and the interaction of K⁺ and Ca²⁺ in the CS/PEO blend matrix.

Keyword: Chitosan, Poly(ethylene oxide) (PEO), Blend, Ion, Electrolyte

1. Introduction

Solid polymer electrolytes (SPEs) have been reported as promising materials for use in batteries to allow fabrication of the compact, lightweight, highly reliable, and safe batteries [1-3]. The use of SPEs can avoid problems associated with liquid electrolytes such as leakage and gas formation due to solvent decomposition, thereby enabling an improved battery design. SPEs consist of salts dissolved in high molecular weight polymers. The polymers dissolving salt must include O, N or S atom because these atoms can interact with cation and enhance the salt dissociation to enlarge the conductivity [4].

Chitosan (CS) is a cationic biopolymer belonging to this class of polymers useful for the batteries. This polymer, obtained through full/partial deacetylation of chitin, is the second most abundant biopolymer in nature. CS includes O and N atoms in the form of the amino (-NH₂) and hydroxyl (-OH) functional groups and the lone pair electrons of O and N enable the chelation of a proton donor. Thus, CS satisfies

one of the criteria to use as a polymer host for solid polymer electrolyte in the fabrication of proton batteries [5-8]. However, CS chain is quite rigid at ambient temperature; its high glass transition temperature, $T_g \sim 203^\circ\text{C}$ [9], results in poor mechanical/physical properties (such as the brittleness) that frequently restrict the application of CS [10, 11].

A convenient and effective method to improve the CS properties is to blend CS with other flexible polymers. In this respect, PEO was selected as a suitable blending partner for CS. PEO is a synthetic, uncharged and flexible polymer [10-12] with $T_g \sim -59^\circ\text{C}$. PEO is one of the most widely used host polymers in SPEs because of its ability to solvate a variety of inorganic salts to provide a significant ionic conductivity [4]. PEO shows sufficient thermal and chemical stability, and the spacing between the ether groups along the PEO backbone is ideal for cation solvation [4]. However, the disadvantage of PEO as a salt host becomes evident, because pure PEO has 70-95% crystallinity at room temperature [13]. The high crystallinity gives a major barrier for ion transportation and always ends up with an undesirably low ionic conductivity [14] and also unfavorably high rigidity and low transparency of the SPE film [15].

Blending with an essentially amorphous polymer, CS, is a suitable method to prevent PEO from crystallizing. It has been shown that blending of PEO with CS does not lead to phase separation [16]. Accordingly, amorphous CS chains may facilitate a decrease in PEO crystallinity in the blend to improve the conductivity and transparency; at the same time, a flexible PEO chains may compensate the rigidity of CS in the blend thereby giving a suitable material for SPE application [6, 16-19]. Compared to the pure CS and pure PEO films, CS/PEO blends exhibit the improvement in the thermal, chemical, mechanical and conductive properties and acquire additional functionality because of the specific interactions between the amino groups of CS and the ether groups of PEO [10, 11]. Thus, CS can act as a proton donor while PEO can act as a proton acceptor, giving rise to a homogeneous polymeric blends [20]. The maximum interaction between CS and PEO was reported to occur at 20 wt% PEO content [21]. It was also demonstrated that PEO decreases its tendency of spherulitic crystallization in the blends with a large CS content (> 50 wt%) [11]. Moreover, the mechanical properties of CS films are improved on blending with PEO; a six times larger elongation at break and a two times higher tensile strength have been reported for the CS/PEO blends containing 16.7 wt% of PEO [10]. This improvement can be related to an increase in the packing density of the polymer chains in blends through filling of the cavities in the rigid structure of CS by flexible PEO [12] as well as to an attractive interaction between the polymer components.

The conductivity of SPE materials is strongly affected not only by the feature of the host polymers (e.g., CS and PEO) but also by the choice of doped ions. Thus, this study adopts the CS/PEO blend as a promising host polymer matrix for the ion

conduction and examines, to the first time as long as the authors know, the effects of doping the alkali and alkali earth metal ions on the structure/property of the blends. The focus of this study is placed on a role of the ion valency in the interaction between the metal ions and each polymer component. In this respect, K^+ and Ca^{2+} were chosen as the doped ions because of their similarity in both size and mass ($Z_K = 19$, $M_K = 39$ g/mol; $Z_{Ca} = 20$, $M_{Ca} = 40$ g/mol), and the interactions between metal ions and CS/PEO through coulombic and more chemical (chelation) mechanisms were of particular focus of this study. Differential scanning calorimetry (DSC) and wide angle X-ray diffraction (WAXD) measurements as well as Fourier transform infrared (FTIR) spectroscopy were conducted for the CS/PEO blends with/without doped K^+ and Ca^{2+} to examine the miscibility between CS and PEO and the effects of the ion doping on the miscibility, structure and thermodynamic properties of the blends. Molecular dynamics (MD) simulation was also conducted to examine the experimentally inaccessible microscopic aspects underlying the macroscopic structure/properties. The correlation between the ion diffusion and the interaction/complex formation of the ions with the CS/PEO blend matrix was also investigated through the simulation. The results presented in this paper provide us with a clue for developing the novel CS/PEO blends films suitable for SPE applications.

2. Experimental Section

A CS sample from Aquatic Nutrition Lab, Thailand, having the viscosity-average molecular weight $M_v = 1.13 \times 10^6$ g/mol (determined with dilute solution viscometry in our lab) and the degree of deacetylation %DD = $75 \pm 3\%$ (determined with the titration, FTIR, and potentiometric methods) and a PEO sample from Aldrich (weight-average molecular weight $M_w = 2 \times 10^5$ g/mol; manufacture's data) were used without further purification. In preparation of a series of CS/PEO blends of different PEO content (total mass = 0.6 g for each blend), prescribed masses of CS and PEO were dissolved in 40 ml of 0.1 M aqueous acetic acid to obtain clear homogeneous solutions. For preparation of K^+ and Ca^{2+} doped blends, 0.0495 g of K_2SO_4 and 0.0978 g of $CaSO_4 \cdot 2H_2O$, respectively, were added to each CS/PEO blend solution to obtain the constant amount of metal ions (9.47×10^{-4} mol ions/g of polymer mixture). The solutions were stirred overnight at room temperature to achieve complete dissolution, cast onto polystyrene *Petri* dish, and dried at room temperature in a dust free chamber. The resulting dry films (with diameter = 90 mm and thickness ~0.1 mm) were peeled off, rinsed with diethyl ether to eliminate the solvent [9] and dried again under reduced pressure at room temperature for 24 h. The films were then kept in zipper plastic bags and stored in desiccators for continuous drying before use.

Differential scanning calorimetry (DSC) measurements were performed with a calorimeter (TA instrument Model DSC-Q20 V24.2 Build 107). Accurately weighed specimens (~10 mg) were placed in aluminum pans and sealed. An empty pan was

used as a reference and all measurements were performed under nitrogen atmosphere (purge flow = 50 ml/min). The specimen was firstly heated to 100°C and then annealed at 100°C for 7 min, thereby allowing the PEO crystallines therein to fully melt. Then the specimen was suddenly quenched (-50°C/min) to/annealed at a given holding temperature for 60 min, and the isothermal state for the PEO crystallization was achieved within 2 min after the quench. On the successive heating to 100°C, the thermal behavior including the PEO melting was examined at a scanning rate of 5°C/min. The cycles of heating and quenching at several holding temperatures (T_c) were used to obtain the information about the equilibrium PEO melting temperature (T_m°).

In the other type of thermal test, the specimen was first heated to 100°C and annealed at 100°C for 7 min to erase its thermal history, suddenly quenched to -80°C and held for 10 min, and then heated at a scanning rate of 2°C/min (up to -20°C) to examine the glass transition temperature T_g of PEO. The specimen was further heated to 350°C at a scanning rate of 5°C/min, and the dehydration behavior as well as the degradation temperature (T_d) of CS were examined.

Wide-angle X-ray diffraction (WAXD) measurements were conducted for specimens at room temperature with an X-ray diffractometer (Rigaku, RINT 2002). A monochromic $\text{CuK}\alpha$ (1.54 Å) X-ray source was operated at 40 kV and 50 mA, and the scattering intensity was measured at a scattering angle 2θ scanned from 5° to 30°.

Fourier transform infrared (FTIR) spectroscopy was performed at Synchrotron Light Research Institute (SLRI) of Thailand on a Bruker Vertex 70 Fourier Transform Infrared spectrometer with a resolution of 4 cm^{-1} in a measurement range of 4000-800 cm^{-1} using a MCT (HgCdTe) detector cooled with liquid nitrogen. The infrared spectra of all sample films were obtained with ATR-FTIR method (PIKE MIRacle Crystal Plate: Single Reflection Ge Crystal Plate). The FTIR measurements were made for several points on each side of the films and recorded after scanning for 32 times, and no significant difference was noted for the test points on the two sides exposed to the *Petri* dish and the air (bottom and top sides of the cast film). The spectra were converted to absorbance using OPUS 5.0 software (Bruker Optics Ltd, Ettlingen, Germany).

3. Computational Section

For the CS/PEO blend of the PEO content $w_{\text{PEO}} = 20$ wt% and with/without doping by K^+ and Ca^{2+} (with atomic charge of +1 and +2, respectively), molecular dynamics (MD) simulations were conducted using Materials Studio 4.2 [22]. The COMPASS [23-25] force field was employed for all calculations. Each simulation system was minimized using Discover module. It should be pointed out that the COMPASS field does not accurately consider the gauche effect in OCCO dihedral angles of the PEO chain and is approximate. However, significant differences were noted for the spatial distribution of the functional groups and ions in the K^+ - and Ca^{2+} -

doped blends simulated under the same force field (as explained later in more detail), which allowed us to utilize the simulation results and discuss the differences of the interaction in these blends at least qualitatively.

The amorphous phase of CS/PEO blend as well as the blend doped by K^+ and Ca^{2+} were constructed inside the simulation box with periodic boundary conditions. For the CS/PEO blend ($w_{PEO} = 20$ wt%) without ions, 1 chain with 32 monomer units of CS and 1 chain with 29 monomer units of PEO were constructed in the periodic box with the dimensions of $20.62 \times 20.62 \times 20.62 \text{ \AA}^3$. Density of the blend was first estimated from the average density of individual pure polymers. Then NPT MD was run to equilibrate the structure and the blend density was obtained at 0.76 g/cm^3 . The amorphous assembly was energy-minimized using the Smart minimization method [22] with a convergence level of $0.01 \text{ kcal/mol/\AA}$. The Smart minimizer starts with the steepest descent method, followed by the conjugate gradient method and ends with a Newton method. Atom-based cutoff of 9.5 \AA and a switching function with the spline and buffer widths of 5 and 2 \AA , respectively, were applied to evaluate non-bonded interactions. Since the density of the amorphous CS/PEO blend is different from those of the crystalline structures of the starting pure polymers, the simulations were carried out with isothermal-isobaric (NPT) ensemble based on Andersen-Berendsen method [26-28]. These NPT simulations were performed at atmospheric pressure as previously described [29]. Subsequently, short NVT simulations were run for 0.2 ns at 800 K to relax the structures to obtain the equilibrium density. Then another NVT simulation was performed for 1 ns at 298 K with a time step of 1 fs. The radial distribution functions (RDFs), $g(r)$, were calculated in this equilibrated state.

For ion doped systems, ten K^+ units and five SO_4^{2-} units were added into the periodic simulation box of the equilibrated CS/PEO blend for the simulation of the K^+ -doped blend, while ten Ca^{2+} units and ten SO_4^{2-} units for the simulation of the Ca^{2+} -doped blend. (These number of ions corresponded to the actual ion concentration in the blends examined, $9.47 \times 10^{-4} \text{ mol ions/g}$ of polymer mixture.) The simulated systems were allowed to relax in a manner similar to that for the neat CS/PEO blend as mention above. The radial distribution functions (RDFs), $g(r)$, were calculated after another NVT simulation performed for 1 ns at 298 K. The NVT simulation was then performed in this equilibrated state for another 1 ns at high temperature (800 K) with a time step of 1 fs to examine the dynamics of ions in the CS/PEO blend matrix. The temperature, 800 K, was not the temperature in real experiments but was chosen to quantify the difference of the mobility between K^+ and Ca^+ . (At lower temperature, even the mobile K^+ exhibited no large diffusive displacement within the time scale of the simulation.)

4. Thermodynamics

For polymer blends, the melting point depression is usually discussed on the basis of the work of Nishi and Wang who derived the expression for A/B polymer blends as [30]:

$$\frac{1}{T_m} - \frac{1}{T_m^0} = -\frac{RV_{Bu}}{\Delta H_{Bu}V_{Au}} \chi_{AB} v_A^2 \quad (1)$$

Here, T_m and T_m^0 are the melting point of the crystallizable polymer component B (PEO for our case) in the blends and in pure bulk, respectively, and R is the gas constant. ΔH_{Bu} and V_{Bu} are the molar enthalpy of fusion and molar volume of the repeating unit of B. V_{Au} and v_A are the molar volume of the repeating unit of the non-crystallizable component A (amorphous CS in our case) and the volume fraction of this component in the blends, respectively. Finally, χ_{AB} is the Flory-Huggins interaction parameter between the components A and B.

Equation (1) allows us to estimate the interaction parameter χ_{AB} from the measured melting point depression, $\Delta T_m = T_m^0 - T_m$. If a $\Delta T_m/T_m^0$ ratio is much smaller than unity (with ΔT_m and T_m^0 being expressed in K unit), Eq. (1) is rewritten as:

$$\Delta T_m = -T_m^0 \left(\frac{V_{Bu}}{\Delta H_{Bu}} \right) v_A^2 B \quad (2)$$

with

$$B = \left(\frac{RT_m^0}{V_{Au}} \right) \chi_{AB} \quad (3)$$

It follows from Eqs. (2) and (3) that the ΔT_m is proportional to v_A^2 and χ_{AB} is obtained from the proportionality constant.

5. Results and Discussions

5.1 Miscibility of CS/PEO Blends Containing no Salt

WAXD measurements were conducted for pure PEO and CS/PEO neat blends (containing no salt) to verify the decrease of PEO crystallinity on blending with CS. The decrease in PEO crystallinity results from the miscibility/compatibility between CS and PEO; namely, the specific attractive interaction between CS and PEO chains may suppress the crystallization of PEO. Since CS is the fully amorphous component, only the semi-crystalline PEO portion in the CS/PEO blends exhibits the unique X-ray diffraction pattern. Figure 1 shows WAXD patterns of CS/PEO blends films. All CS/PEO blends exhibit two main peaks at 2θ of 19.2° and 23.4° corresponding to 120 and $112/004$ reflections, respectively, from PEO crystallites [31].

In Fig. 1, the intensities of two main diffraction peaks decrease monotonically while their relative ratio hardly changes with w_{CS} in the range of 0-40 wt%. For $w_{CS} \geq 60$ wt%, the relative intensities between these two peaks deviated from this dilution behavior as expected from a simple law of mixtures, as discussed by Radhakrishnan for PEO/PMMA blends [31]. Namely, the variation of WAXD intensity of certain reflection may be caused by the inhibition of the growth of PEO crystallites along particular directions and a distortion from the general monoclinic unit cell. For our CS/PEO blends, the deviation seen at $w_{CS} \geq 60$ wt% [32] is possibly due to the strong hydrogen bond formation between ether groups of PEO and amino groups of CS [11, 12]. At high CS content, the interaction between CS and PEO is stronger than that between PEO and PEO.

DSC measurements were conducted to determine the melting temperatures, T_m^0 and T_m for pure PEO and CS/PEO blends, respectively. The measurements also gave the crystallinity of PEO (defined as the mass of the PEO crystalline per unit mass of all PEO chains in blends) as:

$$X_c^m = \frac{\Delta H_m}{f_w \Delta H_m^0} \quad (4)$$

Here, ΔH_m is the enthalpy of PEO fusion measured for unit mass of the sample, while ΔH_m^0 is the enthalpy of fusion for unit mass of perfect crystalline PEO ($\Delta H_m^0 = 196.8$ J/g [33]) and f_w is the weight fraction of PEO in the blends. The X_c^m values thus obtained for a series of CS/PEO blends are shown in Table 1 and the plots as a function of PEO weight fraction (w_{PEO}) are shown later in Fig. 6.

In the DSC measurements, the T_m measured for the pure PEO and the PEO in the CS/PEO blends are not necessarily identical to the melting temperature T_m^e of fully equilibrated/developed PEO crystalline. T_m is smaller than T_m^e due to insufficient crystalline growth (giving thin crystalline lamellae) and a consequent high surface energy of lamellae and/or of defects. Thus, we utilized the Hoffman and Weeks (HW) method [34] to evaluate T_m^e : The PEO component in bulk and blends was allowed to crystallize at different holding temperatures T_c , and then the melting temperature T_m was measured on heating. Figure 2 shows plots of T_m against T_c thus obtained. The plots obey the HW relationship among T_m , T_c , and T_m^e ,

$$T_m = \phi T_c + (1 - \phi) T_m^e \quad (5)$$

where ϕ is the slope of the plots. (The crystalline is perfectly stable if $\phi = 0$, while it is inherently unstable if $\phi = 1$.)

From Eq. (5), T_m^e is evaluated from a crossing point between the HW plots and the $T_m = T_c$ line. The T_m^e and ϕ values thus obtained are summarized in Table 1. $T_m^{0,e}$ for neat PEO is 333.1 K. From Table 1, ϕ for neat PEO is close to 0 and thus the crystallines therein are highly stable. In contrast, ϕ for CS/PEO blends are

considerably larger than 0 and increases with increasing w_{CS} , which suggests that the PEO crystallines are destabilized by CS. Correspondingly, both T_m^e and X_c^m also decreases with w_{CS} . All these results suggest that the PEO-PEO interaction is interrupted by CS because of the hydrogen bond formation between the ether groups of PE and the amino groups of CS. The attractive interaction between CS and PEO due to the hydrogen bond formation also leads to an increase of the degradation temperature (T_d) of CS component (as shown later in Fig. 7).

In Table 1, we also note that X_c^m hardly changes with w_{CS} and is close to that in pure PEO with increasing w_{CS} up to 60 wt% but considerably decreases on a further increase of w_{CS} up to 80 wt%. This result, together with the literature data indicating the maximum PEO-CS interaction occurring at $w_{CS} = 80$ wt% [21], suggests the stoichiometric/optimum hydrogen bond formation at $w_{CS} \cong 80$ wt%. (The FTIR data discussed later in Fig. 4 were also in harmony with this argument.) The PEO crystalline content seems to decrease significantly when the stoichiometric amount of CS significantly retards the large scale motion of the PEO thereby reducing the PEO crystalline growth rate. Since the PEO crystalline growth should be faster than the diffusion of amorphous CS chains away from the PEO crystalline surface, the growth front is always facing to the CS chains [35]. Therefore, when ϕ increases significantly with increasing w_{CS} to 80 wt%, both T_m and ΔH_m ($\sim X_c^m$) of PEO decreases, as noted in Table 1.

In Fig. 3, the melting point depression (ΔT_m), evaluated from the T_m^e data shown in Table 1, is plotted against the square of CS volume fraction in blends, v_A^2 (v_A was estimated from the density of amorphous CS and PEO melt as 1.33 g/cm³ [36] and 1.09 g/cm³ [37], respectively, under an assumption of volume additivity). The density of PEO melt was utilized because the interaction parameter was estimated at the melting point.

The melting point depression reflects a favorable interaction between PEO and CS. The least-squares fit of ΔT_m against v_A^2 shown in Fig.3 gives a straight line with its intersect being close to zero, which is in accord with Eq.(2). A tiny positive intersect is insignificant and within a typical range seen for compatible polymers that is attributed to the effect of morphological changes [38] and/or the result of a residual entropic effect [39, 40]. Equation (2) with the $T_m^{0,e}$ value of 333.1 K (Table 1) was utilized to estimate the CS-PEO interaction parameter χ_{AB} . The other parameters utilized in this estimation were: $\Delta H_{Bu} = 196.8$ J/g for perfectly crystalline PEO [33], $V_{Au} = 128.57$ cm³/mol and $V_{Bu} = 40.37$ cm³/mol for amorphous CS and PEO, respectively. (The method of calculating V_{Au} and V_{Bu} is explained in the appendix). The estimation gave $\chi_{AB} = -0.21$. This negative χ_{AB} value suggests a considerable attractive interaction between CS and PEO due to the hydrogen bond formation and dipolar interaction [11, 12].

Figure 4 shows the FTIR spectra of CS, PEO, and CS/PEO blend films. For the CS film ($w_{\text{PEO}} = 0$) [11, 41], the main characteristic peaks of amino groups and amide groups (O=CR-NH attributed to chitin unit) are seen at 1568 cm^{-1} and 1655 cm^{-1} , respectively. The broad bands for stretching vibration of OH and NH_2 group are observed at 3429 cm^{-1} (O-H stretching) and 3346 cm^{-1} (N-H stretching), respectively, and this hydroxyl band is responsible for the vibration of both C3-OH and C6-OH in CS structure. The bands at 2931 and 1410 cm^{-1} , being attributed to the vibration of pyranose ring, are assigned to CH_2 stretching and OH/CH vibrations, respectively. The other bands at 1153 , 1072 and 1028 cm^{-1} are assigned to the vibration of C-O-C in CS glycosidic linkage. For the PEO film ($w_{\text{PEO}} = 1$) [11, 42, 43], we note the CH stretching (2895 cm^{-1}), CH_2 scissoring (1475 cm^{-1}), CH_2 wagging (1367 , 1350 and 968 cm^{-1}) and CH_2 twisting (1288 , 1250 and 847 cm^{-1}). The main characteristic peaks due to C-O-C stretching are seen at 1157 (C-C stretching), 1111 and 1086 cm^{-1} (CH_2 rocking). The FTIR spectrum of CS/PEO blends changes considerably from that of neat CS. The vibration bands of amino (1568 cm^{-1}), amide (1655 cm^{-1}) and hydroxyl (3429 cm^{-1}) of CS are shifted to 1555 cm^{-1} , 1643 cm^{-1} and 3385 cm^{-1} , respectively, at $w_{\text{PEO}} = 0.2$. At $w_{\text{PEO}} = 0.8$, C-O-C stretching at 1157 , 1111 , 1086 cm^{-1} are shifted to 1148 , 1101 , 1061 cm^{-1} , respectively. Moreover, the vibration bands of CH_2 groups of PEO are also shifted to lower frequency. These results suggest the specific interaction between the ether groups of PEO and the amino, amide, and hydroxyl groups of CS. For the blends with $w_{\text{PEO}} > 0.2$, the vibration bands of amino, amide and hydroxyl groups are slightly shifted to higher frequency. Among the tested compositions, the optimum interaction (the maximum change of the spectrum) is observed at $w_{\text{PEO}} = 0.2$ where the molar ratio between PEO ether oxygen and amino/hydroxyl groups of CS is 1:1. Indeed, the maximum PEO-CS interaction has been reported to occur at $w_{\text{PEO}} = 0.2$ [21]. Correspondingly, the spectra corresponding to the C-O-C stretching (seen in Fig. 4 at the wave number between 1050 cm^{-1} and 1200 cm^{-1}) hardly changes with decreasing w_{PEO} from 1 to 0.4 but are significantly distorted on a further decrease of w_{PEO} to 0.2. This result lends support to the discussion of the DSC and WAXD data made for Figs 1-3, 6.

5.2 CS and PEO Doped with Metal Ions

Krajewska [44] studied the interaction and complex formation behavior of CS doped with metal ions. He reported that K^+ does not strongly interact with CS while Ca^{2+} interacts with CS amino groups to form chelation network. These features are consistent with our observation of the degradation temperature of CS (data shown later in Fig.7): $T_d = 273.6^\circ\text{C}$, 280.0°C and 278.4°C for neat CS, Ca^{2+}/CS and K^+/CS , respectively. The highest T_d for Ca^{2+}/CS reflects the stabilization due to the chelation network formation. The Ca^{2+}/CS film was more brittle compared to the neat CS and K^+/CS films (as noted during the sample manipulation), and this property of the Ca^{2+}/CS film could also reflect the chelation. The chelation network is primarily

formed at the amino and hydroxyl groups that behave as the complex-forming ligand for metal ions. The complex formation is more significant for Ca^{2+} than K^+ , which reflects a difference in cation valency. Bi-valence metal ions are known to interact strongly with the amino groups to form inclusion complex [44], while the mono-valence metal ions are bound only peripherally with the amino groups and have a minimal effect on the thermal degradation behavior [45, 46].

For the ions-doped PEO, DSC measurements indicated a decrease in PEO crystallinity (X_c^m) in the order of $\text{Ca}^{2+}/\text{PEO} < \text{K}^+/\text{PEO} < \text{PEO}$ (data shown later in Fig.6). This decrease is attributable to the weak coulombic interaction between metal ions and PEO ether groups [47]. Weak coordination of metal ions on ether groups could also reduce X_c^m . The glass transition temperature (T_g) of K^+/PEO (-62.3°C) and $\text{Ca}^{2+}/\text{PEO}$ (-57.6°C) were lower and higher than that of neat PEO (-59.4°C), respectively. Thus, Ca^{2+} interacts with ether groups more strongly than K^+ . This complex formation naturally reduces the segmental mobility and increase T_g of $\text{Ca}^{2+}/\text{PEO}$ [48].

Figs. 8 and 9, respectively, show the FTIR spectra of K^+/CS and Ca^{2+}/CS . We note changes the vibration bands of amino, amide and hydroxyl groups of CS due to the metal ions doping. The amino, amide and hydroxyl bands in K^+/CS shifted to 1555 cm^{-1} , 1643 cm^{-1} and 3403 cm^{-1} , respectively, and those in Ca^{2+}/CS shifted to 1551 cm^{-1} , 1639 cm^{-1} and 3378 cm^{-1} , respectively. As noted from these low-wavenumber shifts, the interaction between metal ions and CS mainly occurs at the amino, amide and hydroxyl groups, and the interaction is more significant for Ca^{2+} than for K^+ . Addition of K^+ and Ca^{2+} into bulk PEO also changed the infrared spectrum compared to pure PEO (cf. Figs. 8 and 9). In K^+/PEO and $\text{Ca}^{2+}/\text{PEO}$, the C-O-C stretching vibration of pure PEO at 1157 , 1111 , 1086 cm^{-1} shifted to 1149 , 1103 , 1063 cm^{-1} and 1148 , 1099 , 1061 cm^{-1} , respectively. This result indicates that the interaction with the metal ions mainly occurs at ether groups and that the interaction is more significant for Ca^{2+} than K^+ .

5.3 CS/PEO Blends Doped with Metal Ions

The DSC measurement was conducted for K^+ - and Ca^{2+} -doped CS/PEO blends to determine T_m and X_c^m of PEO as well as T_d of CS. The melting temperature of well equilibrated PEO crystalline (T_m^e) was obtained from Hoffman-Weeks (HW) plots. In Figs. 5, 6, and 7, T_m^e , X_c^m , and T_d are plotted against w_{PEO} , respectively. The data for the ion-doped PEO ($w_{\text{PEO}} = 1$) and ion-doped CS ($w_{\text{PEO}} = 0$) are also shown.

As noted in Figs. 5 and 6, T_m^e and X_c^m of PEO decrease on the ion doping, and these decrease is larger for Ca^{2+} -doped PEO than for K^+ -doped PEO. For the CS/PEO blends, the decreases are more significant for larger w_{CS} . These results suggest that the ions are favorably interact with the ether groups of PEO to form complex [47] and this interaction is cooperatively enhanced in the presence of CS, as noted from the larger decreases of T_m^e and X_c^m at larger w_{CS} . This molecular picture of the

cooperative interaction is consistent with the increase in T_d of CS with increasing w_{PEO} shown in Fig. 7.

The FTIR spectra of K^+ - and Ca^{2+} -doped CS ($w_{\text{PEO}} = 0.0$), PEO ($w_{\text{PEO}} = 1.0$), and CS/PEO blends ($w_{\text{PEO}} = 0.2, 0.4, 0.6, 0.8$) films are shown in Figs. 8 and 9, respectively. For K^+ doped blends, DSC and WAXD data indicated that the doped salt, K_2SO_4 , was fully dissolved in blends (no residual K_2SO_4 crystals) and fully dissociated to K^+ at all w_{PEO} . In contrast, CaSO_4 was partially dissolved in particular for large w_{PEO} . Complete dissociation into Ca^{2+} and SO_4^{2-} was confirmed only for pure CS, suggesting a favorable interaction between Ca^{2+} with CS more than PEO.

As noted in Figs. 8 and 9, the vibration modes of K^+ -doped blends are not significantly different from those of undoped blends, which imply a weaker interaction between K^+ and polymers. In contrast, the Ca^{2+} doping substantially changes the vibration bands of amino, amide and hydroxyl groups of CS (at 1568, 1655, and 3429 cm^{-1} , respectively) and of the ether groups of PEO (at 1157, 1111, 1086 cm^{-1}), despite the incomplete dissociation of the doped salt, CaSO_4 explained earlier. In the presence of Ca^{2+} , the vibration bands of the blends corresponding to the functional groups of CS and PEO shifted to lower frequencies. These results suggest that Ca^{2+} interacts specifically with the amino, amide and hydroxyl groups of CS as well as with the ether groups of PEO. Ca^{2+} seems to serve as a transient cross-linker to form a stable CS/ Ca^{2+} /PEO complex and less significant complex formation occurs for K^+ [48]. The hydrogen bonding between CS and PEO in the undoped CS/PEO blend was replaced by ion-dipole interaction between Ca^{2+} and polymers. Specifically, the vibrational frequencies of the amino, amide and hydroxyl groups are the lowest at $w_{\text{PEO}} = 0.2$ (CS:PEO molar ratio 1:1) and increase for $w_{\text{PEO}} > 0.2$, suggesting that, among the tested concentrations, the ion-dipole interaction is the strongest at $w_{\text{PEO}} = 0.2$. This w_{PEO} value coincides with the literature value for the maximum PEO-CS interaction in undoped blends [21], which suggests that the effect of Ca^{2+} doping is the largest when the PEO-CS interaction in the absence of the ions is the strongest.

Here, a comment needs to be made for the CS/Metal/PEO molar ratio. In the ion-doped blend with $w_{\text{PEO}} = 20$ wt%, this ratio was CS/Metal/PEO = 5/1/5 and thus the ion concentration C_{ion} was 20 mol% of the stoichiometric concentration C_{ion}^* required for full bridging of all active functional groups of the PEO and CS chains. Nevertheless, the effect of Ca^{2+} -doping was the strongest for $w_{\text{PEO}} = 20$ wt% (as explained above), possibly because of the following reason. In the absence of Ca^{2+} , the blend with $w_{\text{PEO}} = 20$ wt% exhibited the strongest PEO-CS interaction through the stoichiometric hydrogen bonding (as discussed earlier), and Ca^{2+} replaced this hydrogen bond by the stronger PEO- Ca^{2+} -CS bond (thereby effectively destabilizing the hydrogen bond). A considerable fraction of the functional groups of the PEO and CS chains would have been bridged through Ca^{2+} (having $C_{\text{ion}} = 0.2C_{\text{ion}}^*$) and thus the conformation of these chains would have been largely distorted, which should hinder

the remaining (unbridged) hydrogen bonds from surviving substantially. Then, in the range of w_{PEO} examined, the strongest effect of the Ca^{2+} -doping (strongest destabilization of the hydrogen bond) would emerge at $w_{\text{PEO}} = 20$ wt%, as observed above.

5.4 MD Simulation and RDF Analysis

Molecular dynamics (MD) simulations of the CS/PEO blend were carried out to investigate the specific groups of CS and PEO that interact with each other. To obtain clear molecular pictures for the CS/PEO blends and the complex with metal ions, the CS hydroxyl groups were separated into C3-OH and C6-OH for the radial distribution function analysis. The results (not shown here) suggested that the miscibility of CS and PEO was mainly attributed to the amino (NH_2), hydroxyl (C3-OH) and hydroxymethyl (C6-OH) groups in CS interacting with the ether groups (-O-) in PEO. Among all CS functional groups, NH_2 was found to have the highest activity to interact with the ether groups of PEO. The C6-OH groups had more room to interact with PEO ether groups compared to C3-OH groups.

The interaction between CS and PEO in cation-doped blends was also investigated through the simulation. Although the COMPASS field utilized in the simulation is approximate (as explained earlier), significant differences were observed for the K^+ - and Ca^{2+} -doped blends under the same force field. Thus, the simulation results can be safely utilized to discuss the differences of the interaction in these blends at least qualitatively.

The radial distribution function $g(r)$ was evaluated from the MD simulation (in a stable simulation period). Fig. 10 shows plots of $g(r)$ against a radial distance (r) from the metal ions in the K^+ -doped and Ca^{2+} -doped blends at $w_{\text{PEO}} = 0.2$. The $g(r)$ peaks seen at $r = 2.3\text{-}2.9$ Å are indicative of the definite correlation between atoms and correspond to the specific distance of the closely coupled atoms. The absence of peaks at $r > 4$ Å indicates that there is no long-range correlation in the systems.

As can be noted in Fig.10, the NH_2 , C3-OH and C6-OH groups of CS as well as the ether groups of PEO are located within the first solvation shell of the cations in the doped blends. For all these groups, the radial distance r^* for the $g(r)$ peak (the distance in the first coordination shell) is smaller whereas the $g(r)$ peak is higher in the Ca^{2+} -doped blend than in the K^+ -doped blend. As judged from these results, the number of active sites available for the interaction with those functional groups of polymers is possibly larger for the multi-valent Ca^{2+} than for the mono-valent K^+ (and the stable CS/ Ca^{2+} /PEO complex was formed accordingly [48]). Both Ca^{2+} and K^+ seem to interact more strongly with CS than with PEO because CS has a larger number of interacting functional groups.

As noted in Figure 10, r^* is smaller for the C3-OH and C6-OH groups than for the NH_2 group and thus the interaction between the NH_2 groups and metal ions could be weaker than that between the OH groups and the ions. (The NH_2 group may be

subjected to a larger steric effect due to the two H atoms connecting to N, which could weaken the interaction.) The interaction with the metal ions may be a little stronger for the C3-OH group than for the C6-OH group, as suggested from the smaller r^* and higher $g(r)$ peak for the former group. This difference may be attributed to the location of the C3-OH and C6-OH groups on the CS chain with respect to the NH_2 group; the C3-OH and NH_2 groups are located at the same side of the pyranose ring while C6-OH group is located at the other side. Thus, the C3-OH and NH_2 groups could interact with the metal ion cooperatively, while this cooperativity does not exist for the C6-OH group (to weaker the interaction with the metal ion).

Fig. 11 compares $g(r)$ obtained from NVT simulation at 298 K for neat and metal-doped CS/PEO blends. The correlation between PEO ether group with C3-OH, C6-OH and NH_2 of CS is larger in the presence of Ca^{2+} (solid curves) than in the absence (dashed and dotted curves), and Ca^{2+} appears to enhance the interactions between PEO ether groups and all CS functional groups. This result offers a comprehensible picture of the CS/ Ca^{2+} /PEO complex formation [48]. Due to the strong interaction between Ca^{2+} and polymers, Ca^{2+} should act as a transient cross-linker to enlarge the interaction of all neighborhood functional groups of CS and PEO and enhance the correlation of all these groups. In contrast, K^+ weakens the correlation between PEO ether groups and all CS functional groups as compared to that in the neat blend. This observation reflects an insignificant and unstable complex formation in the K^+ -doped system. As a result, K^+ appears to interact separately/individually with CS and/or PEO functional groups.

The dynamics of K^+ and Ca^{2+} in CS/PEO matrix was also studied by the MD simulations. Snapshots of Ca^{2+} -doped blend clearly indicated that Ca^{2+} cannot diffuse even at the unrealistically high simulation temperature ($T = 800$ K). Ca^{2+} ions were trapped within the chelation structure between CS and PEO that corresponded to a stable CS/ Ca^{2+} /PEO complex formation. This result is consistent with a very low direct current conductivity of the Ca^{2+} -doped blend (a little lower even compared to the conductivity of undoped blends) seen in a preliminary electrical test [48]. In contrast, at 800 K, K^+ was found to diffuse over a large distance (in a rather limited time scale of our simulation) through the hopping mechanism within CS/PEO matrix and had a large diffusion coefficient, $D \cong 1.7 \times 10^{-6}$ cm^2/s . This result, again consistent with the result of the preliminary electrical test (conductivity much higher for the K^+ -doped blend than for the undoped blend) [48], reflects a weak interaction between K^+ with CS and PEO. This weak interaction is in harmony with the insignificant and unstable complex formation in the K^+ -doped system suggested from the WAXD, DSC, and FTIR data presented in this paper. Thus, the simulation made in this study appears to capture the behavior of real Ca^+ and K^+ cations in the CS/PEO blends (although the *effective* valences of these real cations could be somewhat different from the nominal valences of +2 and +1 utilized in the simulation).

6. Conclusion

This study examined the interaction in CS/PEO blends, a material useful as a host matrix for solid polymer electrolyte (SPE). CS and PEO were found to be miscible ($\chi_{AB} = -0.21$) through CS-PEO hydrogen binding. The optimum blend composition for the strongest PEO-CS interaction (most enhanced miscibility) was close to the stoichiometric composition for the full CS-PEO hydrogen bonding, $w_{PEO} = 0.2$ (where the ether oxygen of PEO and amino and hydroxyl groups of CS had 1:1 composition). Because of the miscibility, CS tended to suppress the crystallization of PEO, whereas PEO suppressed thermal degradation of CS. These features, together with compensation of the CS rigidity/brittleness due to PEO, allow the CS/PEO blends to be utilized for the SPE application.

In the K^+ - and Ca^{2+} -doped blends, the metal ions favorably interacted with the PEO ether groups to form complexes. This interaction was cooperatively enhanced in the presence of CS (through the interaction with the amino and hydroxyl groups of CS). Ca^{2+} appeared to behave as a transient cross-linker to form stable CS/ Ca^{2+} /PEO complex. On the other hand, K^+ interacted with PEO/CS much less significantly. Accordingly, for SPE with high conductivity, the alkali metal ion is more suitable as a dopant compared to the alkali earth metal ion. The conductivity and ions mobility will be focused in our future work.

APPENDIX

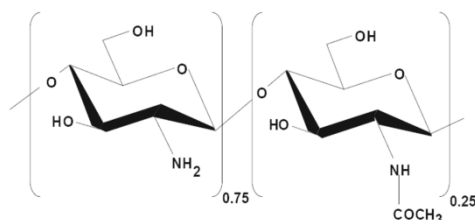
Calculation of Molar Volume of PEO and CS Repeating Unit

PEO: MW of repeat unit of PEO = 44 g/mol

Density of PEO is 1.09 g/cm³ [37]

Molar volume of PEO repeat unit, $V_{Au} = MW/d = 44/1.09 = 40.37$ cm³/mol

CS: The degree of deacetylation of 75%



MW of repeat unit of CS = $(161 \times 0.75) + (203 \times 0.25) = 171.5$ g/mol

Density of CS is 1.33 g/cm³ [36]

Molar volume of CS repeat unit, $V_{Au} = MW/d = 171.5/1.33 = 128.57$ cm³/mol

Acknowledgement

NR would like to thank the Office of the Higher Education Commission, Thailand for supporting by grant fund under the program Strategic Scholarships for Frontier Research Network for the Joint Ph.D. Program Thai Doctoral degree for this research. The authors would like to thank National Nanotechnology Center (NANOTEC), National Science and Technology Development Agency (NSTDA), Thailand for the permission to use molecular simulation software through National Nanoscience Consortium (CNC) and thanks Synchrotron Light Research Institute (SLRI), Thailand for our collaboration, in particular Dr. Waraporn Tanthanuch and Dr. Kanjana Thumanu, at IR beamline.

References

1. Yahya MZA and Arof AK. *European Polymer Journal* 2003;39(5):897-902.
2. Winie T and Arof A. *Ionics* 2006;12(2):149-152.
3. Mohamed NS and Arof AK. *Journal of Power Sources* 2004;132(1-2):229-234.
4. Vincent CA. *Electrochimica Acta* 1995;40(13-14):2035-2040.
5. Kadir MFZ, Majid SR, and Arof AK. *Electrochimica Acta* 2010;55(4):1475-1482.
6. Kadir MFZ, Teo LP, Majid SR, and Arof AK. *Materials Research Innovations* 2009;13:259-262.
7. Khair ASA, Majid SR, Idris NH, Hassan MF, Puteh R, and Arof AK. *Journal Materials Science Forum* 2006;517:237-241.
8. Buraidah MH, Teo LP, Majid SR, Yahya R, Taha RM, and Arof AK. *International Journal of Photoenergy* 2010;2010:7.
9. Sakurai K, Maegawa T, and Takahashi T. *Polymer* 2000;41(19):7051-7056.
10. Alexeev VL, Kelberg EA, Evmenenko GA, and Bronnikov SV. *Polymer Engineering & Science* 2000;40(5):1211-1215.
11. Zivanovic S, Li J, Davidson PM, and Kit K. *Biomacromolecules* 2007;8(5):1505-1510.
12. Sashina E, Vnuchkin A, and Novoselov N. *Russian Journal of Applied Chemistry* 2006;79(10):1643-1646.
13. Takahashi Y and Tadokoro H. *Macromolecules* 1973;6(5):672-675.
14. Shuo Z. *Poly(ethylene oxide)-Based Composite Polymer Electrolytes for The Secondary Lithium Batteries*. Chemical and Environmental Engineering, vol. Master. Singapore: National University of Singapore, 2004.
15. Fuentes S, Retuert PJ, and González G. *Electrochimica Acta* 2007;53(4):1417-1421.
16. Mohamad SA, Yahya R, Ibrahim ZA, and Arof AK. *Solar Energy Materials and Solar Cells* 2007;91(13):1194-1198.

17. Donoso JP, Lopes LVS, Pawlicka A, Fuentes S, Retuert PJ, and González G. *Electrochimica Acta* 2007;53(4):1455-1460.
18. Idris N, Senin H, and Arof A. *Ionics* 2007;13(4):213-217.
19. Idris N, Majid S, Khair A, Hassan M, and Arof A. *Ionics* 2005;11(5):375-377.
20. Neto CGT, Dantas TNC, Fonseca JLC, and Pereira MR. *Carbohydrate Research* 2005;340(17):2630-2636.
21. Wang W and Roberts GAF. *Advances in Chitin Science* 1997;2:561-566
22. *Materials studio 4.2*. San Diego: Accelrys, 2007.
23. Sun H. *Journal of Physical Chemistry B* 1998;102(38):7338-7364.
24. Sun H. *Computational and Theoretical Polymer Science* 1998;8(1-2):229-246.
25. Rigby D, Sun H, and Eichinger BE. *Polymer International* 1997;44(3):311-330.
26. Andersen HC. *The Journal of Chemical Physics* 1980;72(4):2384-2393.
27. Andersen HC. *Journal of Computational Physics* 1983;52(1):24-34.
28. Berendsen HJC, Postma JPM, van Gunsteren WF, DiNola A, and Haak JR. *The Journal of Chemical Physics* 1984;81(8):3684-3690.
29. Rigby D. *Fluid Phase Equilibria* 2004;217(1):77-87.
30. Nishi T and Wang TT. *Macromolecules* 1975;8(6):909-915.
31. Radhakrishnan S and Venkatachalapathy PD. *Polymer* 1996;37(16):3749-3752.
32. Rakkapao N, Vao-soongnern V, Watanabe H, and Masubuchi Y. Miscibility of Chitosan/Poly(ethylene oxide) Blends: Simulation and Experiment. Unpublished results.
33. Pielichowski K, Flejtuch K, and Pielichowski J. *Polymer* 2004;45(4):1235-1242.
34. Hoffman JD and Weeks JJ. *J. Res. Nat. Bur. Stand. Sect. A.* 1962;66(1):13-28.
35. Lisowski MS, Liu Q, Cho J, Runt J, Yeh F, and Hsiao BS. *Macromolecules* 2000;33(13):4842-4849.
36. Deepak AM and Ashwani K. *Journal of Applied Polymer Science* 2000;77(8):1782-1793.
37. Roe R-J. *Journal of Physical Chemistry* 1968;72(6):2013-2017.
38. Walsh D and Rostami S. The miscibility of high polymers: The role of specific interactions. *Key Polymers Properties and Performance*, 1985. pp. 119-169.
39. Paul DR and Barlow JW. *Polymer* 1984;25(4):487-494.
40. Ziska JJ, Barlow JW, and Paul DR. *Polymer* 1981;22(7):918-923.
41. Pawlak A and Mucha M. *Thermochimica Acta* 2003;396(1-2):153-166.
42. Su Y-l, Wang J, and Liu H-z. *Journal of Colloid and Interface Science* 2002;251(2):417-423.
43. Ramesh S, Yuen TF, and Shen CJ. *Spectrochimica Acta Part A: Molecular and Biomolecular Spectroscopy* 2008;69(2):670-675.
44. Krajewska B. *Reactive and Functional Polymers* 2001;47(1):37-47.

45. Sreenivasan K. *Polymer Degradation and Stability* 1996;52(1):85-87.
46. Trimukhe KD and Varma AJ. *Carbohydrate Polymers* 2009;75(1):63-70.
47. Jaipal Reddy M and Chu PP. *Solid State Ionics* 2002;149(1-2):115-123.
48. Rakkapao N, Watanabe H, Masubuchi Y, Matsumiya Y, and Vao-soongnern V. Mobility of Alkali and Alkali Earth Metal Ions within Chitosan/Poly(ethylene oxide) Blends Matrix. Unpublished results.

Table Captions

Table 1 Equilibrium melting temperatures (T_m^e), degree of crystallinity (X_c^m) and stability parameters (ϕ) of PEO crystal for pure PEO and CS/PEO blends.

Figure Captions

- Figure 1 Wide angle X-ray diffraction (WAXD) patterns for CS/PEO blends. The numbers adjacent to the WAXD patterns indicates the CS content, w_{CS} (in wt %)
- Figure 2 Hoffman-Weeks plots of the melting temperature (T_m) and crystallisation temperature (T_c), for CS/PEO blends with different w_{CS} .
- Figure 3 Melting point depression analysis for CS/PEO blends. The interaction energy density, obtained as the slope of the plot, was $B = -1.06 \text{ cal/cm}^3$.
- Figure 4 FTIR spectra of CS, PEO and CS/PEO blends.
- Figure 5 Depression of melting temperature of fully equilibrated PEO crystalline (T_m^e) in CS/PEO blends and the ion-doped blends.
- Figure 6 Degree of crystallinity (X_c^m) of PEO in CS/PEO and ion-doped blends.
- Figure 7 Degradation temperature (T_d) of CS in undoped and ion-doped CS/PEO blends.
- Figure 8 FTIR spectra of K^+ doped into pure CS, pure PEO and CS/PEO blends.
- Figure 9 FTIR spectra of Ca^{2+} doped into pure CS, pure PEO and CS/PEO blends.
- Figure 10 Radial distribution functions (RDFs) for the system of K^+ - and Ca^{2+} -doped CS/PEO blends with w_{PEO} of 0.2. This function represents the relative distances between metal ions (K^+ and Ca^{2+}) and nitrogen atom in the amino (NH_2) group, oxygen atom in the hydroxyl (C3-OH) and hydroxymethyl (C6-OH) groups of CS as well as ether oxygen atom of PEO.
- Figure 11 Radial distribution functions (RDFs) for undoped CS/PEO blends with w_{PEO} of 0.2 and for the K^+ - and Ca^{2+} -doped blends.

Tables

Table 1 Equilibrium melting temperatures (T_m^e), degree of crystallinity (X_c^m) and stability parameters (ϕ) of PEO crystal for pure PEO and CS/PEO blends.

% wt of CS in blends (w_{CS})	Mole fraction of CS in blends	T_m^e (K)	% X_c^m	$\phi (\times 10^{-3})$
0 wt%	0.00	333.1	77	2
20 wt%	0.06	332.2	71	4
40 wt%	0.15	331.3	71	11
60 wt%	0.28	330.0	72	13
80 wt%	0.51	328.3	62	20

Figures

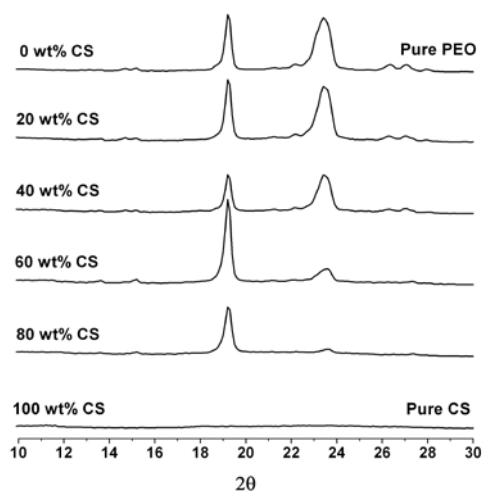


Figure 1 Wide angle X-ray diffraction (WAXD) patterns for CS/PEO blends. The numbers adjacent to the WAXD patterns indicates the CS content, w_{CS} (in wt %).

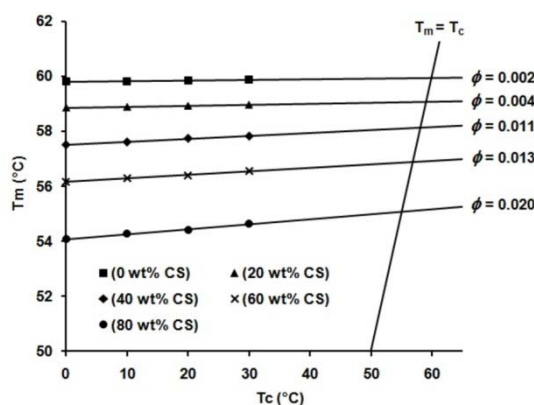


Figure 2 Hoffman-Weeks plots of the melting temperature (T_m) and crystallisation temperature (T_c), for CS/PEO blends with different w_{CS} .

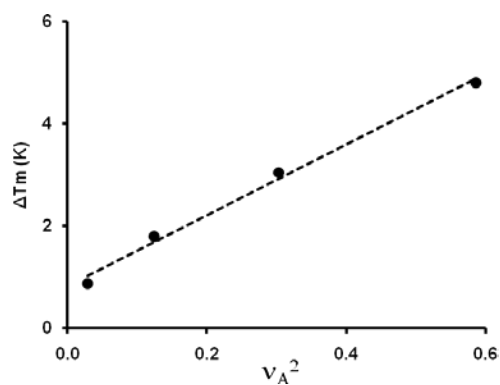


Figure 3 Melting point depression analysis for CS/PEO blends. The interaction energy density, obtained as the slope of the plot, was $B = -1.06 \text{ cal/cm}^3$.

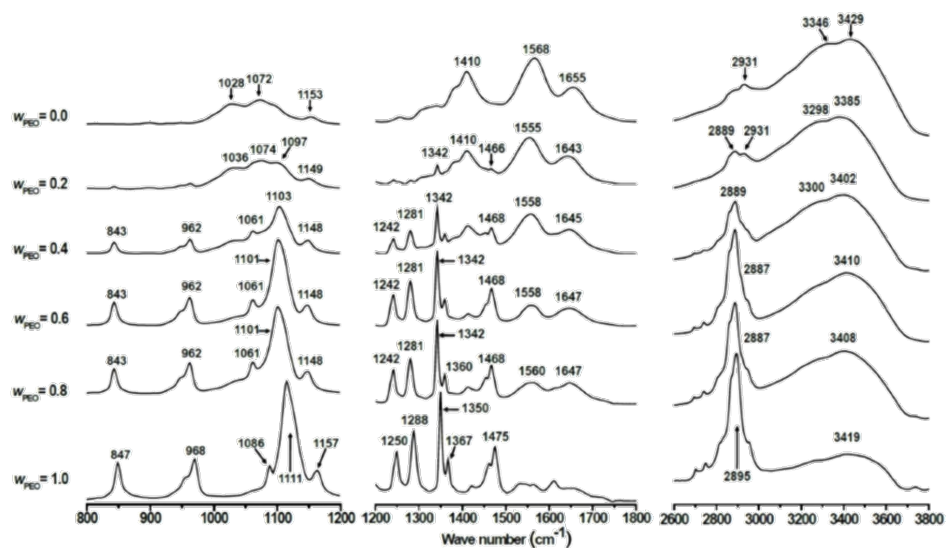


Figure 4 FTIR spectra of CS, PEO and CS/PEO blends.

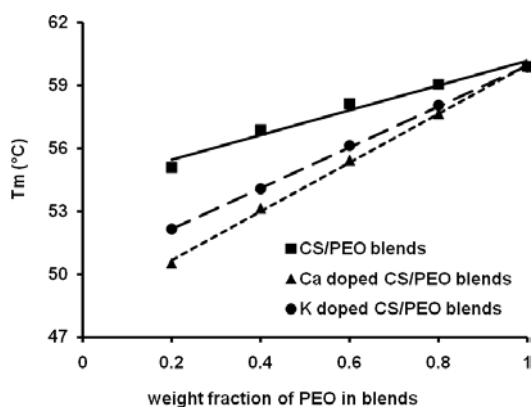


Figure 5 Depression of melting temperature of fully equilibrated PEO crystalline (T_m) in CS/PEO blends and the ion-doped blends.

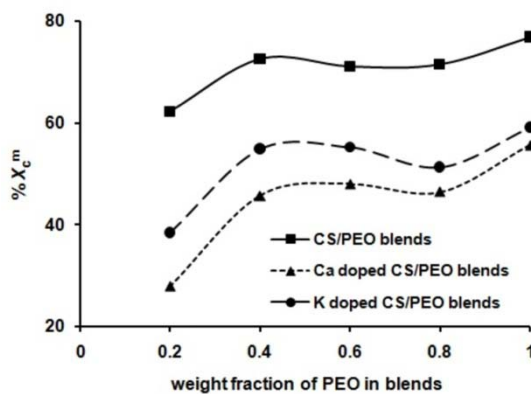


Figure 6 Degree of crystallinity (X_c^m) of PEO in CS/PEO and ion-doped blends.

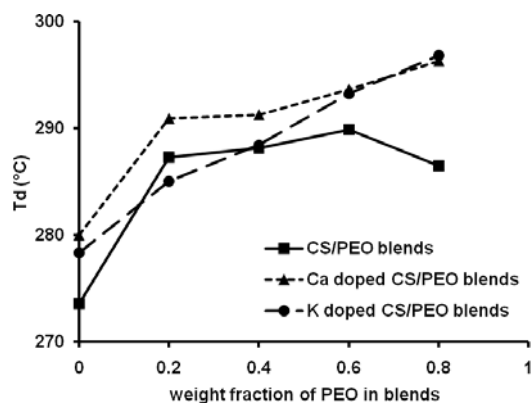


Figure 7 Degradation temperature (T_d) of CS in undoped and ion-doped CS/PEO blends.

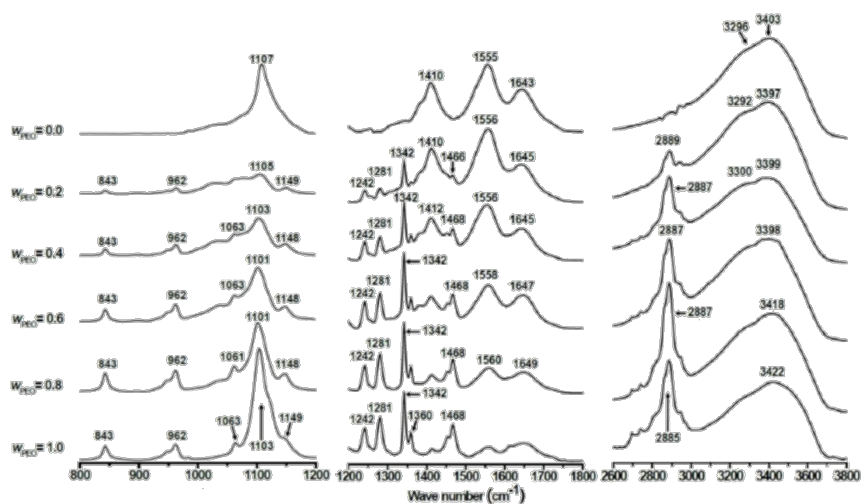


Figure 8 FTIR spectra of K^+ doped into pure CS, pure PEO and CS/PEO blends.

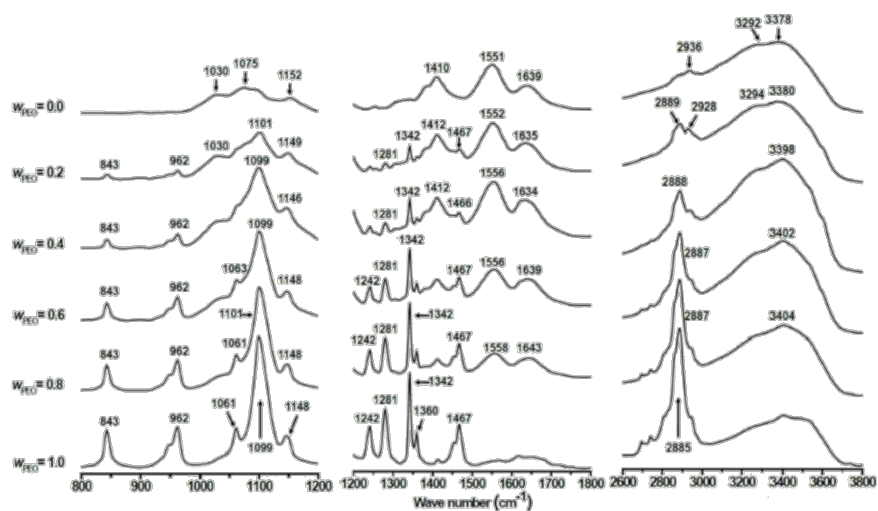


Figure 9 FTIR spectra of Ca^{2+} doped into pure CS, pure PEO and CS/PEO blends.

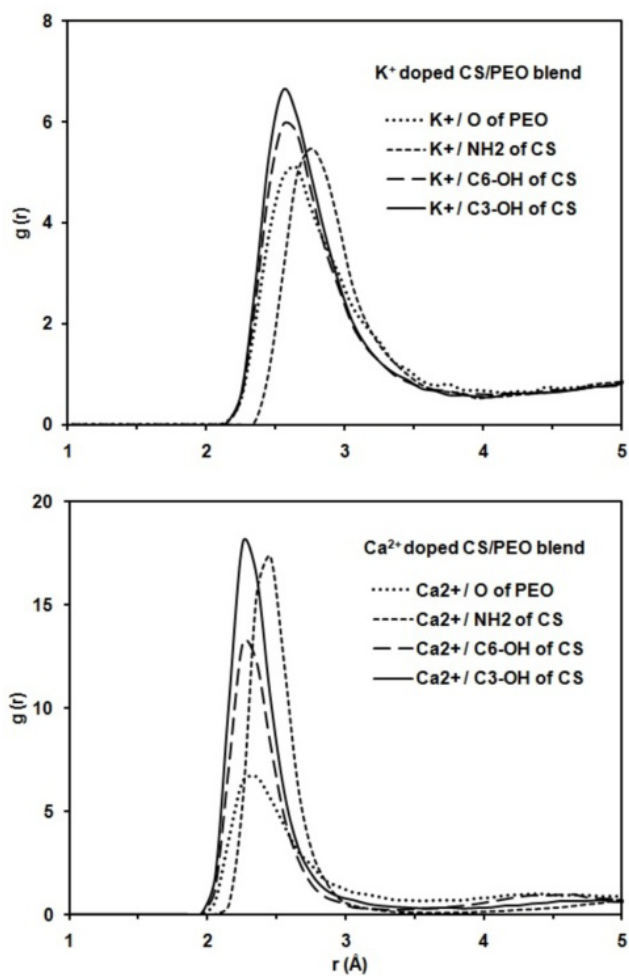


Figure 10 Radial distribution functions (RDFs) for the system of K⁺- and Ca²⁺-doped CS/PEO blends with w_{PEO} of 0.2. This function represents the relative distances between metal ions (K⁺ and Ca²⁺) and nitrogen atom in the amino (NH₂) group, oxygen atom in the hydroxyl (C3-OH) and hydroxymethyl (C6-OH) groups of CS as well as ether oxygen atom of PEO.

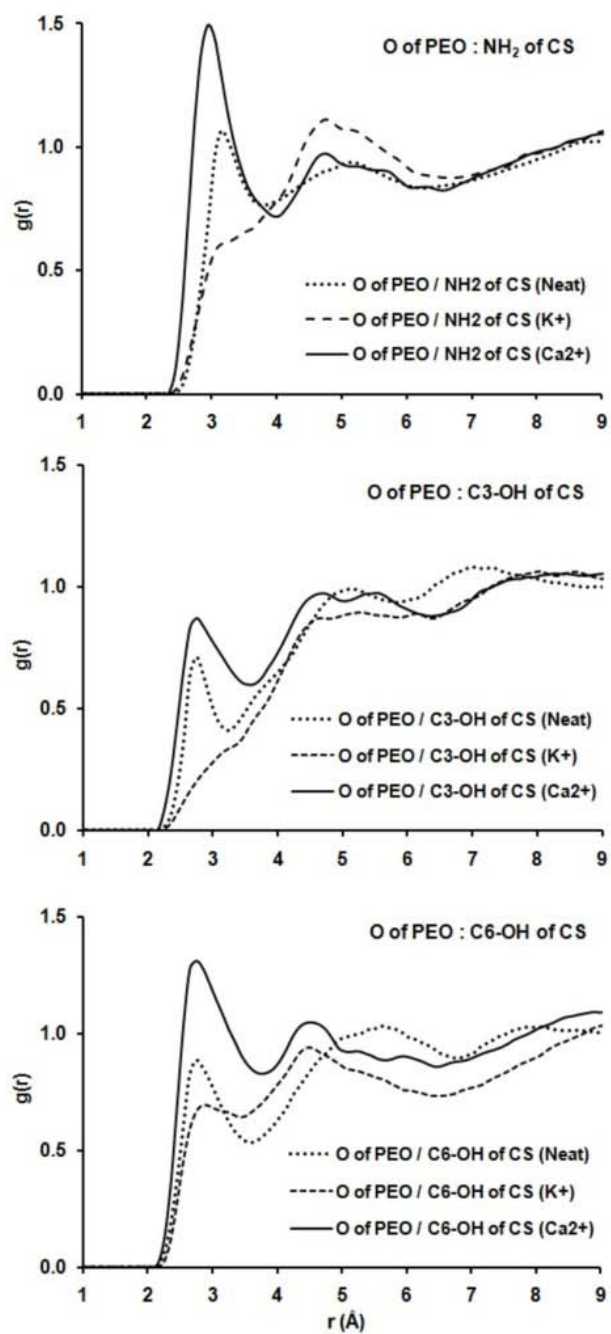


Figure 11 Radial distribution functions (RDFs) for undoped CS/PEO blends with w_{PEO} of 0.2 and for the K^+ - and Ca^{2+} -doped blends.

CURRICULUM VITAE

NATTHIDA RAKKAPAO

E-mail: dearnattida@hotmail.com

Born: April 3, 1983, Suratthani, Thailand

Citizenship: Thailand

Education:

2001-2004 B.Sc. in Chemistry (2nd Class Honors), Maejo University, Thailand

Scholarship:

2005-2007 Scholarship for Student with Outstanding Academic Performance, Suranaree University of Technology, Nakhon Ratchasima, Thailand.

2006-2010 The Program Strategic Scholarships for Frontier Research Network for the Joint Ph.D. Program Thai Doctoral Degree from the Office of the Higher Education Commission, Thailand. (Sandwich Program)

Research Experience:

2005-2007 Assistant researcher of National Nanotechnology Center, Thailand.

2007-2008 Assistant researcher of National Synchrotron Research Center, Nakhon Ratchasima, Thailand.

2008-2009 Visiting researcher for 1 year in Laboratory of Molecular Rheology, Institute for Chemical Research, Kyoto University, Japan under the supervision of Professor Dr. Hiroshi Watanabe.